

UNIVERSITÀ DI PISA

Facoltà di Ingegneria

Corso di Laurea Specialistica in Ingegneria Aerospaziale

Development of FPGA-based Controllers for a Laboratory Model of a Spherical Inertial Reference Sensor with Optical Readout

Supervisors:

Prof. Giovanni Mengali

Dr. Dennis Weise

Dipl.-Ing. Harald Kögel

Candidate:

Jessica Cenni

A.A. 2014/2015

A mia sorella.

*Our greatest glory is, not in never falling,
but in rising every time we fall.*

O. Goldsmith

Abstract

Field Programmable Gate Arrays (FPGAs) are powerful and flexible instruments, particularly suited for the implementation of servo loops for experimental setups since they allow to frequently change the system without hardware modifications, thus resulting in a time and cost effective solution. Two FPGA-based controllers are presented in this thesis, developed in the frame of the construction of a laboratory model to investigate a novel inertial sensor concept for laser ranging space missions.

The specific context of this work is the study of an alternative opto-mechanical architecture for the eLISA mission payload, for which an inertial reference sensor with a spherical test mass and optical readout has been proposed. Thanks to the possibility to operate the system in a full drag-free mode offered by the geometry of the test mass and to the high accuracy of the interferometric measurement of its center of mass, an advantage in terms of noise sensitivity of the sensor should be achieved with respect to the current baseline design. To validate this concept, a proof of its feasibility and an assessment of its performance need to be obtained with an earthbound laboratory model, whose success also relies, among other things, on the possibility to have stable laser signals for interferometric detection and a free-flying test mass kept in a steady position by a levitation system.

Both these targets can be achieved through the implementation of an active control system stabilizing laser intensity via acousto-optic modulation in one case, and test mass height by means of a current modulated magnetic field in the other. The used servo loops, based on PID control scheme and implemented on a National Instruments FPGA board, are here described, focusing on the experimental characterization of the sensing and actuation hardware and on the controllers' design through LabVIEW programming. Finally, the experimental trials carried out are illustrated, presenting the achieved results in terms of laser RIN reduction, the issues encountered for the test mass levitation and possible strategies for overcoming them in the continuation of the project.

Sommario

Gli FPGA sono strumenti potenti e flessibili, particolarmente adatti all'implementazione di servocontrollori per *setup* sperimentali dal momento che permettono di cambiare frequentemente il sistema senza modifiche *hardware*, traducendosi così in una soluzione efficiente in termini di risparmio sia di costo che di tempo. In questa tesi vengono presentati due controllori basati sull'uso di FPGA, sviluppati nell'ambito della costruzione di un modello di laboratorio per investigare un nuovo concetto di sensore inerziale per missioni spaziali di metrologia laser.

Il contesto specifico di questo lavoro è quello dello studio di un'architettura opto-meccanica alternativa per il *payload* della missione eLISA, per il quale è stato proposto l'uso di un sensore di riferimento inerziale con una massa di prova sferica e un sistema di misura ottico. Grazie alla possibilità di operare il sistema in modalità completamente *drag-free* offerta dalla geometria della massa di prova e all'elevata precisione del sistema interferometrico di misura del suo centro di massa, si dovrebbe ottenere un vantaggio in termini di sensibilità al rumore del sensore rispetto alla soluzione di riferimento. Per convalidare questo concetto, la prova della sua fattibilità e una stima delle sue prestazioni devono essere ottenute tramite un modello sperimentale terrestre, la cui riuscita dipende anche, tra le altre cose, dalla possibilità di avere a disposizione segnali laser stabili per il rilevamento interferometrico e una massa di prova sospesa in una posizione fissa tramite un sistema di levitazione.

Entrambi questi obiettivi possono essere raggiunti tramite l'implementazione di un sistema di controllo attivo che stabilizzi l'intensità del laser tramite modulazione acusto-ottica in un caso, e l'altezza della massa di prova attraverso un campo magnetico regolato da corrente elettrica nell'altro. I servosistemi usati, basati su uno schema di controllo PID e implementati su una scheda FPGA della National Instruments, vengono qui descritti, concentrandosi sulla caratterizzazione sperimentale dei dispositivi di rilevazione e attuazione e sulla progettazione dei controllori tramite programmazione LabVIEW. Infine, vengono illustrate le prove sperimentali condotte, presentando i risultati ottenuti in termini di riduzione del rumore di ampiezza relativo (RIN) del laser, i problemi incontrati per la levitazione della massa di prova e alcune possibili strategie per il superamento degli stessi nell'avanzamento del progetto.

Acknowledgments

This thesis is the result of an amazing stage experience at the Laboratory of Enabling Technologies of Airbus DS in Friedrichshafen: the time I spent there was highly formative, from so many points of view, and I'm deeply grateful for it. Therefore I want to thank Prof. Giovanni Mengali and Stefano Lucarelli who opened the door for this possibility in the first place. My sincere thanks also to Dr. Ulrich Johann, Head of the Department AED41, who enabled this thesis and to Dr. Dennis Weise and Dr. Ewan Fitzsimmons, who gave me the opportunity to work in such an interesting context and supervised my work.

Many thanks to all the LET work team, who warmly welcomed me and always gave me big support: it was great to work with and learn from all of you. A special thanks to Harald, who followed my work day by day with great patience and provided me with incomparable help: it was an honor to be your student and a real pleasure to get to know you.

My warm thanks also to all the friends I've met during this German adventure: to the students and interns who made my days in the Company and outside so amusing, to the well established 'Italian connection' on the Bodensee who made me feel a bit closer to home and, last but not least, to Marica and Maja: two wonderful women I'm really glad to have met and whose friendship sustained me so much in the toughest moments of the past year.

This experience was certainly an important part of my studies, nevertheless it was only the closure of a bigger path, which proofed longer and harder than expected but also as rich and intense as I would have never imagined. Therefore I want to spend a few words here to express my gratitude to all those people who shared a part of this path with me. To the University mates and flatmates of the years in Pisa, to all the Italian and international pals of the adventures overseas, especially my dearest 'Urbanini', to all my friends: thanks for helping me to get closer to the woman I want to be and the engineer I hope to become.

A special thanks to Alice, who's been bearing my wandering nature for so many years and still finds some time to meet up whenever I head back home; to Marilena, a reference as engineer and a unique friend, who understands my difficulties as no one else; to Fabio, one of the most generous person I've ever met, for never stop helping me and believing in my capabilities; to Claudia: we've shared so much and gone through so many things together in the last years that every thing I could say would sound reductive...so, simply, thank you.

A huge thanks goes to all my family: my parents, my sister Deborah and all my kins, included the 'newbies' Matilde and Federico whose pure and joyful love was one of the best cure I could receive during stressful periods. Thank you all for having always supported and sustained me, and never stopped to show me your affection, no matter how distant I was.

Finally, a thanks from the bottom of my heart to my mum: for the unconditioned love and the strength you always show me and for giving me the smile with which I did and always will try to face every challenge of my life.

Questa tesi è il risultato di un'incredibile esperienza di tirocinio al Laboratory for Enabling Technologies di Airbus DS a Friedrichshafen: il tempo trascorso lì è stato altamente formativo, sotto tanti punti di vista, e ne sono profondamente grata. Perciò voglio ringraziare il Prof. Giovanni Mengali e Stefano Lucarelli che hanno in primo luogo aperto la porta a questa possibilità. Un sincero ringraziamento anche al Dr. Ulrich Johann, capo del Dipartimento AED41, che ha reso possibile questa tesi e al Dr. Dennis Weise e Dr. Ewan Fitzsimmons che mi hanno dato l'opportunità di lavorare in un contesto così interessante e hanno supervisionato il mio lavoro.

Grazie a tutto il gruppo di lavoro del LET, che mi ha accolto calorosamente e mi ha sempre dato un gran sostegno: è stato un piacere lavorare e imparare da tutti voi. Un ringraziamento speciale a Harald, che ha seguito il mio lavoro giorno per giorno con grande pazienza e mi ha dato un aiuto incomparabile: è stato un onore essere una tua studentessa e un vero piacere conoscerti.

Un affettuoso ringraziamento anche a tutti gli amici incontrati durante questa avventura tedesca: agli studenti e i tirocinanti che hanno reso così divertenti le giornate in azienda e fuori, alla ormai consolidata ‘Italian connection’ sul Bodensee che mi ha fatto sentire un po’ più vicina a casa e, ultime ma non per importanza, a Marica e Maja: due donne eccezionali che sono veramente felice di aver conosciuto e la cui amicizia mi ha sostenuto così tanto nei momenti più duri dell’ultimo anno.

Questa esperienza è stata certamente una parte importante dei miei studi, ma nonostante ciò è solo la conclusione di un percorso ben più ampio, che si è dimostrato più lungo e duro del previsto ma anche ricco e intenso come mai avrei immaginato. Perciò voglio ora spendere qualche parola per esprimere la mia gratitudine a tutti coloro che hanno condiviso con me una parte di questo cammino. Ai colleghi di Università e alle coinquiline degli anni pisani, a tutti i compagni italiani e internazionali delle avventure oltroceano, specialmente i miei cari ‘Urbanini’, a tutti i miei amici: grazie per avermi aiutato ad avvicinarmi alla donna che voglio essere e all’ingegnere che spero di diventare.

Un ringraziamento speciale ad Alice, che ormai da tanti anni sopporta la mia natura girovaga e trova sempre un po’ di tempo per rivedersi ogni volta che torno a casa; a Marilena, un riferimento come ingegnere e un’amica unica, che capisce come nessun’altro alcune mie difficoltà; a Fabio, una delle persone più generose che abbia mai conosciuto, per non aver mai smesso di aiutarmi e di credere nelle mie capacità; a Claudia: abbiamo condiviso così tanto e affrontato così tante cose insieme negli ultimi anni, che qualsiasi cosa possa dire suonerebbe riduttiva...quindi, semplicemente, grazie.

Un enorme grazie va poi a tutta la mia famiglia: i miei genitori, mia sorella Deborah e tutti i miei parenti, inclusi i ‘nuovi arrivati’ Matilde e Federico il cui affetto puro e gioioso è stata una delle migliori cure che potessi ricevere nei periodi di stress. Grazie a tutti voi per avermi sempre supportato e sopportato e non aver mai smesso di farmi sentire il vostro affetto, non importa quanto fossi distante.

Infine, un grazie dal profondo del cuore a mia mamma: per l'amore incondizionato e la forza che mi dai continuamente e per avermi donato il sorriso con cui ho sempre cercato e cercherò di affrontare ogni sfida della mia vita.

Contents

| | |
|---|-------------|
| List of Acronyms and Abbreviations | viii |
| List of Figures | xi |
| List of Tables | xii |
| 1 Introduction and outline of the thesis | 1 |
| 2 Scientific and technical framework of the project | 3 |
| 2.1 The eLISA mission | 3 |
| 2.1.1 The scientific target of the mission: gravitational waves | 3 |
| 2.1.2 Mission overview and baseline payload design description | 5 |
| 2.2 An alternative opto-mechanical architecture for eLISA payload | 9 |
| 3 Laboratory model of the inertial reference sensor | 12 |
| 3.1 Optical readout system | 12 |
| 3.2 Surface characterization of a spherical test mass through optical readout | 17 |
| 3.3 Levitation test bed | 18 |
| 3.4 Integration of the overall system and experimental validation | 19 |
| 4 Fundamentals of FPGA-based PID controllers | 21 |
| 4.1 Assets and liabilities of digital PID controllers | 21 |
| 4.2 NI-PXI 7852R | 22 |
| 4.3 LabVIEW implementation of the PID Controller VI | 24 |
| 5 Intensity Stabilization | 27 |
| 5.1 Objective | 27 |
| 5.2 Setup and components description | 29 |
| 5.2.1 Plant | 32 |
| 5.2.2 Actuator | 34 |
| 5.2.3 Sensor | 36 |
| 5.2.4 Controller | 36 |
| 5.3 System Characterization | 36 |
| 5.4 Implementation of the digital controller | 41 |
| 5.5 Tuning and Performance Tests | 45 |
| 5.5.1 Measurement of free running laser intensity | 45 |
| 5.5.2 Measurement of stabilized laser intensity | 51 |

| | |
|--|------------|
| 6 Height Controller | 54 |
| 6.1 Objective | 54 |
| 6.2 Setup and component description | 55 |
| 6.2.1 Plant | 56 |
| 6.2.2 Actuator | 60 |
| 6.2.3 Sensor | 60 |
| 6.2.4 Controller | 63 |
| 6.3 System Characterization | 64 |
| 6.3.1 Sensing system characterization | 64 |
| 6.3.2 Two-stages electromagnet and relative current sources characterization . . . | 68 |
| 6.4 Implementation of the digital controller | 73 |
| 6.5 Experimental tryouts | 77 |
| 7 Conclusions and Outlook | 79 |
| A Data Sheets | 81 |
| A.1 FPGA-board NI PXI-7852R | 82 |
| A.2 Laser Innolight Mephisto 1000NE | 92 |
| A.3 AOM Crystal Technologies 3080-194 | 94 |
| A.4 Frequency Mixer Mini-Circuits ZP-3 | 97 |
| A.5 First sensor PC20-Q | 99 |
| A.6 Stanford Research System Low Noise Pre-amplifier SR560 | 101 |
| A.7 Schäfter+Kirchhoff Fiber Collimators 60FC-.... | 102 |
| A.8 Thorlabs Iris ID5MS/M | 106 |
| A.9 Thorlabs Plano-convex Lens LA1213-C-ML | 107 |
| A.10 Servowatt Linear Power Operational Amplifier DCP130/60 | 108 |
| B Circuit Diagrams | 123 |
| B.1 Circuit layout Singleelement Photodetektor | 124 |
| B.2 PCB layout Singleelement Photodetektor | 125 |
| B.3 DCP 130/60 adaption circuit layout | 126 |
| Bibliography | 128 |

List of Acronyms and Abbreviations

- LET** Laboratory for Enabling Technologies
- eLISA** evolved Laser Interferometer Space Antenna
- ESA** European Space Agency
- GRS** Gravitational Reference Sensor
- IFP** In-Field Pointing
- FPGA** Field Programmable Gate Array
- LabVIEW** Laboratory Virtual Instrument Engineering Workbench
- LISA** Laser Interferometer Space Antenna
- NASA** National Aeronautics and Space Administration
- LIGO** Laser Interferometer Gravitational wave Observatory
- aLIGO** advanced Laser Interferometer Gravitational wave Observatory
- EPTA** European Pulsar Timing Array
- QPD** Quadrant Photodiode
- TP** Telescope Pointing
- IFPM** In-Field Pointing Mechanism
- NPRO** Non Planar Ring Oscillator
- AOM** Acousto-Optic Modulator
- RF** Radiofrequency
- PD** Photodiode
- DWS** Differential Wavefront Sensing
- CTE** Coefficient of Thermal Expansion
- PXI** PCI eXtensions for Instrumentations
- PXIe** PCI express eXtensions for Instrumentations
- PI** Proportional-Integrative
- FEM** Finite Element Method
- PID** Proportional-Integral-Derivative

DSP Digital Signal Processor

I/O Input/Output

A/D Analogue/Digital

ADC Analogue/Digital Converter

DAC Digital/Analogue Converter

VI Virtual Instrument

RIN Relative Intensity Noise

IF Intermediate Frequency

LO Local Oscillator

DDS Direct Digital Synthesizer

DAQ Data Acquisition

PSD Power Spectral Density

ASD Amplitude Spectral Density

D/A Digital/Analogue

OpAmp Operational Amplifier

PCB Printed Circuit Board

List of Figures

| | |
|--|----|
| 2.1.1 Overview of gravitational waves sources observable by different classes of detectors | 4 |
| 2.1.2 Orbital geometry of the eLISA constellation | 5 |
| 2.1.3 Annual motion of the eLISA constellation | 6 |
| 2.1.4 Schematic of the eLISA science measurement | 7 |
| 2.1.5 Partition of the eLISA measurement | 7 |
| 2.1.6 Annual inter-arm breathing of the LISA constellation | 8 |
| 2.1.7 Baseline design of the GRS for eLISA payload | 9 |
| 2.2.1 Comparison between the concepts of Telescope Pointing and In-Field Pointing . . . | 10 |
| 3.1.1 Scheme of the heterodyne frequency generation and control system | 13 |
| 3.1.2 Scheme of a heterodyne interferometer with spatially separated beams | 14 |
| 3.1.3 Photograph of the heterodyne interferometers for the optical readout | 15 |
| 3.1.4 Photograph of the optical setup for heterodyne frequency generation | 16 |
| 3.1.5 Photograph of the electric setup for heterodyne frequency generation | 16 |
| 3.2.1 CAD rendering of the setup for the characterization of the spherical test mass surface | 17 |
| 3.3.1 Photo of the assembled levitation test bed | 18 |
| 4.2.1 NI PXI-7852R Block Diagram | 23 |
| 4.3.1 Block diagram of the <i>PID Controller.vi</i> | 25 |
| 4.3.2 Computation of the integral error and anti-windup algorithm | 26 |
| 4.3.3 Computation of the derivative error | 26 |
| 5.1.1 Thermal influence on laser intensity | 27 |
| 5.1.2 Diagram of a common closed loop control scheme with negative feedback | 28 |
| 5.1.3 Typical noise spectrum of a signal | 28 |
| 5.2.1 Schematic of the intensity stabilization setup | 30 |
| 5.2.2 Scheme of the optical setup for intensity stabilization performance assessment . . . | 31 |
| 5.2.3 Photo of the optical setup for intensity stabilization performance assessment . . . | 31 |
| 5.2.4 Schematic of the optical setup for heterodyne frequency generation | 33 |
| 5.2.5 Simplified scheme of an AOM | 34 |
| 5.2.6 Schematic of the AOM driving signal generation chain | 35 |
| 5.3.1 Measurement setup for the characterization of the actuating system | 37 |
| 5.3.2 Characteristic curve of the actuating system | 37 |
| 5.3.3 Characteristic response of the photodiode | 38 |
| 5.3.4 Setup for the characterization of actuating and sensing system frequency response | 39 |
| 5.3.5 Frequency response of the actuating and sensing system | 39 |
| 5.3.6 Setup for the measurement of the phase lag due to data sampling and processing . | 40 |

| | |
|---|----|
| 5.3.7 Phase lag due to digital conversion and data processing | 40 |
| 5.4.1 Front panel of <i>Intensity Stabilization.vi</i> | 42 |
| 5.4.2 Block diagram of <i>Intensity Stabilization.vi</i> | 43 |
| 5.4.3 Code of the first sequence of the main while loop of the <i>Intensity Stabilization.vi</i> | 44 |
| 5.4.4 Code for the inversion of the error signal computation | 44 |
| 5.4.5 Code of the second sequence of the main while loop of the <i>Intensity Stabilization.vi</i> | 45 |
| 5.5.1 Initial setup for low frequency measurement of free running intensity | 46 |
| 5.5.2 Initial low frequency measurement of the ASD of free running laser RIN | 47 |
| 5.5.3 Enhanced setup for low frequency measurement of free running intensity | 48 |
| 5.5.4 Enhanced low frequency measurement of the ASD of free running laser RIN. | 49 |
| 5.5.5 Schematic of the setup for high frequency measurement of free running intensity . . | 50 |
| 5.5.6 High frequency measurement of the ASD of free running laser RIN | 51 |
| 5.5.7 Schematic of the setup for the intensity stabilization performance test | 52 |
| 5.5.8 Comparison of the ASD of the stabilized laser beam RIN with the curves for free running intensity and detector noise | 53 |
| 5.5.9 Comparison of the free running and stabilized laser RIN in the time domain | 53 |
| | |
| 6.2.1 Schematic of the height control setup | 55 |
| 6.2.2 Reference frame for the description of test mass dynamics | 57 |
| 6.2.3 Photographs of the main components of the plant | 59 |
| 6.2.4 Photograph of the Servowatt linear power operational amplifier DCP130/60 | 60 |
| 6.2.5 Geometrical configuration of the sensing system for height detection | 61 |
| 6.2.6 Scheme of the height sensing system used for the levitation test bed | 61 |
| 6.2.7 Basic principle of sensing signal generation | 63 |
| 6.2.8 Cascade control scheme | 64 |
| 6.3.1 Description of the MATLAB model for the simulation of the height sensing signal . | 65 |
| 6.3.2 Simulation results for a centered test mass | 65 |
| 6.3.3 Simulation results for off-center test mass | 66 |
| 6.3.4 Sensing signals comparison for different values of off-axis displacements | 66 |
| 6.3.5 Sensing system characterization setup | 67 |
| 6.3.6 Comparison between simulated and measured sensing signal | 68 |
| 6.3.7 Measurement setup for the characterization of the power amplifier on-load behavior | 69 |
| 6.3.8 Linear response of the power amplifiers with the two inductive loads | 70 |
| 6.3.9 Schematic of the setup for measuring the electromagnet transfer function | 70 |
| 6.3.10 Frequency response of the two-levels electromagnet. | 71 |
| 6.3.11 Schematic of the setup for test mass dynamics measurement | 72 |
| 6.4.1 Front panel of <i>Height Controller.vi</i> | 73 |
| 6.4.2 Block diagram of <i>Height Controller.vi</i> | 74 |
| 6.4.3 Code for the generation of the sensing signal | 76 |
| 6.4.4 Code for the configuration of the two control units | 76 |
| 6.4.5 Code for the adjustment of the output signal | 77 |
| | |
| 7.0.1 Control scheme modification by addition of a feed-forward controller | 80 |
| 7.0.2 Control scheme modification by addition of a linearization feedback | 80 |

List of Tables

| | |
|---|----|
| 4.2.1 Virtex-5 LX50 Specifications | 23 |
| 5.2.1 Coupling ratios at input and output of the heterodyne frequency generation | 32 |
| 5.4.1 Digital range and resolution of the normalized PI parameters for the intensity stabilizer | 45 |
| 5.5.1 Tuned parameters for the Intensity Stabilization PI controller. | 51 |
| 6.3.1 Electric parameters of the two coils | 69 |

1 Introduction and outline of the thesis

This thesis is the outcome of a work conducted at Airbus Defence&Space (former Astrium GmbH) in Friedrichshafen (Germany), in the frame of the development and experimental investigation of a new concept of inertial reference sensor with a spherical test mass and optical readout. This activity is currently being carried on by the company at the Laboratory for Enabling Technologies (LET), within the context of the study of an alternative payload architecture for the evolved Laser Interferometer Space Antenna (eLISA) mission.

eLISA is a future mission of the European Space Agency (ESA) aimed to detect and measure low frequency gravitational waves through interferometric measurements conducted between three spacecrafts arranged in a triangular formation flown on a heliocentric orbit. The inertial references for the mission are free-flying test masses contained in each satellite and drag-free controlled, acting both as geodesic reference test particles and as end points of the optical length measurement. The original baseline configuration proposed for the mission foresees a V-shaped payload, which consists of two identical units containing a steerable telescope, a Gravitational Reference Sensor (GRS) with an embedded cubical test mass, an optical bench and the relative electronics.

One of the most promising alternative opto-mechanical architecture proposed for the payload combines the use of a single active test mass per spacecraft and the technique of In-Field Pointing (IFP) for the accommodation of seasonal constellation dynamics. According to this concept the payload consists of a common optical bench with a single GRS and two telescopes rigidly attached to it, while the necessary steering of their lines of sight is accomplished by an actuated mirror inside each telescope. The benefits that this configuration can provide with respect to the original baseline architecture, could be further increased when combining it with the use of a spherical, rather than cubical, test mass. Indeed, this would allow to get a virtually pure drag-free condition, with no more need of electrostatic guidance and the possibility of a larger gap between the test mass and the housing, thus enabling an all optical readout of the test mass and the possibility of a better performance thanks to the expected lower noise.

In order to investigate this alternative concept of inertial reference sensor and its actual performance, a laboratory model is under construction at the LET. As a first step, an experimental setup including two heterodyne Michelson interferometers and a spherical test mass mounted on a rotation table will be used to characterize the surface of the sphere and to gain experience with the optical readout. Then, in order to reproduce the free-flying condition of the proof mass in a terrestrial laboratory, an electromagnetic levitation system will be implemented in the setup. With the test mass levitated, the acceleration of its center of mass will then be measured by the interferometers and surface errors will be compensated by calibration or spinning of the test mass, finally allowing to reach the target sensitivity of a few $\text{pm}/\sqrt{\text{Hz}}$.

In the frame of this research project, this thesis has focused on two main activities: on one hand, the development, implementation and performance proof of a digital controller to stabilize the intensity of the laser beams used as input signals by the interferometers; on the other hand, the experimental investigation of a control system to levitate and actively stabilize the position of the spherical test mass through a cascade controller.

The results of this work are presented in this report. In chapter 2 an overview of the general context of the project is given, with particular attention to the main features of the alternative payload architecture studied by Airbus DS and to its potential benefits. Chapter 3 describes the experimental setup under construction at the LET for the investigation of the novel inertial sensor concept, while Chapter 4 gives the fundamentals for the design and implementation of digital FPGA-based PID controllers. In chapter 5 the development of the servo loop for the stabilization of laser intensity is illustrated. Starting from the introduction of system requirements, the different components of the setup and their experimental characterization are then described. Lastly, the implementation of the control loop in the FPGA through LabVIEW programming and the results of the tests conducted are detailed. Similarly, chapter 6 presents the work fulfilled for the height control loop for the levitation system. In the end, chapter 7 provides a summary of the accomplished tasks and suggests guidelines for further development of the project.

2 Scientific and technical framework of the project

This chapter intends to provide a brief overview of the eLISA mission and of an alternative payload concept proposed by Airbus DS and currently under experimental investigation, in order to delineate the scientific and technical framework this thesis is included in.

2.1 The eLISA mission

The eLISA mission is the present, European-led variation of the LISA experiment, which was originally a joint project of NASA and ESA. As its forerunner, eLISA is aimed to detect and measure gravitational waves, predicted by Einstein's Theory of General Relativity. It will be the first space-based observatory to investigate the Gravitational Universe, allowing to gather information about a variety of cosmic events and thus to complement our knowledge about the origin, evolution and structure of our Universe, besides providing stringent tests of general relativity. The project has been chosen in the frame of ESA's Cosmic Vision program as its L3 mission, with a tentative launch date in 2034.

2.1.1 The scientific target of the mission: gravitational waves

In the Theory of General Relativity time and space are described as woven together in a four-dimensional fabric called space-time and gravity is represented as a curvature of this fabric, generated by the presence of matter and energy. As a result, gravitational waves can be described as ripples of the space-time curvature, originated by the accelerated asymmetric motion of massive objects and then traveling outwards from their source. As they move through space, they produce a time-varying squeezing and stretching of the space-time fabric which can be detected as fractional changes in the distances between free floating bodies (i.e. bodies subject to no other forces than gravity). Due to the extreme stiffness of space-time, the interaction of gravitational waves with matter is very weak and consequently it takes huge energies to produce even minimum distortions. This means that gravitational waves travel essentially unhindered through the space-time and, when observed, they would bring unaltered information about their source and offer therefore a unique insight into the very distant Universe, not accessible through traditional astronomical observation of electromagnetic waves. Unfortunately, the weakness of

gravitational interaction also means that the strain¹ generated by a gravitational wave is exceedingly small and consequently extremely hard to detect. That's the reason why, until now, the existence of gravitational waves have only been confirmed indirectly², but a direct proof is still pending.

What is required for direct detection of gravitational waves is both a very strong source and an extremely sensitive detector. The strong gravitational waves produced by great astrophysical objects or events, like super-massive black holes and ultra-compact galactic binaries, should have a characteristic strain generally no larger than $h \approx 10^{-20}$ when passing through the Earth and are predicted to be emitted in a frequency spectrum going from $f \approx 10^{-10}$ Hz to $f \approx 10^3$ Hz. Thus, instruments with a correspondent sensitivity over the frequency ranges of interest are required, as shown in Figure 2.1.1 for a selection of the main operational or planned detectors.

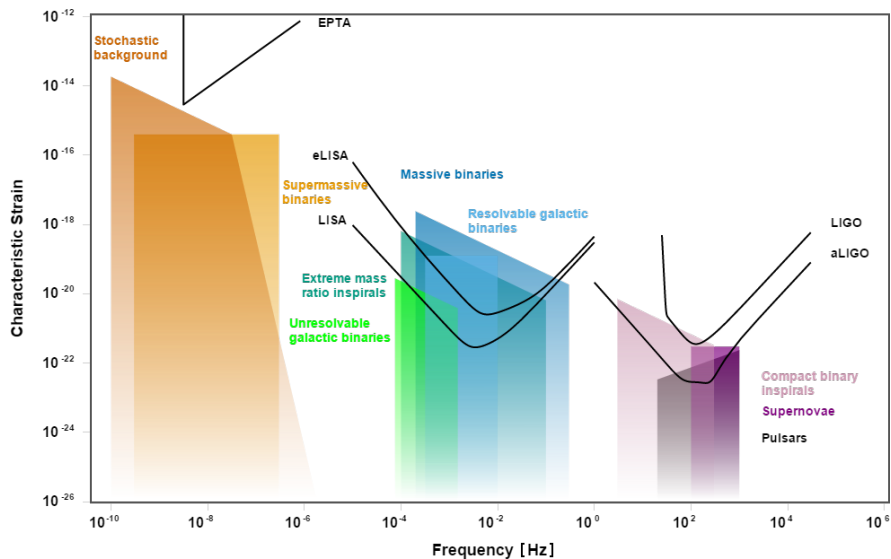


Figure 2.1.1: Overview of gravitational waves sources observable by different classes of detectors. Black lines are the noise curves for the selected detectors, while the colored areas define the characteristic strain of potential astrophysical sources in the different bands of the frequency spectrum. To be detectable the characteristic strain of a signal must be above the noise curve. Source: [1].

The majority of detectors conceived for this purpose use the technique of laser interferometry to measure the distance between two objects and detect the oscillation consequent to the passage of a gravitational wave. So far, a number of ground-based interferometric detectors have been

¹The strain of a gravitational wave is the dimensionless parameter commonly used to describe its amplitude. It represents the expansion or compression of the space a gravitational wave travel into, and is therefore proportional to the fractional change in distance between two masses due to the passage of the wave:

$$h \propto \frac{\Delta d}{d} .$$

²Indirect evidence for the existence of gravitational waves has been derived from the observation of binary pulsars, whose orbital period decrease precisely matches the predictions of energy loss through general relativistic gravitational-wave emission. The first achievement in this sense was the measurements of the Hulse-Taylor binary pulsar, awarded with the Nobel Prize in Physics in 1993.

designed, implemented and operated (e.g. LIGO, VIRGO, TAMA 300 and GEO 600), and studies for upgrades and further generations of these instruments are ongoing (e.g. aLIGO and aVIRGO). Due to disturbances generated by Earth's own gravitational field and seismic activity, together with the limitation on the usable interferometer arm length, these detectors can only access the waves in the frequency band $f \approx 10 \div 10^3$ Hz, produced by events that last only one second or less, such as supernova explosions and collisions of black holes formed from stars in earlier supernova explosions.

A different approach is used by pulsar timing arrays, such as the European Pulsar Timing Array (EPTA), which intend to detect gravitational waves by measuring the shift between signals coming from an array of well-known millisecond pulsars, produced by the differential compression and expansion of the space in different directions consequently to the passage of the wave. In this way, they should be able to detect waves in the nanohertz frequency range, expected to be produced for example by pairs of merging supermassive black holes.

In this framework, we can look at eLISA as an instrument to fill the gap left in the search for gravitational waves. Being designed as a space-based interferometric detector, it overcomes the limitations seen for the earthbound interferometers, thanks to the avoidance of ground-related noise and to the possibility to use an arm length of the order of a million kilometers. Therefore it will be able to target the frequency band $f \approx 10^{-4} \div 1$ Hz, which is exactly complementary to those of the ground-based interferometers and pulsar timing arrays and it's furthermore expected to be the richest in terms of interesting and strong gravitational waves, such as those emitted by coalescing binary black-holes and ultra-compact galactic binaries.

2.1.2 Mission overview and baseline payload design description

The eLISA mission will consist of a cluster of three spacecrafts set in a near-equilateral triangle configuration, with an edge length of 10^6 km (rather than the $5 \cdot 10^6$ km initially chosen for LISA), as shown in Figure 2.1.2.

The center of the constellation will move along a heliocentric orbit lying in the ecliptic plane with a semi-major axis of 1 AU, trailing the Earth at an angular distance of about 20° , chosen as a trade-off between the requirement to minimize the gravitational disturbances from the Earth-Moon system and the communications needs. The constellation plane is tilted by an angle of

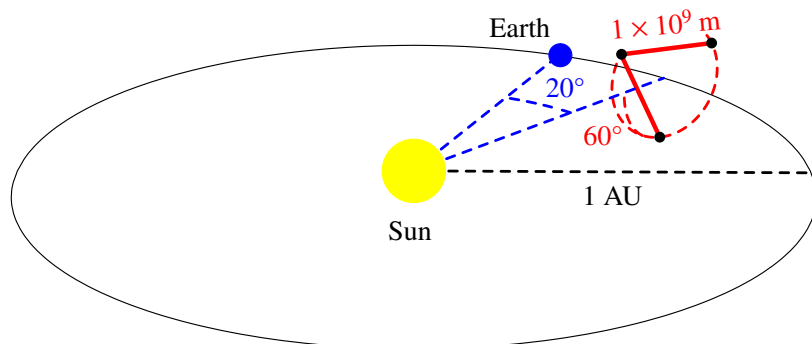


Figure 2.1.2: Orbital geometry of the eLISA constellation. Source: [2].

60° with respect to the ecliptic plane, which allows the spacecrafts to maintain their triangular formation throughout the year and provides an extremely stable thermal environment, thanks to the almost constant Sun-angle with respect to the normal to the top of the spacecraft. During its annual motion around the Sun, the triangle also appears to counter-rotate around its center, thus providing angular information about the gravitational wave sources (Figure 2.1.3).

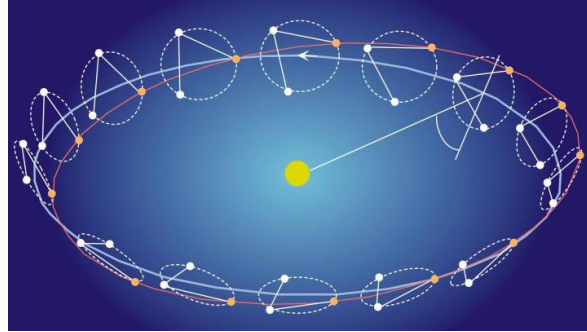


Figure 2.1.3: Annual motion of the eLISA constellation. Source: NASA

The satellites constellation forms a high precision Michelson interferometer, with the two measurement arms defined by the paths between one of the spacecrafts, serving as a ‘central hub’, and the other two (differently from the symmetrical configuration originally foreseen for LISA). Monitoring the time-varying changes of the optical path-length between free-falling masses contained inside the spacecrafts with a resolution of the order of a few picometers over a distance of 10^9 m, eLISA will then be able to detect the passage of a gravitational wave with a strain sensitivity of about 10^{-21} .

The baseline payload architecture is defined migrating a large part of the design and technological key features from LISA, even if with some differences [2]. It consists of four identical units, two on the mother spacecraft, arranged in a V-shaped configuration, and one on each daughter spacecraft, as shown in Figure 2.1.4. Each payload unit includes first of all a Gravitational Reference Sensor (GRS), which embeds the test mass serving as end-point for the interferometer arms. In front of the GRS there’s an optical bench, which houses all the optics and electronics needed to perform the interferometric measurement. Finally, a telescope with a 20 cm diameter transmits and receives the laser light traveling between two spacecrafts.

The basic concept used for the measurement is that of heterodyne interferometry. Each payload unit on the mother spacecraft sends a laser beam (with a power of about 2 W at 1064 nm) at a frequency f_1 to the correspondent unit on one of the daughter spacecrafts, and receives the light coming back from the other end. On the optical bench, the received beam is interfered with light from the local laser source at frequency f_2 to generate a heterodyne beat note signal (with frequency $f_{\text{het}} = f_1 - f_2$). A Quadrant Photodiode (QPD) detects the beat note signal and an electronic phasemeter measures its phase with a $\mu\text{cycle}/\sqrt{\text{Hz}}$ sensitivity. The time history of the phase reflects the laser light Doppler shift generated by changes on the interferometer arms length and provides therefore a measurement of the relative motion of the two optical benches fixed to the spacecrafts. In order to isolate the tiny fluctuations of distance induced by the passage of a gravitational wave (of the order of picometers, with timescales of seconds to hours) from the much noisier motion of the spacecraft, due to thruster and radiation pressure noise (of the order

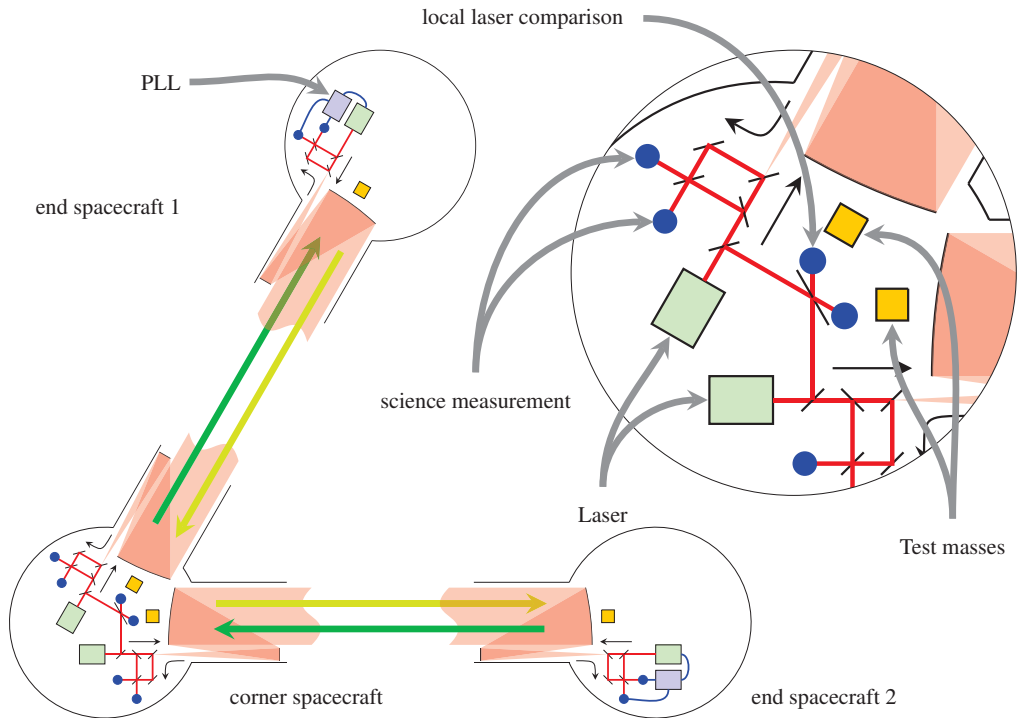


Figure 2.1.4: Schematic of the eLISA science measurement. The central spacecraft accommodates two payload units with master laser sources, while the end spacecraf... have one unit each, whose laser is phase-locked to the incoming light. Source: [2].

of 10^4 km, with timescales of months to years), this long-range measurement is combined with two similar local measurements, conducted between each optical bench and the relative test mass (see Figure 2.1.5). A similar scheme is employed for the other arm of the interferometer, and the two measurements are then processed together with a specific algorithm to remove the laser frequency noise and finally get the pure gravitational wave signal.

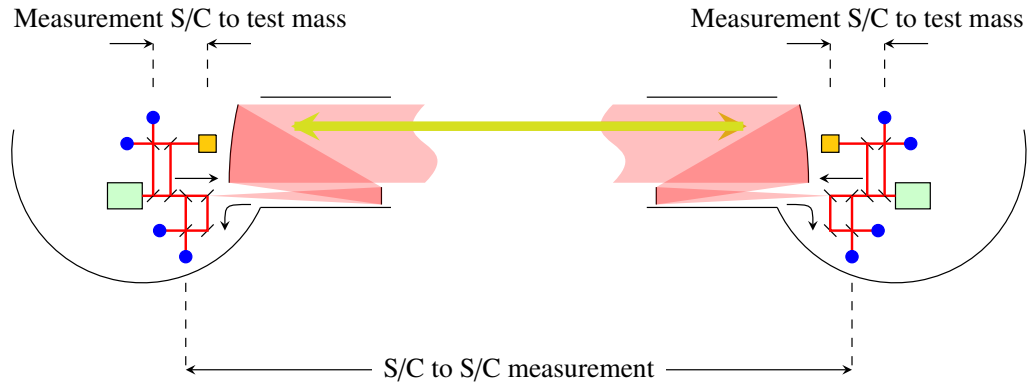


Figure 2.1.5: Partition of the eLISA measurement. Each measurement between the test masses is split into three portions: two measurements between the respective test mass and the spacecraft and one between the two spacecraft. The blue dots represent the points where the interferometric measurements are taken. Source: [2].

While the whole experiment can be thought of as a simple Michelson interferometer, the actual operation of such an instrument implies some crucial practical challenges which require the implementation of specifically designed features to be overcome. First of all, the use of a classic interferometer scheme relying on the ‘round-trip’ of a laser beam reflected at one end of the measurement arm is not feasible, because the reflected beam would be much too weak due to the large distances involved and to the low power available for the laser in a spaceborne application. Therefore, a ‘transponder’ mode operation is used: a laser beam is sent from the central spacecraft to an end spacecraft, where a local laser source is phase-locked to the incoming beam, thus returning a high-power phase replica that is sent back to the central spacecraft, where it can be used for the heterodyne interferometry.

Another specific feature to implement is a system to compensate the seasonal geometrical changes of the constellation. Indeed, the orbital dynamics of the satellites induces cyclic changes of the angle between the interferometer arms of about $\pm 1^\circ$ over a annual period (Figure 2.1.6), that must be actively corrected. To this end, the technique of Telescope Pointing (TP) is applied: essentially, a steering mechanism is used to adjust the telescopes and the correspondent payload units in order to apply the needed pointing compensation.

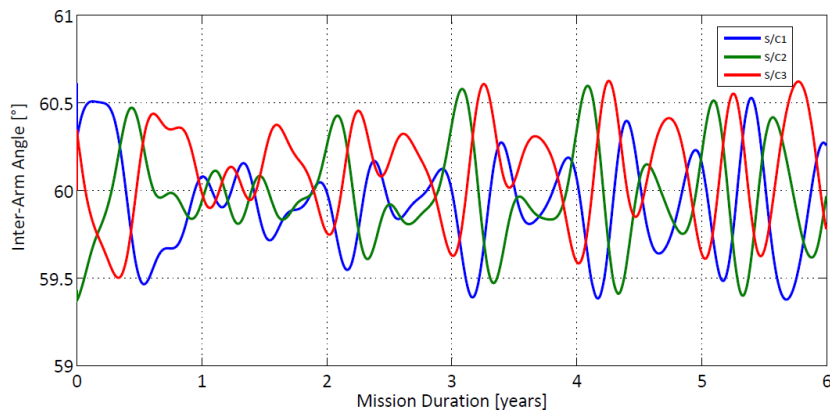


Figure 2.1.6: Annual inter-arm breathing of the LISA constellation, shown through the evolution of the angles between the two laser RX directions on board of each spacecraft. Source: [3].

Finally, a key feature to meet the sensitivity requirements and get significant measurements lies on drag-free operation of the spacecraft, which is actively controlled to follow the free-falling test mass while shielding it to the maximum extent possible from all disturbances other than gravity (e.g. spacecraft maneuvers, solar radiation pressure, magnetic fields, outgassing environment, gravity field from the spacecraft itself). For this purpose, the same test masses used as endpoints for the optical length measurements also serve as inertial references for the drag-free control system. The core of this system is the GRS, which mainly includes the test mass (made of a dense non-magnetic gold-platinum alloy, in the shape of a 46 mm cube) and a housing with electrodes installed at few millimeters separation from the test mass, providing both capacitive sensing and electrostatic actuation capability (Figure 2.1.7). Due to its cubic shape, the test mass needs active guidance in the rotational degrees of freedom so to keep the reference surface for the science measurement always perpendicular to the laser beam. Moreover, since the most practical way to implement a cube is to use a single axis drag-free satellite, also the two translational

degrees of freedom perpendicular to measurement axis must be guided. Therefore, the drag-free and attitude control is essentially realized according to the following strategy:

- along the scientific measurement axis the test mass is free-falling and the relative position of the spacecraft is optically measured with picometer precision by the interferometer setup and actively corrected by a set of micronewton thrusters, so to keep the spacecraft centered with respect to the test mass;
- the other degrees of freedom are instead monitored through the capacitive readout with nanometer precision and actively guided by the combined action of the thrusters on the spacecraft and of electrostatic suspension on the test mass, being careful that the control torque and forces do not also introduce stray forces on the measurement direction, where the mass must be free-falling at femtonewton level.

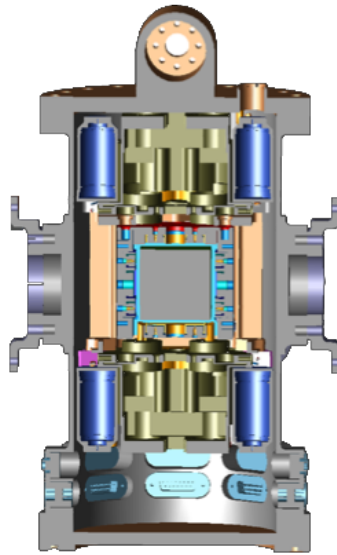


Figure 2.1.7: Baseline design of the GRS for eLISA payload, with an embedded cubic test mass, capacitive readout and electrostatic actuation system. Source: Max Planck Institute for Gravitational Physics.

2.2 An alternative opto-mechanical architecture for eLISA payload

Although the payload architecture described in § 2.1.2 represents a well consolidated baseline, such a challenging project requires the investigation of alternative approaches in order to guarantee that the optimum configuration for the mission is found. For this purpose, several alternative payload concepts have been analyzed in the LISA Mission Formulation study carried out by Astrium GmbH (now Airbus DS) that can be transferred to eLISA.

A potential architecture under investigation [4], is one that combines the application of In-Field Pointing (IFP) as alternative technique for accommodating the changes in the satellites formation driven by orbital dynamics with the use of a single active spherical test mass for each spacecraft, whose position is monitored through an all optical readout.

The technique of IFP consists in the use of a small mirror placed in an intermediate pupil plane inside the telescope and actuated through a mechanism in order to steer the active line of sight within the telescope's field of view. In this way, the pointing corrections needed to compensate for the seasonal variation of the constellation, can be applied through the motion of a small mirror instead of the actuation of a whole payload subassembly, as shown in Figure 2.2.1. This opens the possibility to rigidly attach the telescopes to a common optical bench, with no more need of a back-link fiber to provide a common optical phase reference to adjacent payload units. In addition, a single active GRS can be used for each spacecraft, thus realizing an elegant configuration with only one test mass for each spacecraft, located at the corners of the constellation triangle.

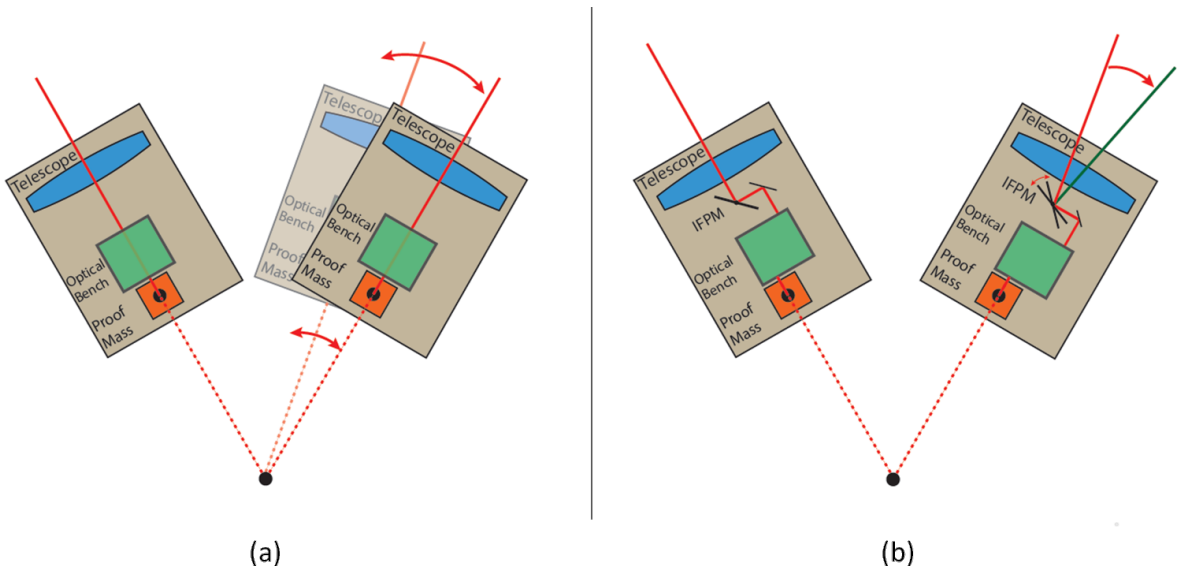


Figure 2.2.1: Comparison between the concepts of Telescope Pointing (TP) (a) and In-Field Pointing (IFP) (b). With TP, all the payload unit must be steered to compensate for pointing errors. On the other side, with IFP only the telescope's line of sight is adjusted through the actuation of a steerable mirror moved by the In-Field Pointing Mechanism (IFPM). Adapted from: [3].

Further benefits can be obtained when combining this configuration with the use of a spherical rather than cubical test mass. With this geometry, the spacecraft can be controlled in a full drag-free mode and no forces or torques are applied to the test mass during the science runs. A correction is still needed to compensate for surface errors since the required accuracy is not feasible with practically achievable roughness, even with the best polishing at hand. This can be done either by spinning the test mass so to average its roughness, or by accurate surface calibration [5]. Either way, the correction would require the application of an active torque only during the initial spin-up phase. With no more need of the electrostatic guidance system, the test mass can then be installed in the housing with a larger gap (few centimeters) and a complete optical readout can be adopted.

A possibility to implement the optical readout is through heterodyne interferometry, for which a compact and effective layout has been studied and progressively improved at Airbus DS [6, 7], in order to meet the mission scientific requirements (more details are given in § 3.1).

In spite of a very demanding technical implementation, this alternative configuration offers a number of significant potential advantages with respect to the baseline design. First of all, the use of IFP removes the need to actuate large payload sub-assemblies; this eliminates the demand for a flexible harness to connect the movable units to the payload core and for launch locks for the pointing devices and minimizes the continuous changes in self gravity due to breathing accommodation. Besides, it guarantees full on-ground testability of the beam pointing, oppositely to the TP technique for which the actuation of large masses with extremely low torque noise may be not feasible under 1g condition. IFP also introduces a high flexibility for the choice of the overall payload layout which can result in potential savings in terms of mass, volume and power consumption. Moreover, the use of a single active GRS at a time enables the realization of a full cold redundancy when a second GRS is present on board. As previously discussed, the use of a single test mass also allows the reduction of active guidance during the experiment runs, especially when a spherical shape is chosen so to realize a pure drag-free condition. This, combined with the use of a complete optical readout, which means higher sensitivity and lower spurious forces applied to the test mass, should result in an overall reduction of the measurement noise.

Considering the crucial benefits that have been pointed out, several projects have been carried out and are still ongoing at Airbus DS in order to experimentally validate the different features of this alternative concept. Particular attention is given in the next chapter to the development of an experimental model to investigate the use of a spherical mass with optical readout for the inertial reference sensor, since this is the project this thesis has actively contributed to.

3 Laboratory model of the inertial reference sensor

In order to investigate the novel concept of an inertial sensor based on the use of a free-falling spherical test mass and a complete optical readout, an experimental model must be built, going through the following main steps:

- an interferometric system for the readout of the test mass position must be set up, with a target sensitivity of a few pm/\sqrt{Hz} in the frequency range of interest for eLISA;
- the surface of an accurately polished spherical test mass, with roundness tolerance less than one wavelength λ of the used laser light and surface roughness less than $\lambda/4$, must be characterized through optical measurement;
- a levitation system implementing a control loop for stabilization of the test mass position must be realized in order to be able to perform measurements on a flying test mass in a earthbound laboratory;
- the interferometer and levitation systems must be integrated into a common setup through which measurement of the test mass barycenter must be accomplished and the correspondent performance assessed.

Details of the different systems and of the tasks to complete for each step are given in the following sections.

3.1 Optical readout system

For the optical readout, a setup based on two highly symmetric heterodyne interferometers with spatially separated beams is currently under construction.

The system is made up of three main parts. First of all, a structure for heterodyne frequency generation and laser control is needed to generate two stable, phase-locked heterodyne signals to be used as input to the interferometers. A schematic of the main elements of this structure is given in Figure 3.1.1 for one of the two interferometer lines. As shown in the picture, the input laser light, generated by a Non Planar Ring Oscillator (NPRO) Nd:YAG laser at 1064 nm, is first split into two beams which are frequency shifted by two Acousto-Optic Modulators (AOMs), driven by two RF signals respectively at $F_1 = 78.00$ MHz and $F_2 = 78.01$ MHz. In this way, at the output of the AOMs we get two beams at frequencies $f_1 = f_{laser} + F_1$ and $f_2 = f_{laser} + F_2$, which are then fiber coupled to polarization maintaining single-mode fibers and sent to the interferometers. In order to guarantee a good stability of these input beams, a system for the active control of the

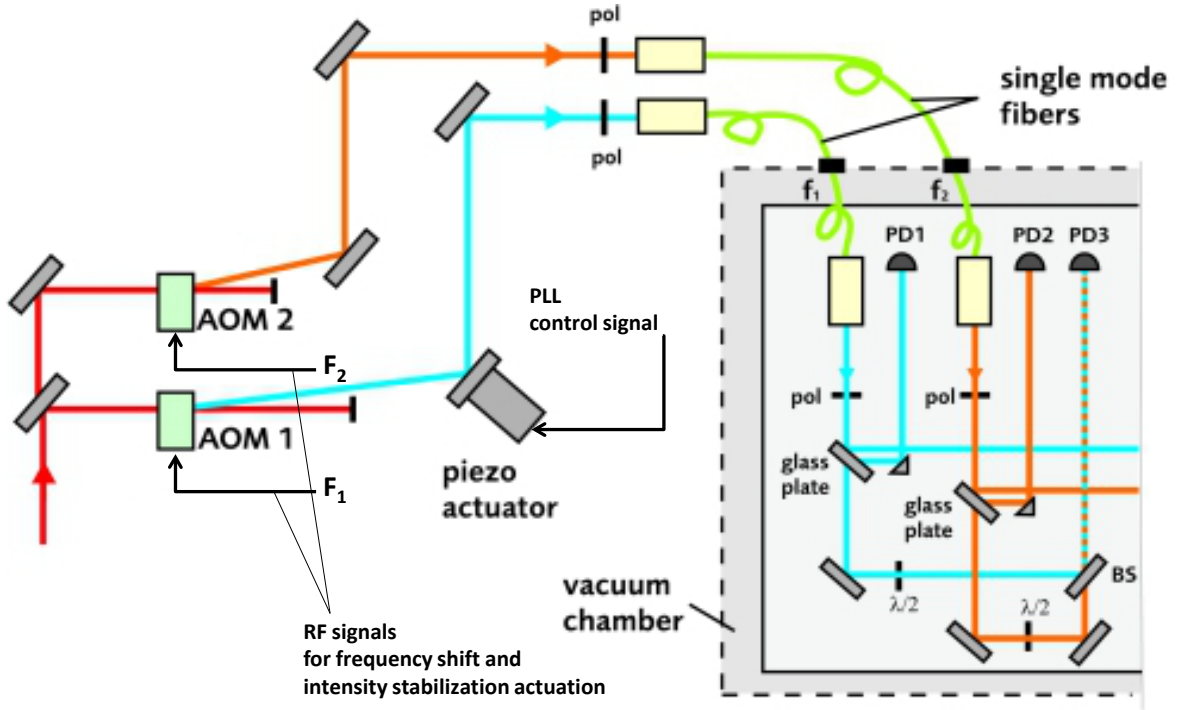


Figure 3.1.1: Scheme of the heterodyne frequency generation and control system. The red paths stand for the input laser beam at frequency f_{laser} , while the orange and azure paths represent the shifted optical lines at f_1 and f_2 , respectively. Adapted from: [8].

light intensity is also required. This can be implemented by measuring the beams intensity with two monitor photodiodes (PD1 and PD2) just after fiber outcoupling and consequently using the detected intensity as input for two identical servo loops. The actuation is done by double-balanced frequency mixers driven by the control signal from the servo loops and used to regulate the amplitudes of the RF signals for the AOMs, so to correspondingly modulate the intensity of the output laser beams. Another key feature to achieve the target noise level is the minimization of differential phase effects produced by slight differences in the optical path lengths introduced by the fibers and the AOMs. For this purpose, a phase-lock loop is implemented that monitors through a third photodiode (PD3) the signal generated by the superposition of the input beams to the interferometers, compares it to a reference signal obtained by mixing the two RF input signals and actively correct it through piezo-electric actuation of a mirror used to modulate the optical length of one of the path so to correct the resulting phase of the measurement signal.

The functioning core of the system is constituted by the two interferometers, whose basic measurement principle is illustrated in Figure 3.1.2. The two generated beams at frequencies f_1 and f_2 are now used as input for the interferometric measurement. Both frequencies are split into two parallel beams. The beams at frequency f_1 are reflected by the measurement mirror (represented by the test mass) and by a reference mirror and then superimposed to the beams at frequency f_2 , so to generate the final signals at the heterodyne frequency of 10 kHz.

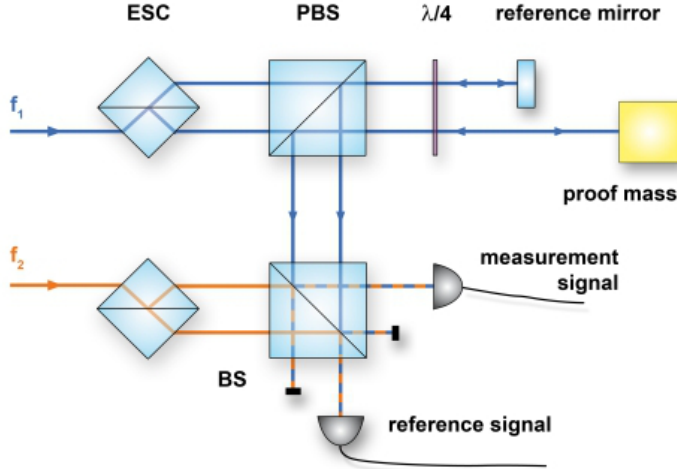


Figure 3.1.2: Scheme of a heterodyne interferometer with spatially separated beams (f_1 and f_2 : input frequencies generated by the setup in Fig. 3.1.1, ESC: energy separator cube, PBS: polarizing beam splitter, BS: beam splitter). Source: [8].

($f_{\text{het}} = F_1 - F_2$). If A and B are respectively the amplitudes of the beams at frequency f_1 and f_2 , the measurement and reference signals are accordingly given by:

$$I_{\text{meas}} \propto AB \cos(\Delta\omega t - \phi(t)) , \quad (3.1.1)$$

$$I_{\text{ref}} \propto AB \cos(\Delta\omega t) , \quad (3.1.2)$$

with $\Delta\omega = 2\pi \cdot f_{\text{het}}$. Two detectors measure these two signals, whose phase difference ϕ is proportional to the relative translation Δl between the reference and measurement mirror, according to the equation:

$$\phi(t) = \frac{4\pi n}{\lambda} \Delta l(t) , \quad (3.1.3)$$

where λ is the vacuum wavelength of the light and n the refractive index of the medium the light is traveling in. Thanks to the use of position-sensitive devices such as QPDs for signal detection and to the application of the method of Differential Wavefront Sensing (DWS) [9, 10], also the tilt of the measurement mirror can be measured. For this purpose, the phase difference between signals of opposing halves of the same detector is computed and using the equation relating the phase difference $\Delta\phi$ between two opposing spots on the beam cross section, both at distance r to the center, and the angle β between the beams:

$$\Delta\phi = \frac{2\pi r\beta}{\lambda} , \quad (3.1.4)$$

the proof mass tilt angle α (equal to $\beta/2$) is derived.

Once the signals from the QPDs are generated (from the sum of the four AC signals of each quadrant and the sum of each two signals of adjoining quadrants), they need to be elaborated in order to extract the desired information about the tilt and translation of the measurement mirror. Thus, the last part of the system consists of data acquisition and signal post-processing. After some filtering and amplification, the signals are sampled and elaborated by a digital phasemeter

that calculates phase shifts between the different signals and derives the correspondent translation and tilt of the measurement mirror as from Equations (3.1.3) and (3.1.4).

The actual implementation of the overall system is obtained by means of the following components integration:

- Two interferometer boards realized with Zerodur¹ baseplate and optical mounts for high thermal and mechanical stability (Figure 3.1.3), housing all the optical elements needed for the interferometric measurement itself and the detectors used for the control loops. They're currently under construction and, for better performance, they're planned to be operated inside a vacuum chamber, with pressures below 10^{-3} mbar.
- A setup for the heterodyne frequency generation and the actuation of the beam intensity stabilization and phase-lock loops, serving both the interferometer lines and installed outside the vacuum chamber, on a commercial optical table. It can be split into an optical and an electrical setup, mounted separately and with the optical part protected by a covering box to reduce the influence of air turbulences and thermal changes. This system has been already built up and tested (see Figures 3.1.4-3.1.5) and it's therefore ready for integration with the interferometer boards.
- Two FPGA boards (PXI-7845R and PXI-7852R by National Instrument) mounted on a PXIe chassis (NI PXIe-1082) and programmed with LabVIEW to realize respectively the phasemeter and the digital control loops for phase-lock and intensity stabilization. The digital implementation and test of a PI servo loop for intensity stabilization has been carried out as part of this thesis, as detailed in chapter 5.

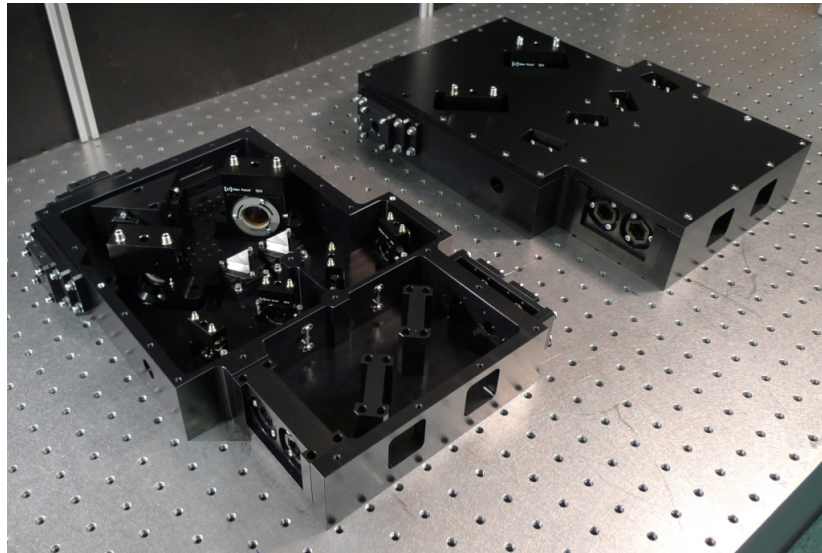


Figure 3.1.3: Photograph of the heterodyne interferometers for the optical readout (currently under construction). Source: [11].

¹ZERODUR® is an inorganic, non-porous lithium aluminum silicon oxide glass ceramic characterized by evenly-distributed nano-crystals within a residual glass phase. It's produced by Schott AG and find large application in the field of high-precision optical metrology thanks to its extremely low Coefficient of Thermal Expansion (CTE) of about $2 \cdot 10^{-8} \text{ K}^{-1}$.

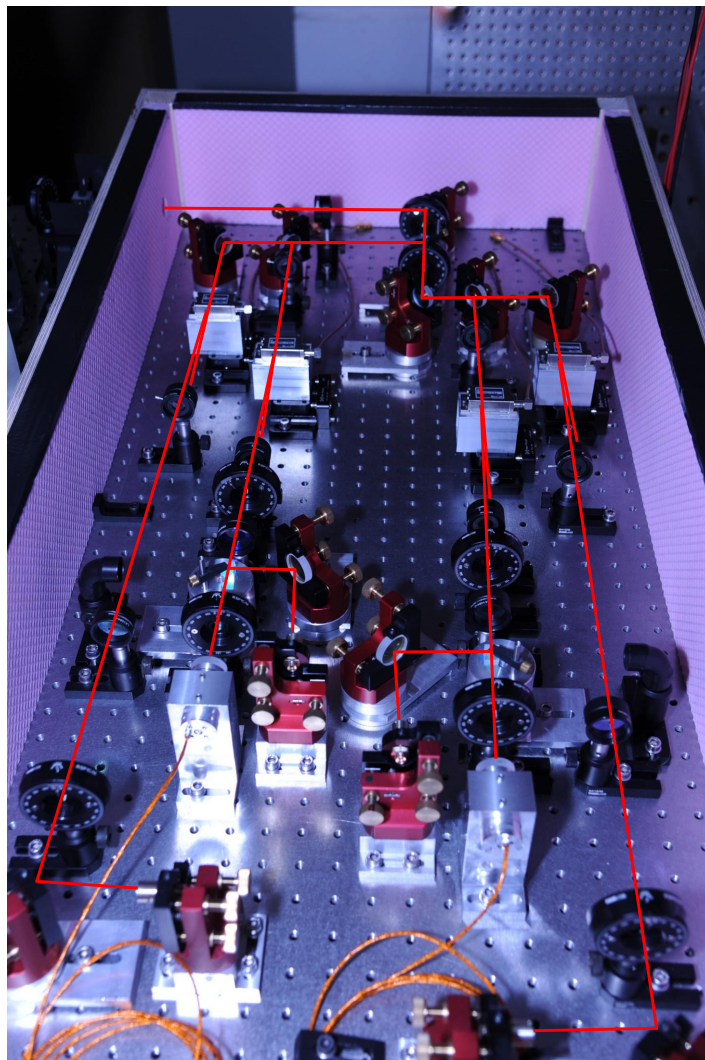


Figure 3.1.4: Photograph of the optical setup for heterodyne frequency generation.
Source: [12].

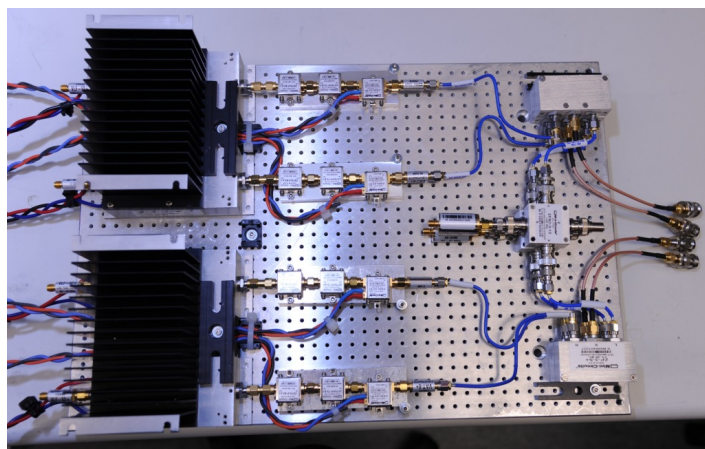


Figure 3.1.5: Photograph of the electric setup for heterodyne frequency generation.
Source: [12].

3.2 Surface characterization of a spherical test mass through optical readout

Once the system for the interferometric measurement will be ready, a first step to be done for the inertial sensor investigation is to gain experience with the optical readout of a spherical test mass and to characterize its surface, in order to have a reference measurement to be used for compensation of the surface error.

The test mass that will be used is a 40 mm diameter monolithic sphere made of mu-metal². The dimension is chosen as a compromise between the need for a relative large curvature radius for easier surface readout and the seek for lightness in order to allow levitation with a smaller electromagnet. The sphere is manufactured using drop forging; subsequently, a special soft annealing process is applied to restore the magnetic properties of the material, necessary to meet the requirements for the electromagnetic levitation system; this is followed by lapping and polishing, in order to get the shape tolerance and surface finish needed for the optical readout. What we finally get is a test mass with the following characteristics [13]:

- mass: $m \approx 300 \text{ g}$,
- relative magnetic permeability: $\mu_r > 1200$,
- magnetic saturation flux density: $J > 800 \text{ mT}$,
- roundness tolerance: $t = 1 \mu\text{m}$,
- surface roughness: $R_a = 0.04 \mu\text{m}$.

The setup for this first test phase is currently under construction in the LET and consists of a high precision rotation table with an isostatic support where the test mass and the reference mirrors will be mounted and of an isostatic frame to install the two interferometer boards. All the supporting structures are made of Zerodur and the system is qualified for vacuum operation. A representation of the final setup is shown in Figure 3.2.1.

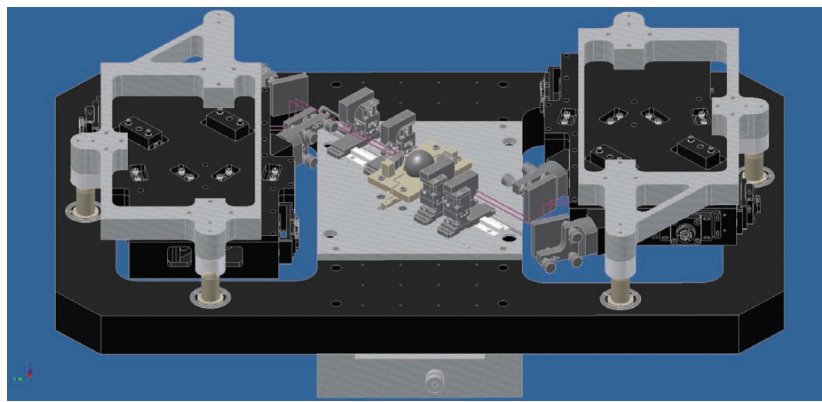


Figure 3.2.1: CAD rendering of the final setup for the characterization of the spherical test mass surface through optical readout. Source: [11].

²Mu-metal is a nickel-iron alloy, composed of approximately 77% nickel, 16% iron, 5% copper and 2% chromium or molybdenum, that is notable for its high magnetic permeability.

3.3 Levitation test bed

Meanwhile, a system to overcome gravity and get a free flying test mass on ground, whose position can be measured within some pm/\sqrt{Hz} , must be developed. To this end, a levitation test bed was fully designed in a previous work [13] and then built and characterized for this thesis. A photo of the complete assembled system is shown in Figure 3.3.1.

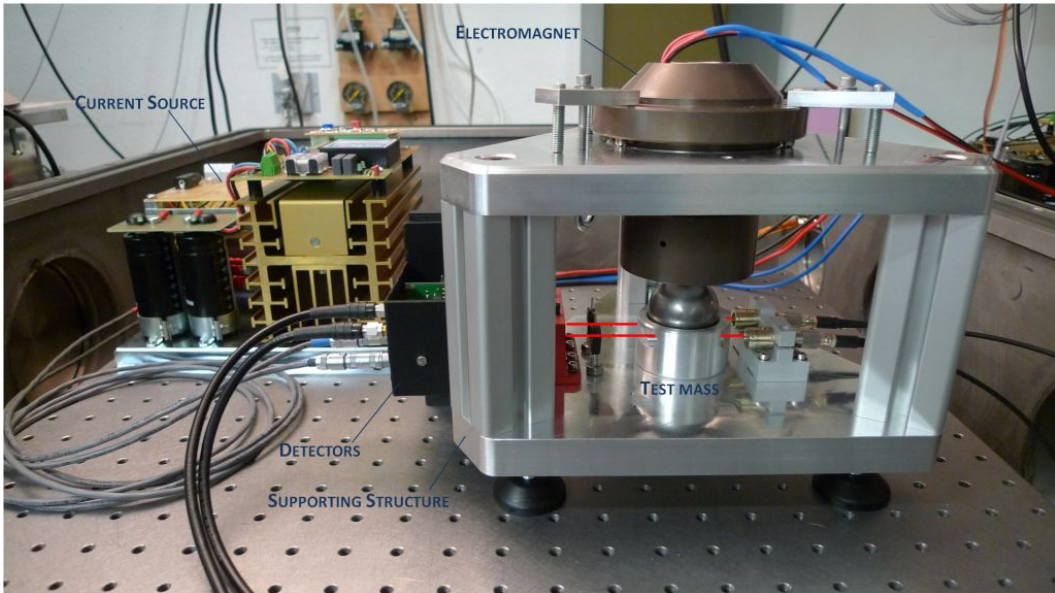


Figure 3.3.1: Photo of the assembled levitation test bed. The main components of the setup are indicated, while the red lines represent the laser beams used for the sensing system.

Electromagnetic (rather than ultrasonic or laminar gas-flow) levitation was chosen due to the need to operate the system under vacuum for the final performance test of the overall inertial sensor model. The required magnetic field is generated by a custom solenoid, consisting of a copper coil wound around a magnetic core and surrounded by a carefully designed housing, both made of the same material of the test mass. The solenoid magnetic properties were optimized through FEM simulation and the mechanical design was specified to provide interchangeability of the parts and allow vacuum usability.

The electromagnet is installed on the top plate of a supporting structure, on the base plate of which the optics for position sensing and a static support for the test mass are also mounted. A system for height adjustment of the solenoid (to fit with the fixed beam height of the optical sensing system) and alignment of the magnetic field lines is also provided, thanks to three fine-threaded adjustment screws arranged at 120° to each other in the housing of the magnet.

The feeding current for the solenoid is generated by an operational amplifier driven as transfer impedance amplifier, with an inductance compensating circuit.

Since the magnetic potential field is unstable, an active control is needed to solve the instability and levitate the test mass. For this purpose a sensing system is first of all required to monitor the test mass position. The sensing principle chosen for the test bed is that of light barriers,

in which the power of two laser beams partly covered by the test mass is measured by two photodetectors. Changing the height of the test mass, the portion of the beam blocked by it varies proportionally and so does the light power detected by the diodes. Theoretically, this method could be implemented with the use of a single laser beam, but in that case a displacement of the test mass in a transverse direction with respect to the levitation direction would also result in a change of the detected light and could therefore cause a misinterpretation of the mass height. On the contrary, the chosen configuration, in which two beams located in symmetrical positions with respect to the levitation axis are used and the sum of the power detected by two diodes is considered, allows to get a signal which is insensitive to small transverse displacements of the test mass and only reflects the variation in its height.

Starting from the measured height of the test mass, a control signal for the current source is generated by a digital controller to modulate the electromagnetic force for the levitation. The servo loop is implemented on the FPGA board which also embeds the intensity stabilization and phase-lock servo loops for the interferometers. To respond to the opposing needs to provide a magnetic force high enough to compensate the test mass weight (that imposes a high inductance for the solenoid) and to guarantee a fast enough modulation for the control (for which the inductance related delay must be reduced), the actuating system is made of two coils with significantly different inductances:

- a big coil, with 6000 turns, slow but capable of a high actuation force, used to provide the main levitation force;
- a small coil, with 500 turns, with smaller actuation capability but also much faster response, used to modulate the levitation force for controlling.

A cascade servo loop can then be used to control the system, whose development and digital implementation were carried out during the second part of this thesis. Unfortunately, the first experimental tryouts proved unsuccessful for the test mass levitation. Therefore a deeper investigation of the system and consequent changes on the control loop design will be needed as a prosecution of this work to guarantee the operation of the test bed.

3.4 Integration of the overall system and experimental validation

Once the feasibility of the optical readout of the spherical surface and of the test mass levitation will be validated, the two systems must be integrated in a single setup, implementing the levitation system in the structure first used for the surface characterization of the test mass. With this setup it will then be possible to start characterizing the actual performance of the inertial sensor, testing the interferometric measurement of the position of the center of mass of a flying spherical test mass under vacuum.

In order to be able to reach the target performance, improved features will be thereafter implemented in the setup:

- two additional interferometers will be added along the orthogonal axis with respect to the first one;

- to improve the precision of the test mass position control, the DWS signal generated by the interferometers will be implemented in the sensing system for the height control loop, which should result in a major improvement of the control performance thanks to its higher sensitivity with respect to the light barrier technique;
- to extend the stabilization of the test mass position and get a complete guidance in all its three translational degrees of freedom, additional electromagnets will be implemented in the levitation system;
- as already discussed, the achievement of the required accuracy in the interferometric measurement of the test mass position is subject to implementation of a compensation system for surface error, which could consist either in calibration of the reference surface or spin of the test mass to average its roughness; in order to test both the techniques, a method to apply a specified torque and therefore spin up the test mass will be defined and implemented in the levitation system.

Testing the complete model of the inertial sensor a performance proof should then be obtained, demonstrating the capability of the system to achieve the target accuracy and providing comparison terms to assess its performance against that of the alternative designs.

4 Fundamentals of FPGA-based PID controllers

Since both the servo loops developed for this thesis are essentially based on the implementation of a Proportional-Integral-Derivative (PID) control scheme on a FPGA board, this chapter aims to provide the fundamentals of the digital design of PID controllers and to give a general overview of the main features of the National Instruments board used in the laboratory setup. The LabVIEW program of the PID controller used as elementary unit for the two servo loops is also described in detail.

4.1 Assets and liabilities of digital PID controllers

PID controllers are characterized by robust performance and simple implementation and represent therefore a well suited control technique for a large number of processes, especially with first and second order dynamics.

Moreover, the use of a digital rather than analogue system produces a very flexible controller, especially when combined with FPGA-based implementation. FPGAs are reprogrammable chips housing a number of configurable logic blocks such as flip-flops and Digital Signal Processors (DSPs), together with memory blocks and several Input/Output (I/O) pads, that can be connected through different digital channels so that the user can ‘build’ the desired circuit and easily reconfigure it when needed. Programming can be done through dedicated software supporting high-level languages. Therefore they offer high computational power and speed, together with an unrivaled flexibility and ease of use. This is particularly useful for application to experimental setups since it easily allows frequent system modifications without changes in the hardware.

In spite of the above mentioned advantages, digital implementation requires some specific precautions to be applied in the design of the controller to guarantee a good performance and avoid potential drawbacks.

Attention must be paid, for example, to the choice of the sampling frequency for A/D conversion, in order to avoid aliasing problems and control the phase lag of the system. For this purpose we can refer to the prescriptions of Nyquist-Shannon Sampling Theorem, which ensures correct reconstruction of a sampled signal without aliasing issues whether its bandwidth is below the so called ‘Nyquist frequency’, given by:

$$f_N = \frac{f_s}{2} , \quad (4.1.1)$$

and therefore imposes to choose, as a rule of thumb, a sampling frequency at least twice the required bandwidth of the system. At the same time the sampling period T_s must be long enough to allow to execute the complete flow of operations, meaning that the execution time of the system τ must be monitored and the minimum condition:

$$T_s > \tau \quad (4.1.2)$$

must be respected.

Another aspect to consider is the discrete signal resolution attainable with digital conversion, that depends on the number of bits n and voltage range ΔV of the converters used, and is given by:

$$\delta V = \frac{\Delta V}{2^n} . \quad (4.1.3)$$

Furthermore, when fractional data are needed to implement the required algorithm, specific data type must be used such as floating or fixed-point data. Since the LabVIEW module for FPGA compiling used in this context does not allow the implementation of the floating-point data type, fixed-point data were chosen to this end. This implies that attention must be paid to the data configuration so to reach a trade off between the need for reduced data length, in order to keep the execution rate high, and the requirements on the data range and resolution attainable in the conversion from integer to fixed-point data type. This means that the number of integer and fractional bits, n_I and n_F respectively, must be chosen trying to minimize them but also taking into account that the correspondent digital range of the fixed-point data is described either by Eq. (4.1.4a) (for unsigned data) or Eq. (4.1.4b) (for signed data, where the first integral bit is actually used as a sign bit):

$$0 \leq u \leq 2^{n_I} - 2^{-n_F} , \quad (4.1.4a)$$

$$-2^{n_I-1} \leq u \leq 2^{n_I-1} - 2^{-n_F} , \quad (4.1.4b)$$

while the digital resolution is given by:

$$\delta u = 2^{-n_F} . \quad (4.1.5)$$

Finally, the design should be carried on always taking into account the resources present on the adopted FPGA and consequently trying to optimize their usage. A short overview of the available resources for the device of interest in this context is given in the following section.

4.2 NI-PXI 7852R

The developed controllers are both implemented on the National Instruments FPGA board PXI-7852R, whose complete specifications are given in Appendix A.1.

In this board a Virtex-5 LX50 FPGA [14] is installed, surrounded by fixed analogue and digital I/O resources, together with a bus interface to access the FPGA via software to configure it.

The major resources for the mounted FPGA are given in Table 4.2.1.

| Slices | Flip-flops | Look-up tables | Multipliers | Block RAM [kb] |
|--------|------------|----------------|-------------|----------------|
| 7200 | 28800 | 28800 | 48 | 1728 |

Table 4.2.1: Virtex-5 LX50 Specifications.

Figure 4.2.1 shows instead the operational block diagram for the overall board. The I/O resources include a connector (Connector 0, MIO) for 8 analogue inputs and 8 analogue outputs and the correspondent Analogue/Digital Converters (ADCs) and Digital/Analogue Converters (DACs), which are 16 bits converters, working with a voltage range of ± 10 V (thus resulting into a resolution of about 0.3 mV, according to Eq. (4.1.3)) and independent sampling rates up to 750 kHz for the input and 1 MHz for the output. Additional digital connectors are moreover available, for a total of 96 digital lines interfacing the FPGA and configurable as inputs, outputs, counters or custom logic at rates up to 40 MHz. An on-board Flash memory is also present to store the FPGA program when the system is powered off and directly reload it during startup, with consequent time saving.

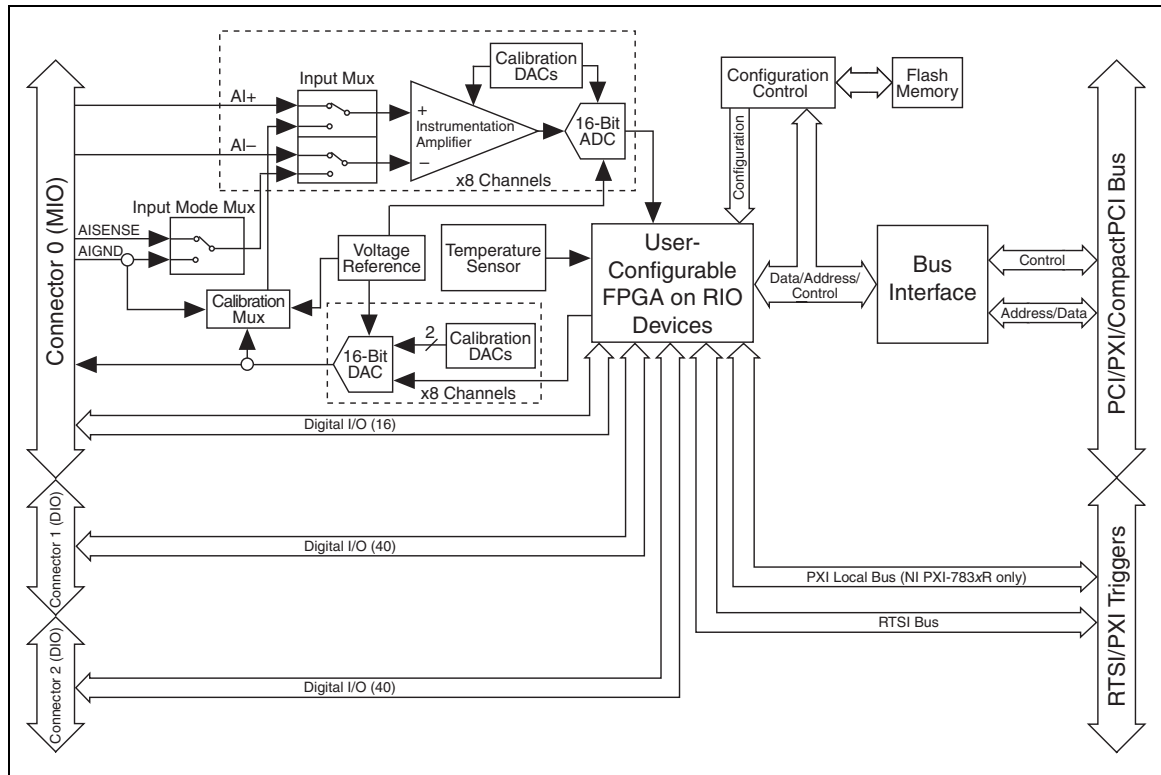


Figure 4.2.1: NI PXI-7852R Block Diagram. Source: [15].

Configuration is done via PXI bus interface, through which a custom program can be downloaded to the FPGA. Programming is carried out using LabVIEW FPGA Module [16], where the

implemented programs, called Virtual Instruments (VIs), are graphically designed in the form of a ‘block diagram’ using language G. Every LabVIEW VI also presents an interactive user interface, called ‘front panel’, which simulates the control panel of a real physical instrument, with buttons, controls and indicators, through which the user can handle selected features of the program. To design more complex programs, different subVIs can be nested inside a higher level instrument, to which they’re interfaced through dedicated I/O lines.

This kind of structure was used for the developed servo loops, whose basic core is in both cases a simple subVI implementing a PID controller. The complete design and functionalities of the *PID Controller.vi* are detailed in the following section.

4.3 LabVIEW implementation of the PID Controller VI

Figure 4.3.1 shows the complete block diagram of the *PID Controller.vi*.

The main functionality of this subVI is to execute the classic discrete algorithm for PID control, given by the equation:

$$u_j = k_P e_j + k_I T_s \sum_{i=1}^j e_i + k_D \frac{e_j - e_{j-1}}{T_s} . \quad (4.3.1)$$

Therefore, the first operation to execute is the computation of the discrete error e_j as difference between a given setpoint, w_j , and the controller input, y_j :

$$e_j = w_j - y_j . \quad (4.3.2)$$

Then the integral and derivative error must be derived, respectively discretized as sum and difference of the error signal e_j of previous iterations. Finally, the control signal u_j is obtained summing three different components:

- a proportional part, simply given by multiplication of the error by the proportional gain, k_P ;
- an integral part, given by multiplication of the integral error by the normalized integral coefficient $K_I = k_I T_s$ (where T_s is the sampling period);
- a derivative part, given by multiplication of the derivative error by the normalized derivative coefficient $K_D = k_D / T_s$.

To guarantee the correct sequentiality of the different operations, the VI is organized through flat sequences. Each sequence (numerated in Figure 4.3.1 and that will now be described) can be executed only after the operations of the previous sequence have been completed.

1. The first sequence simply takes the input coming from the main VI at a fixed rate, already discretized and converted to fixed-point data type.
2. In the second sequence the error signal is computed. Besides being sent to next sequence for computation of the proportional part of the control signal, the error is also used here to derive the integral and derivative errors (as shown in Figures 4.3.2 and 4.3.3), through the

4 Fundamentals of FPGA-based PID controllers

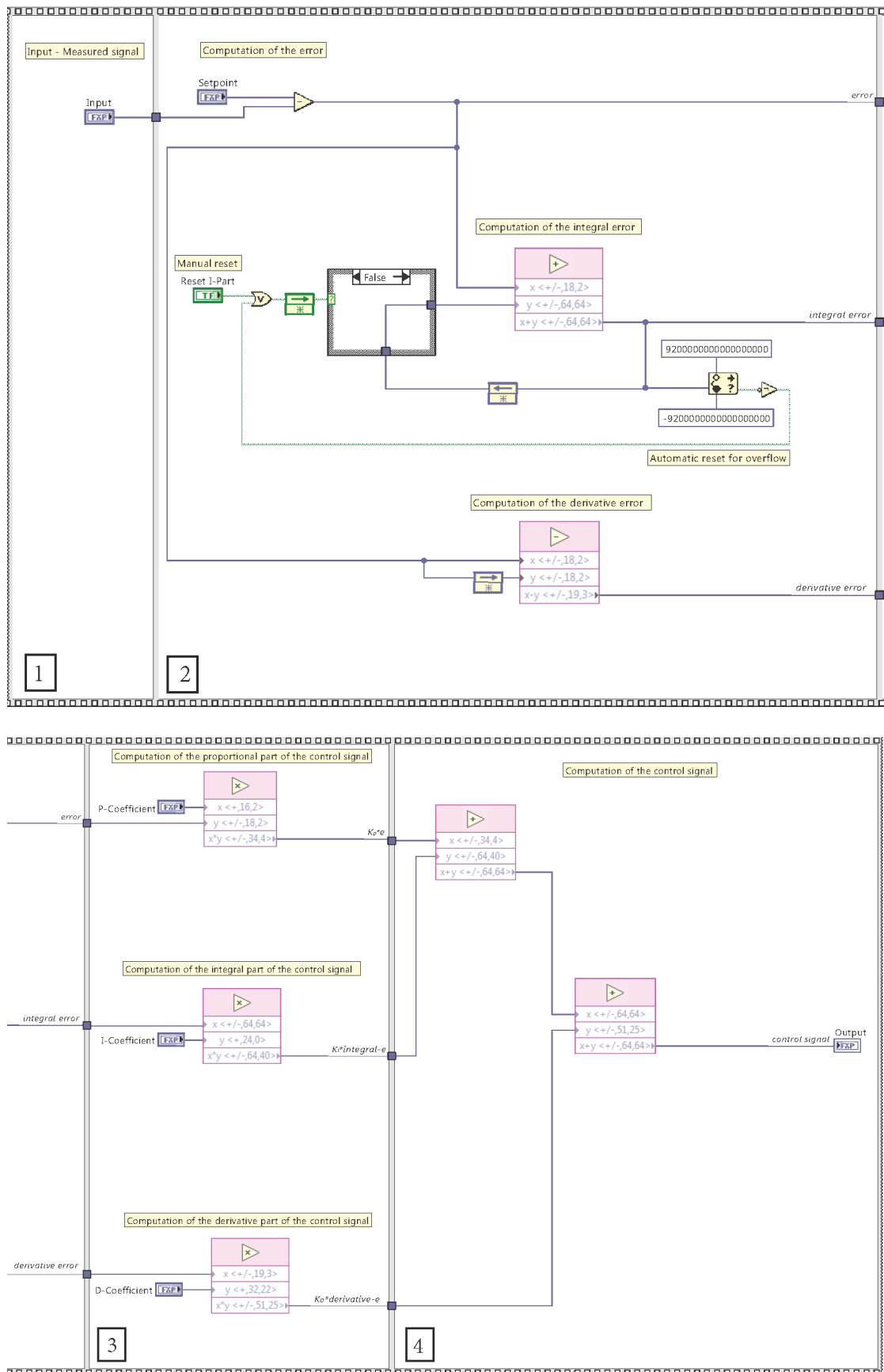


Figure 4.3.1: Block diagram of PID Controller.vi.

use of feedback nodes to store data from previous loop iterations. An anti-windup system is also implemented to avoid the integral part of the controller to saturate the output when the sum should exceed the available data length and thus result in an overflow. For this purpose the possibility to reset the computation of the integral error is introduced, that can be activated either manually, through a user-commanded button, or automatically, every time the integral error goes in overflow.

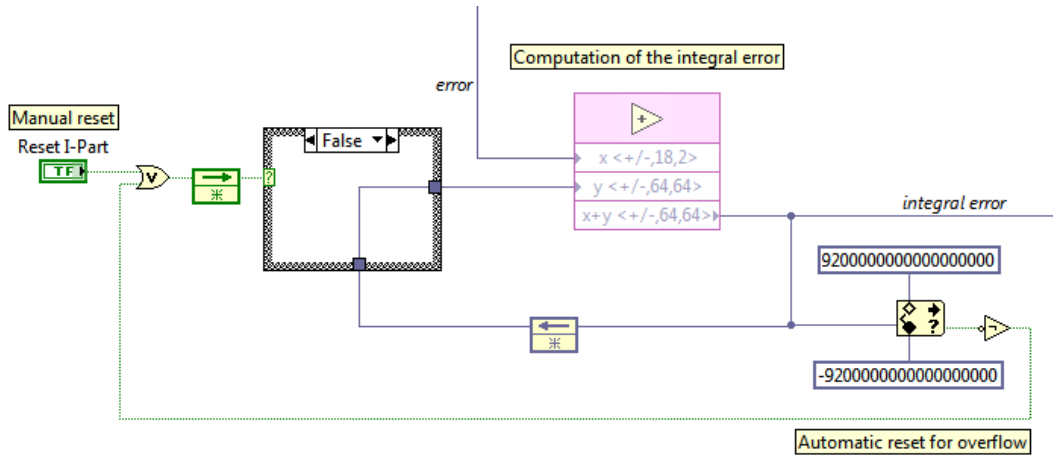


Figure 4.3.2: Computation of the integral error and anti-windup algorithm.

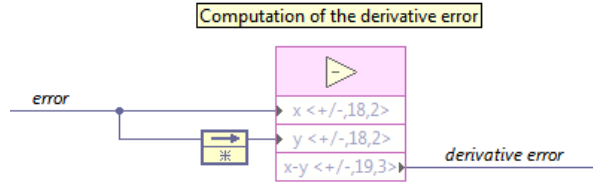


Figure 4.3.3: Computation of the derivative error.

3. In the third sequence of the VI the three parts of the control signal are computed by multiplication of the three error terms with the correspondent normalized coefficients, K_P , K_I and K_D .
4. Finally, in the last sequence the total control signal is computed by summation of its proportional, integral and derivative part and sent to the output of the VI.

The customization done to include this subVI in the two developed controllers, will be later described in the correspondent chapters.

5 Intensity Stabilization

As described in Chapter 3, the laboratory model of the inertial sensor under investigation requires the implementation of a servo loop to stabilize the intensity of each laser beam used for the optical readout. This chapter presents the work done within this thesis to implement and validate an FPGA-based controller able to respond to this requirement.

5.1 Objective

The purpose of the servo loop is to reduce fluctuations of the laser beams intensity in the two frequency bands of interest for the experimental setup:

- the measurement band for the eLISA experiment, $f = 10^{-4} \div 1 \text{ Hz}$, where the performance of the sensor must be proofed;
- the band centered around the heterodyne frequency used by the interferometers, $f_{\text{het}} = 10 \text{ kHz}$.

In this way, producing stable reference signals for the detection of test mass position, we can guarantee a reduction of the noise affecting the measurement and improve system performance.

The main disturbances that can produce fluctuations of the laser beam intensity are refraction effects in the different optical components of the setup, polarization drifts in the fibers, converted to intensity drifts by polarizing optical devices, and most of all temperature variations in the measuring environment (whose influence on the Relative Intensity Noise (RIN) of a free running laser beam is shown in Figure 5.1.1).

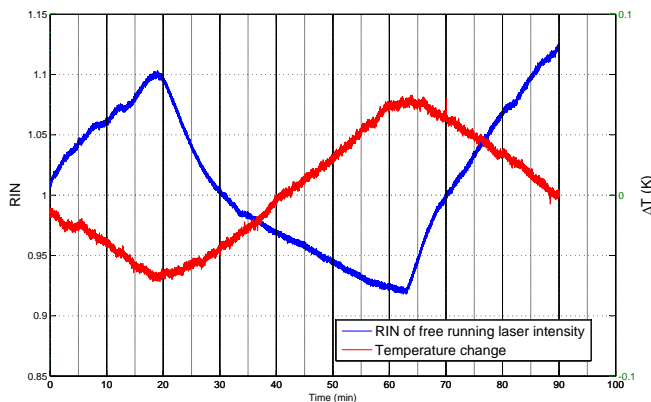


Figure 5.1.1: Thermal influence on laser intensity. The plot shows the correlation between temperature drift and the RIN of a non stabilized laser intensity measurement over a period of 90 minutes.

In order to compensate the fluctuations introduced by the different disturbances, an active stabilization with negative feedback must be used, according to the common control scheme shown in Figure 5.1.2.

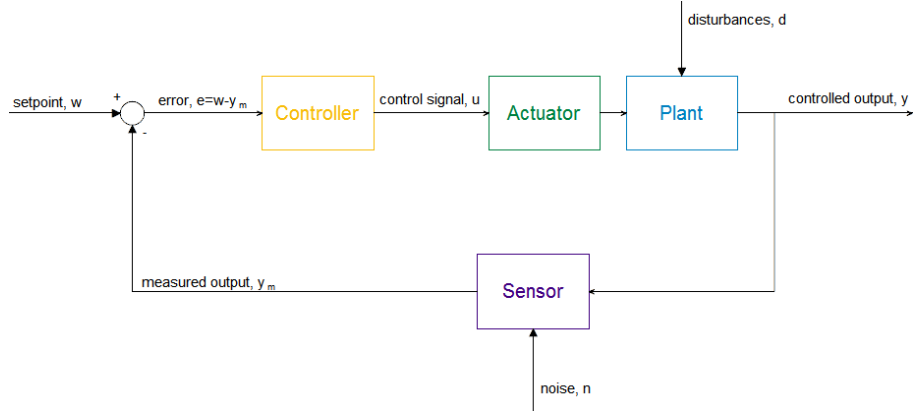


Figure 5.1.2: Diagram of a common closed loop control scheme with negative feedback. The variable to be controlled, y , is measured by a sensor which generates a signal that describes the measured output, y_m , and can be affected by measurement noise, n . This signal is compared to a reference signal or setpoint, w , corresponding to the desired value of the controlled variable. The subtraction of y_m from w generates the error signal, e , used by the controller to define the needed correction. This correction is commanded through the control signal, u , to an actuator, which acts on the plant to modify the value of the controlled variable and keep it stable in spite of the disturbances, d , that tend to make it fluctuate.

In addition to the described disturbances, the noise introduced by the electronics must be taken into account (Figure 5.1.3 shows the typical noise spectrum of a common signal). This is an intrinsic source of fluctuations, which can be reduced through a careful design of the used devices but can not be controlled by active stabilization and can therefore represent a limiting factor for the achievement of the desired stability. Particular attention in this sense will be put on the assessment of the detector noise, since it appears to be the limiting component in the intensity stabilization setup.

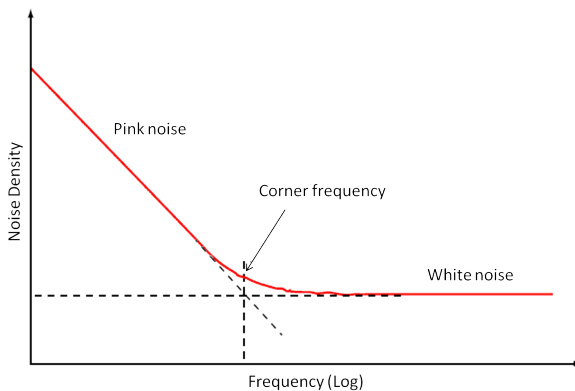


Figure 5.1.3: Typical noise spectrum of a signal. Below the corner frequency pink noise (characterized by a $1/f$ behavior) is predominant, rising out of the intrinsic white noise, which has instead a constant spectral noise density.

5.2 Setup and components description

Since the laboratory model of the inertial sensor implements two heterodyne interferometers, each using two input laser beams for their measurement, four identical servo loops are needed for the overall intensity stabilization.

Figure 5.2.1 gives a schematic of the main components of the setup for one of the four control lines. The plant to control includes first of all a laser source, which also serves another setup in the laboratory from which the input beam is extracted and transported to the input of the system via an optical fiber. Subsequently the beam passes the whole setup for heterodyne frequency generation, where it is split and processed as described in § 3.1 and where the AOM used for the intensity control actuation is also contained. At the output of this system, the laser beam is fiber coupled and sent via feed-through to the interferometer boards mounted inside the vacuum chamber. Immediately after outcoupling, a fraction of the beam power is extracted and measured with a Photodiode (PD), representing the sensor of the servo loop. The measured intensity signal is then sent via an I/O connector block to the FPGA where the digital controller is implemented. After A/D conversion the signal is processed by the digital controller, which compares it to a reference value, compute the correspondent error signal and generates at the output the control signal to drive the actuation system to correct the light intensity. The digital output is then converted back to analogue and sent to the Intermediate Frequency (IF) port of a frequency mixer working as a current controlled attenuator and fed at the Local Oscillator (LO) port with an RF signal at frequency 78.00 or 78.01 MHz, generated by a Direct Digital Synthesizer (DDS). In this way, through the control signal we can regulate the power of the output RF signal, which is subsequently amplified and used to drive the AOM, that finally translates the control signal into an adaption of the laser beam intensity.

For the experimental verification of the stabilizer, since an out of loop measurement of the beam intensity is needed as a reference for the performance assessment, the interferometer board is replaced with a simple measurement setup, according to the scheme in Figure 5.2.2. Figure 5.2.3 also shows a photograph of the measurement setup, in which the different components installed on a commercial optical table are shown; the photodiodes are mounted with two translation stages to provide two degrees of freedom for fine centering of the diode with respect to the laser beam; furthermore, a polystyrene shielding box is put around the setup to shield it from major external disturbances and reduce temperature variation, which by the way is monitored through the resistance bridge that can be seen on the left side of the picture.

The following sections will describe the major features of the main components of the above illustrated setup and present the experimental characterization done in order to obtain the information needed for the implementation of the control loop.

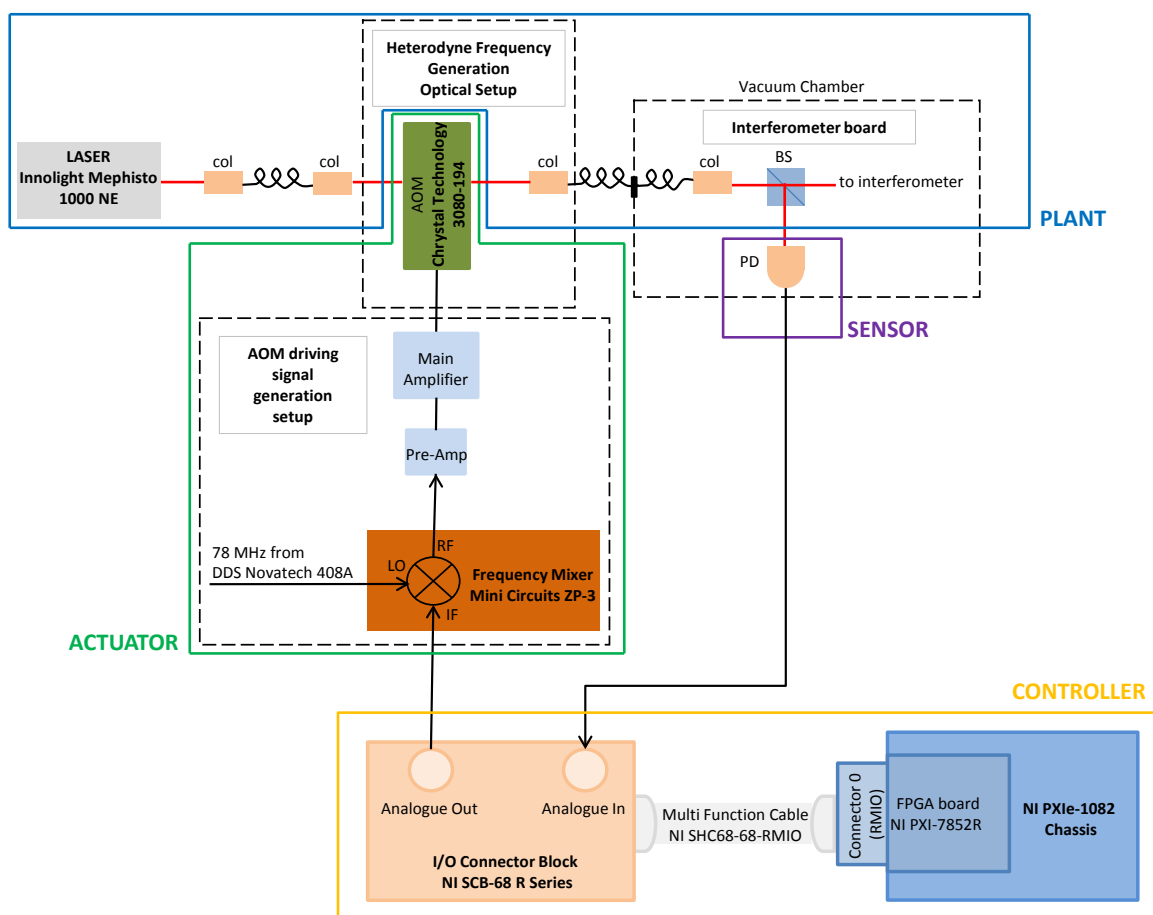


Figure 5.2.1: Schematic of the intensity stabilization setup.

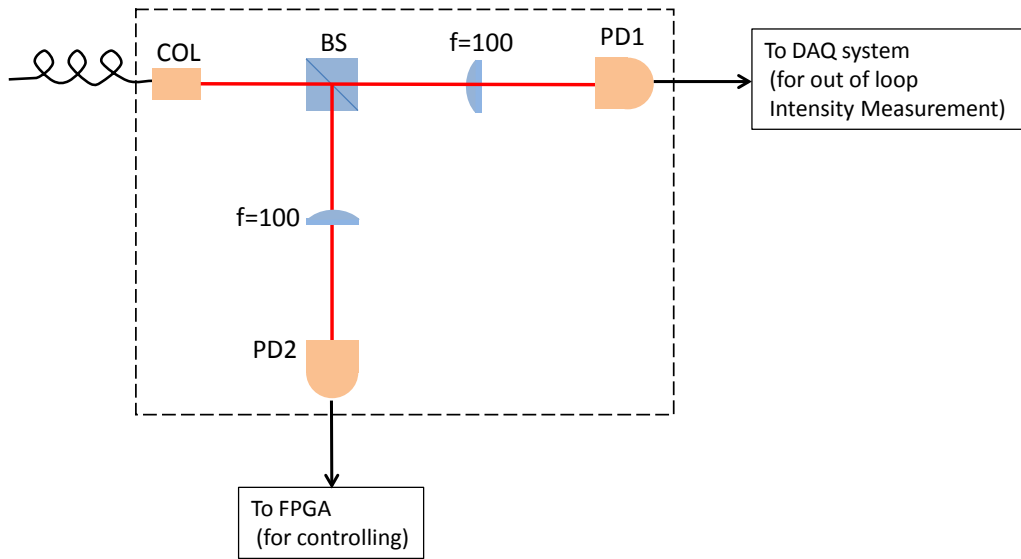


Figure 5.2.2: Scheme of the optical setup for intensity stabilization performance assessment. The laser beam coming from the heterodyne frequency generation system is outcoupled with a collimator (COL) and split at a beam splitter (BS) which generates two separate beams: one for the controller and one for the out of loop measurement. The two beams are then focused through lenses into two identical photodiodes (PD1 and PD2) and their intensity is converted into voltage signals that can be finally sent to the FPGA and to a DAQ system, respectively.

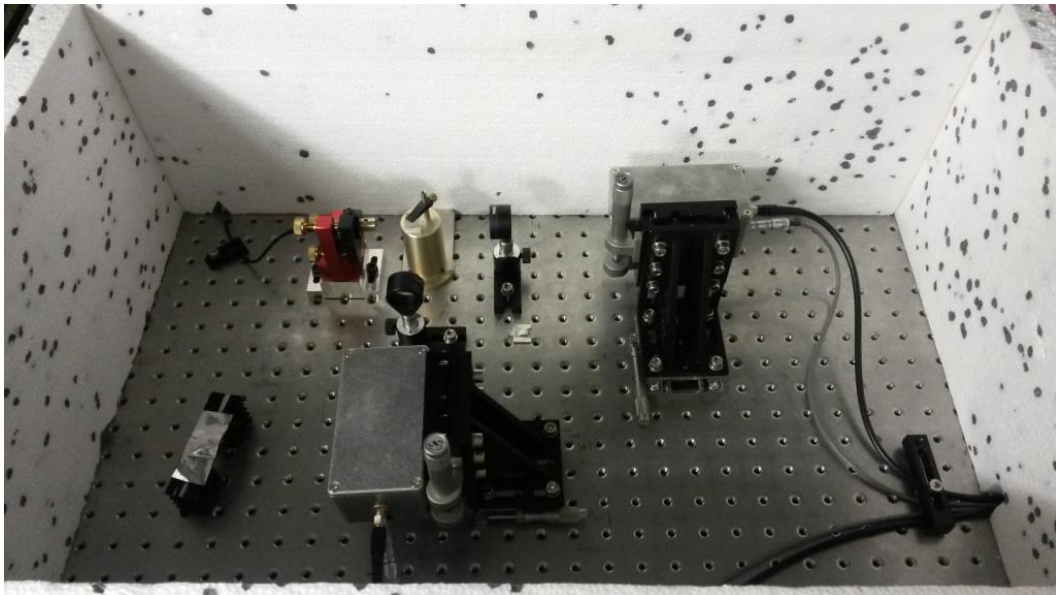


Figure 5.2.3: Photo of the optical setup for intensity stabilization performance assessment.

5.2.1 Plant

Laser source

The main component of the plant to control is the laser source. A NPRO Nd:YAG laser (Innolight Mephisto 1000NE) is used for the current setup. This is a very stable and rugged single-frequency laser source designed for application in the field of precision laser interferometry, producing a beam with wavelength $\lambda = 1064\text{ nm}$ and maximum power of 2 W. It comes with a built-in stabilization, thanks to which it guarantees a RIN lower than -10 dB/Hz in the frequency range $f = 10\text{ kHz} \div 10\text{ MHz}$ (as specified in the Data Sheet in Appendix A.2), while no specifications are given for lower frequencies.

Fiber coupling

Other elements of the setup that are possible sources of major disturbances are the optical fibers used to transfer the laser beam between the different parts of the setup. To reduce this effect, polarization maintaining single mode short fibers by Schäfter+Kirchhoff are used. Moreover, before to start the measurement the different coupling components of the setup were tried out and adjusted so to maximize the coupling efficiency of each line. The coupling ratios (defined as the ratio between output and input laser power) for the final configuration adopted are given in Table 5.2.1.

| | P_{in}/P_{out} |
|-----------------|------------------|
| IN channel | 65 % |
| OUT channel 1.1 | 47 % |
| OUT channel 1.2 | 37 % |
| OUT channel 2.1 | 55 % |
| OUT channel 2.2 | 48 % |

Table 5.2.1: Coupling ratios measured, respectively, on the input line of the heterodyne frequency generation system and on the four output lines serving the two inputs of each interferometer board.

Heterodyne frequency generation optical setup

Finally, a certain number of other optical components (such as lenses, beam splitters and wave plates) are included in the heterodyne frequency generation system, whose effect on beam fluctuation is however minor. For a complete description of the optical setup of the heterodyne frequency generation board and of technical details of its components, see the schematic in Figure 5.2.4 and the reference [12], which also includes all the relative Data Sheets.

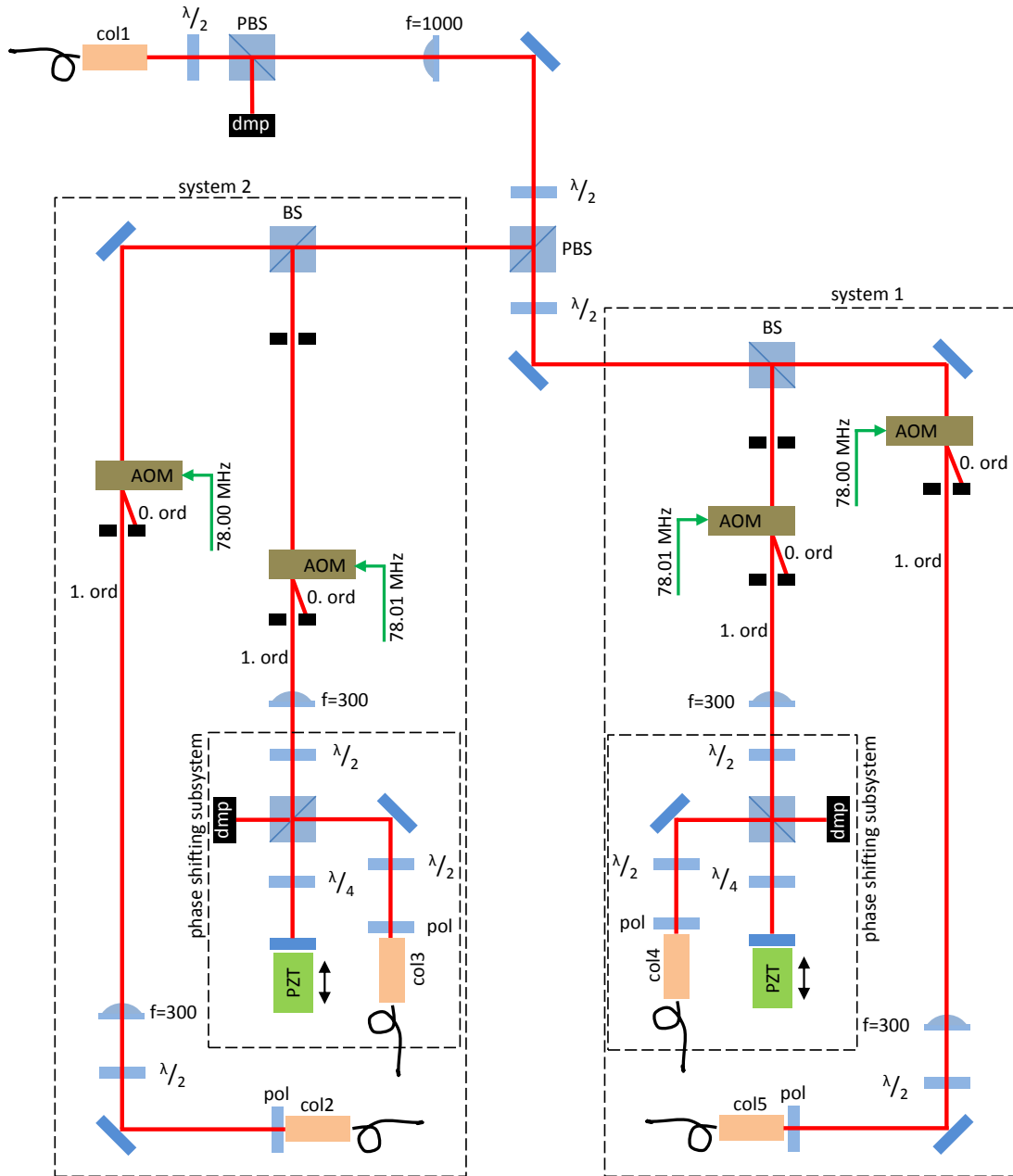


Figure 5.2.4: Schematic of the optical setup for heterodyne frequency generation and control (col: collimator, PBS: polarizing beam splitter, f: lens with focal length, dmp: beam dump, BS: beam splitter, AOM: acousto-optic modulator, pol: polarizing filter, PZT: piezoelectric transducer). Source: [12].

5.2.2 Actuator

Acousto-Optic Modulator

The core of the actuation system is an AOM by Crystal Technologies (model: 3080-194) with center frequency $f_c = 80\text{ MHz}$, bandwidth $f_b = 10\text{ MHz}$ and designed for the wavelength $\lambda = 1064\text{ nm}$, so to get the maximum diffraction efficiency with the used laser light.

The basic working principle of an AOM is illustrated in Figure 5.2.5. The input laser beam propagates through a transparent crystal crossed by an acoustic wave, excited by a piezoelectric transducer at one side of the crystal and absorbed at the other side. Due to the passage of the acoustic wave, a traveling periodic refractive index grid is generated that diffracts the input light into several orders. The first order scattered beam has an optical frequency equal to the input frequency increased or decreased by the RF frequency of the acoustic wave and an intensity proportional to the acoustic power injected. Therefore, controlling the driving signal of the piezoelectric transducer and dumping the transmitted beam coming out of the AOM we can get at the output a frequency shifted laser beam with modulated intensity.

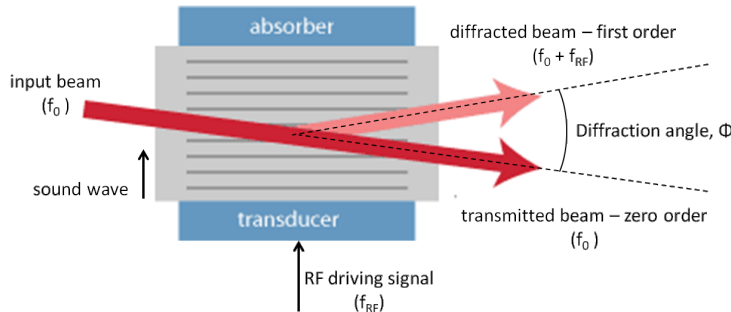


Figure 5.2.5: Simplified scheme of the working principle of an AOM.
Adapted from: [17].

Further technical details of the device used can be found on the Data sheet attached in Appendix A.3.

AOM driving signal generation

To drive the AOM, an RF signal with a fixed frequency $f_{\text{AOM},1} = 78.00\text{ MHz}$ or $f_{\text{AOM},2} = 78.01\text{ MHz}$ (respectively, for the two heterodyne frequencies) and power adjustable around the nominal value $P_{\text{AOM}} = 2.2W$ is used¹.

This signal is produced by an electrical setup specifically designed to this end [12]. Figure 5.2.6 shows a complete schematic of the AOM driving signal generation chain. A reference signal is first generated by a DDS locked on an external 20-MHz clock, provided by a rubidium

¹The operating frequencies are chosen slightly diverse from the AOM center frequency of 80 MHz because this is a harmonic of 20 MHz, recognized to appear as noise in the laboratory. The nominal power, on the other side, is chosen to operate the device with a diffraction efficiency of about 90%, according to the characteristic curve specified in the Data Sheet.

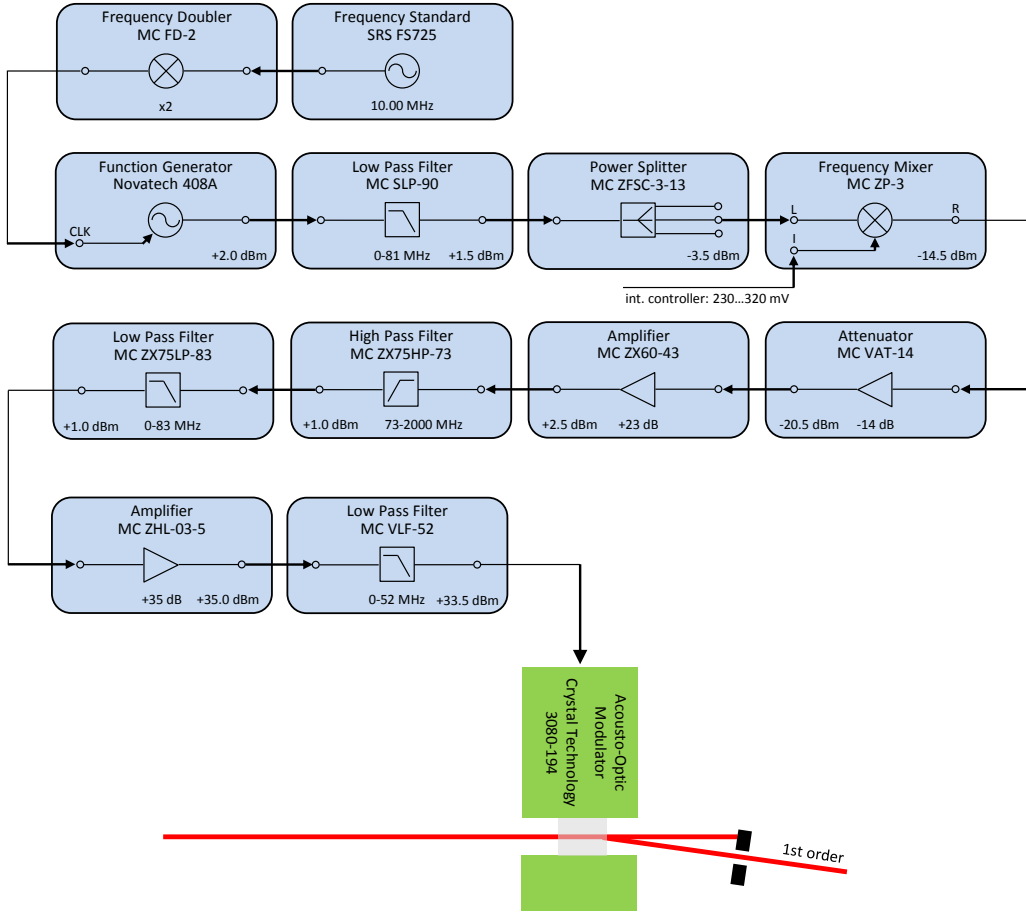


Figure 5.2.6: Schematic of the AOM driving signal generation chain. Source: [12].

standard and a frequency doubler. The signal is then filtered to remove the harmonics of the fundamental frequency and split to obtain three identical signals to be used, respectively: one for each interferometer line and one for the generation of the reference signal for the phase-lock loop. Afterward the power of the signal is modulated through a frequency mixer used as a diode attenuator. In this operation mode a DC signal (which in this case is the control signal generated by the servo loop) is sent as input to the IF port of the mixer and modulates the amplitude of the AC signal entering the LO port (in this case: the reference signal previously generated by the DDS), producing as output at the RF port a signal with the same frequency and modulated amplitude. Hereto is important to note that, due to the presence of a diode bridge inside the frequency mixer, the DC control signal used for the modulation has to be over a certain threshold voltage and possibly within the range for linear operation, in order to provide proper control. Since this is not specified in the Data Sheet of the frequency mixer used (Mini-Circuits ZP-3, see Appendix A.4), a measurement was carried out in order to characterize the operating range for the control signal, which is detailed in § 5.3. Finally, the power of the RF signal must be amplified to meet the AOM's requirements. For this purpose a two-staged amplification system is implemented, including a fixed attenuator for a first rough adjustment of the signal before

amplification and several filters for cleaning the signal spectrum. At this point, the signal is finally ready to be sent as input to the AOM's transducer.

For technical details of the signal generation chain design and of its components, see the reference [12] which also includes the relative Data Sheets.

5.2.3 Sensor

To monitor the laser light intensity during the experimental investigation of the servo loop operation, several couples of available detectors were tried out, so to get identical characteristic response of the signals used for the control system and the out of loop measurement. The sensor finally chosen is a photodetector consisting of a First Sensor PC20C diode and an amplifier circuit board. It was developed in a former work and it's based on the "Singleelement Photodetektor" design [18] in a simplified version without the AC-path. The circuit diagrams of the detector and the Data Sheet of the diode are attached in Appendix B.1, B.2 and A.5, respectively.

For the final implementation of the intensity stabilization in the inertial sensor model a new set of custom designed detectors will be used, which are currently under development and were therefore not available for the tests at the time the work for this thesis was carried out.

5.2.4 Controller

The core of the stabilization system is obviously the control unit, which is realized via a digital program implemented on the National Instruments FPGA board PXI-7852R described in § 4.2 and based on the *PID controller.vi* defined in § 4.3. Since a particularly high control speed is not necessary in this case and to avoid the increased noise sensitivity introduced by the derivative term, a simplified PI configuration is chosen.

5.3 System Characterization

As pointed out in the description of system components, some features of the setup need an experimental investigation in order to provide the information required for a proper implementation of the controller. This section describes the measurements done to this end as prerequisite for the intensity stabilizer development.

First of all, the characteristic of the actuation system was found, with particular attention to locate the linear operational range of the frequency mixers. For this purpose, a programmable power supply (Hameg HM 7044, [19]) was used to feed the IF port of the frequency mixer with variable DC voltage and the correspondent modulation of laser light intensity at the output of the AOM was measured with a power meter (Ophir Photonics NOVA II, [20]), according to the measurement scheme in Figure 5.3.1. The results are depicted in Figure 5.3.2 , which plots the output light power with respect to the input control voltage and shows a linear response in the range $V_{in} = 120 \div 220$ mV. Since a tiny deviation from linearity can be accepted and in order to get a bit larger actuation range for the controller, it was then chosen to limit the control signal within the operational range $V_{in} = 100 \div 240$ mV, with a nominal value of 170 mV.

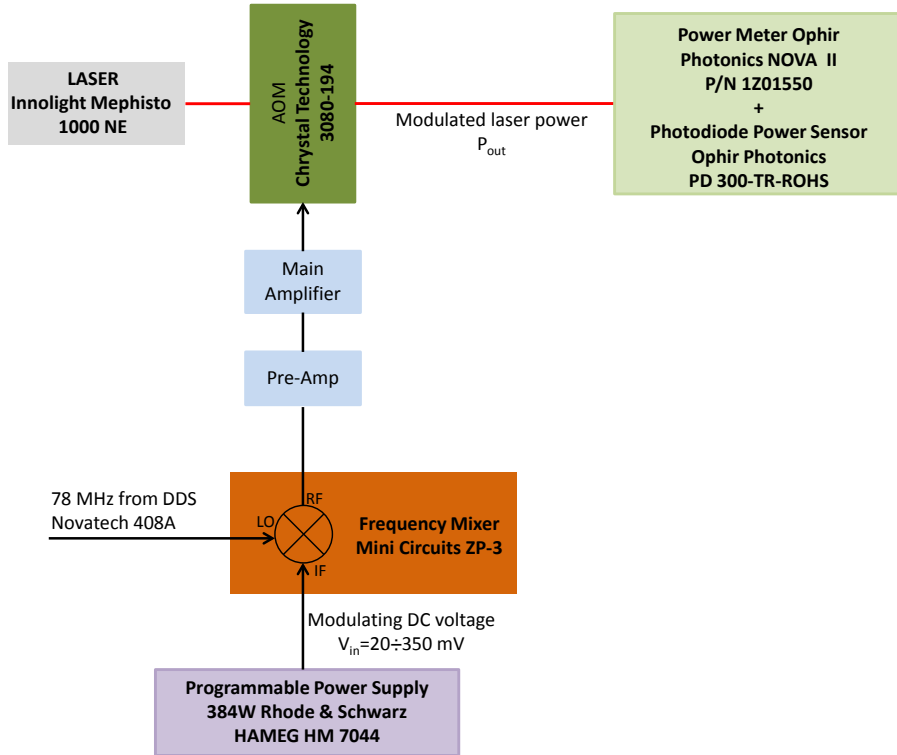


Figure 5.3.1: Measurement setup for the characterization of the actuating system.

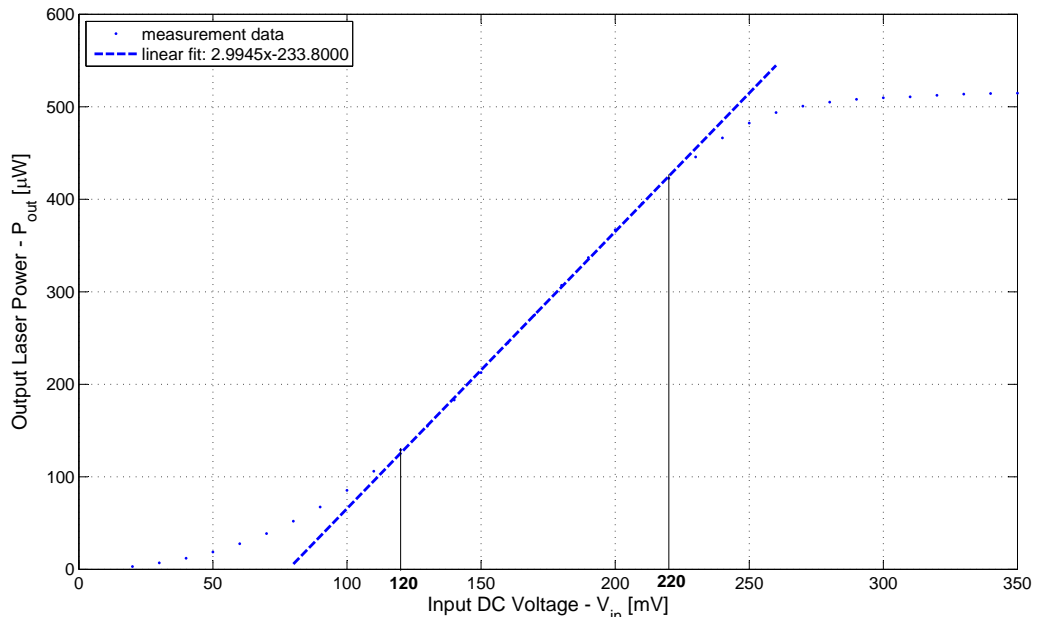


Figure 5.3.2: Characteristic curve of the actuating system. To guarantee linear actuation, the control signal must lie in the voltage range $V_{in} = 120 \div 220$ mV.

A characterization of the photodiode was already available from [13]. The measured curve, reported in Figure 5.3.3, shows:

- a maximum negative voltage output with amplitude of 4.9 V corresponding to a maximum measurable light power of 480 μW ;
- linear gain of $k_{\text{PD}} = 11.17 \text{ mV}/\mu\text{W}$ for a input light power range up to 200 μW .

Therefore, to guarantee proper detection, the overall system was regulated in such a way that the nominal intensity of laser light in front of the two sensors during the performance tests was in the center of the linear range of operation for the diodes, i.e. of about $P_{\text{in}} = 100 \mu\text{W}$.

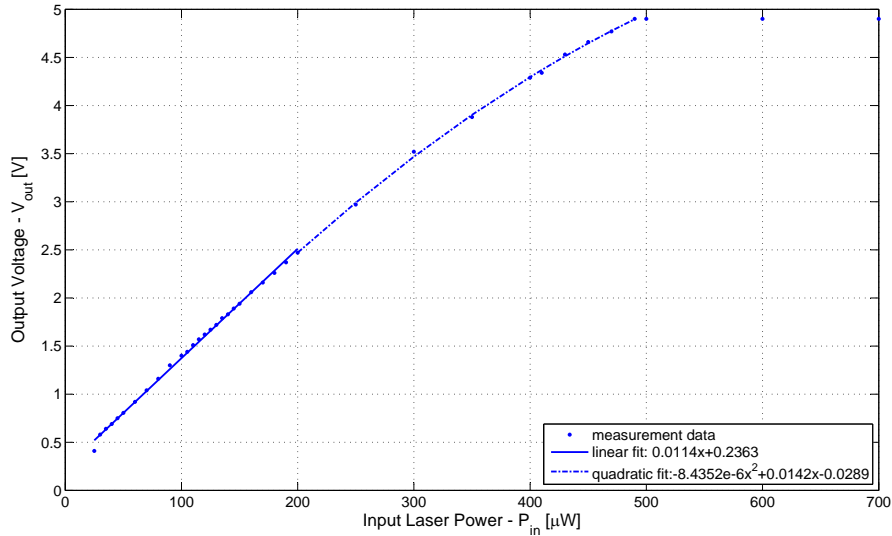


Figure 5.3.3: Characteristic response of the photodiode. Source: [13].

After this first static characterization, the dynamics of the main components of the stabilizer was also investigated, so to check the relative bandwidths and guarantee the possibility to implement a system with the required speed.

First, the transfer function of the actuation and sensing system was measured by manually scanning the frequency range $1 \div 60 \text{ kHz}$ with a signal generator (Stanford Research System DS345) used to drive the frequency mixers and then measuring the light intensity response with a detector, according to the measurement scheme in Figure 5.3.4. Results are depicted in Figure 5.3.5, which fits quite well (at least in the frequency range of interest) the behavior of a first order element with a corner frequency of about $f_c = 20 \text{ kHz}$, that should be enough to effectively control the light intensity up to 10 kHz.

Finally, the phase lag introduced by digital conversion and data processing in the controller was checked out. To measure these effects independently from the behavior of the controller itself, the frequency measurements were taken on the following simplified programs:

- a program that simply returns at the output the received input, after ‘back and forth’ A/D conversion, in order to highlight the sampling-related delay;
- the complete program for the servo loop (fully described in § 5.4), set in a simply proportional control mode, so to evaluate the overall delay of the system.

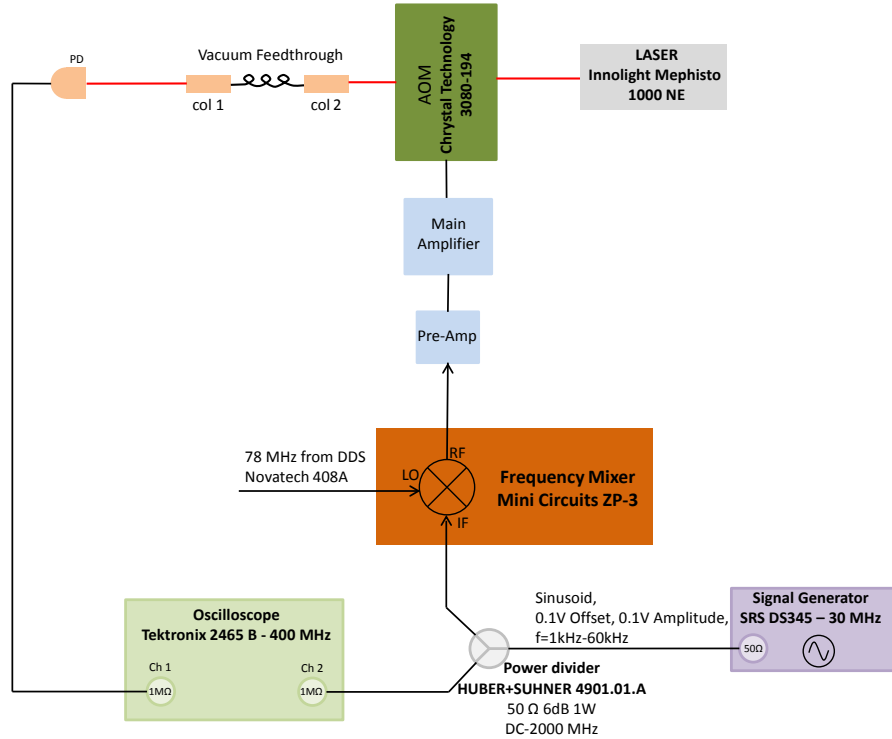


Figure 5.3.4: Setup for the characterization of actuating and sensing system frequency response.

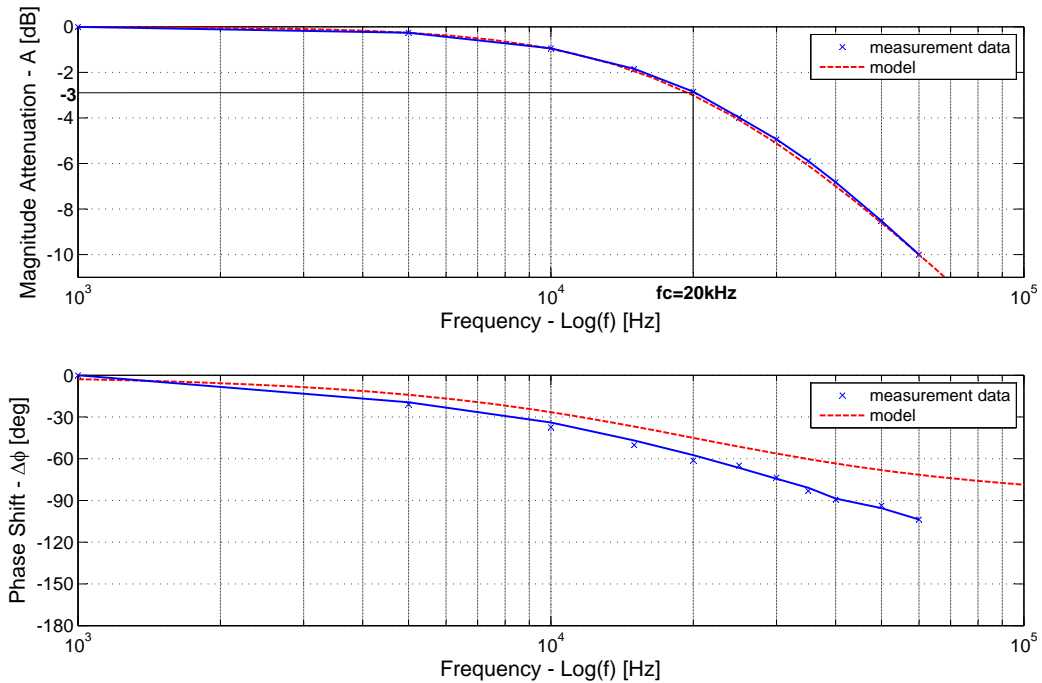


Figure 5.3.5: Frequency response of the actuating and sensing system. The plots show a corner frequency (correspondent to a magnitude attenuation of 3dB) of $f_c \approx 20\text{kHz}$.

Different configurations and sampling frequencies were initially tried out and after some trouble shooting with the connector system at the input of the FPGA and improvements to the implemented program in order to reduce the system delay, a conclusive configuration for the system was fixed and a default value for the sampling frequency of $f_s = 200\text{ kHz}$ was chosen. For this configuration, the phase shift was measured by executing a complete scan of the frequency range $f = 10^2 \div 10^5\text{ Hz}$ with a Network Analyzer (Agilent E5061B, [21]), according to the measurement setup scheme in Figure 5.3.6. The obtained results are depicted in Figure 5.3.7 and show a crossover frequency only slightly less than the theoretical value of 100 kHz foreseen in agreement with Nyquist-Shannon Sampling Theorem (Eq. (4.1.1)) and perfectly acceptable for the controller requirements.

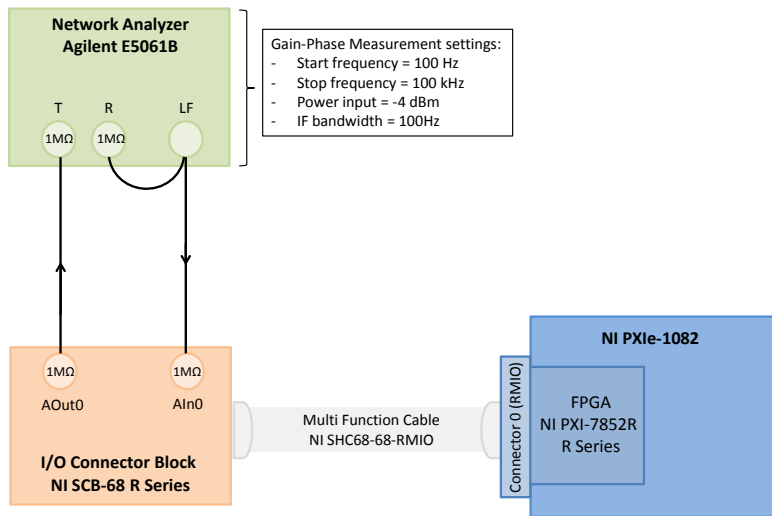


Figure 5.3.6: Setup for the measurement of the phase lag due to data sampling and processing.

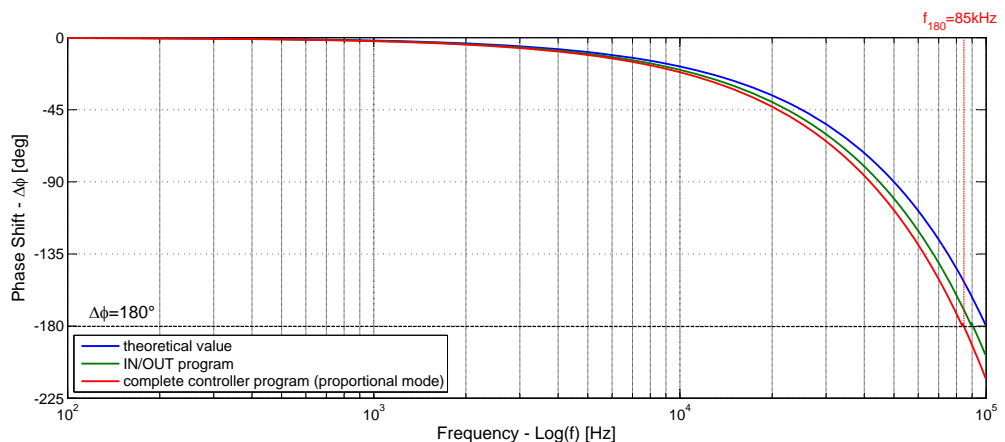


Figure 5.3.7: Phase lag due to digital conversion and data processing. The complete control program (set in pure proportional mode, at $f_s = 200\text{ kHz}$) shows a crossover frequency (correspondent to a phase lag of 180°) of $f_{180} \approx 85\text{ kHz}$.

5.4 Implementation of the digital controller

In this section, the VI implemented in the FPGA for intensity stabilization is described in detail. As already pointed out, this program is based on a simplified version (without derivative term) of the *PID Controller.vi* introduced in § 4.3, used as a nested subVI inside an higher level program that runs the four stabilization lines in parallel and executes some accessory functionalities.

This main instrument is called *Intensity Stabilization.vi* and will now be described referring to the functionalities included in its front panel (shown in Figure 5.4.1) and to the complete flow of operations executed by the correspondent block diagram (reported in Figure 5.4.2). For the sake of clarity the above mentioned figures report only the code for a single stabilization line.

Section 1 of the front panel is common to the four stabilization lines and includes a button to stop the VI, a knob through which the user can choose the sampling rate for the system and two indicators to monitor that the chosen sampling period is enough to complete the execution of the entire program. The *Activate I-Stab i Ifo j* button in Section 2 provides the possibility to switch on and off the single stabilization lines (two lines each, for two interferometers) independently from the others, while the *Invert error* button allows to invert the calculation of error signal depending on the sign of the output voltage of the used photodetector. Moving rightwards in the panel, in Section 3 we find:

- the *Output Offset* slider, through which the user can set an offset voltage to be added to the control signal, whose default value is fixed at 170 mV;
- a set of controls to fix the setpoint for the controller by direct measurement of light power on the photodiode at a certain time and to eventually apply further adjustment.

Section 4 is mainly dedicated to the tuning of the PI controller parameters, that can be executed via two numeric controls (*P-Coefficient* and *I-Coefficient*); besides this, it also provides the possibility to manually reset the integral part of the control signal, when needed, with the *Reset I-part* button. Finally, in section 5 a monitor led labeled *Output in range?* is used to alert the user when the control signal exits the linear range of operation of the actuator and is therefore cut off by the program to the upper or lower limit (set at $100 \div 240$ mV).

The internal structure of the VI is based on the succession of three flat sequences, thus providing the correct sequentiality for the different operations. The first sequence simply initialize the sampling rate of the system, converting the value set by the user in kHz to the correspondent number of ticks of the internal clock, running at 40 MHz, and writing the obtained value into the local variable *Scan Rate*. The second sequence contains the main code, which is continuously executed by a while loop until the conditional terminal is deactivated by pushing the *Stop* button and thus changing the value of the correspondent boolean variable. The rate of the loop timer is set reading the *Scan Rate* variable. A counter is also inserted to keep trace of the number of ticks needed to complete the loop, shown to the user via the *Needed Ticks* indicator. Last sequence is only used to reinitialize the value of the output to the default voltage of 170 mV once the VI is stopped.

Going now in deeper detail of the main code executed by the while loop, we can first of all notice that this is also broken into two flat sequences. In the first structure, whose code is shown in Figure 5.4.3, the input signal coming from the detector and representing the measured laser

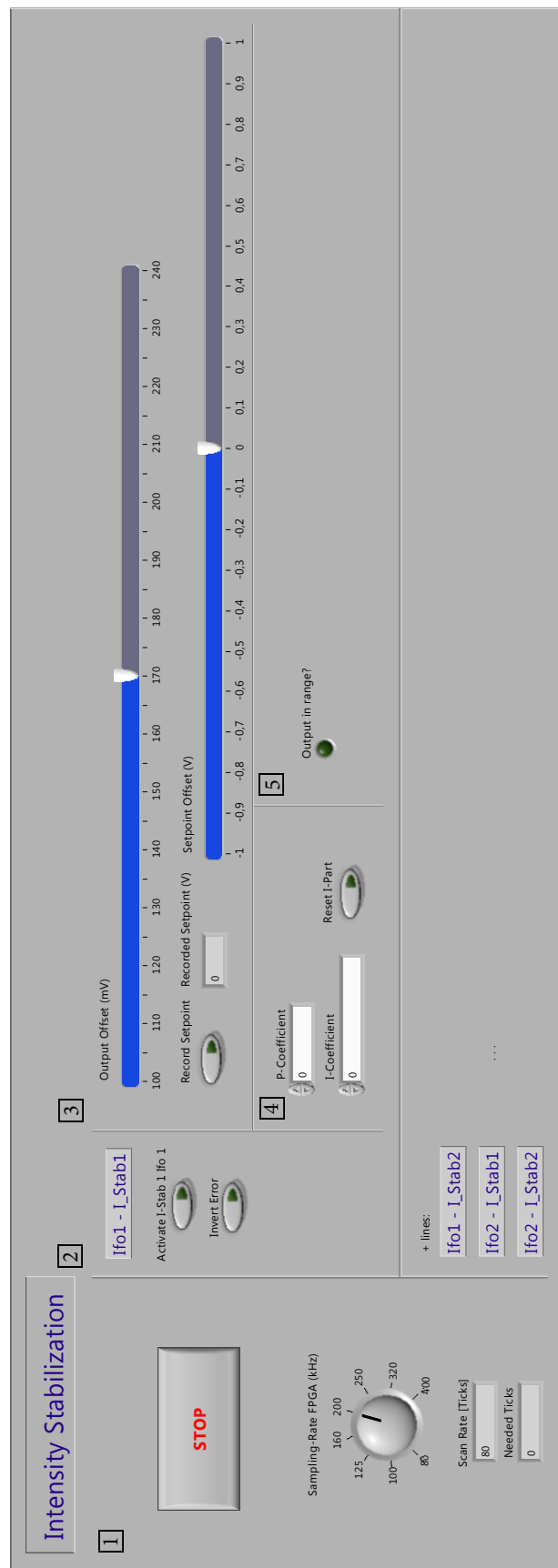


Figure 5.4.1: Front panel of *Intensity Stabilization.vi*.

5 Intensity Stabilization

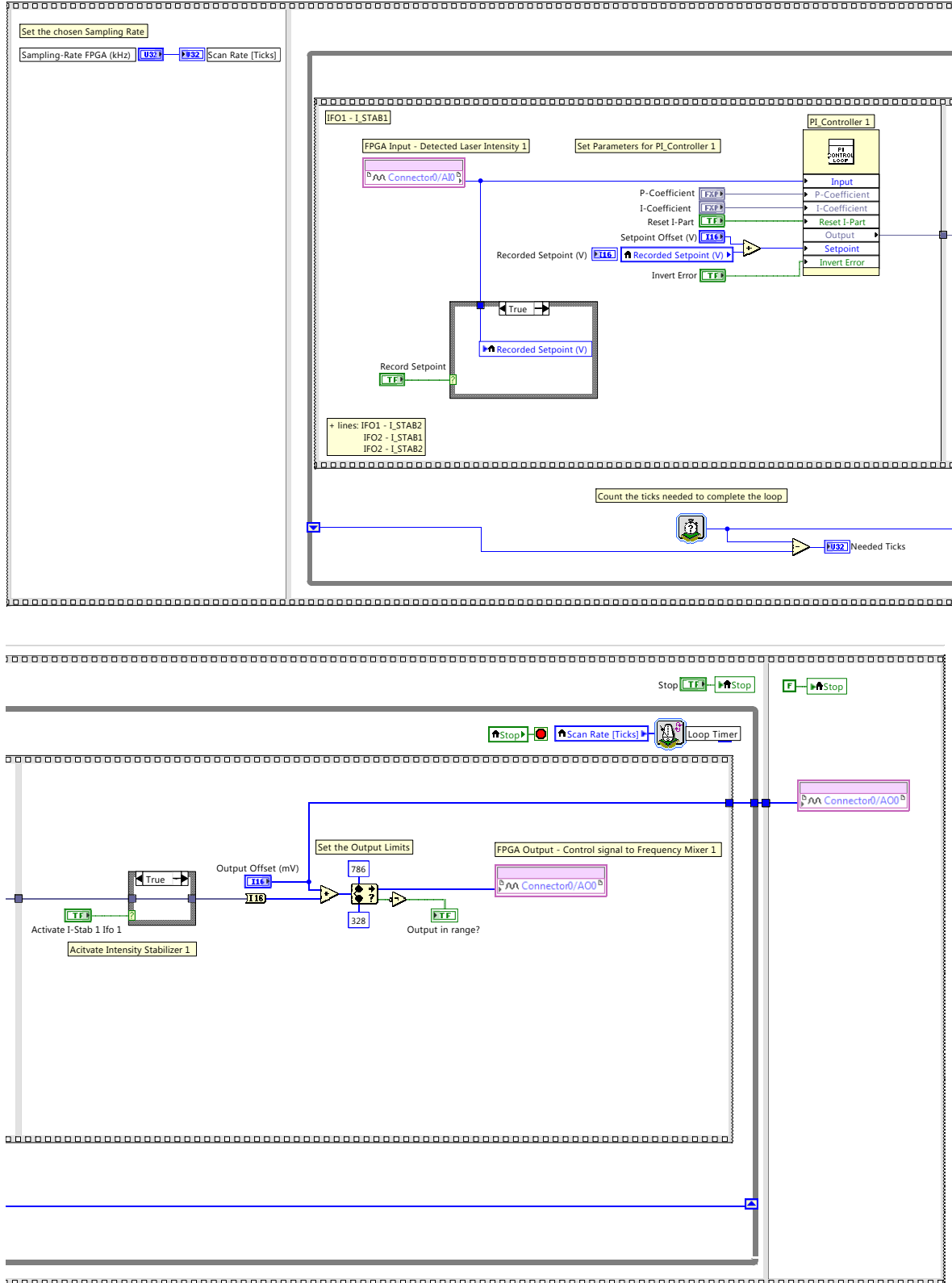


Figure 5.4.2: Block diagram of Intensity Stabilization.vi.

intensity enters one of the analogue input channel (e.g. *Connector0/AI0*) of the FPGA board and, after digital conversion, is sent to the input of the FPGA program as a 16 bits signed integer signal. Here a case structure controlled by the *Record Setpoint* button enables to record the input value of the laser intensity at a certain instant and to use it as setpoint for the *PI Controller*, eventually corrected adding a certain *Setpoint Offset*. Moreover, the parameters of the *PI Controller* are set through the correspondent controls in the front panel, and all these variables are sent to the *PI Controller* subVI to be processed and produce the control signal.

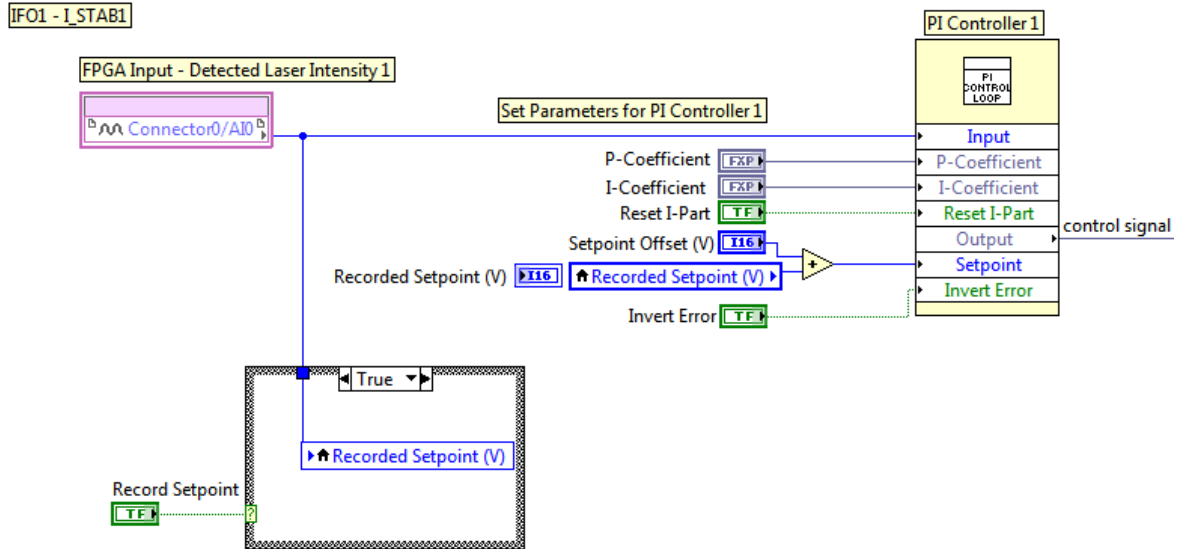


Figure 5.4.3: Code of the first sequence of the main while loop of the *Intensity Stabilization.vi*.

As already said, this VI is a customized version of the *PID Controller.vi* introduced in § 4.3, where the derivative part of the algorithm has been removed and an additional feature has been added to allow the inversion of the error computation depending on the sign of the PD characteristic. This feature is implemented at the input of the subVI, as shown in Figure 5.4.4.

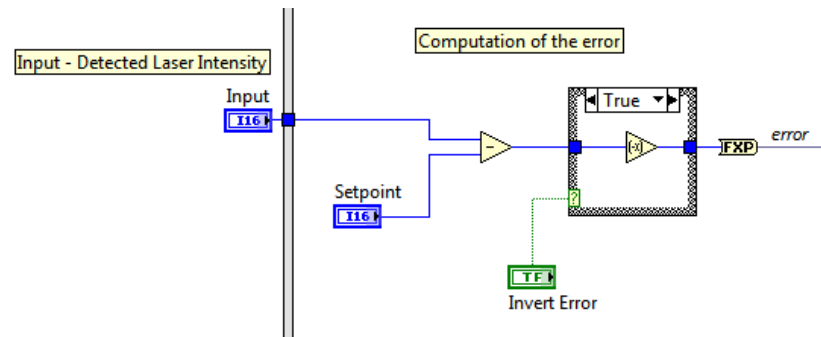


Figure 5.4.4: Code for the inversion of the error signal computation.

Furthermore, the fixed-point data configuration for the controller parameters is customized. Table 5.4.1 shows the chosen configuration and the correspondent digital range and resolution.

| Parameter | Signed/Unsigned | n_I | n_F | Range | Resolution |
|-----------|-----------------|-------|-------|------------|----------------------|
| K_P | U | 2 | 16 | $0 \div 4$ | $6.10 \cdot 10^{-5}$ |
| K_I | U | 0 | 24 | $0 \div 1$ | $5.96 \cdot 10^{-8}$ |

Table 5.4.1: Digital range and resolution of the normalized PI parameters for the intensity stabilizer, as a function of the fixed-point data configuration chosen.

The code in the second sequence, shown in Figure 5.4.5, firstly includes a case structure used to decide whether to deliver or not to the output the control signal generated by the *PI controller* depending on the value of the boolean variable controlled by the *Activate I-Stab i Ifo j* button. The output of this structure (equal either to the control signal, when the line stabilization is active, or to 0, when it's deactivated) is summed to a constant offset which corresponds to the default 170 mV input DC signal for the frequency mixer. The obtained output is then regulated in order to restrain the correspondent voltage within the defined actuator operational boundaries (100 \div 240 mV), and the *Out of Range?* led is enlightened whether cut off is required to keep it in range. Finally, the processed output signal leaves the FPGA, is converted back to analogue and is finally sent to one of the analogue output channel of the FPGA board (e.g. *Connector0/AO0*), from which it will be wired to the IF port of the correspondent frequency mixer to actuate the commanded intensity modulation.

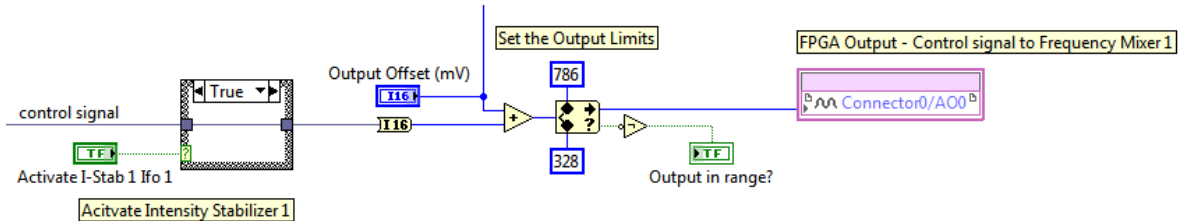


Figure 5.4.5: Code of the second sequence of the main while loop of the *Intensity Stabilization.vi*.

5.5 Tuning and Performance Tests

After completion of the components characterization and digital design phase, the system was experimentally tested to verify the functionality of the stabilizer.

5.5.1 Measurement of free running laser intensity

First of all a free running measurement was conducted with both the detectors available in the setup to get a reference for the fluctuations of laser intensity and an assessment of detectors noise.

For this purpose, two different Data Acquisition (DAQ) systems were used for the two frequency bands of interest, due to the complementary capabilities of the instruments used to this end. The details of the two measurement setups, the results obtained and the subsequent considerations are presented in the following sections.

Low frequency measurement

For the low frequency band ($f = 10^{-4} \div 1\text{ Hz}$), acquisition was executed with the National Instruments DAQ board 6259 [22], using a simple LabVIEW program as interface to record and read the acquired data. The complete measurement setup is depicted in Figure 5.5.1.

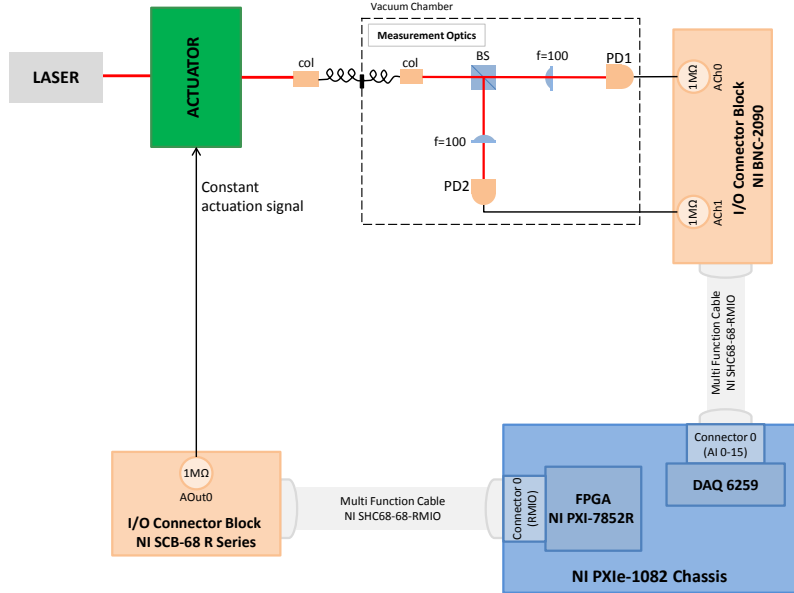


Figure 5.5.1: Initial setup for low frequency measurement of free running intensity. A constant actuation signal is generated by the FPGA and sent to the actuator while the output laser intensity measured by the two PDs is recorded by a DAQ board mounted on the same PXIE chassis as the FPGA board.

The measurements were run overnight to reduce the effect of external disturbances in the laboratory, with an acquisition rate of 25 Hz for a 10 hours time period. The raw data obtained, made up of the measured voltage of the two detectors (whose equivalent laser intensity can be derived according to the PD characteristic derived in § 5.3) and a correspondent time stamp, were later processed to get the ASD of the RIN² of the two measurements and to derive the portion of this noise due to the intrinsic detector noise. For this purpose, the measured intensities were

²Relative Intensity Noise (RIN) describes fluctuations in the optical power of a laser and can be defined as power noise normalized to the average power level:

$$RIN = \frac{\delta P}{\bar{P}} ,$$

where $P(t) = \bar{P} + \delta P(t)$ is the optical power of the laser. Usually it is statistically described with its Power Spectral Density (PSD), given by:

$$S_I(f) = \frac{2}{\bar{P}^2} \int_{-\infty}^{\infty} \langle \delta P(t) \delta P(t + \tau) \rangle \exp(i2\pi f \tau) d\tau ,$$

or with the Amplitude Spectral Density (ASD) of the laser intensity, which corresponds to the square root of the PSD [17].

first normalized with their mean value, the detector noise was then computed as their subtraction divided by $\sqrt{2}$, and the ASD of the three variable was finally computed, using a Blackman-Harris window with 50% overlap.

The results got with the first free running measurement are depicted in Figure 5.5.2, which shows:

- a peak at frequency lower than 10^{-3} Hz, presumably related to the temperature variation induced by the air conditioning;
- a major spike around $3 \cdot 10^{-1}$ Hz deriving from an aliasing problem;
- a shoulder centered around $3 \cdot 10^{-2}$ Hz, linked to the presence of a ground loop which was found on the laboratory setup and added noise to the FPGA output.

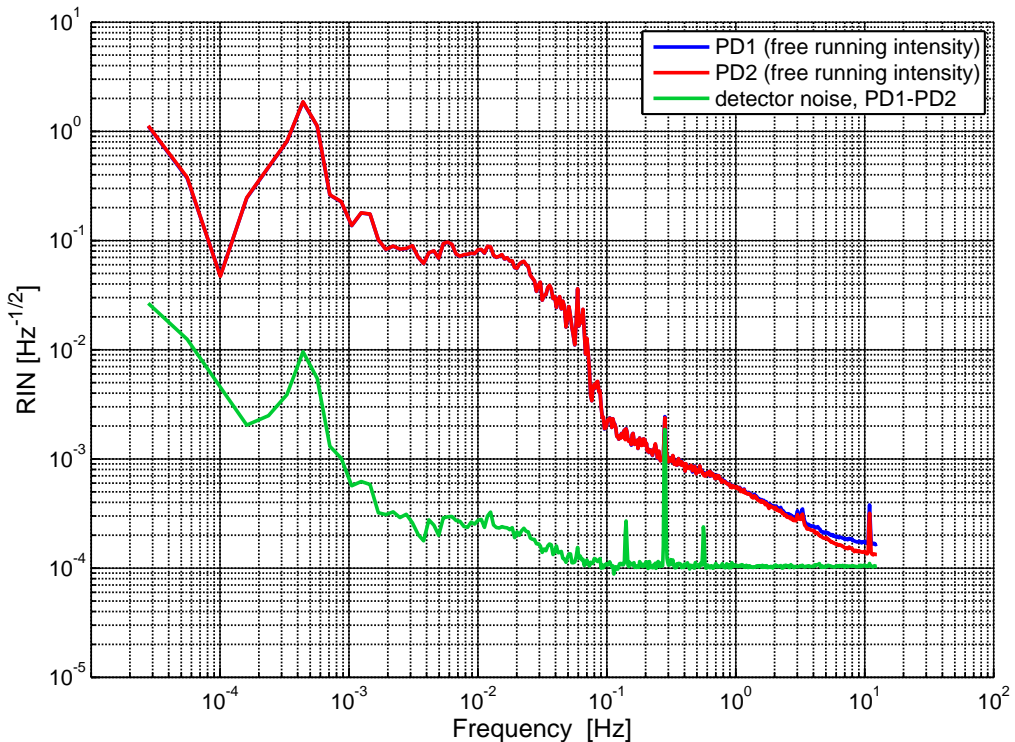


Figure 5.5.2: Initial low frequency measurement of the ASD of free running laser RIN (for the frequency band $f = 10^{-4} \div 1$ Hz).

To face the encountered issues an enhanced setup for the measurement was settled, using the following expedients:

- a resistance bridge was added to the setup in order to record the temperature and monitor the effect of air conditioning;
- two first order low pass filters (Stanford Research System SR560, Specifications in Appendix A.6) with corner frequency of 10 Hz were introduced between the output of the two detectors and the DAQ system to get rid of the aliasing problems;

- a second order low pass filter with corner frequency of 10 Hz was introduced between the FPGA output and the actuator input, which allowed to temporarily bypass the grounding problem without affecting the results in the frequency range of interest for this measurements set (up to 1 Hz); lately, a deeper investigation of the problem was carried out and solved via installation of an isolation transformer on a clean ground of the lab.

The free running intensity measurement was therefore repeated with the improved setup shown in Figure 5.5.3. The final result is given in Figure 5.5.4 , which shows for the detectors a white noise level of about $10^{-4} \text{ } 1/\sqrt{\text{Hz}}$ for frequencies higher than 10^{-2} Hz , rising at lower frequencies with a $1/f$ behavior, increased below 10^{-3} Hz due to the air conditioning disturbance, as it's underlined by the correlation between the correspondent peaks in the laser intensity and temperature plots. This noise level was therefore fixed as a target for the laser RIN to achieve with intensity stabilization.

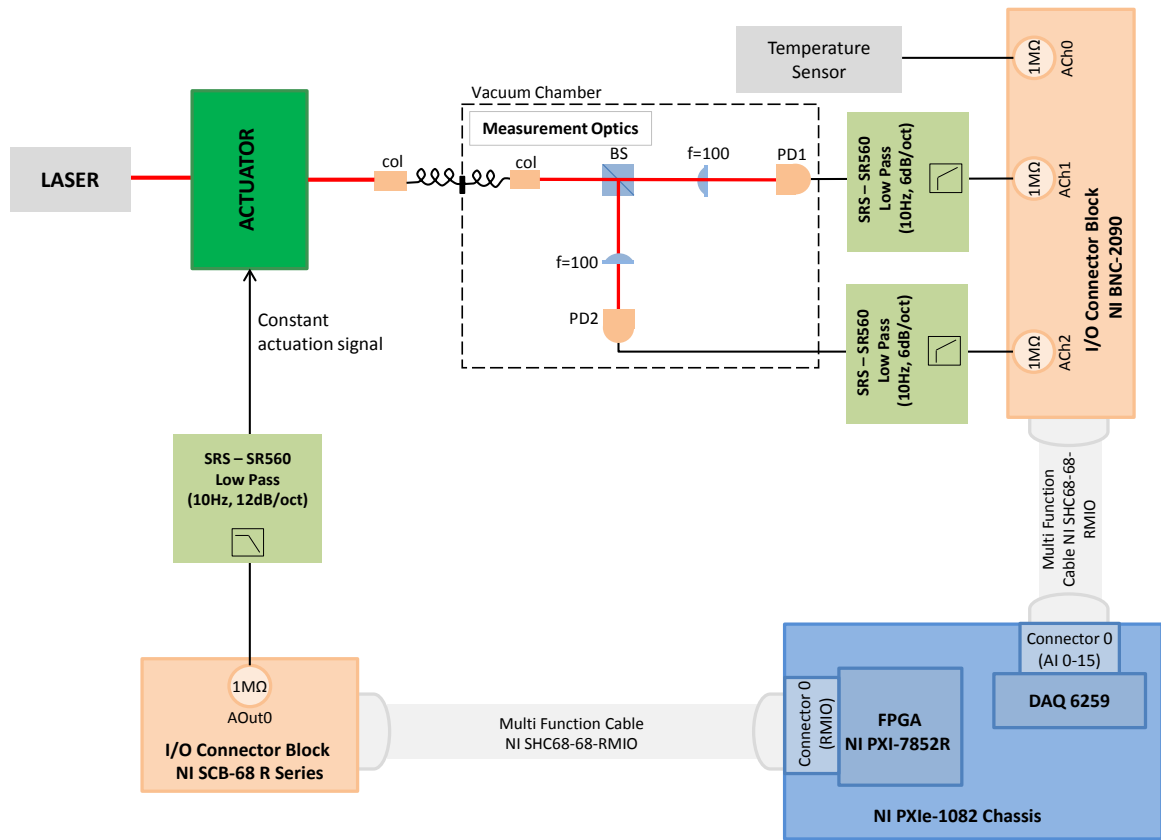


Figure 5.5.3: Enhanced setup for low frequency measurement of free running intensity. Filters are added to the input and output of the digital system and an additional measurement of the environment temperature is led.

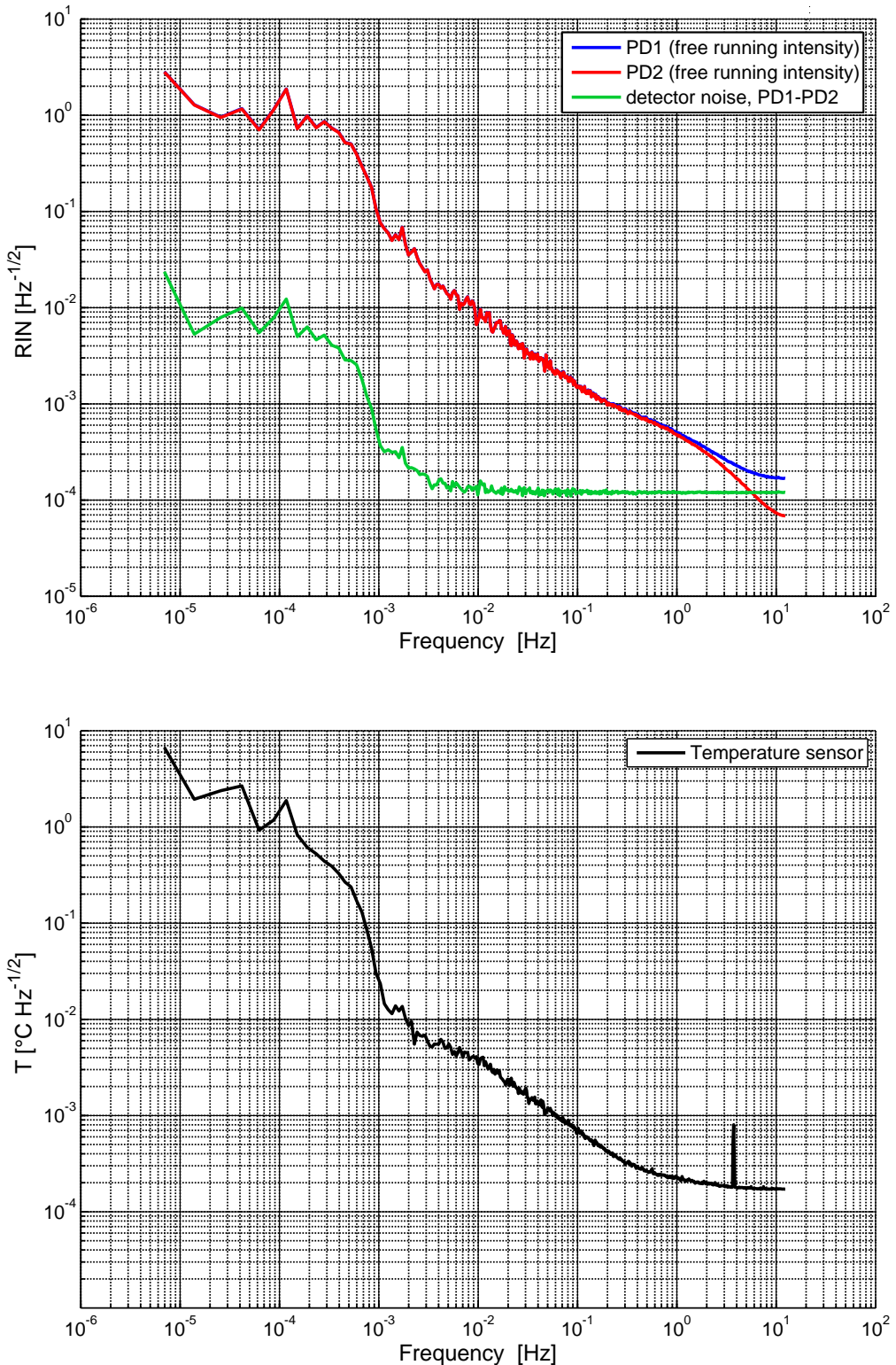


Figure 5.5.4: Enhanced low frequency measurement of the ASD of free running laser RIN (for the frequency band $f = 10^{-4} \div 1 \text{ Hz}$). Temperature ASD is also shown to underline the correlation between the frequency content of laser RIN below 10^{-3} Hz and the characteristic behavior of the air conditioning system.

High frequency measurement

For the high frequency band (up to $f_{\text{het}} = 10 \text{ kHz}$), a digital oscilloscope (LeCroy WaveRunner 204Xi [23]) was instead used for acquisition, according the scheme shown in Figure 5.5.5.

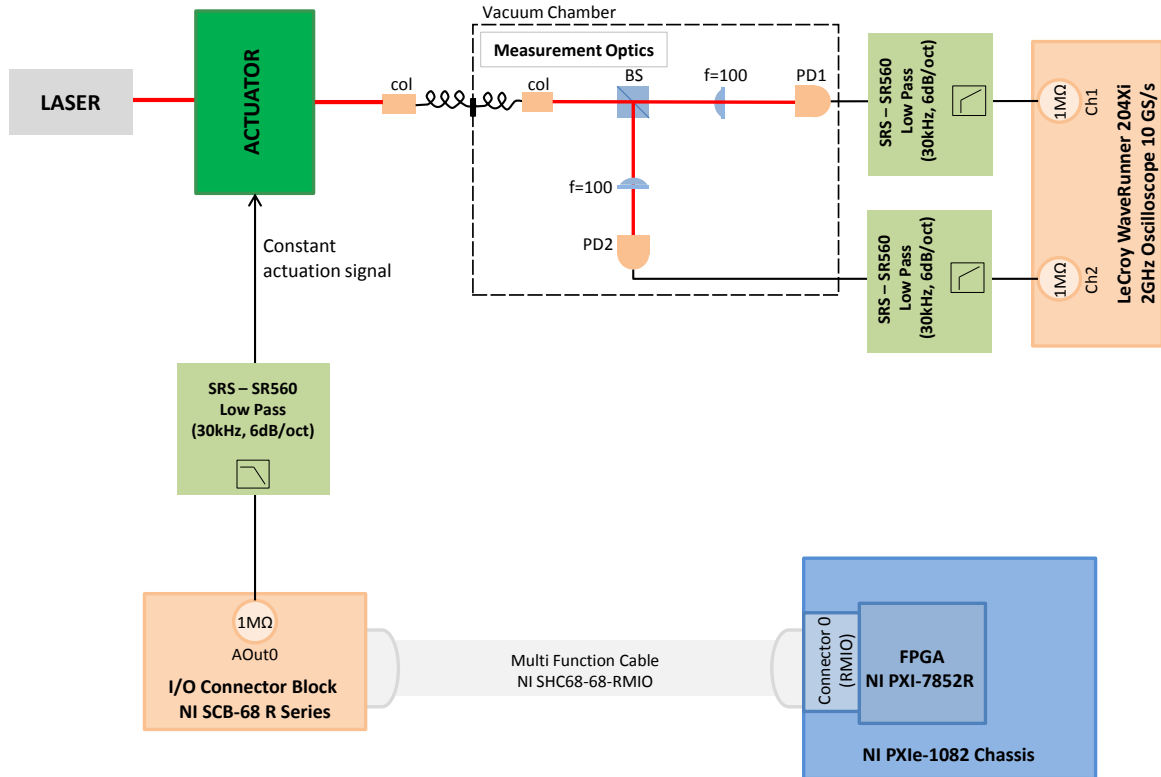


Figure 5.5.5: Schematic of the setup for high frequency measurement of free running intensity.

The measurements were run over a period of 100s with an acquisition rate of 100 kHz. The acquired data were processed similarly to the low frequency case and the ASD shown in Figure 5.5.6 was obtained.

Apart from the spikes around $f = 50 \text{ Hz}$, due to the ground loop problem previously described, a major issue is underlined by this plot: for frequency higher than $\approx 30 \text{ Hz}$ detector noise is larger than laser RIN, meaning that the fluctuations of free running laser intensity can't be distinguished from the detector noise itself and that the control loop performance can't be evaluated with current detectors. Therefore the high frequency measurement of the stabilizer performance was discarded. Once the new custom photodiodes designed for the laboratory model will be ready, for which a much lower noise level is expected, the measurements described in the next section for the low frequency band will need to be repeated for frequencies up to 10 kHz.

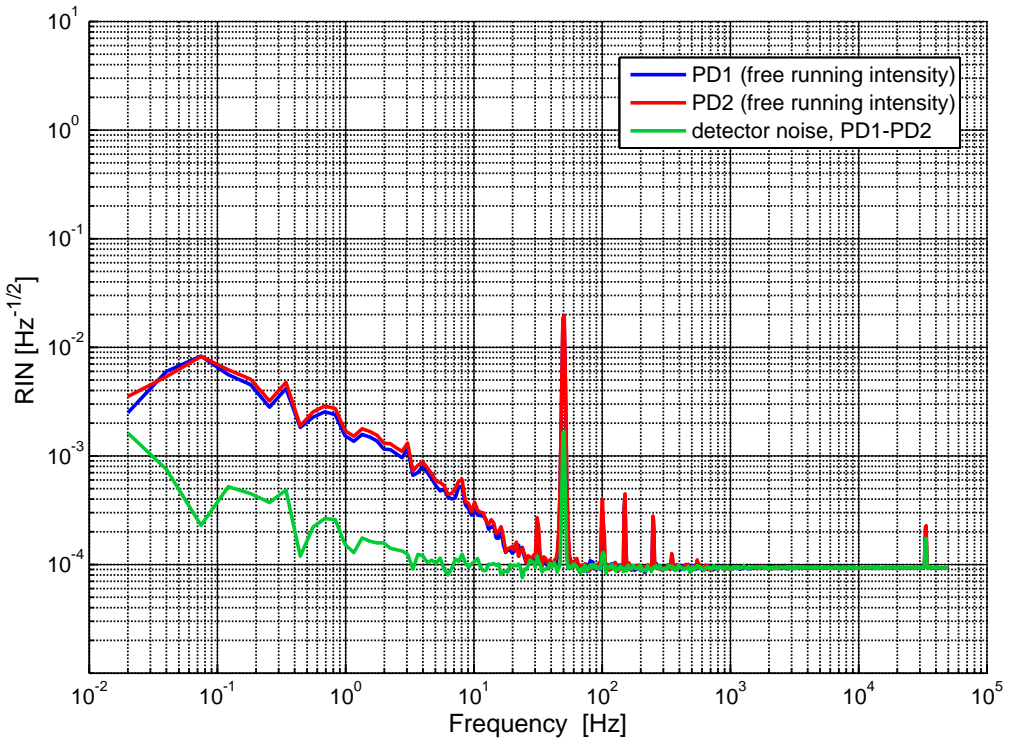


Figure 5.5.6: High frequency measurement of the square root PSD of free running laser RIN (for the frequency band $f = 1 \div 10^4$ Hz).

5.5.2 Measurement of stabilized laser intensity

To measure the performance of the intensity stabilizer in the frequency band $f = 10^{-4} \div 1$ Hz, the setup shown in Figure 5.5.7 was used.

The controller parameters were chosen via trial and error tuning method [24]. The controller is first set in proportional mode and the proportional gain is turned up until the system oscillates, then it's turned down to something between half of its critical value and the value itself so to get a fast but stable response. Afterward integral action is introduced and the integral coefficient is tweaked so to eliminate the setpoint droop generated by the proportional term. Several performance measurements were also carried out for different tuning configurations in order to improve the controller action. The final configuration chosen for the digital normalized parameters is the following:

| K_P | K_I |
|-------|---------------------|
| 0.1 | $1.5 \cdot 10^{-5}$ |

Table 5.5.1: Tuned parameters for the Intensity Stabilization PI controller.

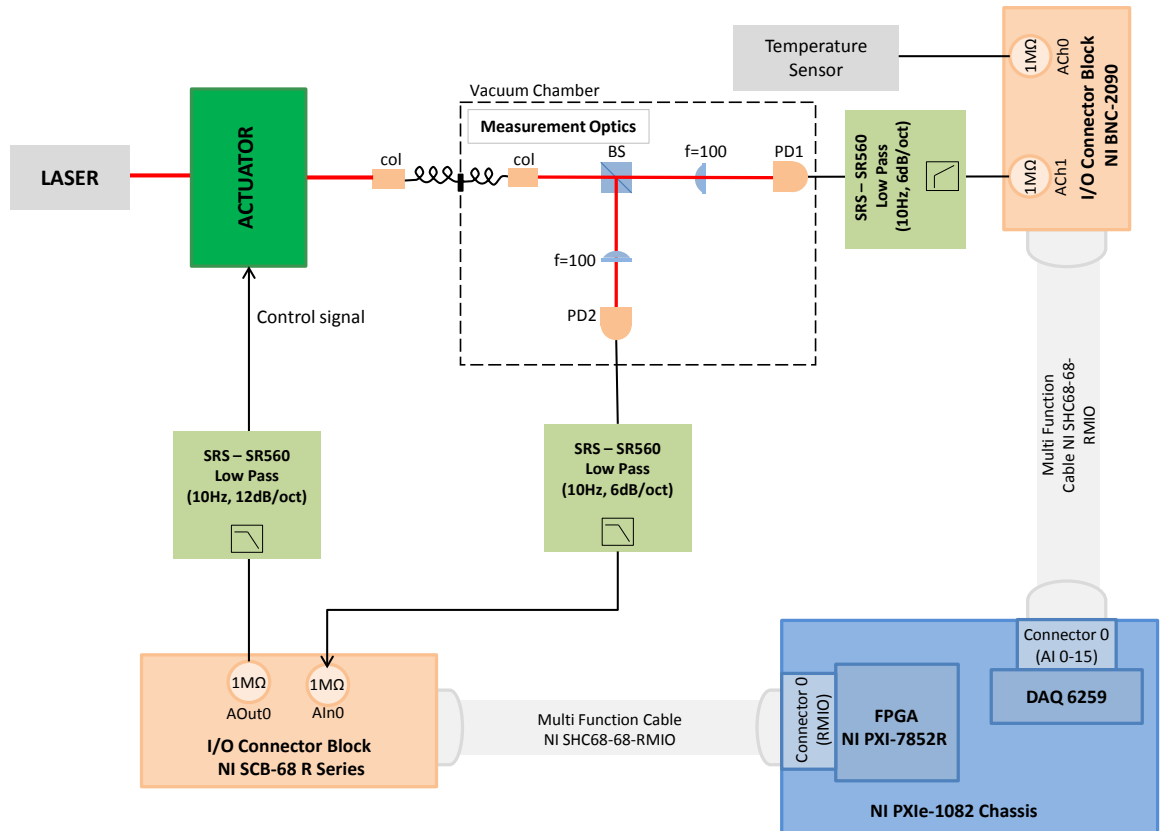


Figure 5.5.7: Schematic of the setup for the intensity stabilization performance test.

The performance of the system was finally verified with repeated measurement for the different signal lines, acquiring data at 25 Hz over a period of 10 hours and processing them as already described for the free running test. The resulting RIN of the stabilized laser light was compared to the free running measurement, as shown in Figure 5.5.8. As we can see, a controlled intensity fluctuation approximately equal to the detector noise was proofed, thus fulfilling the stabilization target and demonstrating a substantial improvement with respect to the situation with no intensity stabilization implemented. To conclude, Figure 5.5.9 shows the RIN of free running and stabilized laser intensity in the time domain, where the validity of the intensity stabilization is also evident.

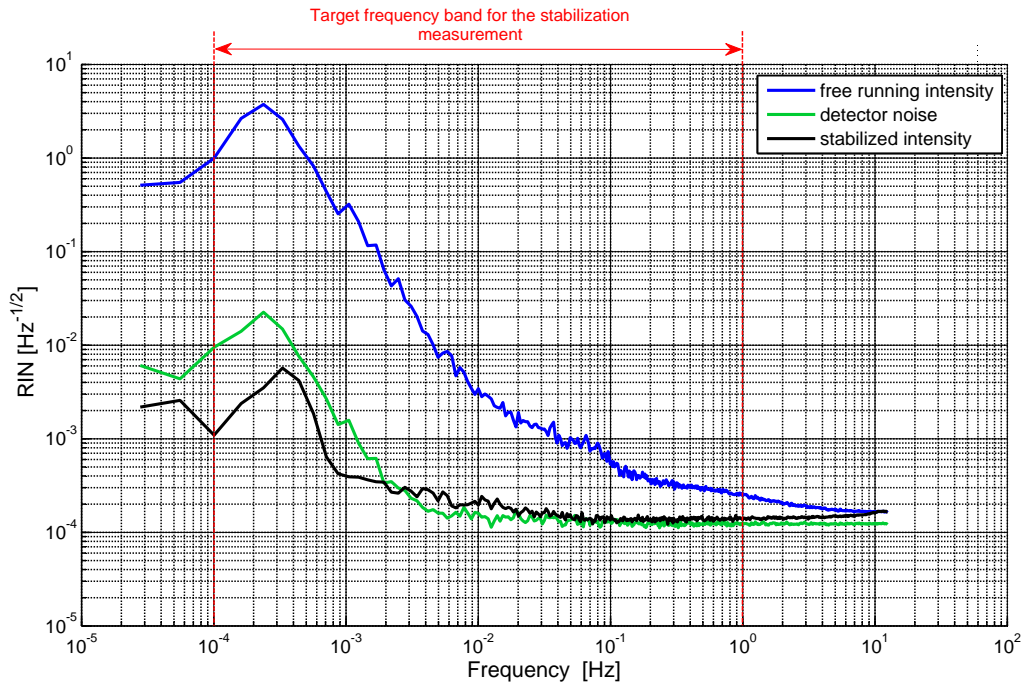


Figure 5.5.8: Comparison of the ASD of the stabilized laser beam RIN with the curves for free running intensity and detector noise.

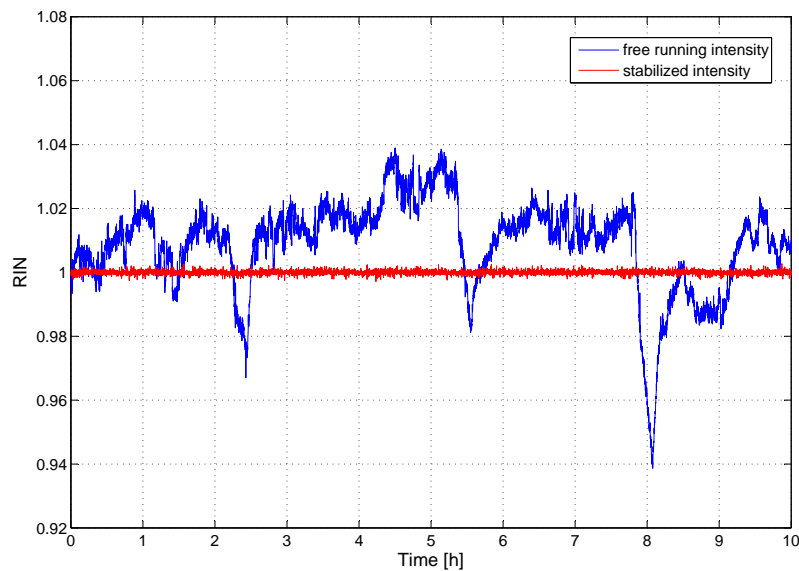


Figure 5.5.9: Comparison of the free running and stabilized laser beam RIN in the time domain.

6 Height Controller

As pointed out in Chapter 3, to have the possibility to investigate the performance of the inertial sensor with an earthbound laboratory model we need to levitate the test mass and keep it in a stable position by means of a stabilizing servo loop which measures the position of the test mass barycenter along one axis and consequently acts on the levitation actuator to modulate the electromagnetic force applied to compensate its weight. This chapter reports the characterization of the levitation system carried out for this thesis and describes the implementation of a digital cascade control loop designed for this purpose.

6.1 Objective

The aim of the servo loop is first of all to make levitation possible, stabilizing the dynamics of the test mass under the combined action of gravitational and electromagnetic force, which is intrinsically unstable as it can be derived by application of Maxwell's equations, [25].

The magnetic force acting on a ferromagnetic object of dipole moment \mathbf{m} due to an external field of magnetic flux density \mathbf{B} is proportional to the gradient of the correspondent magnetic potential energy, $U_m = \mathbf{m} \cdot \mathbf{B}$, as expressed by:

$$\mathbf{F}_m = \nabla U_m = \nabla(\mathbf{m} \cdot \mathbf{B}) . \quad (6.1.1)$$

A statement about the stability of the force field can be therefore inferred studying the laplacian of U_m that, assuming a constant magnetic dipole moment and applying laws of vector calculus, can be written as:

$$\nabla^2 U_m = \mathbf{m} \cdot (\nabla(\nabla \cdot \mathbf{B}) - \nabla \times (\nabla \times \mathbf{B})) . \quad (6.1.2)$$

Application of the magnetostatic formulation of Maxwell's equations (which can be considered a quite accurate approximation also for fields produced by not static currents, when they do not alternate too rapidly) to a volume around the object to be levitated, not containing the field generating source, leads to:

$$\nabla \cdot \mathbf{B} = 0 , \quad (6.1.3a)$$

$$\nabla \times \mathbf{B} = 0 . \quad (6.1.3b)$$

Substituting Eq. (6.1.3) in (6.1.2) the following result about the laplacian of the magnetic potential energy is eventually obtained:

$$\nabla^2 U_m = 0 , \quad (6.1.4)$$

meaning that U_m can only have saddle points and no minima are allowed (for which the condition $\nabla^2 U_m > 0$ should be verified). As a consequence, the correspondent force field \mathbf{F}_m does not present conditions of stable equilibrium, and in every point it has to be unstable at least in one direction. To overcome this limitation and make levitation possible, one possibility is to apply active feedback control, by detecting the mass position and consequently adapting the electromagnetic field by varying the current which is inducing it. In this way, the shape of the magnetic potential energy is modified and a stable condition can be found.

Once the test mass is levitated, a further requirement to be satisfied is to achieve a precision in its positioning better than a few pm/\sqrt{Hz} for the frequency range of interest for eLISA ($f \approx 10^{-4} \div 1 Hz$), so to not invalidate the possibility to fulfill the overall measurement target of the inertial sensor. A crucial factor in this sense is to get a sufficiently precise sensing signal and therefore particular attention will need to be paid in a further development of the project to implement a sensing system with high enough sensitivity.

6.2 Setup and component description

A schematic of the main components of the setup for the levitation system is given in Figure 6.2.1.

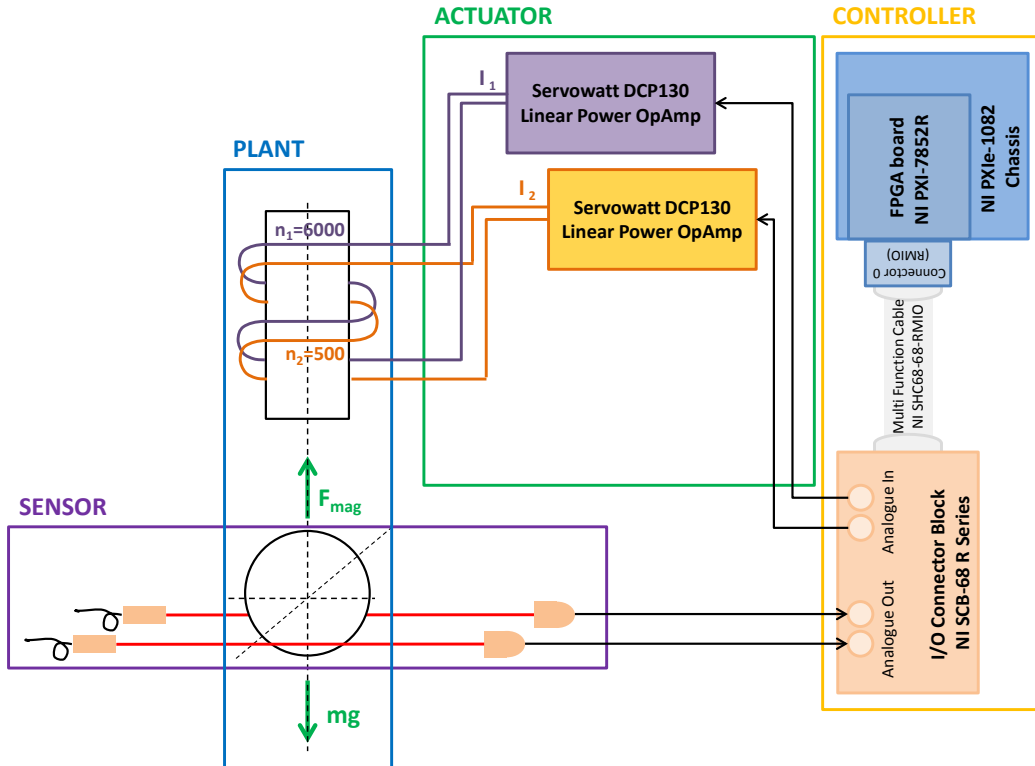


Figure 6.2.1: Schematic of the main components for the height control setup.

The variable to control is the test mass position along the vertical axis, which is basically driven by its weight and by the electromagnetic force generated by the two-stages solenoid. The detection is devolved upon an optical sensing system based on the light barriers technique, as described in § 3.3. Two collimators fixed to the lower plate of the test bed's supporting structure generate two collimated laser beams, in such a position that in the nominal state the levitated test mass covers half of each beam cross section. The residual transmitted light is then detected by two photodiodes, whose signals are sent via an I/O connector block to the FPGA embedding the digital controller. After A/D conversion, the two signals are summed to get an indication of the test mass height which is insensitive to displacements in any direction orthogonal to the levitation axis. The resulting sensing signal is then processed by the controller to generate the actuation signal to control the plant. The actual control unit includes two controllers, set in a cascade structure. Therefore at the output of the FPGA board, after D/A conversion, we have two analogue voltage signals that can be wired through the I/O block to the input of two linear power operational amplifiers, that transform them so to generate two properly amplified and current regulated signals to feed the two coils used for levitation. The variation of the electromagnetic field generated by the modulation of the induction current finally translates the control signal into an adaption of the test mass height.

The major features of the different blocks of this setup will now be described in deeper detail.

6.2.1 Plant

The process that the servo loop aims to control is represented by the dynamics of the test mass m under the effect of gravitational and electromagnetic force, which can be described by the second cardinal equation:

$$m\mathbf{a} = \mathbf{F}_g + \mathbf{F}_m , \quad (6.2.1)$$

where \mathbf{a} is the acceleration of the test mass, \mathbf{F}_g is the gravity force, given by $\mathbf{F}_g = m\mathbf{g}$, and \mathbf{F}_m is the force of magnetic attraction exerted on the test mass by the solenoid, generated by the variation of magnetic potential energy as from Eq. (6.1.1).

Neglecting possible losses, the magnetic potential energy of the considered circuit, U_m , can be described as [26]:

$$U_m = \frac{1}{2}Li^2 , \quad (6.2.2)$$

where i is the current passing through the circuit and L its inductance, defined by the number of turns of the coil, n , and the total magnetic reluctance of the circuit, \mathcal{R}_m :

$$L = \frac{n^2}{\mathcal{R}_m} . \quad (6.2.3)$$

Considering that the reluctance of the circuit is dominated by the reluctance of the gap between the test mass and the magnet, we can approximate it to:

$$\mathcal{R}_m \approx \mathcal{R}_{m,gap} = \frac{\delta}{\mu_0 A} \quad (6.2.4)$$

and finally rewrite the magnetic potential energy, by substituting Eq. (6.2.4) and (6.2.3) in Eq. (6.2.2):

$$U_m = \frac{1}{2} \frac{n^2 i^2 \mu_0 A}{\delta}, \quad (6.2.5)$$

wherein μ_0 is the magnetic permeability of vacuum, A is the overlapping area between the magnet core and the test mass and δ is the width of the gap existing between them.

At this point Eq. (6.2.1) can be rewritten introducing the derived expression of magnetic potential energy. Moreover, thanks to the axial symmetry of the problem, a simplified formulation can be used in any plane passing through the axis of the magnet. In particular, when choosing the reference frame shown in Figure 6.2.2, where δ describes the gap between the test mass and the magnet and r the radial displacement of the test mass with respect to the central axis, Eq. (6.2.1) can be decomposed in its scalar components:

$$m\ddot{\delta} = mg + F_{m,\delta} \quad (6.2.6a)$$

$$m\ddot{r} = F_{m,r} \quad (6.2.6b)$$

where:

$$F_{m,\delta} = \frac{\partial U_m}{\partial \delta} = -\frac{1}{2} \frac{n^2 i^2 \mu_0 A}{\delta^2}, \quad (6.2.7)$$

and:

$$F_{m,r} = \frac{\partial U_m}{\partial r} = \frac{1}{2} \frac{n^2 i^2 \mu_0}{\delta} \frac{dA}{dr}. \quad (6.2.8)$$

According to Eq. (6.2.6b) and (6.2.8), since a transverse displacement δr always generates a reduction of the overlapping area between magnet and test mass and thus always produces a reset force in the direction opposite to the motion, it can be easily deduced that the system is stable with respect to off-axis displacements. The dynamics of the test mass along δ axis is instead described by an unstable non linear system, as shown by Eq. (6.2.6a) and (6.2.7), which therefore needs an active correction to be stabilized. As controlling variable, the current flowing through the solenoid can be used.

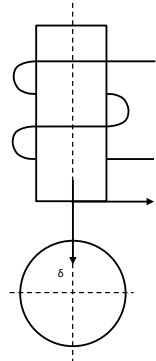


Figure 6.2.2: Reference frame for the description of test mass dynamics. The variable δ describes the axial gap between the tip of the electromagnet and the test mass, while r defines the displacement orthogonal to the electromagnet axis.

In order to get an easy to handle model to describe the system, for small variations of δ and i around an operating point ($\delta = \delta_0$, $i = i_0$) that can be assumed to correspond to a condition where the test mass acceleration is null ($\ddot{\delta} = 0$), the dynamics of test mass height variation can be linearized. A first-order Taylor expansion can be applied for this purpose to the axial component of the magnetic force:

$$(F_{m,\delta})_{lin} \approx F_{m,\delta}|_{\delta_0, i_0} + \frac{\partial F_{m,\delta}}{\partial \delta} \Big|_{\delta_0, i_0} (\delta - \delta_0) + \frac{\partial F_{m,\delta}}{\partial i} \Big|_{\delta_0, i_0} (i - i_0) \\ = F_{m,\delta}|_{\delta_0, i_0} + k_\delta \delta - k_i i , \quad (6.2.9)$$

where the coefficients k_δ and k_i are given by:

$$k_\delta = \frac{n^2 i_0^2 \mu_0 A}{\delta_0^3} , \quad (6.2.10)$$

$$k_i = \frac{n^2 i_0 \mu_0 A}{\delta_0^2} . \quad (6.2.11)$$

Substituting Eq. (6.2.9), (6.2.10) and (6.2.11) in Eq. (6.2.6a), and considering that at the operating point we have:

$$\ddot{\delta} \Big|_{\delta_0, i_0} = 0 \Rightarrow mg + F_{m,\delta}|_{\delta_0, i_0} = 0 , \quad (6.2.12)$$

we finally obtain the equation:

$$m\ddot{\delta} = k_\delta \delta - k_i i \quad (6.2.13)$$

whose Laplace transform is:

$$\delta(s) = -\frac{k_i}{ms^2 - k_\delta} i(s) \quad (6.2.14)$$

which describes a linear, second order, unstable system.

A significant remark to make about the above described model is that the expression therewith used for the magnetic force comes from magnetostatic equations and consequently it doesn't take into account the delayed behavior of the magnetic force with respect to the electric current generating it. Nevertheless, this delay can have a significant effect on the system dynamics, since the large number of windings and the optimization of the magnetic properties of the electromagnet tend to produce a very high inductance and therefore a correspondingly high resistance to energy variation. In first approximation this effect can be modeled introducing a first order element with a cutoff frequency of:

$$f_c \approx \frac{R}{2\pi L} , \quad (6.2.15)$$

where R and L are respectively the resistance and inductance of the circuit, whose value depends on the number of turns of the coil as expressed by the following equations:

$$R_{coil} = \frac{\rho l_{wire}}{A_{wire}} \approx \frac{\rho 2\pi r_m}{A_{wire}} n , \quad (6.2.16)$$

$$L_{coil} = \frac{1}{\mathcal{R}_{m,coil}} n^2 , \quad (6.2.17)$$

where $\mathcal{R}_{m,\text{coil}}$ is the magnetic reluctance of the coil, ρ the specific resistance of the wire material, A_{wire} the area of its cross-section and l_{wire} its length, approximately equal to n circles of radius r_m (i.e. the coil mean radius). Since the two coils are made of the same enamelled copper wire (CuL0,32), wound around the same spool, and installed as a single piece between the same magnet core and housing, the parameters other than the number of turns can be considered constant and the following relation can be derived:

$$\frac{f_{c,1}}{f_{c,2}} = \frac{n_2}{n_1}, \quad (6.2.18)$$

meaning that the two coils are expected to have corner frequencies differing from each other for approximately an order of magnitude.

Moreover, since the two coils are independently fed and controlled, the actual plant must be modeled as a 2-input-1-output system, described in the frequency domain by:

$$\delta(s) = \underbrace{\begin{pmatrix} G_{\text{plant},1}(s) & G_{\text{plant},2}(s) \end{pmatrix}}_{\mathbf{G}_{\text{plant}}(s)} \begin{pmatrix} i_1(s) \\ i_2(s) \end{pmatrix}, \quad (6.2.19)$$

where $\mathbf{G}_{\text{plant}}(s)$ is the system transfer function, that can be finally modeled as:

$$\mathbf{G}_{\text{plant}}(s) = \begin{pmatrix} \frac{K_1}{(s^2/\omega_n^2 - 1)(\tau_1 s + 1)} & \frac{K_2}{(s^2/\omega_n^2 - 1)k(\tau_2 s + 1)} \end{pmatrix}, \quad (6.2.20)$$

with K_j as the static gains of the two subsystems, τ_j the characteristic delays in magnetic energy adaption of the two circuits and ω_n the natural frequency of the test mass dynamics. Experimental measurements were taken to derive the main parameters of this model, which will be detailed in § 6.3.2.

For further technical details about the realization of both the test mass and the electromagnet (for which illustrative photographs are given in Figure 6.2.3), see reference [13], which describes the full design process and includes the drawings for the solenoid core and housing.

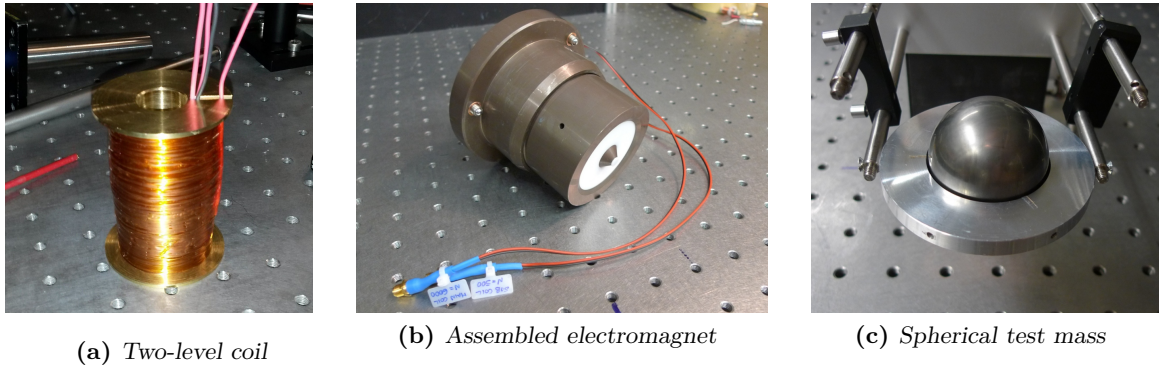


Figure 6.2.3: Photographs of the main components of the plant.

6.2.2 Actuator

The required modulation of the currents flowing through the two coils is actuated by two linear power amplifiers by Servowatt (DCP 130/60), made up of a high quality Operational Amplifier (OpAmp) and a linear output stage with an adaption circuit for high inductive loads, able to guarantee precise and fast amplification of the control signal up to 10 Hz. The devices are designed to operate with an input voltage range of ± 10 V and to provide an output current of ± 500 mA, with maximum output voltage of ± 50 V. Given the guaranteed linear operation up to 10 Hz, they can be described as a simple proportional gain of 50 mA/V within the frequency range of interest for the system. The adaption circuit can nonetheless have a significant effect on the delayed variation of the magnetic field as a response to the actuated current variation, which must be taken into account when modeling the transfer function of the overall electromagnet system. The correspondent experimental characterization is described in § 6.3.2.

Further technical details about the device (depicted in Figure 6.2.4) are reported in the Data Sheet in Appendix A.10. The adaption circuit diagram is also given in Appendix B.3.



Figure 6.2.4: Photograph of the Servowatt linear power operational amplifier DCP130/60.

6.2.3 Sensor

The optical system used to monitor the test mass height derives the sensing signal from the detected power of two laser beams partially covered by the test mass. The two beams are provided by the NPRO Nd:YAG laser (Innolight Mephisto 1000NE) previously described, fiber coupled to the test bed and then outcoupled on its lower plate at a fixed height and in symmetrical positions with respect to the levitation axis. The vertical and lateral placement of the beams with respect to the supporting structure of the test bed are chosen in such a way to have 50% coverage of each beam cross section when the test mass is in its nominal position, as shown in Figure 6.2.5.

The two optical lines, depicted in Figure 6.2.6, are made up of:

- two Schäfter+Kirchhoff collimators (60 FC-4-A8-07), with a 0.72 mm beam diameter, fixedly mounted on the bottom plate of the supporting structure;

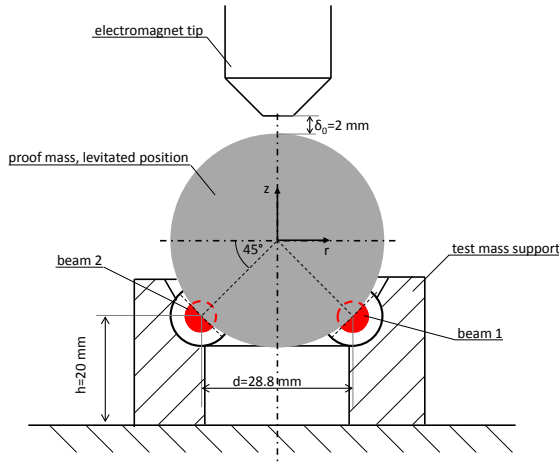


Figure 6.2.5: Geometrical configuration of the sensing system for height detection. For visibility reasons, the beams cross section is magnified.

- two Thorlabs iris diaphragms (ID5MS/M), with an aperture diameter of $1 \div 5$ mm, whose height can be adjusted via a threaded mount in order to allow their centering with respect to the laser beams;
- two photodetectors, already introduced and characterized for the intensity stabilization setup (see § 5.2.3); in this case adjustment capability is offered by the diodes' mounts along the direction transversal to the beams; the correspondent PCBs, on the other hand, are installed in a plastic box fixed externally to the test bed since no more space was available on its lower plate and realized for this purpose with a 3D printer in order to offer a quick and cheap solution, matching with the existent setup.

In case beam focusing is needed, the test bed also gives the possibility to add two Thorlabs lenses (LA1213-C-ML) with 50 mm focal length using two supports with vertical and transversal adjustment capability. Moreover, in the central part of the setup the two beams have to pass through the static support used to hold the sphere before levitation and protect it from falling in case of issues during operation mode. To make this possible without interfering with the sensing system, two holes of 9 mm diameter are present in the support (Figure 6.2.5), which are considered large enough to avoid diffraction effects.

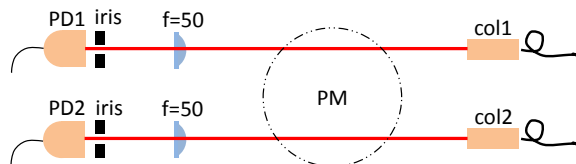


Figure 6.2.6: Scheme of the height sensing system used for the levitation test bed. Each sensing line contains a collimator (col), representing the light source, an iris diaphragm and a photodiode (PD) to detect laser light. A convex lens with focal length f can also be added to focus the beam. Source: [13].

Further technical details of the used optical components are given in the Data Sheets attached in Appendices A.7, A.8 and A.9 (in order of appearance). For details about the mechanical design of the different mounting and adjustment systems, on the other end, refer to [13].

Using the above described setup, the test mass height signal is generated according to the principle of light barriers introduced in § 3.3. Since the beam produced by the used laser source can be described as a Gaussian beam and assuming a constant beam size (which is plausible for a well collimated beam over the distance of interest), the intensity distribution on a plane transversal to the propagation direction is given by:

$$I(x_1, x_2) = I_0 e^{-\frac{2(x_1^2 + x_2^2)}{w_b^2}}, \quad (6.2.21)$$

wherein I_0 is the intensity at the center of the beam, w_b is the beam waist¹, x_1 and x_2 are the coordinates used to span the beam cross section. The total power of the beam can be therefore computed as:

$$P_{\text{tot}} = \int_{-\infty}^{+\infty} \int_{-\infty}^{+\infty} I(x_1, x_2) dx_1 dx_2. \quad (6.2.22)$$

On the other hand, in case of partial coverage the integral must be applied only over the free portion of the beam cross section:

$$P(x_1, x_2) = \int_{\bar{x}_1}^{+\infty} \int_{\bar{x}_2}^{+\infty} I(x_1, x_2) dx_1 dx_2 \quad (6.2.23)$$

and the correspondent transmittance can be defined as:

$$T(x_1, x_2) = \frac{P(x_1, x_2)}{P_{\text{tot}}}. \quad (6.2.24)$$

As from the definition given in Eq. (6.2.24) and referring to the scheme illustrated in Figure 6.2.7, one can easily see that a displacement of the test mass along the vertical axis produces an equal variation of the transmittances T_1 and T_2 of the two beams used for detection. On the contrary, a small displacement across the vertical axis generates transmittance variations of opposite signs and comparable entity, which therefore cancel off when summing T_1 and T_2 . The sensing signal for the test mass height is thus computed as the total transmittance of the two laser beams:

$$T(z) = T_1 + T_2, \quad (6.2.25)$$

which can be considered a function only of the test mass height variation and can be linearized for a range of motion small enough around the nominal height.

Validation of this theoretical analysis was first obtained within this thesis through numerical simulation and then calibrated through an experimental measurement on the actual setup, as it will be described in § 6.3.1.

¹The waist w_b of a Gaussian beam is defined as the radial distance at which the beam intensity has dropped to $1/e^2$ of its peak value I_0 .

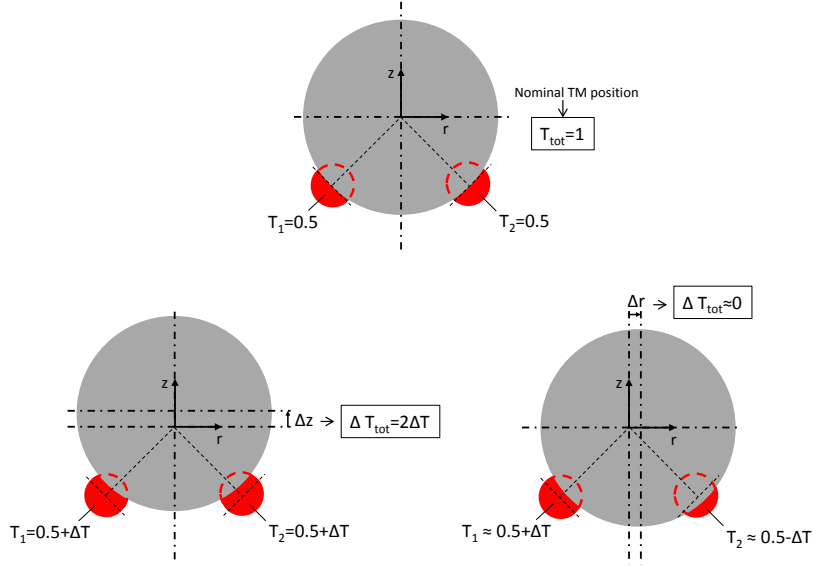


Figure 6.2.7: Basic principle of sensing signal generation. Axial displacements Δz of the test mass with respect to its nominal position generate a proportional variation of the total transmittance, while radial displacements Δr have no effect on it, within a certain limit. Therefore $T_{\text{tot}} \simeq T_{\text{tot}}(z)$ can be used as sensing signal to detect the test mass height.

6.2.4 Controller

The control unit for the levitation system is implemented on the same FPGA board also used for the intensity stabilizer (NI PXI-7852R, described in § 4.2).

As seen in the previous sections, the controller acts on two actuation units:

- a slow unit with a large tuning range, i.e. the big coil with 6000 turns;
- a fast unit with a small tuning range, i.e. the small coil with 500 turns;

both used to control a single process variable, i.e. the test mass distance from the magnet, δ . Considering that, a possible control strategy for combining the features of the two units consists of implementing two controllers in a cascade structure, using the output of the fast controller also as input for the slower one, according to the scheme in Figure 6.2.8. This control scheme should allow to fulfill the stabilization target also using a simple, easy to handle, linear control unit such as a PID controller for both the subsystems. In order to have the possibility to tune and analyze the two control units, the possibility to test them separately and outside of the cascade structure must also be guaranteed. Therefore, a flexible VI was defined in LabVIEW, embedding two nested units consisting of the *PID controller.vi* already implemented for intensity stabilization and described in § 4.3 and allowing to connect them in different possible configurations, so to be able to choose between a cascade and a parallel structure, as well as to use a single control unit and statically command the other, if needed.

The detailed code for this VI will be illustrated in § 6.4.

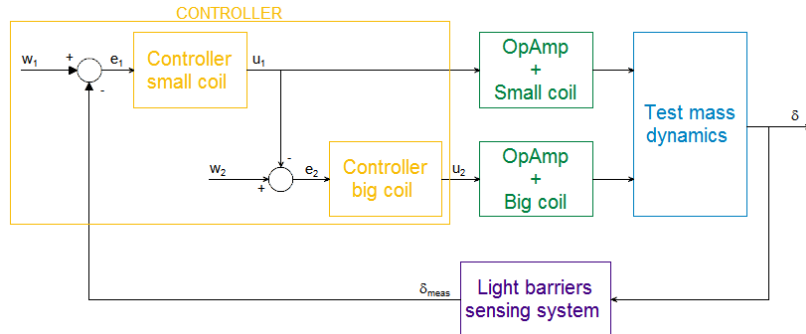


Figure 6.2.8: Cascade control scheme.

6.3 System Characterization

6.3.1 Sensing system characterization

Before to start the characterization of the sensing system, the collimators were adjusted so to get two well collimated beams, parallel with respect to each other and at the same height with respect to the test bed. To verify the quality of the adjustment, a quick measurement of the beam waist was conducted applying the razor blade technique², that proved for both beams a proper collimation and a beam diameter in agreement with the specified value $\phi = 0.72\text{ mm}$; the alignment of the optical components along the beam axis was instead verified using a CCD camera (Data Ray WinCam D).

A model was then defined in MATLAB to get a simulation of the test mass height signal and of its sensitivity to transversal displacements. The model operates numerical integration via trapezoidal method of the intensity of two Gaussian beams over two mirrored square grids, masked in order to null the integrand value both outside the detector active area and in the region covered by the test mass, as illustrated in Figure 6.3.1. In this way the transmittances of the two beams can be evaluated for different on-axis and off-axis displacements, and the deriving sensing signal can be investigated. Simulation results are depicted in Figure 6.3.2 for a perfectly centered test mass and for on-axis displacements in the range $\pm 2\text{ mm}$ with respect to the nominal position (correspondent to a 50% transmittance for both beams). As highlighted by the total transmittance plot, the simulated sensing signal shows a linear behavior with sensitivity of $k = 1.23\text{ 1/mm}$ for height variation in the range $\pm 0.8\text{ mm}$. When introducing an off-axis displacement, we get different transmittances for the two beams but the same response in terms of sensing signal, as shown in Figure 6.3.3 for a displacement of 0.1 mm. In particular a variation less than 5% in the linear sensitivity of the total transmittance was proved for transverse displacements within $\pm 0.2\text{ mm}$, as illustrated in Figure 6.3.4. This evaluation, besides the fact that the test mass dynamics is stable in any direction orthogonal to the levitation axis (as explained in § 6.2.1), allows to validate the use of the total transmittance as sensing signal for the controller.

²Razor blade technique is an experimental method to evaluate the intensity profile of a laser beam in which one gradually cuts off the beam itself by moving a razor blade into it and measures the transmitted intensity. For details, see § 2.2.2 of reference [12].

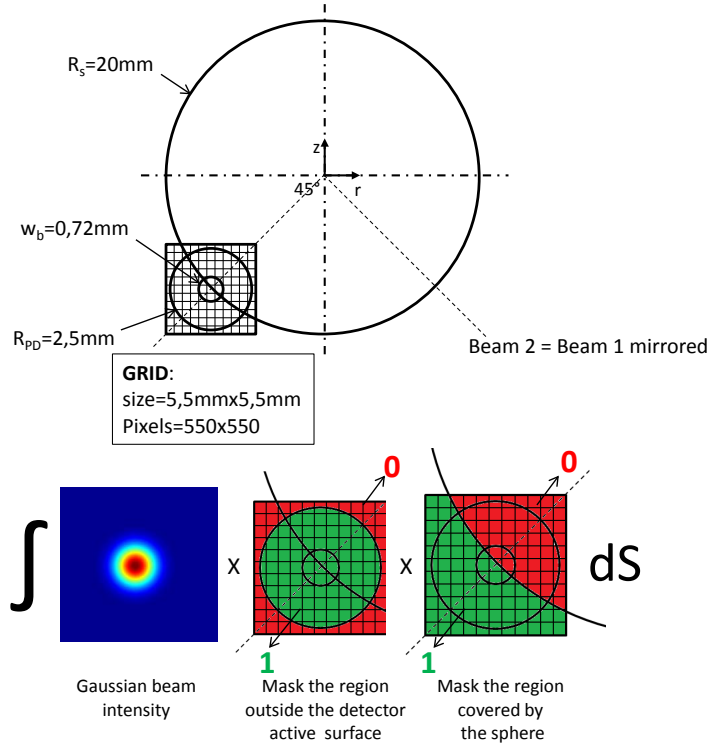


Figure 6.3.1: Description of the MATLAB model for the simulation of the test mass height sensing signal.

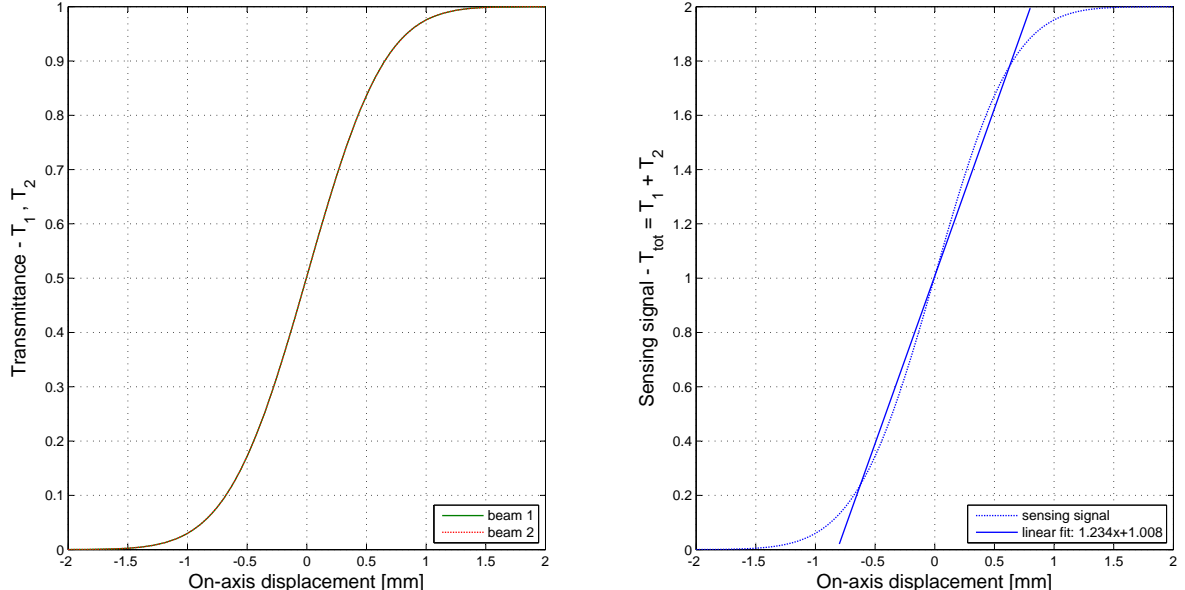


Figure 6.3.2: Simulation results for a centered test mass. For on-axis displacement in the range ± 0.8 mm the sensing signal can be linearized with good approximation (coefficient of determination of the linear fit: $R^2 = 0.9914$).

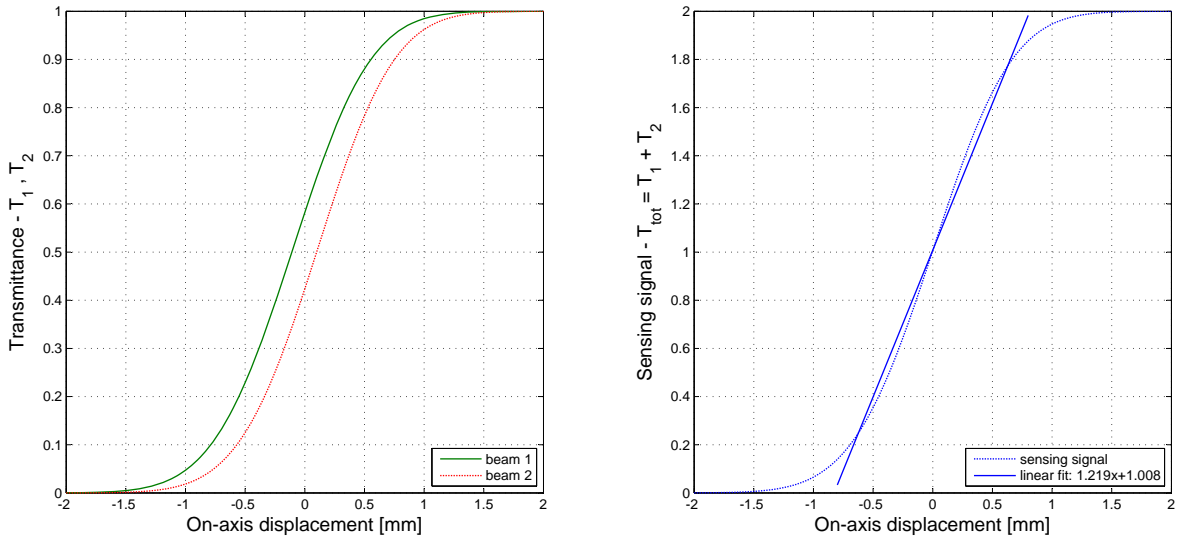


Figure 6.3.3: Simulation results for off-center test mass. An off-axis displacement of 0.1 mm is here introduced.

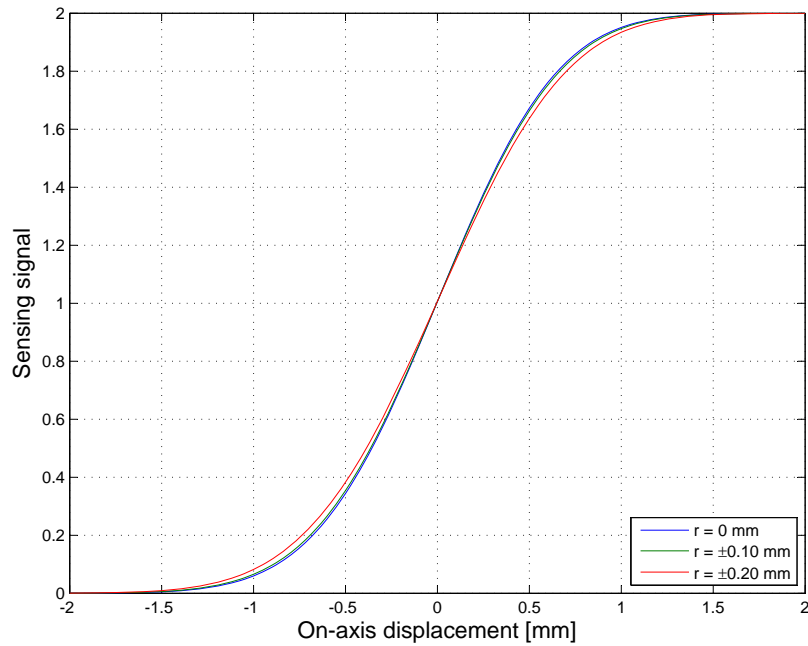


Figure 6.3.4: Sensing signals comparison for different values of off-axis displacements.

The simulated sensing signal was then calibrated through experimental measurement to verify the sensing technique and get a sensitivity evaluation perfectly fitting with the actual setup for the levitation test bed. To this end, a support to hold and move the test mass in a precise and measurable way was assembled fixing a ring with a 16° chamfer (defined to guarantee holding capability and proper positioning for the sphere) to a support mounted on two translation stages with micrometer sensitivity, as shown in Figure 6.3.5. The total power of the two laser beams was regulated at $130\text{ }\mu\text{W}$ and the test mass was moved to its nominal position, corresponding to a 50% transmittance for both the laser beams. The measurement was then conducted manually scanning the whole height range of interest ($\pm 2\text{ mm}$) with $100\text{ }\mu\text{m}$ steps, both for a centered position and for off-axis displacements in the range $\pm 0.4\text{ mm}$. At each step the transmitted light power of the two beams was measured by the photodetectors and read out with a digital oscilloscope (LeCroy WaveRunner 204Xi [23]). Since the laser power needs here to be detected with high accuracy down to zero and the detectors characteristic deviates from linear behavior for small input power, a more accurate fit of their response was derived and used to correct the measured light power. The transmittances of the two beams were then computed and the sensing signal was consequently derived by summation. The result obtained with a centered test mass is depicted in Figure 6.3.6, in comparison with the correspondent simulated signal. The measured signal has a smaller gain, probably due to some diffraction effects generated for example by the interaction of the spherical surface with the laser beams, but nevertheless the response fits quite well the foreseen behavior and, once calibrated, is perfectly suited for application as sensing signal for the servo loop. Concerning the sensitivity to off-axis motion, the measurement confirmed the conclusions derived from the simulation.

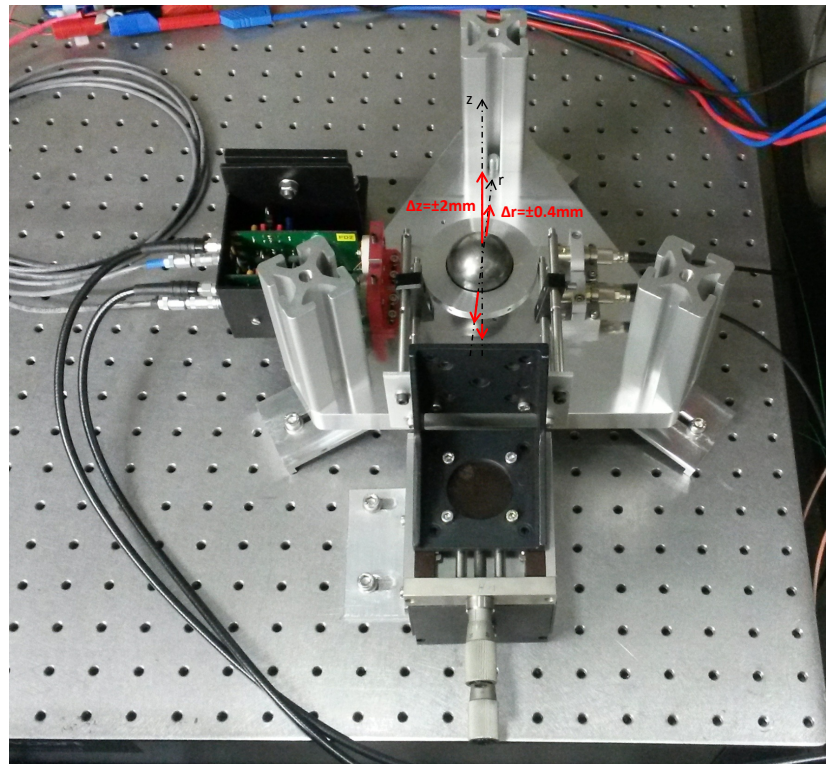


Figure 6.3.5: Sensing system characterization setup.

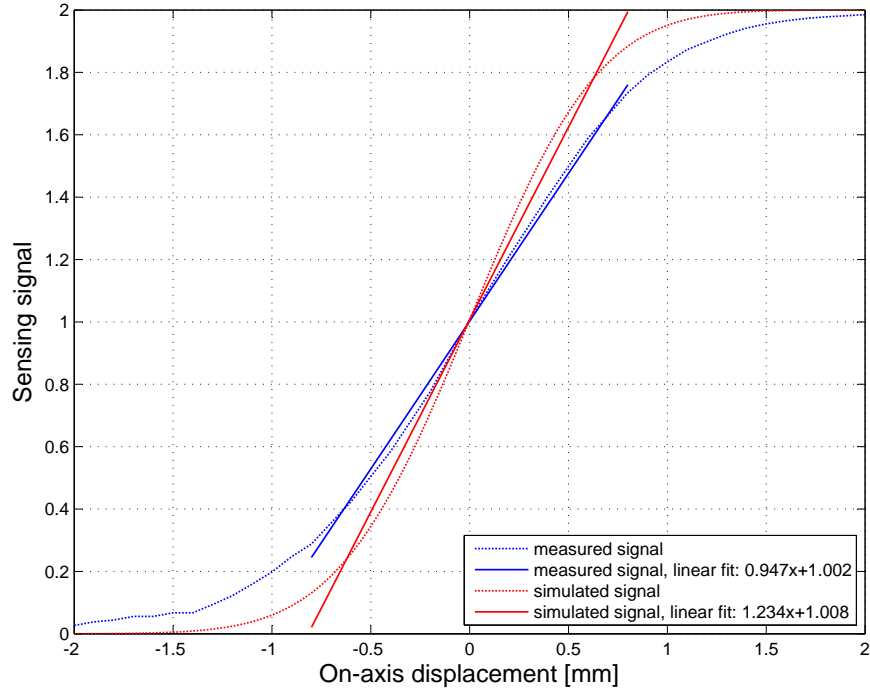


Figure 6.3.6: Comparison between simulated and measured sensing signal for a centered test mass.

Finally, an indication of the frequency response of the system would be needed, but since this is determined by the detectors response, whose corner frequency is $f_c \geq 20$ kHz as proved by the measurement taken for the intensity stabilization system (see Figure 5.3.5), the sensing system can be described as a simple proportional gain in the frequency range of interest for the levitation servo loop.

6.3.2 Two-stages electromagnet and relative current sources characterization

Once the sensing method was validated and calibrated, the focus of the experimental investigation was transferred to the actuation system.

As a first step the electromagnet was assembled and the electric resistance of the two coils measured with a multimeter (Voltcraft M-4660M), providing values in good agreement with the estimation that can be obtained applying the analytic formula for the resistance of a cylindrical conductor (Eq. (6.2.16)). An estimate of the inductances was also derived using the empirical Wheeler formula for multilayer coils [27]:

$$L = \mu_r \frac{0.8a^2 n^2}{6a + 9b + 10c} \quad (6.3.1)$$

where the inductance L is expressed in microhenries, μ_r is the relative permeability of the ferromagnetic core, a , b and c are respectively the mean radius, the length and the depth of the coil (expressed in inches) and finally n is the number of turns of the coil. The derived parameters are

given in Table 6.3.1, together with the correspondent corner frequencies estimated according to the laws of RL circuits (Eq. (6.2.15)).

| | $R(\Omega)$ | $L(H)$ | $f_c(\text{Hz})$ |
|--------------------------|-------------|--------|------------------|
| Big coil ($n = 6000$) | 144.0 | 185.7 | 0.12 |
| Small Coil ($n = 500$) | 9.2 | 1.4 | 1.05 |

Table 6.3.1: Electric parameters of the two coils.

It must be noted that the derived inductances are likely to be an overestimation, due to the fact that the applied formula doesn't take into account either the magnetic flux leakages that are inevitably present (even with an optimized electromagnet design) or the variation of the ferromagnetic core permeability with the applied flux and the consequent inductance variability in correlation with current amplitude and frequency. Therefore a lower inductance is expected to characterize the electromagnet response to the driving current used for levitation, corresponding to smaller actuation capability but also higher corner frequency.

Later, the two power amplifiers were wired to the coils and a stable setup mounting the devices inside a protective cage was built for safety reasons. Their functionality was initially tried out off-load, then the coils were connected and measurements were taken with the setup described in Figure 6.3.7, both with a DC input, to check the linearity of the transfer function between the input voltage and the output current, and with an AC input, to verify its dynamic behavior.

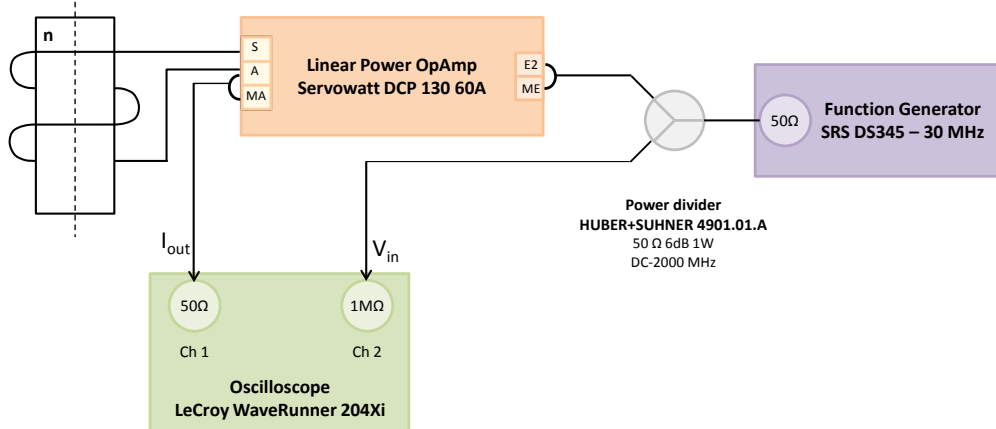


Figure 6.3.7: Schematic of the measurement setup for the characterization of the power amplifier on-load behavior.

At first, an issue was identified for the operation of the small coil, showing an amplified oscillation at $f \approx 20\text{ kHz}$, which was interpreted as a resonance phenomenon probably induced by a parasitic capacitance of the inductive load. To solve this problem, a correction was applied to the adaption circuit introducing a trimmable RC snubber ($R = 10\text{ k}\Omega$ and $C = 100\text{ nF}$) between the inverting and non-inverting input of the OpAmp. With the described correction, the linear

operation was verified for the entire working range, confirming the expected sensitivity of 50 mA/V (Figure 6.3.8). Due to the limitations on the output voltage of the device and considering the resistance of the big coil, the correspondent driving signal must be limited in the range $V_{in} = \pm 7 \text{ V}$.

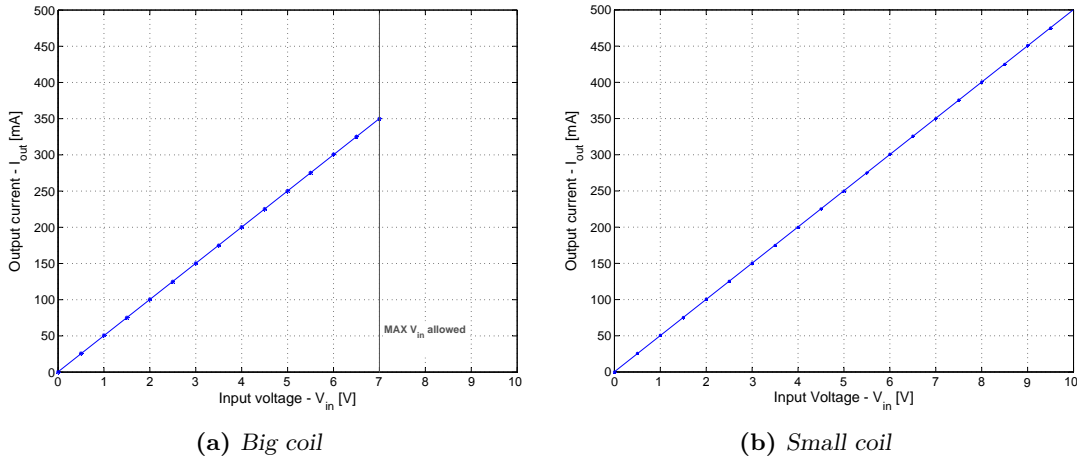


Figure 6.3.8: Linear response of the power amplifiers with the two inductive loads.

Also the dynamic response of the system confirmed the expectations, since no signal attenuation was detected up to 10 Hz, meaning that the two power amplifiers can be described as a simple proportional gain $k = 50 \text{ mA/v}$ in the frequency range of interest.

As a second step, the magnetic field generated by the two coils as a response to the control signal used to drive the power amplifiers was measured in correspondence of the expected operational conditions (a nominal gap of 2 mm and levitating current around 300 mA are foreseen, [13]). A complete scheme of the measurement setup is given in Figure 6.3.9.

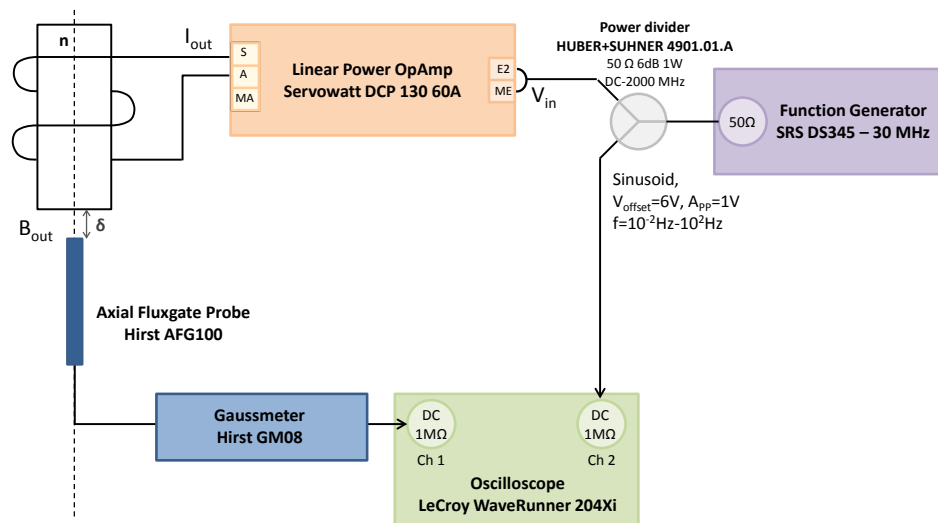


Figure 6.3.9: Schematic of the setup for measuring the electromagnet transfer function.

The input of the device was driven by a signal generator (Stanford Research System DS345), using a sine with 6 V offset and 1 V peak to peak amplitude and scanning the frequency range $f = 10^{-2} \div 10^2$ Hz. The output magnetic field flux was measured via a gaussmeter (Hirst GM08, [28]), installing a compatible axial probe (Hirst AFG100, [29]) under the electromagnet, in an axially centered position and at a distance $\delta = 2$ mm from its tip. A digital oscilloscope (LeCroy WaveRunner 204Xi [23]) was used for data acquisition. Static gains of $k_1 = 372$ mT/v for the big coil and of $k_2 = 33$ mT/v for the small one were derived from the acquired data. Figure 6.3.10 finally presents the measured Bode plots, showing a corner frequency of about $f_{c,1} \approx 9$ Hz for the big coil and $f_{c,2} \approx 12$ Hz for the small one.

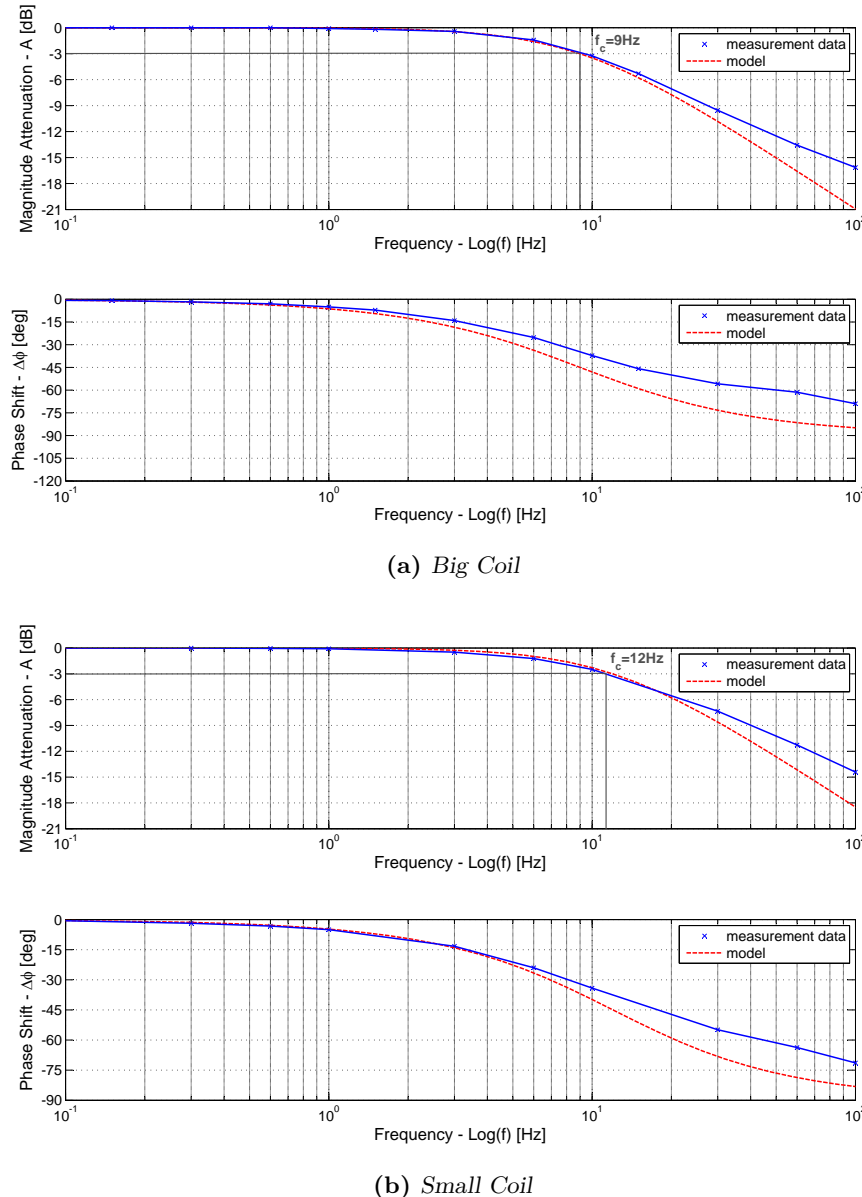


Figure 6.3.10: Frequency response of the two-levels electromagnet. The Bode plots describe the transfer function between control voltage and induced magnetic flux density in the two coils.

This was an unexpected result considering the approximate estimates given in Table 6.3.1. As already noticed, the discrepancy between experimental data and the computed approximation could be possibly explained with the considerable simplification introduced with the formula used to estimate the coil inductance, since no losses are hypothesized and the dependence of the system response on the amplitude of the inductive current is neglected at all. Anyway, considering that the measurements were taken around the expected operating condition and that the results appear adequate to guarantee the desired controlling capability, a linear first order element with the measured parameters was kept to describe the two-levels electromagnet behavior within the simplified model introduced in § 6.2.1.

As a final step, an attempt to characterize the overall system including the test mass dynamic was done using the setup shown in Figure 6.3.11.

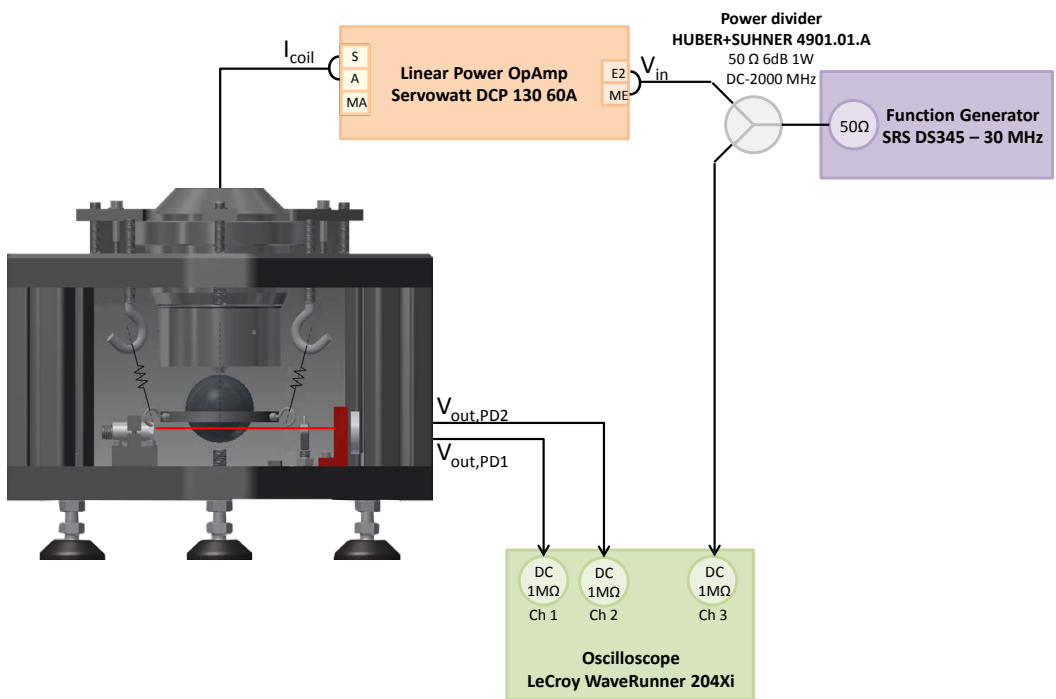


Figure 6.3.11: Schematic of the setup for test mass dynamics measurement.

The spherical test mass was suspended under the electromagnet using the same support ring manufactured for the sensing system characterization, hold by an elastic structure composed of three rubber rings, each one clasped to a couple of hooks respectively fastened to the support ring and to the upper plate of the test bed supporting structure. In this condition the mass is subject to the gravity force, the magnetic force and the elastic force exerted by the rubber rings. In order to be able to remove the effect of the elastic force from the measured transfer function, the equivalent elastic constant of the three rings system was measured ($k_{el,tot} = 105 \text{ N/m}$). A second measurement was also taken using two rubber rings for each suspension point, so to double the stiffness of the elastic system. Before to start data acquisition, the position of the test mass was adjusted by regulating the height of the threaded suspension hooks so to reach the nominal transmittance ($T_{tot} = 1$). At this point the transfer function between the control voltage and

the output height was measured, feeding the power amplifier with the same voltage input used for the magnetic flux density measurement. The output motion of the test mass in response to the applied input was derived by acquiring the signals from the two photodetectors with an oscilloscope and processing them so to derive the correspondent transmittance and consequently the test mass height signal. Due to the natural frequency of the spring-mass system ($f \approx 2.9$ Hz for the first measurement and $f \approx 4.1$ Hz for the second one), the measured transfer function was highly altered by the additional elastic force in the frequency range of interest. Nevertheless it was possible to get at least an indication about the static gain of the overall actuation system, for which the following values were derived:

- $k_1 \approx 58 \mu\text{m}/\text{v}$, for the big coil;
- $k_2 \approx 722 \mu\text{m}/\text{v}$, for the small coil.

6.4 Implementation of the digital controller

Taking into account the outcomes of the experimental investigation, a LabVIEW program was then designed for the levitation test bed, which embeds two *PID Controller.vi* nested inside the higher lever instrument called *Height Controller.vi*. This VI will be now described in detail listing the functions that can be accessed through its front panel (Figure 6.4.1) and explaining the operations lying behind these functionalities referring to the program's block diagram (Figure 6.4.2).



Figure 6.4.1: Front panel of Height Controller.vi.

6 Height Controller

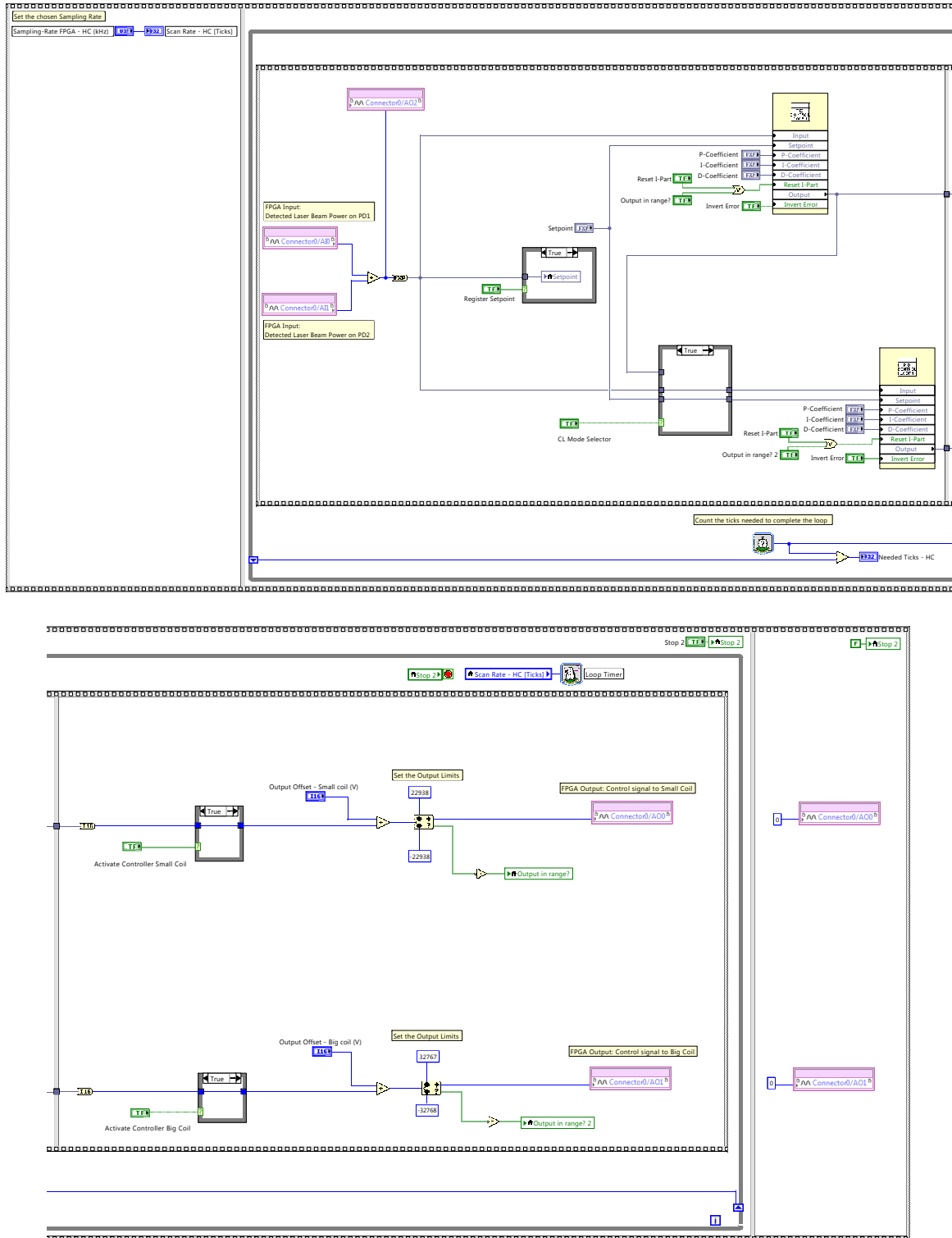


Figure 6.4.2: Block diagram of Height Controller.vi.

The front panel of the instrument is organized similarly to what was done for the *Intensity Stabilization.vi* described in § 5.4. Section 1 provides the possibility to interrupt the execution of the VI via a *Stop* button and to select the sampling rate for the system via a dedicated knob. Two indicators are also present to easily compare the chosen sampling period with the time needed to complete the overall program execution, in order to guarantee correct operation. Section 2 allows to fix the setpoint for the test mass height by measuring the total transmittance of the two detectors when the sphere is put in a reference position (through the *Register Setpoint* button) and then to adjust it with a manual control. Moreover, the *CL Mode Selector* switch gives the possibility to choose the configuration of the controller between cascade or parallel structure. Section 3 is dedicated to the control unit for the big coil. Moving rightwards inside it, the first two buttons encountered can be used to activate/deactivate the control unit and to invert the error computation when needed. The *Output Offset* slider allows to set an offset voltage to be added to the control signal or to be used as static input to feed the coil in case the control unit is off. Three numeric controls (*P-Coefficient*, *I-Coefficient* and *D-Coefficient*) can then be regulated to tune the PID controller. Finally, a monitor led called *Output in range?* informs the user when the output signal sent to the coil is outside the operation range of the power amplifier and it's therefore cut off by the controller to its upper or lower limit ($\pm 7V$). Section 4 duplicates the same functionalities just described for the small coil control unit.

The internal structure of the program, as for the *Intensity stabilizer.vi*, is based on the succession of three flat sequences used to guarantee the correct sequentiality of the operations. In the first sequence the controller sampling rate is set converting the value chosen by the user in kHz to the correspondent number of ticks of the FPGA internal clock, and recording it into the local variable *Scan Rate*. The second sequence contains a while loop that continuously performs the main code of the instrument in so far as the conditional terminal is true (i.e. until the moment when the *Stop* button is pushed to interrupt the execution). The rate of the loop timer is set reading the *Scan Rate* variable. A counter is also inserted to keep trace of the number of ticks needed to complete the loop, shown to the user via the *Needed Ticks* indicator. Last sequence is finally used to reinitialize the value of the output to a default zero voltage once the VI is stopped.

If we now break down the main code executed by the while loop, we can see that once again we have two flat sequences, one dedicated to the actual generation of the control signals for the two coils and the other used for potential adjustments. As a first step, the sensing signal is generated by summation of the digitized inputs coming from the two photodiodes, representing the transmitted power of the two laser beams used for height detection. At this point we have a 16 bits signed integer signal which is first sent to an analogue output of the FPGA board for debugging, then converted to fixed point data type and finally sent to the input of the control units. Possibility to record the sensing signal at a certain instant in order to use it as setpoint is also offered by a case structure commanded by the *Record Setpoint* button (Figure 6.4.3). Two *PID Controller.vi* are then inserted in the block diagram, with two possible configurations that can be selected using a case structure commanded by the *CL Mode Selector* switch (Figure 6.4.4). When the cascade structure is chosen, the output of the small coil controller is sent to the input terminal of the big coil controller and the correspondent setpoint is set to zero. On the contrary, if the user selects a parallel structure both the control units receive the height sensing signal as input and the same setpoint is fixed for them. In both cases, at the output of the two subVIs we get the processed control signals that can eventually be used to modulate the current for the two

6 Height Controller

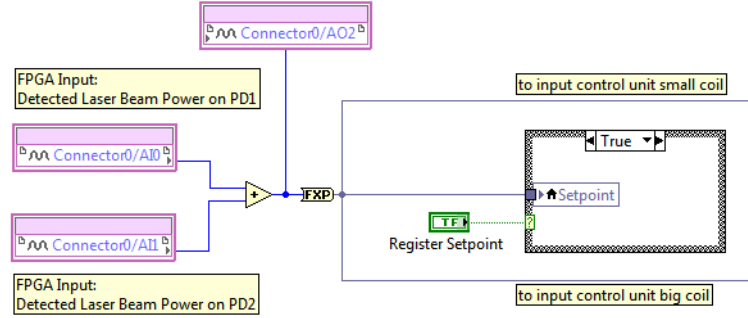
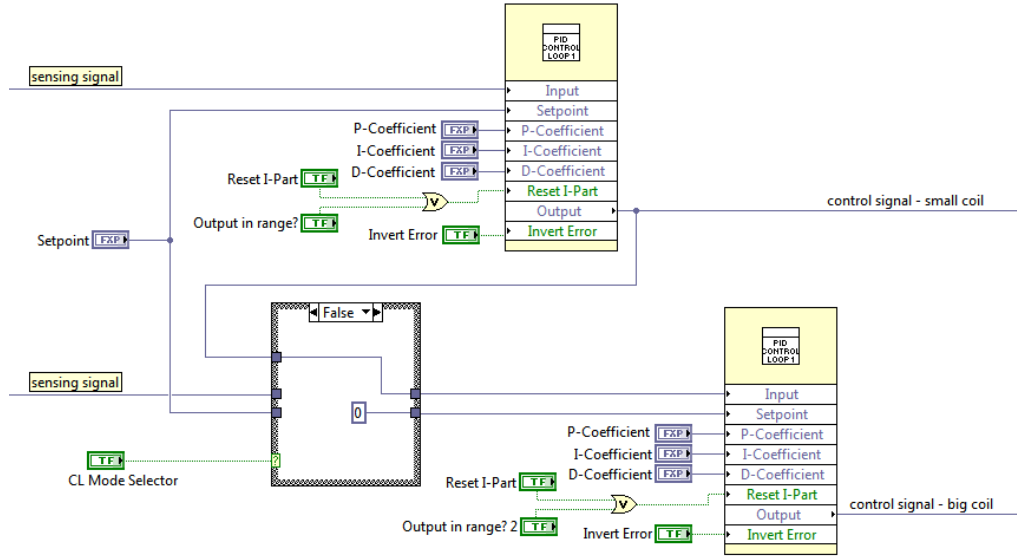
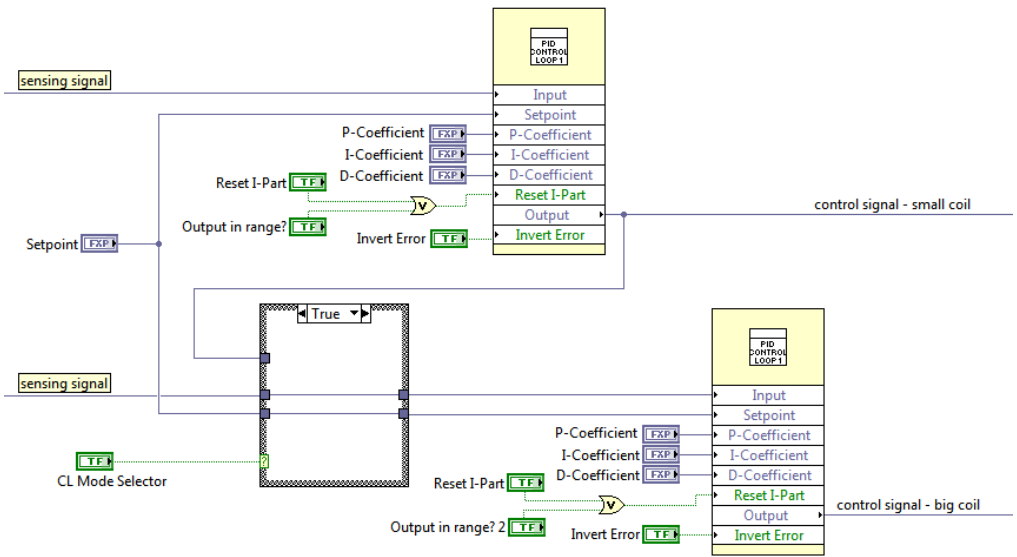


Figure 6.4.3: Code for the generation of the sensing signal.



(a) Cascade configuration



(b) Parallel configuration

Figure 6.4.4: Code for the configuration of the two control units.

coils. Figure 6.4.5 shows the consequent elaboration of these signals applied before to send them to two analogue channels of the FPGA, wired to the input of the power amplifiers. Both the lines first give the possibility to block the modulation signal whether the correspondent control unit is deactivated. An offset voltage is then added and the total outgoing signal is compared to the limits set for the controller output and coerced to fall within that range. A boolean variable is also set to FALSE state and used to correspondingly switch the *Output in range?* led whether correction is needed.

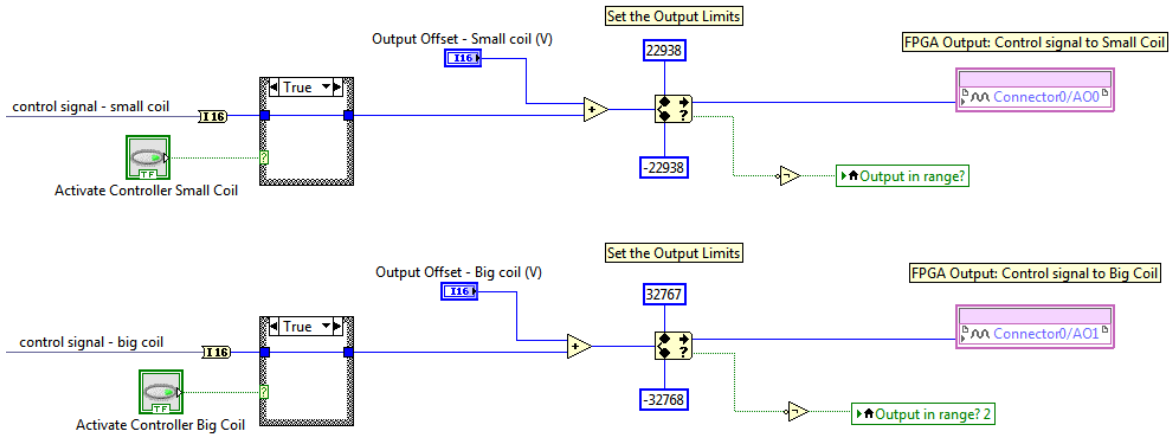


Figure 6.4.5: Code for the adjustment of the output signal.

6.5 Experimental tryouts

After the system characterization phase and digital implementation of the controller, a few levitation tryouts were conducted.

An important aspect to take into account is that when the test mass lies on its static support, the sensing signal is not available since the two beams are completely blocked by the mass itself. A strategy to initiate the levitation is therefore needed and different approaches were experimented for this purpose in the performed tests. At first, an attempt was done to lift off the test mass from the static support by applying a force high enough to get it stuck to the electromagnet and then gradually releasing it, with the controller switched on so to stabilize its dynamics. A sacrificial PTFE spacer with a thickness of 1 mm was first applied to the ferromagnetic core tip in order to avoid that the test mass surface could be damaged by the collision. Another solution that was considered consists in holding the test mass with the support structure used for the sensing system characterization (Figure 6.3.5), lifting it up to its nominal position with the vertical translation stage and then, with the controller activated, gradually reducing the support provided by the platform by lowering it step by step.

In both cases the plan was to provide the necessary force to compensate the test mass weight applying a static current to the big coil and to actively correct it with the small coil so to reach a levitated condition. One of the advantages of PID controllers is that they can be tuned quite easily also without a detailed knowledge of the system transfer function. Therefore it should

be possible to adjust the controller for the small coil empirically, trying to make it follow a sinusoidal signal applied to the big coil. Once the test mass would be levitated, a more accurate measurement of the transfer function of the actuated test mass dynamics could be taken and a better characterization obtained, thus providing a much more precise model of the system dynamics that could then be used for a proper loop shaping of the cascade controller.

Several tryouts were conducted in this sense, using different configurations for the controller. At first only the small coil was activated and tuned excluding the derivative part of the PID algorithm, since this is more tricky to adjust and tend to have a destabilizing effect on the control. To provide additional control capability, that could be needed during the release phase when the acceleration of the test mass can be too high to be controlled only by the small coil due to the force variation generated by the detachment, the controller for the big coil was then switched on and the system was tested with the combined action of the two control units. Unfortunately the different tests all proved eventually unsuccessful, demonstrating the levitation of the test mass to be more challenging than expected. Some ideas are proposed in the conclusive chapter of this work, which couldn't be tried out within the available time frame for this thesis but can represent an useful guideline for further investigation.

7 Conclusions and Outlook

In this thesis the development of two FPGA based controllers for use within the experimental model of a spherical inertial reference sensor with optical readout was presented.

The first part of the work focused on a servo loop for intensity stabilization of the laser beams used for the interferometric measurement of the sensor. The stabilization is realized via an active feedback PI controller, detecting the laser intensity with a photodiode and modulating it with an AOM. The system was characterized and the digital control unit was realized via a LabVIEW program implemented on a FPGA board. An experimental setup to validate the stabilization performance was assembled and an assessment of the detectors noise was obtained, showing a white noise level of about $10^{-4} \text{ } 1/\sqrt{\text{Hz}}$. This proved to be a major limitation for the intensity stabilization at frequencies higher than $\approx 30 \text{ Hz}$, since being the detector noise larger than the laser RIN the intensity fluctuations can't be sensed and stabilization can't be consequently performed. A detector with lower noise (currently under development) is therefore needed to be able to extend the intensity stabilization up to the heterodyne frequency used for the interferometric measurement, $f_{\text{het}} = 10 \text{ kHz}$. Nevertheless a performance proof was obtained in the measurement band of the eLISA experiment ($f = 10^{-4} \div 1 \text{ Hz}$), demonstrating a significant reduction of the stabilized laser RIN with respect to the free running intensity, with a final value approximately equal to the detector noise.

In the second part of this work a magnetic levitation test bed to be used to reproduce the free flying condition for the sensor test mass on an earthbound laboratory was assembled and characterized. The system consists of a two-level electromagnet driven by two linear power operational amplifiers controlled by a cascade servo loop based on PID algorithm, that can be used to control the test mass position along one degree of freedom. Measurements of the transfer function of the different components of the plant were performed, with particular attention to determine the corner frequencies of the two actuation units. This is considered to be crucial for the controller development, since the high inductance of the two coils is expected to produce a significant delay in the variation of the magnetic field as a response to the input current and it could therefore limit the performance of the levitation system. Values of about 9 Hz and 12 Hz were found in the operational condition for the big ($n = 6000$) and small ($n = 500$) coil, respectively. Height detection is realized via two laser beams, applying the light barriers technique. To validate this principle, a numerical model was defined in MATLAB and later calibrated via experimental measurement. The dependence of the sensing signal on the test mass on-axis displacement was therefore investigated and a linear behavior was verified with good approximation in the range $\pm 1 \text{ mm}$. Negligible sensitivity to small off-axis displacements ($\leq 0.2 \text{ mm}$) was also proved. A LabVIEW program including two PID units independently configurable was finally implemented on the FPGA board dedicated to the control systems for the inertial sensor. Tests were conducted in the attempt to reach a free flying test mass condition, from which a better characterization of

the system could be performed and a proper configuration of the cascade controller obtained, so to guarantee the required stability in the test mass positioning.

Since the performed tests failed in levitating the test mass, further investigation and possible system modification will be needed in order to enable a successful operation of the test bed. To this end, since a slight misalignment of the electromagnet was remarked during the experimental tryouts, causing a small rolling movement of the test mass when detaching from the magnet tip that could affect the validity of the correspondent sensing signal, a more accurate adjustment could be obtained by mapping the electromagnet misalignment for different positions of its fine thread adjusters and consequently finding the correspondent minimum. Another attempt can be done repeating the procedure described for mass release with spacers of different thickness applied between the test mass and the magnet tip. This would allow to get a map of the tuned controller parameters for different relative position of the test mass which could then be used to find a better tuning for the controller. If this approach should also result unsuccessful, a more elaborate control scheme will be probably needed, taking into account the non-linear nature of the system. A possible choice could reside in the introduction of a feed-forward controller in combination with the feedback PID controller, according to the scheme in Figure 7.0.1. Feed-forward control acts on the plant predicting the variation of the process variable and correcting it before it happens. Therefore it needs an accurate mathematical model of the system to be implemented but on the other side can offer a major improvement of the controller performance.

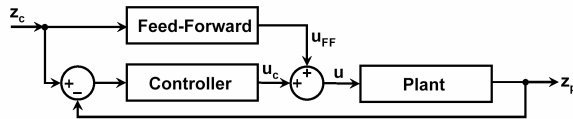


Figure 7.0.1: Control scheme modification by addition of a feed-forward controller.
Source: [30].

Another possibility is to use a feedback linearization controller, in which an additional feedback is added to the system to cancel the nonlinear effects of the actual plant (scheme in Figure 7.0.2).

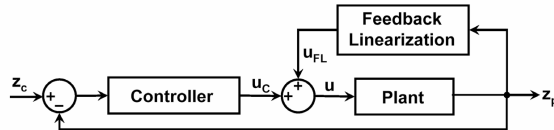


Figure 7.0.2: Control scheme modification by addition of a linearization feedback.
Source: [30].

Once levitation will be fulfilled, further development will be needed to reach the final fine positioning of the test mass; for this purpose an accurate loop shaping will be applied to the chosen controller and the interferometer's DWS signal will replace the light barriers technique as sensing system in order to increase detection sensitivity, which should finally allow to reach the target accuracy in the test mass height control.

Appendix A

Data Sheets

A.1 FPGA-board NI PXI-7852R

NI R Series Multifunction RIO Specifications

This document lists the specifications of the NI 781xR/783xR/784xR/785xR. These specifications are typical at 25 °C unless otherwise noted.

Français Deutsch 日本語 한국어 简体中文
ni.com/manuals

Analog Input (NI 783xR/784xR/785xR Only)

Input Characteristics

| | |
|---|--|
| Number of channels | Input impedance |
| NI 7830R 4 | Powered on 10 GΩ in parallel with 100 pF |
| NI 7831R/7833R/7841R/7842R/ 7851R/7852R/7853R/7854R 8 | Powered off/overload 4.0 kΩ min |
| Input modes DIFF, RSE, NRSE (software-selectable; selection applies to all channels) | Input signal range ±10 V |
| Type of ADC Successive approximation | Input bias current |
| Resolution 16 bits, 1 in 65,536 | NI 783xR ±2 nA NI 784xR/785xR ±5 nA |
| Conversion time | Input offset current |
| NI 783xR/NI 784xR 4 µs | NI 783xR ±1 nA NI 784xR/785xR ±5 nA |
| NI 785xR 1 µs | Input coupling DC |
| Maximum sampling rate | Maximum working voltage (signal + common mode) Inputs should remain within ±12 V of ground |
| NI 783xR/784xR 200 kS/s (per channel) | Overvoltage protection |
| NI 785xR 750 kS/s (per channel) | Powered on ±42 V Powered off ±35 V |



Accuracy Information

NI 783xR

| Nominal Range (V) | | Absolute Accuracy | | | | | | Relative Accuracy | | |
|---------------------------|---------------------------|-------------------|--------|----------------------|------------------------------------|----------|------------------------------------|---|-------|-----|
| | | % of Reading | | Offset (μ V) | Noise + Quantization (μ V) | | Temp Drift (%/ $^{\circ}$ C) | Absolute Accuracy at Full Scale (\pm mV) | | |
| Positive Full Scale | Negative Full Scale | 24 Hours | 1 Year | | Single Point | Averaged | | Resolution (μ V) | | |
| 10.0 | -10.0 | 0.0496 | 0.0507 | 2.542 | 1,779 | 165 | 0.0005 | 7.78 | 2,170 | 217 |

Note: Accuracies are valid for measurements following an internal calibration. Averaged numbers assume dithering and averaging of 100 single-channel readings. Measurement accuracies are listed for operational temperatures within ± 1 $^{\circ}$ C of internal calibration temperature and ± 10 $^{\circ}$ C of external or factory-calibration temperature.

NI 784xR/785xR

| Nominal Range (V) | | Absolute Accuracy | | | | | | Relative Accuracy | | |
|---------------------------|---------------------------|-------------------|--------|----------------------|------------------------------------|----------|------------------------------------|---|-------|-----|
| | | % of Reading | | Offset (μ V) | Noise + Quantization (μ V) | | Temp Drift (%/ $^{\circ}$ C) | Absolute Accuracy at Full Scale (\pm mV) | | |
| Positive Full Scale | Negative Full Scale | 24 Hours | 1 Year | | Single Point | Averaged | | Resolution (μ V) | | |
| 10.0 | -10.0 | 0.0186 | 0.0228 | 1,591 | 1,029 | 91.6 | 0.0005 | 3.97 | 1,205 | 121 |

Note: Accuracies are valid for measurements following an internal calibration. Averaged numbers assume dithering and averaging of 100 single-channel readings. Measurement accuracies are listed for operational temperatures within ± 1 $^{\circ}$ C of internal calibration temperature and ± 10 $^{\circ}$ C of external or factory-calibration temperature.

DC Transfer Characteristics

INL

NI 783xR ± 3 LSB typ, ± 6 LSB max
NI 784xR/785xR ± 1 LSB typ, ± 3 LSB max

DNL

NI 783xR -1.0 to +2.0 LSB max
NI 784xR/785xR ± 0.4 LSB typ,
 ± 0.9 LSB max

No missing codes

NI 783xR 16 bits typ, 15 bits min
NI 784xR/785xR 16 bits guaranteed

CMRR, DC to 60 Hz -86 dB

Dynamic Characteristics

Bandwidth

NI 783xR
Small signal (-3 dB) 650 kHz
Large signal (1% THD) 55 kHz

NI 784xR/785xR

Small signal (-3 dB) 1 MHz
Large signal (1% THD) 500 kHz

Settling Time

| Device | Step Size | Accuracy | | |
|--------------------|--------------|--------------|--------------|-------------|
| | | ± 16 LSB | ± 4 LSB | ± 2 LSB |
| NI 783xR | ± 20.0 V | 7.5 μ s | 10.3 μ s | 40 μ s |
| | ± 2.0 V | 2.7 μ s | 4.1 μ s | 5.1 μ s |
| | ± 0.2 V | 1.7 μ s | 2.9 μ s | 3.6 μ s |
| NI 784xR/ 785xR | ± 20.0 V | 2.1 μ s | 4.2 μ s | 8 μ s |
| | ± 2.0 V | 1.3 μ s | 1.6 μ s | 1.8 μ s |
| | ± 0.2 V | 0.8 μ s | 1.1 μ s | 1.2 μ s |

Crosstalk -80 dB, DC to 100 kHz

Analog Output (NI 783xR/784xR/785xR Only)

Output Characteristics

| | | | |
|--|---------------------------------|--------------------------|----------------------|
| Output type | Single-ended, voltage output | Resolution..... | 16 bits, 1 in 65,536 |
| Number of channels | | Update time | 1.0 μ s |
| NI 7830R | 4 | Maximum update rate..... | 1 MS/s |
| NI 7831R/7833R/7841R/7842R/ 7851R/7852R/7853R/7854R | 8 | Type of DAC | Enhanced R-2R |

Accuracy Information

| Nominal Range (V) | | Absolute Accuracy | | | Absolute Accuracy at Full Scale (mV) | |
|---------------------|---------------------|-------------------|--------|-------------------|---|------|
| | | % of Reading | | Offset (μ V) | | |
| Positive Full Scale | Negative Full Scale | 24 Hours | 1 Year | | | |
| 10.0 | -10.0 | 0.0335 | 0.0351 | 2366 | 0.0005 | 5.88 |

Note: Accuracies are valid for analog output following an internal calibration. Analog output accuracies are listed for operation temperatures within ± 1 $^{\circ}$ C of internal calibration temperature and ± 10 $^{\circ}$ C of external or factory calibration temperature. Temp Drift applies only if ambient is greater than ± 10 $^{\circ}$ C of previous external calibration.

DC Transfer Characteristics

| | |
|-------------------|---|
| INL..... | ± 0.5 LSB typ, ± 4.0 LSB max |
| DNL | ± 0.5 LSB typ, ± 1 LSB max |
| Monotonicity..... | 16 bits, guaranteed |

Voltage Output

| | |
|-----------------------|-------------------------|
| Range | ± 10 V |
| Output coupling | DC |
| Output impedance | |
| NI 783xR | 1.25 Ω |
| NI 784xR/785xR..... | 0.5 Ω |
| Current drive | ± 2.5 mA |
| Protection | Short-circuit to ground |
| Power-on state..... | User configurable |

Dynamic Characteristics

| Step Size | Accuracy | | |
|--------------|--------------|-------------|-------------|
| | ± 16 LSB | ± 4 LSB | ± 2 LSB |
| ± 20.0 V | 6.0 μ s | 6.2 μ s | 7.2 μ s |
| ± 2.0 V | 2.2 μ s | 2.9 μ s | 3.8 μ s |
| ± 0.2 V | 1.5 μ s | 2.6 μ s | 3.6 μ s |

| | |
|--|--|
| Slew rate..... | 10 V/ μ s |
| Noise..... | 150 μ V _{rms} , DC to 1 MHz |
| Glitch energy at midscale transition..... | ± 200 mV for 3 μ s |

Digital I/O

| | |
|--|-----|
| Number of channels | |
| NI 781xR..... | 160 |
| NI 7830R..... | 56 |
| NI 7831R/7833R/7841R/7842R/ 7851R/7852R/7853R/7854R | 96 |
| Compatibility..... | TTL |

Digital logic levels

| Level | Min | Max |
|---|-------|-------|
| Input low voltage (V_{IL}) | 0.0 V | 0.8 V |
| Input high voltage (V_{IH}) | 2.0 V | 5.5 V |
| Output low voltage (V_{OL}), where $I_{OUT} = -4$ mA | 0 V | 0.4 V |
| Output high voltage (V_{OH}), where $I_{OUT} = 4$ mA | 2.4 V | 3.3 V |

Output current

| | |
|--------------|--------|
| Source | 4.0 mA |
| Sink | 4.0 mA |

Input leakage current

$\pm 10 \mu\text{A}$

Power-on state

Programmable, by line

Protection

Input

| | |
|----------------------|------------------------------|
| NI 781xR/783xR..... | -0.5 to 7.0 V, single line |
| NI 784xR/785xR | -20.0 to 20.0 V, single line |

Output

Short-circuit
(up to eight lines may be
shorted at a time)

Minimum pulse width

| | |
|--------------|---------|
| Input | 25 ns |
| Output | 12.5 ns |

Minimum sampling period

5 ns

Reconfigurable FPGA

| | |
|--|-----------------|
| NI 7811R/7830R/7831R | |
| FPGA type..... | Virtex-II V1000 |
| Number of flip-flops..... | 10,240 |
| Number of 4-input LUTs..... | 10,240 |
| Number of 18×18 multipliers ... | 40 |
| Embedded block RAM..... | 720 kbits |

| | |
|--|-----------------|
| NI 7813R/7833R | |
| FPGA type..... | Virtex-II V3000 |
| Number of flip-flops..... | 28,672 |
| Number of 4-input LUTs..... | 28,672 |
| Number of 18×18 multipliers ... | 96 |
| Embedded block RAM..... | 1,728 kbits |

| | |
|--|---------------|
| NI 7841R/7851R | |
| FPGA type..... | Virtex-5 LX30 |
| Number of flip-flops..... | 19,200 |
| Number of 6-input LUTs..... | 19,200 |
| Number of DSP48 slices (25×18 multipliers)..... | 32 |
| Embedded block RAM..... | 1,152 kbits |

| | |
|--|---------------|
| NI 7842R/7852R | |
| FPGA type..... | Virtex-5 LX50 |
| Number of flip-flops..... | 28,800 |
| Number of 6-input LUTs..... | 28,800 |
| Number of DSP48 slices (25×18 multipliers)..... | 48 |
| Embedded block RAM..... | 1,728 kbits |

| | |
|--|---------------|
| NI 7853R | |
| FPGA type..... | Virtex-5 LX85 |
| Number of flip-flops..... | 51,840 |
| Number of 6-input LUTs..... | 51,840 |
| Number of DSP48 slices (25×18 multipliers)..... | 48 |
| Embedded block RAM..... | 3,456 kbits |

| | |
|--|---------------------------------|
| NI 7854R | |
| FPGA type..... | Virtex-5 LX110 |
| Number of flip-flops..... | 69,120 |
| Number of 6-input LUTs..... | 69,120 |
| Number of DSP48 slices (25×18 multipliers)..... | 64 |
| Embedded block RAM..... | 4,608 kbits |
| Timebase..... | 40, 80, 120, 160, or 200 MHz |

| | |
|--|--|
| Timebase reference sources | Bus Interface |
| NI PCI-781xR/783xR Onboard clock only | PCI/PCIe/PXI Master, slave |
| NI PCIe-784xR/785xR Onboard clock only | Data transfers DMA, interrupts, programmed I/O |
| NI PXI-78xxR Onboard clock, phase-locked to PXI 10 MHz clock | Number of DMA channels 3 |
| Timebase accuracy, onboard clock ±100 ppm, 250 ps peak-to-peak jitter | Power Requirement |
| Phase locked to PXI 10 MHz | +5 VDC (±5%) ¹ |
| Clock (NI PXI-78xxR only) Adds 350 ps peak-to-peak jitter | NI 781xR 9 mA typ NI 7830R/7831R 330 mA typ NI 7833R 364 mA typ NI PXI-7841R/7851R 125 mA typ NI PXI-7842R/7852R 136 mA typ NI 7853R 460 mA typ NI 7854R 484 mA typ |
| Additional frequency-dependent peak-to-peak jitter | +3.3 VDC (±5%) ² |
| NI 781xR/783xR | NI 7811R 650 mA typ NI 7813R 850 mA typ NI 7830R/7831R 462 mA typ NI 7833R 727 mA typ NI PCIe-7841R/7851R 847 mA typ NI PCIe-7842R/7852R 984 mA typ NI PXI-7841R/7851R 525 mA typ NI PXI-7842R/7852R 604 mA typ NI 7853R 640 mA typ NI 7854R 843 mA typ |
| NI 784xR/785xR | +12 V |
| 40 MHz None | NI 784xR/785xR 0.5 A |
| 80 MHz 400 ps | -12 V |
| 120 MHz 720 ps | NI PXI-784xR/785xR 0.25 A |
| 160 MHz 710 ps | +5V terminal |
| 200 MHz 700 ps | Connector 0 0.5 A max ³ Connector 1 0.5 A max ³ Connector 2 0.5 A max ³ All connectors 1.5 A max ^{3,4} |

Calibration (NI 783xR/784xR/785xR Only)

Recommended warm-up time 15 minutes

Calibration interval 1 year

Onboard calibration reference

DC level 5.000 V (±3.5 mV)
(actual value stored in Flash memory)

Temperature coefficient ±5 ppm/°C max
Long-term stability ±20 ppm/√1,000 h

 **Note** Refer to *Calibration Certificates* at ni.com/calibration to generate a calibration certificate for the NI 78xxR.

¹ Does not include current drawn from the +5 V line on the I/O connectors.

² Does not include current sourced by the digital outputs.

³ (NI PCIe-78xxR only) Total maximum terminal current for all connectors is 100 mA unless disk drive connector is attached.

⁴ (NI 784xR/785xR only) The NI 784xR/785xR has a user-replaceable socketed fuse that opens when current exceeds the current specification. Refer to the *NI R Series Multifunction RIO User Manual*, available at ni.com/manuals, for information about fuse replacement.

To calculate the total current sourced by the digital outputs, use the following equation:

$$\sum_{i=1}^j \text{current sourced on channel } i$$

Power available at I/O connectors...4.50 to 5.25 VDC at 1 A
total, 250 mA per I/O connector pin

Physical

Dimensions (not including connectors)

| | |
|--------------------------|--|
| NI PCI-781xR/783xR..... | 17 cm by 11 cm (6.7 in. by 4.3 in.) |
| NI PCIe-784xR/785xR..... | 17 cm by 11 cm (6.7 in. by 4.3 in.) |
| NI PXI-78xxR | 16 cm by 10 cm (6.3 in. by 3.9 in.) |

Weight

| | |
|--------------------------|-------|
| NI PCI-781xR/783xR..... | 112 g |
| NI PCIe-784xR/785xR..... | 127 g |
| NI PXI-78xxR | 152 g |

I/O connectors

| | |
|---------------------------|---|
| NI 781xR..... | Four 68-pin female high-density VHDCI type |
| NI 7830R..... | Two 68-pin female high-density VHDCI type |
| NI 783xR/784xR/785xR..... | Three 68-pin female high-density VHDCI type |

Disk drive power connector

(PCIe devices)Standard ATX peripheral connector (not serial ATA)

Maximum Working Voltage (NI 783xR/784xR/785xR Only)

Maximum working voltage refers to the signal voltage plus the common-mode voltage.

Channel-to-earth.....±12 V, Measurement Category I

Channel-to-channel±24 V, Measurement Category I



Caution Do not use the NI 783xR/784xR/785xR for connection to signals in Measurement Categories II, III, or IV.

Environmental

The NI 78xxR is intended for indoor use only.

Operating Environment

NI 781xR.....0 °C to 55 °C,
tested in accordance with
IEC-60068-2-1 and
IEC-60068-2-2.

NI 7830R, NI 7831R
40 MHz or 80 MHz timebase0 °C to 55 °C,
tested in accordance with
IEC-60068-2-1 and
IEC-60068-2-2.

NI PCI/PXI-7833R
40 MHz timebase0 °C to 55 °C,
tested in accordance with
IEC-60068-2-1 and
IEC-60068-2-2.

80 MHz timebase0 °C to 55 °C except the following: 0 °C to 45 °C when installed in an NI PXI-1000/B or NI PXI-101X,
tested in accordance with
IEC-60068-2-1 and
IEC-60068-2-2.

NI PXI-7841R/7842R/7851R/7852R/7853R/7854R
40 MHz timebase0 °C to 55 °C,
tested in accordance with
IEC-60068-2-1 and
IEC-60068-2-2.

80 MHz timebase0 °C to 55 °C except the following: 0 °C to 45 °C when installed in an NI PXI-1000/B or NI PXI-101X,
tested in accordance with
IEC-60068-2-1 and
IEC-60068-2-2.

NI PCIe-7841R/7842R/7851R/7852R
40 MHz or 80 MHz timebase0 °C to 40 °C,
tested in accordance with
IEC-60068-2-1 and
IEC-60068-2-2.

Relative humidity range.....10% to 90%,
noncondensing,
tested in accordance with
IEC-60068-2-56.

Altitude2,000 m at 25 °C ambient temperature

Storage Environment

| | |
|---------------------------------|--|
| NI PCI/PXI-781xR/783xR | -20 °C to 70 °C, tested in accordance with IEC-60068-2-1 and IEC-60068-2-2. |
| NI PCIe-784xR/785xR | -20 °C to 70 °C, tested in accordance with IEC-60068-2-1 and IEC-60068-2-2. |
| NI PXI-784xR/785xR | -40 °C to 70 °C, tested in accordance with IEC-60068-2-1 and IEC-60068-2-2. |
| Ambient temperature range | -20 °C to 70 °C, tested in accordance with IEC-60068-2-1 and IEC-60068-2-2. |
| Relative humidity range..... | 5% to 95%, noncondensing, tested in accordance with IEC-60068-2-56. |



Note Clean the device with a soft, non-metallic brush. Make sure that the device is completely dry and free from contaminants before returning it to service.

Shock and Vibration (for NI PXI-78xxR Only)

| | |
|-------------------------|---|
| Operational shock | 30 g peak, half-sine, 11 ms pulse; tested in accordance with IEC-60068-2-27. Test profile developed in accordance with MIL-PRF-28800F. |
| Random vibration | |
| Operating | 5 Hz to 500 Hz, 0.3 g _{rms} |
| Nonoperating | 5 Hz to 500 Hz, 2.4 g _{rms} , tested in accordance with IEC-60068-2-64. Nonoperating test profile exceeds the requirements of MIL-PRF-28800F, Class 3. |

Safety

The NI 78xxR is designed to meet the requirements of the following standards of safety for electrical equipment for measurement, control, and laboratory use:

- IEC 61010-1, EN 61010-1
- UL 61010-1, CSA 61010-1



Note For UL and other safety certifications, refer to the product label or the [Online Product Certification](#) section.

Electromagnetic Compatibility

The NI 78xxR is designed to meet the requirements of the following standards of EMC for electrical equipment for measurement, control, and laboratory use:

- EN 61326 (IEC 61326): Class A emissions;
Basic immunity
- EN 55011 (CISPR 11): Group 1, Class A emissions
- AS/NZS CISPR 11: Group 1, Class A emissions
- FCC 47 CFR Part 15B: Class A emissions
- ICES-001: Class A emissions



Note For the standards applied to assess the EMC of this product, refer to the [Online Product Certification](#) section.



Note For EMC compliance, operate this device with shielded cabling.

CE Compliance

This product meets the essential requirements of applicable European Directives as follows:

- 2006/95/EC; Low-Voltage Directive (safety)
- 2004/108/EC; Electromagnetic Compatibility Directive (EMC)

Online Product Certification

Refer to the product Declaration of Conformity (DoC) for additional regulatory compliance information. To obtain product certifications and the DoC for this product, visit ni.com/certification, search by model number or product line, and click the appropriate link in the Certification column.

Environmental Management

NI is committed to designing and manufacturing products in an environmentally responsible manner. NI recognizes that eliminating certain hazardous substances from our products is beneficial to the environment and to NI customers.

For additional environmental information, refer to the *NI and the Environment* Web page at ni.com/environment. This page contains the environmental regulations and directives with which NI complies, as well as other environmental information not included in this document.

Waste Electrical and Electronic Equipment (WEEE)



EU Customers At the end of their life cycle, all products *must* be sent to a WEEE recycling center. For more information about WEEE recycling centers and National Instruments WEEE initiatives, visit ni.com/environment/weee.htm.

电子信息产品污染控制管理办法（中国 RoHS）



中国客户 National Instruments 符合中国电子信息产品中限制使用某些有害物质指令 (RoHS)。关于 National Instruments 中国 RoHS 合规性信息，请登录 ni.com/environment/rohs_china。（For information about China RoHS compliance, go to ni.com/environment/rohs_china.)

Device Pinouts

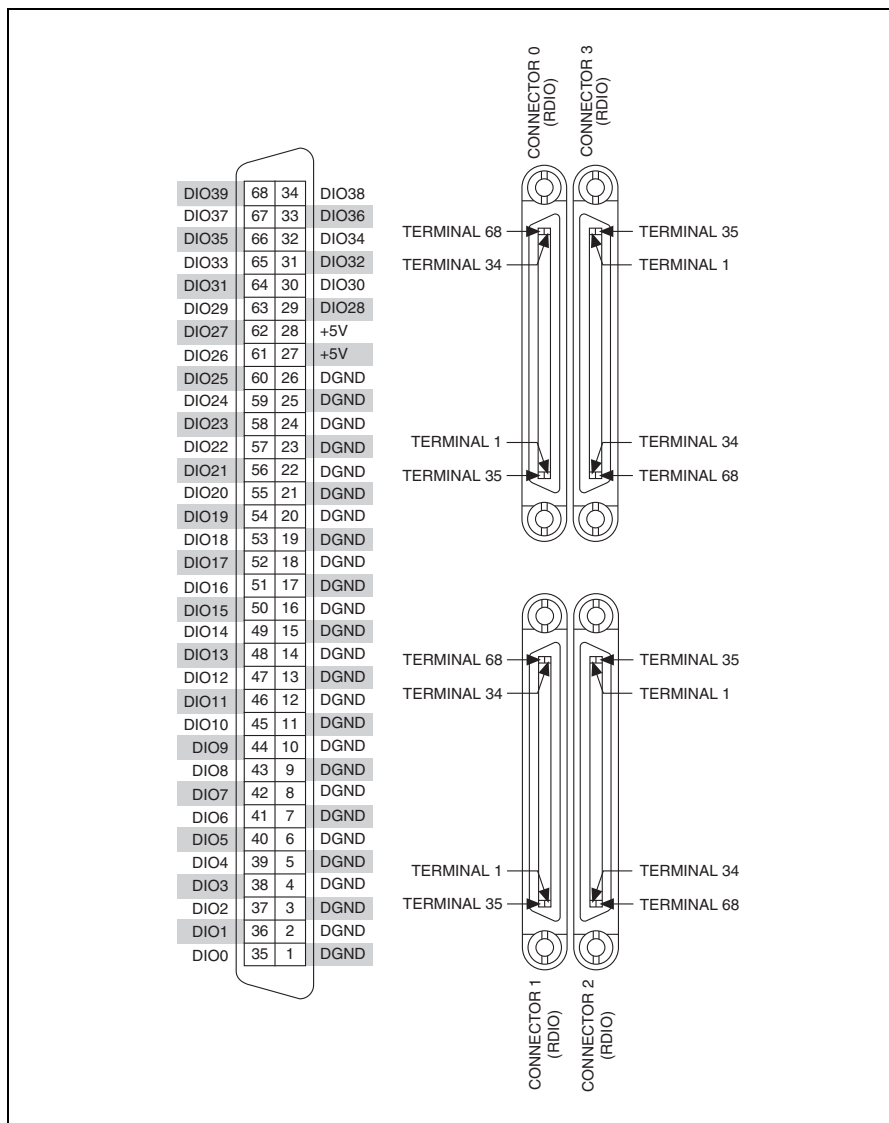


Figure 1. NI 781xR Connector Pin Assignments and Locations

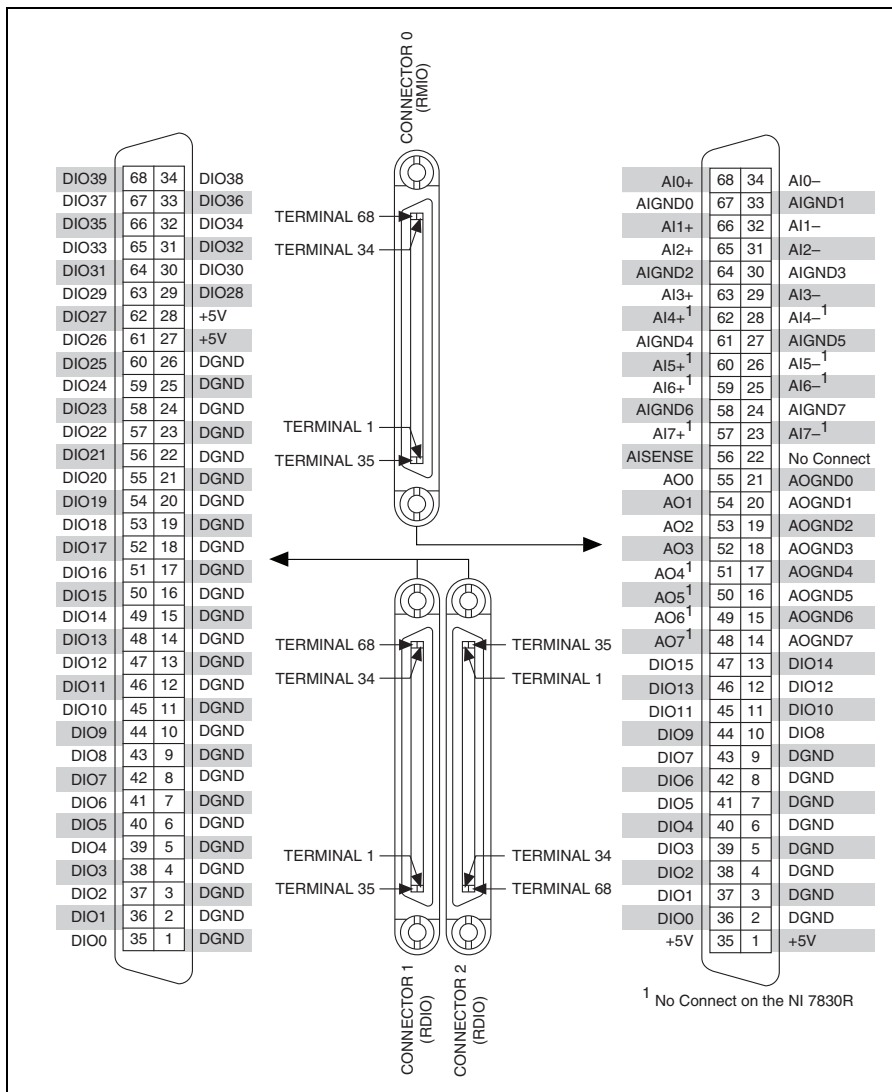


Figure 2. NI 783xR/784xR/785xR Connector Pin Assignments and Locations

National Instruments, NI, ni.com, and LabVIEW are trademarks of National Instruments Corporation. Refer to the *Terms of Use* section on ni.com/legal for more information about National Instruments trademarks. Other product and company names mentioned herein are trademarks or trade names of their respective companies. For patents covering National Instruments products/technology, refer to the appropriate location: **Help>Patents** in your software, the *patents.txt* file on your media, or the *National Instruments Patent Notice* at ni.com/patents.

© 2008–2009 National Instruments Corporation. All rights reserved.

372492C-01

Jun09

A.2 Laser Innolight Mephisto 1000NE



Ultra-stable single-frequency cw laser · low noise · 1064 nm · 1319 nm · up to 2 W

MEPHISTO / MEPHISTO S · PRODUCT LINE

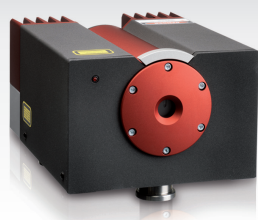
APPLICATIONS

- Laser-based metrology (precision laser interferometry, spectroscopy, fiber optic sensing, LIDAR applications)
- Injection locking and seeding of high power lasers (e.g. gravitational wave detection)
- Optical length and frequency standards
- Quantum optics (optical trapping, optical lattice, squeezing)
- Nonlinear optics pump source (SHG, DFG, OPO)
- Optical heterodyning and coherent communication
- General scientific research

GENERAL FEATURES

- True single-frequency operation using reliable nonplanar ring oscillator (NPRO) technology
- All solid-state, diode-pumped system with monolithic cavity for ultra-stable emission
- Narrow linewidth, extremely long coherence length
- Active intensity noise reduction (Noise Eater)
- Turnkey systems
- Low noise control electronics
 - Frequency and power modulation inputs
 - Safety circuitry (soft start, interlock, temperature guard)

MEPHISTO



MEPHISTO S

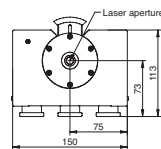
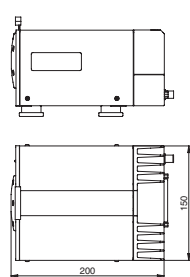


SPECIFICATIONS

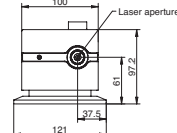
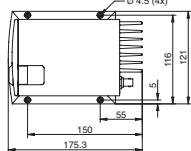
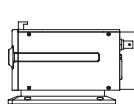
| | MEPHISTO | MEPHISTO S | Unit |
|---------------------------|--|--|------|
| Laser power @ 1064 nm | 500 ¹⁾⁻³⁾ , 1000 ¹⁾⁻²⁾ , 2000 ¹⁾⁻²⁾ | 200 ¹⁾⁻³⁾ , 500 ¹⁾⁻³⁾ | mW |
| Laser power @ 1319 nm | 200 ¹⁾⁻²⁾ , 500 ¹⁾⁻²⁾ , 800 ¹⁾⁻²⁾ | not available | mW |
| Laser control electronics | Analog, stand-alone (best stability) | Analog, stand-alone (good stability) ⁴⁾ | |

Options: ¹⁾ NE (Noise Eater); ²⁾ FC (fiber coupling); ³⁾ ETR (Extended Tuning Range).

⁴⁾Fewer functions than Mephisto controller.



All numbers in mm.



All numbers in mm.

InnoLight follows a policy of continuous improvement of its products. Specifications are subject to change without notice.

www.innolight.de

THE ART OF SOLID-STATE LASERS

Ultra-stable single-frequency cw laser • low noise • 1064 nm • 1319 nm • up to 2 W

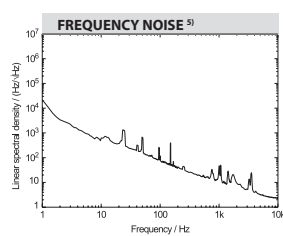
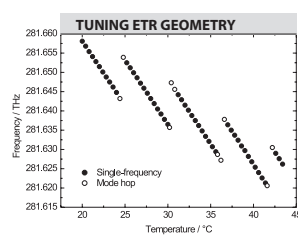
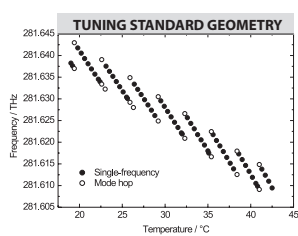
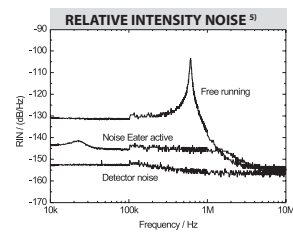
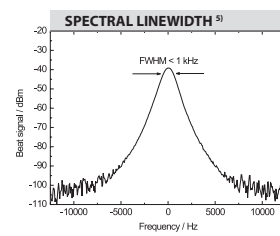
MEPHISTO / MEPHISTO S • PRODUCT LINE

SPECIFICATIONS @ 1064 nm

| | MEPHISTO | MEPHISTO S | Unit |
|--|-----------------------------------|-----------------------------------|---------|
| Operational mode | Continuous wave | Continuous wave | |
| Spatial mode | TEM_{00} ($M^2 < 1.1$) | TEM_{00} ($M^2 < 1.1$) | |
| Beam roundness | < 1.1 | < 1.1 | |
| Thermal tuning coefficient | -3 | -3 | GHz/K |
| Thermal tuning range | 30 | 30 | GHz |
| Thermal response bandwidth | $\cong 1$ | $\cong 1$ | Hz |
| PZT tuning coefficient | $\cong 1$ | $\cong 1$ | MHz/V |
| PZT tuning range | ± 100 | ± 100 | MHz |
| PZT response bandwidth | 100 | 100 | kHz |
| Emission spectrum | Single-frequency | Single-frequency | |
| Spectral linewidth (over 100 ms) | $\cong 1$ | kHz range | kHz |
| Coherence length | > 1 | > 1 | km |
| Frequency stability ^{a)} | $\cong 1$ | $\cong 10$ | MHz/min |
| Relative intensity noise (RIN), $f > 10$ kHz | < -100 | < -90 | dB/Hz |
| RIN with Noise Eater (NE) option, $f > 10$ kHz | < -140 | < -120 | dB/Hz |
| Intensity noise without NE, 10 Hz to 2 MHz | < 0.1 | < 0.5 | % rms |
| Intensity noise with NE, 10 Hz to 2 MHz | < 0.03 | < 0.2 | % rms |
| Waist location (inside laser head) | $\cong 105$ | $\cong 95$ | mm |
| Laser head size, w · h · d | 150 · 113 · 200 | 121 · 97 · 175 | mm |
| Laser head weight | 3.9 | 2.6 | kg |

^{a)} Only for Mephisto product line.

^{b)} Measured Allan deviation at constant room temperature.



OPTIONS AND ACCESSORIES

Options

Noise Eater

Extended Tuning Range (ETR)

Fiber coupling (> 60 % coupling efficiency)

InnoLight – Innovative Laser und Systemtechnik GmbH
Garbsener Landstrasse 10 · 30419 Hannover · Germany
Phone: +49 511 760 727-0 · Fax: +49 511 760 727-99
E-mail: sales@innolight.de · Web: www.innolight.de



A.3 AOM Crystal Technologies 3080-194

Acousto Optic Theory

Basic Theory

As shown in Figure 1 (a) and (b), acousto optic devices operate by Bragg diffraction of an incident light beam from a moving acoustic wavefront. The intensity of light diffracted into the output beam is dependent on the power of the acoustic beam which is in turn dependent on the modulation signal input to the driver. The modulation signal to optical output transfer function is monotonic but non-linear. This is unimportant for digital modulation.

Alignment

For proper modulator operation, the optical beam and sound beam must interact with the proper relationship. This requires several conditions be met simultaneously.

First, the acoustic beam (modulator housing) must be slightly rotated off perpendicular to the optical beam so that the Bragg angle condition is met as shown in Figure 1. This can be accomplished either side of perpendicular with only a slight difference in performance as described later. The proper Bragg angle for each device is tabulated on the individual data sheets.

Second, the modulator must be translated vertically so the optical beam passes through the acoustic beam. This adjustment is more critical for the high-performance (wideband) units which have acoustic beams of very small height. In fact, a slight design compromise is made in these units to avoid having this adjustment be excessively critical. An estimate of the required precision and stability of this adjustment is 25% of the "active aperture", as tabulated on the data sheets, e.g. ~.001" for Model 3350.

Third, the focusing lens for the incident optical beam must be positioned longitudinally so that the optical beam focus (beam waist) is located at the acoustic column. If the beam waist location is determined in air before the modulator is introduced, then the lens should be moved away from the modulator location to account for the increased optical path length inside the modulator crystal. This

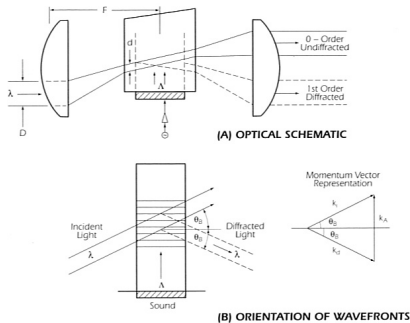


Figure 1. Modulator Configuration

increment is ~6.2 mm for Models 3080 and 3110, and ~1.7 mm for Model 3200.

To obtain the proper optical beam waist diameter (d) stipulated in the device data sheets requires the following relationship:

$$d = \frac{1.27F\lambda}{D}$$

Where: D = Input laser beam, diameter ($1/e^2$ intensity points)
 F = Focal length of input focusing lens
 λ = Light wavelength

A single-element, plano-convex lens, oriented as shown, will give satisfactory results.

Finally, in the case of the Model 3350, the optical beam should be positioned close to the acoustic transducer to minimize effects of acoustic attenuation and acoustic beam spreading from diffraction.

Figure 2 is included as an aid in obtaining correct adjustments. The images are shown as outputs without the recollimating optics. However, they should not be viewed directly, but as reflections from a diffuse surface such as a 3 x 5-inch file card. The zero and first orders are point to point complementary (sum = 1). The missing area in the zero order beam corresponds to light diffracted into the first order. In practice, the zero order may be easier to interpret, particularly if the laser power can be reduced to avoid eye saturation.

It should be noted that there is a slight variation in diffraction efficiency with the polarization of the incident optical beam. Polarization perpendicular to the mounting surface of the modulator is usually preferred in TeO_2 devices.

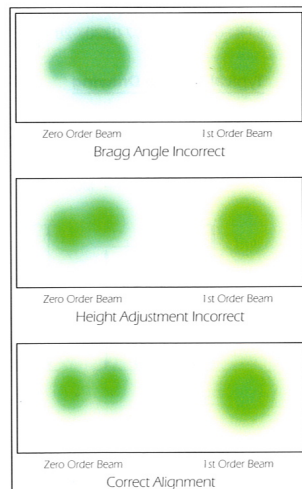
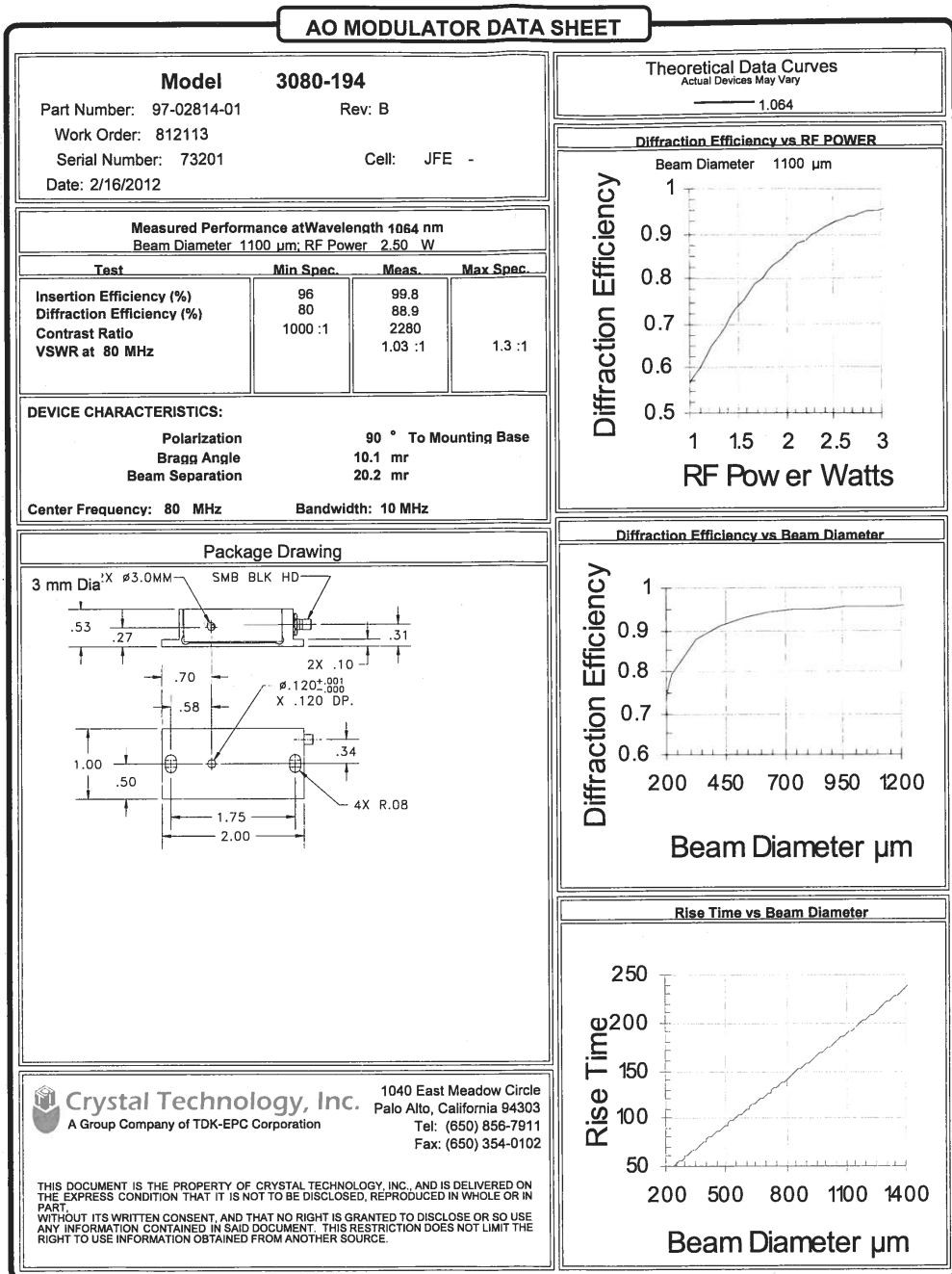


Figure 2. Alignment Beam Patterns

| SPECIFICATIONS | | Outline Drawing: | | Package 97-02814-01rB | |
|--|------------------------|--------------------|--|--|--------------|
| AO Medium | TeO ₂ | 4.2 mm/ μ s | 2X ϕ 3.0MM | SMB BLK HD | |
| Acoustic Velocity | 2.5 mm'L' X | 1.75 mm 'H' | | | |
| Active Aperture* | 80 MHz | | | | |
| Center Frequency (Fc) | 10 MHz @ | -13 dB Return Loss | .53 | .31 | |
| RF Bandwidth | 50 Ohms Nominal | | .27 | | |
| Input Impedance | 1.3:1 Max | | .70 | 2X .10 | |
| VSWR @ Fc | 1060 nm | | .58 | ϕ .120 ^{+.00} _{.00} | X .120 DP. |
| Wavelength | 4 % Max | | .50 | .34 | |
| Insertion Loss | 0.5 % Max | | | | |
| Reflectivity per Surface | MIL-C-48497 | | | | |
| Anti-Reflection Coating | 10 MW/cm ² | | | | |
| Optical Power Density | 10000:1 Min | | | | |
| Contrast Ratio | 90 ° To Mounting Plane | | | | |
| Polarization | | | | | |
| PERFORMANCE VS WAVELENGTH | | | | | |
| Wavelength (nm) | 1060 | | | | |
| Saturation RF Power (W) | 2.5 | | | | |
| Bragg Angle (mr) | 10.1 | | | | |
| Beam Separation (mr) | 20.2 | | | | |
| PERFORMANCE VS BEAM DIAMETER | | | | | |
| Beam Diameter (um) | 1100 | | | | |
| at Wavelength (nm) | 1060 | | | | |
| Diffraction Efficiency (%) | 80 | | | | |
| Rise Time (nsec) | 200 | | | | |
| Modulation Bandwidth | 3 | | | | |
| Beam Ellipticity | NA | | | | |
| DOCUMENT CONTROL | | | | | |
| JUN 06 2005 | | | | | |
| Notes: Diffraction Efficiency at 2.0 Watts RF Power. | | | | | |
| THIS DOCUMENT IS THE PROPERTY OF CRYSTAL TECHNOLOGY, INC. IT IS NOT TO BE REPRODUCED OR DISCLOSED IN WHOLE OR IN PART OTHER THAN BY EMPLOYEES OF CRYSTAL TECHNOLOGY AND ITS CONTRACTED REPRESENTATIVES AND DISTRIBUTORS. ANY EXCEPTION REQUIRES THE WRITTEN CONSENT OF AN AUTHORIZED REPRESENTATIVE OF CRYSTAL TECHNOLOGY. | | | | | |
| TOOLING: | XX ± .01 | DR | Gef Scholtz | CRYSTAL TECHNOLOGY, Inc. | |
| XX ± .005 | | 5/23/2005 | | | |
| MATERIAL: | CHK | APP | DESCRIPTION: AOMO 3080-194 Internal Heat Sink | | |
| FINISH: | | | PART NUMBER: 97-02814-01 | REF: B | SHEET 1 OF 1 |

*Active Aperture: Aperture over which performance specifications apply.

Appendix A Data Sheets



A.4 Frequency Mixer Mini-Circuits ZP-3

Coaxial Frequency Mixer

Level 7 (LO Power +7 dBm) 0.15 to 400 MHz

Maximum Ratings

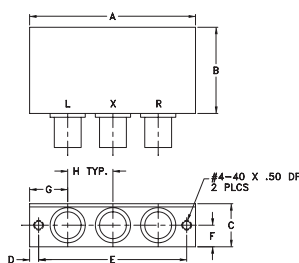
| | |
|-----------------------|----------------|
| Operating Temperature | -55°C to 100°C |
| Storage Temperature | -55°C to 100°C |
| RF Power | 50mW |
| IF Current | 40mA |

Permanent damage may occur if any of these limits are exceeded.

Coaxial Connections

| | |
|----|---|
| LO | L |
| RF | R |
| IF | X |

Outline Drawing



Outline Dimensions (inch mm)

| A | B | C | D | E | F | G | H | wt |
|-------|-------|-------|------|-------|------|-------|-------|-------|
| 2.31 | 1.20 | .60 | .125 | 2.062 | .30 | .53 | .63 | grams |
| 58.67 | 30.48 | 15.24 | 3.18 | 52.37 | 7.62 | 13.46 | 16.00 | 75.0 |

Features

- low conversion loss, 4.7 dB typ.
- IF response to DC
- excellent L-R isolation, 46 dB typ., L-I, 47 dB typ.
- rugged shielded case

Applications

- VHF/UHF
- cellular
- instrumentation

ZP-3+
ZP-3



BNC version shown
CASE STYLE: GG60

| Connectors | Model | Price | Qty. |
|------------|-----------|-------------------|------|
| BNC | ZP-3+ | \$39.95 ea. (1-9) | |
| SMA | ZP-3-S(+) | \$44.95 ea. (1-9) | |

+ RoHS compliant in accordance
with EU Directive (2002/95/EC)

The +Sufix identifies RoHS Compliance. See our web site
for RoHS Compliance methodologies and qualifications.

Electrical Specifications

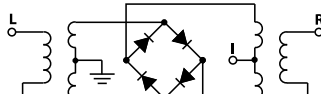
| FREQUENCY (MHz) | CONVERSION LOSS (dB) | | | LO-RF ISOLATION (dB) | | | LO-IF ISOLATION (dB) | | | | | | | | | | | |
|--------------------|-------------------------|----|---------------|-------------------------|-----------|-----------|-------------------------|-----------|-----------|-----------|----|----|----|----|----|----|----|----|
| | LO/RF $f_L - f_U$ | IF | Mid-Band m | Total Range Max. | L | M | U | L | M | U | | | | | | | | |
| | | | \bar{X} | σ | Typ. Min. | Typ. Min. | Typ. Min. | Typ. Min. | Typ. Min. | Typ. Min. | | | | | | | | |
| 0.15-400 | DC-400 | | 4.7 | 0.10 | 7.0 | 8.0 | 60 | 50 | 46 | 30 | 35 | 25 | 60 | 40 | 47 | 25 | 35 | 20 |

1 dB COMP: +1 dBm typ.
For phase detection, DC output has positive
polarity with in-phase LO and RF signals.

Typical Performance Data

| Frequency (MHz) | Conversion Loss (dB) | | VSWR RF Port (:1) | Frequency (MHz) | Isolation L-R (dB) | Isolation L-I (dB) | VSWR LO Port (:1) |
|--------------------|----------------------------|------|-------------------------|--------------------|--------------------------|--------------------------|-------------------------|
| | RF | LO | | LO +7dBm | LO +7dBm | LO +7dBm | |
| 0.15 | 30.15 | 5.37 | 1.57 | 10.00 | 68.68 | 61.84 | 2.59 |
| 0.23 | 30.23 | 5.27 | 1.41 | 20.00 | 65.36 | 56.87 | 2.60 |
| 0.30 | 30.30 | 5.21 | 1.33 | 30.00 | 63.22 | 54.20 | 2.59 |
| 0.50 | 30.50 | 5.16 | 1.25 | 40.00 | 61.75 | 52.09 | 2.58 |
| 1.00 | 31.00 | 5.08 | 1.21 | 76.00 | 57.56 | 47.59 | 2.54 |
| 2.80 | 32.80 | 4.91 | 1.21 | 94.00 | 56.48 | 45.97 | 2.50 |
| 6.40 | 36.40 | 4.91 | 1.21 | 112.00 | 54.90 | 44.70 | 2.50 |
| 10.00 | 40.00 | 4.73 | 1.21 | 149.00 | 52.63 | 42.36 | 2.57 |
| 28.00 | 58.00 | 4.71 | 1.21 | 168.00 | 54.13 | 42.02 | 2.55 |
| 64.00 | 94.00 | 4.75 | 1.17 | 206.00 | 49.62 | 38.81 | 2.62 |
| 100.00 | 130.00 | 4.83 | 1.14 | 225.00 | 48.10 | 38.56 | 2.66 |
| 138.00 | 168.00 | 4.85 | 1.13 | 244.00 | 48.03 | 37.82 | 2.68 |
| 157.00 | 187.00 | 4.88 | 1.10 | 282.00 | 53.65 | 37.79 | 2.67 |
| 195.00 | 225.00 | 4.92 | 1.08 | 301.00 | 55.10 | 38.07 | 2.76 |
| 233.00 | 263.00 | 4.97 | 1.10 | 320.00 | 54.03 | 37.59 | 2.82 |
| 252.00 | 282.00 | 5.10 | 1.12 | 340.00 | 52.86 | 36.62 | 2.76 |
| 271.00 | 301.00 | 5.17 | 1.14 | 360.00 | 51.53 | 35.44 | 2.69 |
| 290.00 | 320.00 | 5.15 | 1.17 | 390.00 | 47.44 | 33.11 | 2.86 |
| 370.00 | 340.00 | 5.38 | 1.10 | 410.00 | 45.39 | 32.24 | 3.05 |
| 400.00 | 370.00 | 5.41 | 1.05 | 430.00 | 44.42 | 32.17 | 3.06 |

Electrical Schematic



Mini-Circuits®

ISO 9001 ISO 14001 AS 9100 CERTIFIED

IF/RF MICROWAVE COMPONENTS

P.O. Box 350166, Brooklyn, New York 11235-0003 (718) 934-4500 Fax (718) 332-4661 The Design Engineers Search Engine Provides ACTUAL DATA Instantly at minicircuits.com

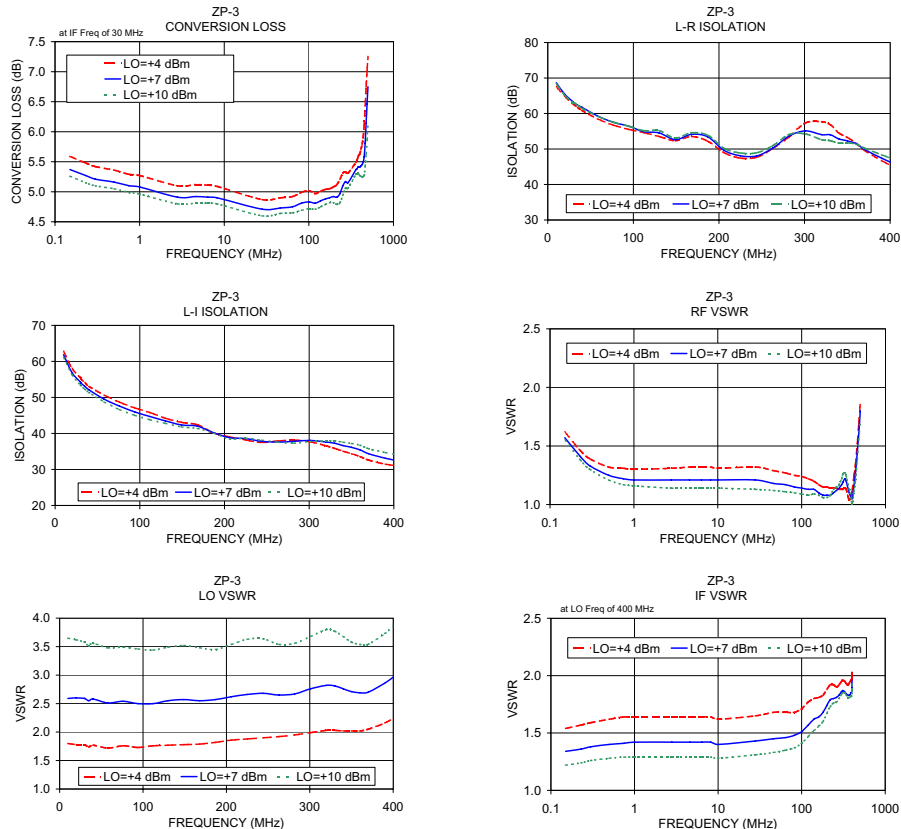
For detailed performance specs & shopping online see web site

Notes: 1. Performance and quality attributes and conditions not expressly stated in this specification sheet are intended to be excluded and do not form a part of this specification sheet. 2. Electrical specifications and performance data contained herein are based on Mini-Circuit's applicable established test performance criteria and measurement instructions. 3. The parts covered by this specification sheet are subject to Mini-Circuits standard limited warranty and terms and conditions (collectively, "Standard Terms"); Purchasers of this part are entitled to the rights and benefits contained therein. For a full statement of the Standard Terms and the exclusive rights and remedies thereunder, please visit Mini-Circuits' website at www.minicircuits.com/MCLStore/terms.jsp.

REV. B
M108294
ZP-3
D/T/DOP
07/04/12
Page 1 of 2

Performance Charts

**ZP-3+
ZP-3**



Mini-Circuits®
ISO 9001 ISO 14001 AS 9100 CERTIFIED
P.O. Box 350166, Brooklyn, New York 11235-0003 (718) 934-4500 Fax (718) 332-4661 The Design Engineers Search Engine Provides ACTUAL Data Instantly at minicircuits.com

Notes: 1. Performance and quality attributes and conditions not expressly stated in this specification sheet are intended to be excluded and do not form a part of this specification sheet. 2. Electrical specifications and performance data contained herein are based on Mini-Circuit's applicable established test performance criteria and measurement instructions. 3. The parts covered by this specification sheet are subject to Mini-Circuits standard limited warranty and terms and conditions (collectively, "Standard Terms"). Purchasers of this part are entitled to the rights and benefits contained therein. For a full statement of the Standard Terms and the exclusive rights and remedies thereunder, please visit Mini-Circuits' website at www.minicircuits.com/MCLstore/terms.jsp.

For detailed performance specs & shopping online see web site
minicircuits.com

Page 2 of 2

A.5 First sensor PC20-Q

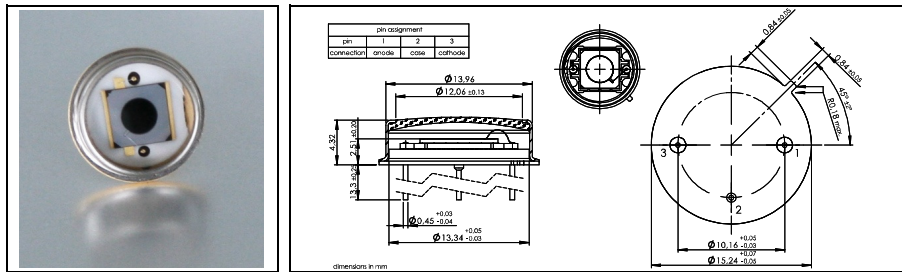


First Sensor PIN PD Data Sheet

Part Description PC20-Q TO

Order # 501447

Preliminary version 18-09-12



Features

- 20 mm² PIN detector
- Low dark current
- Fast rise time, low capacitance
- High QE at 1064 nm
- Fully depletable

Description

Circular active area PIN photodiode with 20 mm² active area. Metal can type isolated and hermetic TO8S package with clear glass window.

Application

- Precision photometry
- 1064 nm laser detection
- Pulsed light sensor

RoHS

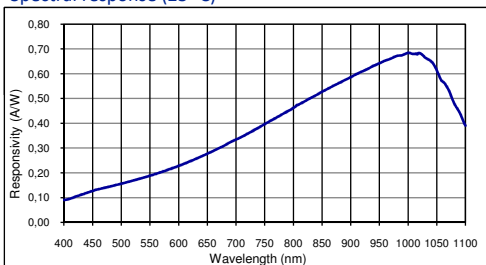
2002/95/EC



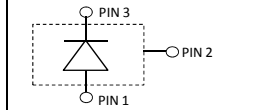
Absolute maximum ratings

| Symbol | Parameter | Min | Max | Unit |
|-------------------|---------------------|-----|-----|------|
| T _{STG} | Storage temp | -55 | 125 | °C |
| T _{OP} | Operating temp | -40 | 100 | °C |
| V _{max} | Max reverse voltage | | 200 | V |
| I _{PEAK} | Peak DC current | | 10 | mA |

Spectral response (23 °C)



Schematic



Electro-optical characteristics @ 23 °C

| Symbol | Characteristic | Test Condition | | Min | Typ | Max | Unit |
|-------------------------------|-------------------------|---|--|------|---------------|------|-----------------|
| | | | | | | | |
| | Active area | | | | diameter 5046 | | μm |
| | Active area | | | | 20 | | mm ² |
| I _D | Dark current | V _R = 10 V V _R = 150 V | | 10 | 25 | nA | |
| | | | | 15 | 30 | nA | |
| T _{K(I_D)} | Temperature coefficient | V _R = 10 V; change of dark current | | 13 | | | %/K |
| C | Capacitance | V _R = 10 V; f = 10 kHz V _R = 150 V; f = 10 kHz | | 7 | | | pF |
| | | | | 3.5 | | | pF |
| | Responsivity | λ = 900 nm λ = 1064 nm | | 0.60 | | | A/W |
| t _R | Rise time | V _R = 150 V; λ = 1064 nm; R _L = 50 Ω | | 0.48 | 0.55 | 0.65 | A/W |
| | Shunt Resistance | V _R = 10 mV | | 12 | | | ns |
| | N.E.P. | V _R = 150 V; λ = 1064 nm | | 10 | | | MΩ |
| V _{BR} | Breakdown voltage | I _g = 2 μA | | 200 | 300 | | V |

European, International Sales:



First Sensor AG
Peter-Behrens-Strasse 15
12459 Berlin
Germany
T +49 30 6399 2399
F +49 30 639923-752
sales.opto@first-sensor.com

USA:



First Sensor Inc.
5700 Corsa Avenue #105
Westlake Village
CA 91362 USA
T +1 818 706 3400
F +1 818 889 7053
sales.us@first-sensor.com

Appendix A Data Sheets

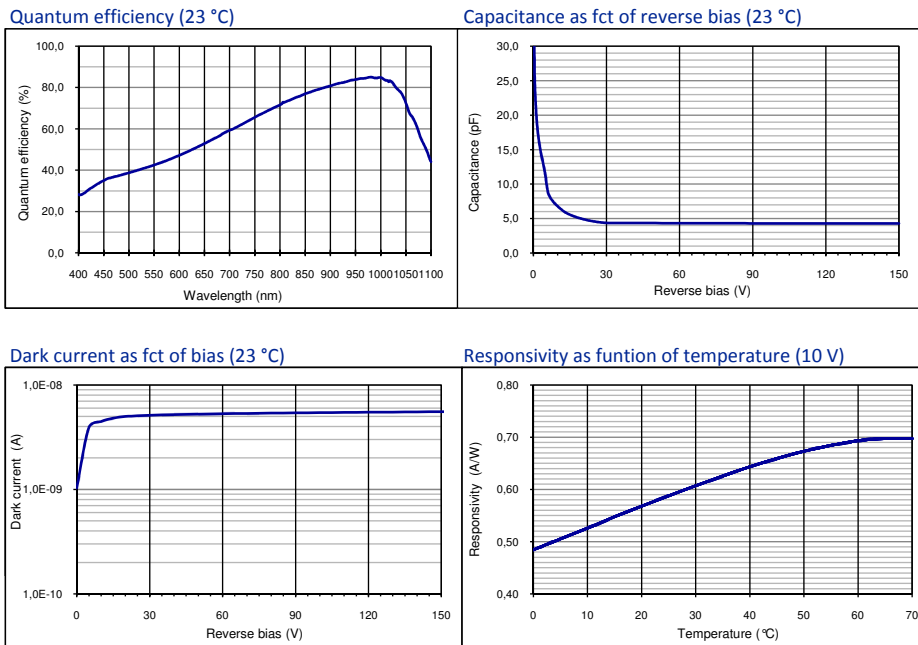


First Sensor PIN PD Data Sheet

Part Description PC20-Q TO

Order # 501447

Preliminary version 18-09-12



Package dimension:

Small quantities: Foam pad, boxed (12 cm x 16.5 cm)

Handling:

Please refer to document "Instructions for handling and processing"

Disclaimer: Due to our strive for continuous improvement, specifications are subject to change within our PCN policy according to JESD46C.

European, International Sales:



First Sensor AG
Peter-Behrens-Strasse 15
12459 Berlin
Germany
T +49 30 6399 2399
F +49 30 639923-752
sales.opto@first-sensor.com

USA:



First Sensor Inc.
5700 Corsa Avenue #105
Westlake Village
CA 91362 USA
T +1 818 706 3400
F +1 818 889 7053
sales.us@first-sensor.com

A.6 Stanford Research System Low Noise Pre-amplifier SR560

SPECIFICATIONS

| SR560 LOW-NOISE PREAMPLIFIER SPECIFICATIONS CHART | |
|--|--|
| Inputs | Single-ended or true differential |
| Impedance | 100 MΩ + 25 pF, DC-coupled |
| Maximum Inputs | 1 VDC before overload; 3 V peak to peak max AC coupled; protected to 100 VDC |
| Maximum Output | 10 Vpp |
| Noise | <4 nV/√Hz at 1 kHz |
| CMRR | >90 dB to 1 kHz, decreasing by 6 dB / octave (20 dB / decade) above 1 kHz |
| Gain | 1 to 50,000 in 1-2-5 sequence vernier gain in 0.5% steps |
| Flatness | ±0.3dB to 300kHz (gains up to 1000) -3 dB at 1 MHz, 1 Vpp output |
| Gain Stability | 200 ppm /°C |
| DC Drift | 5 μV/°C referred to input (DC coupled) |
| Filters | 0.03 Hz to 1 MHz, 10% typical accuracy |
| Distortion | 0.01% typical |
| Power | 100, 120, 220, 240 VAC (50/60 Hz), 60 Watts Max Internal Batteries: 3 x 12 V, 1.9 Ah sealed lead-acid (rechargeable) ±12 VDC in / out through rear panel banana jacks. |
| Battery Life | 15 hours nominal 250-1000 charge / discharge cycles |
| Charge Time | 4 hours to 80% of capacity |
| Mechanical | 1/2 Rack-Mount width, 3 1/2" height, weight 15 lbs. |
| Dimensions | 14-7/8" x 8-1/8" x 3-1/2" |
| Warranty | 1 year parts and labor on materials and workmanship |

A.7 Schäfter+Kirchhoff Fiber Collimators 60FC-...



Fundamentals: Fiber Collimators

Fig. 1: Fiber collimator 60FC-... with lens attachments and adjustment tools

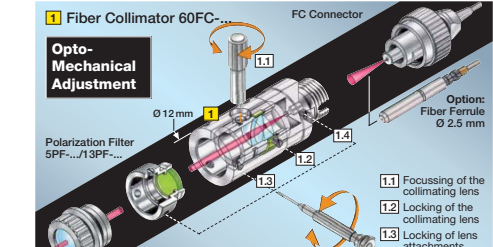
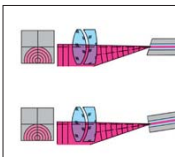
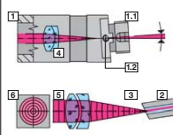


Figure 4: Combination Mismatch



When a combination mismatch occurs, either between an 8°-polish fiber inappropriately attached to a coaxially coupled fiber collimator or vice versa, a 0°-polish fiber connected to an inclined coupled fiber collimator, then the resultant diffraction produces a collimated beam that is axially displaced, asymmetric and differs significantly from a Gaussian profile.

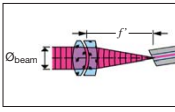
Figure 2: Fiber Collimator with inclined fiber connection



The 8°-polish of the singlemode fiber causes the emitted radiation to be defracted and the optical path is inclined. The design of the inclined fiber connection of this fiber collimator compensates for the beam deflection. The collimated beam is centered and concentrically symmetric.

Fig. 1 Fiber collimator 60FC-... with inclined coupling axis for singlemode fibers with connectors type FC-APC (8°-polish)
 ① Fiber connection (inclined)
 ② Grub screw for additional locking of the fiber ferrule
 ③ Singlemode fiber with 8°-polish
 ④ Diverging emission $\alpha = 10.4^\circ$ for a fiber with $NA = 0.11$ ($1/e^2$)
 ⑤ Collimating lens
 ⑥ Collimated laser beam
 ⑦ Concentrically symmetric beam profile with a Gaussian intensity distribution

Figure 5: Beam Diameter



The beam diameter is given by the focal length of the collimating lens and by the numerical aperture of the singlemode fiber. The beam diameter is defined as the $1/e^2$ level (13.5% value) of the Gaussian intensity distribution.

For singlemode fibers, the numerical aperture NA is given at the 5% level. To account for the differences in definition, a correction factor of 0.82 is introduced and the beam diameter calculated according to:

| | |
|--|---|
| Beam diameter: $\varnothing_{beam} = 2 \cdot f' \cdot NA \cdot 0.82$ | Example: Focal length $f' = 4.5$ mm, Numerical Aperture $NA = 0.11$ $\varnothing_{beam} = 2 \cdot 4.5\text{mm} \cdot 0.11 \cdot 0.82 = 0.81\text{mm}$ |
|--|---|

Figure 3: Fiber Collimator with coaxial fiber connection

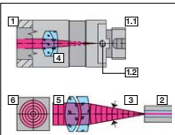
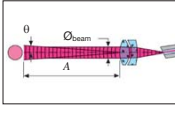


Fig. 1 Fiber Collimator 60FC-0... with coaxial coupling axis for singlemode fibers with connectors type FC-PC (0°-polish)
 ① Fiber connection (coaxial)
 ② Grub screw for an additional locking of the fiber ferrule
 ③ Singlemode fiber with 0°-polish
 ④ Diverging emission $\alpha = 10.4^\circ$ for a fiber with $NA = 0.11$ ($1/e^2$)
 ⑤ Collimating lens
 ⑥ Collimated laser beam
 ⑦ Concentrically symmetric beam profile with a Gaussian intensity distribution

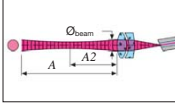
Figure 6: Beam Divergence



In principle, a collimated beam has a divergence greater than zero, i.e. the beam diameter varies with distance A from the fiber collimator. The beam divergence θ depends (for large distances of A) on the beam diameter \varnothing_{beam} at the position of the fiber collimator and on the wavelength λ . Also, the beam diameter depends on the numerical aperture NA of the singlemode fiber and the focal length f' of the collimating lens.

| | |
|---|--|
| $\theta = \frac{2\lambda}{\pi \cdot \varnothing_{beam}}$ $= \frac{\lambda}{\pi \cdot f' \cdot NA \cdot 0.82}$ | Example: Wavelength $\lambda = 670$ nm Focal length $f' = 4.5$ mm Numerical aperture $NA = 0.11$ Beam diameter $\varnothing_{beam} = 0.81$ mm Beam divergence $\theta = 0.53$ mrad |
|---|--|

Figure 7: Pilot Beam with approximate constant beam diameter across working range A



A pilot beam is a Gaussian beam of essentially constant diameter within a certain working range A , which is achieved by fine adjustment. The optimum position of the beam waist is defined as distance A_2 (see Table 12 on page 38).

The maximum working range A of a pilot beam is limited because of diffraction:

$$A \leq 2f' + \frac{\varnothing_{beam}^2 \cdot \pi}{4\lambda}$$

where \varnothing_{beam} is the collimated beam diameter, as in Figure 5.

01-2014 E 29

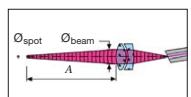
FiberCollimator_Theory_E01.indd 29

Schäfter + Kirchhoff GmbH
 Kieler Str. 212, 22525 Hamburg, Germany • Tel: +49 40 85 39 97-0 • Fax: +49 40 85 39 97-79 • info@SuKHamburg.de • www.SuKHamburg.com

102



Figure 8: Focussed Laser Spot



Readjustment of the collimating lens generates a focussed beam. At distance A , relative to the fiber collimator, a beam waist with diameter $\varnothing_{\text{spot}}$ is formed.

$$\text{Ø}_{\text{spot}} = MFD \cdot \left(\frac{A}{f'} + 1 \right)$$

The mode field diameter MFD is calculated from the numerical aperture NA at wavelength λ as:

$$MFD = \frac{2 \cdot \lambda}{\pi \cdot NA \cdot 0.82}$$

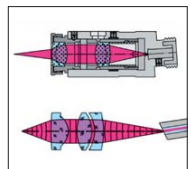
Deflection limits the maximum distance of the focus, where

$$A \leq A_{\max} = f' + \frac{\emptyset^2 \text{beam} \cdot \pi}{8 \cdot \lambda}$$

and \emptyset_{beam} is the collimated beam diameter, as in figure 5.

Notes

Figure 9:
Focussed Laser Spot: Fiber Collimator 60FC-...
and Micro-Focus Optics 5M-... / 13M-... / 25M-...



Focussing a beam using a fiber collimator alone is only suitable for extended working distances (figure 8), where the spot size of the focused beam is a multiple of the fiber mode field diameter.

Focussed micro-spots $<1\text{ }\mu\text{m}$ are generated by using micro-focus optics. The micro-focus optics are form-fitted to the fiber collimators.

The spot size is determined by the focal length ratio (micro-focus / collimator) and by the mode field diameter of the singlemode fiber.

To a good approximation, the spot size is given by:

$$\Omega_{\text{spot}} = \frac{f'_{\text{micro-focus}}}{f'_{\text{collimator}}} \cdot MFD$$

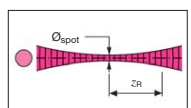
Example:

| | |
|--------------------------|--|
| Fiber collimator | $f' = 4.5 \text{ mm}$ |
| Micro-focus lens | $f' = 11 \text{ mm}$ |
| Mode field \varnothing | $MFD = 4.3 \mu\text{m}$ |
| Spot diameter | $\varnothing_{\text{spot}} = 10.5 \mu\text{m}$ |

| | |
|--------------------------|--------------------------|
| Singlemode fiber NA 0.11 | |
| Wavelength λ | Mode field \varnothing |
| 480 nm | 3.4 μm |
| 630 nm | 4.3 μm |
| 780 nm | 5.7 μm |
| 980 nm | 6.2 μm |

Adequate consideration of the mode field diameter wavelength dependency (see examples and table) should be made, as a small change in focus alters the focus position and the spot size.

Figure 10: Rayleigh Range



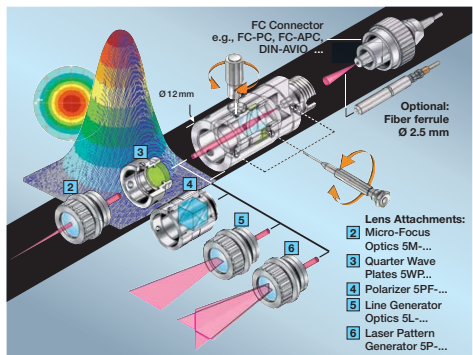
The **Rayleigh range** is the depth of sharpness of the laser focus retaining a Gaussian intensity distribution. Within the range $2 \cdot z_R$, the beam waist increases by a factor of 1.41.

$$2 \cdot z_R = \frac{2 \cdot \pi \cdot \varnothing_{\text{spot}}^2}{\lambda \cdot 4}$$

$$z_R \equiv \frac{\pi 10.5^2 \mu\text{m}^2}{129 \mu\text{m}} = 129 \mu\text{m}$$

Schäffer + Kirchhoff

Fiber Collimators 60FC....



- Focal lengths from 2.7 to 20 mm (for Fiber Collimators with a longer focal length see 60FC-L..., Table 6)
 - Beam diameters from 0.5-3.6 mm ($1/e^2$ -value of Gaussian intensity distribution)
 - Amagnetic collimators made from Titanium on request
 - Front connector accepts micro-focus optics of the series 5M-... and polarizers of the series 5P-...
 - Numerous AR coatings for individual ranges covering 370 to 2300 nm
 - Infrared optics made of Chalcogenide glass for wavelengths >1000 nm (see Table 1, column 5, lens designed for $\lambda = 2.5 \mu\text{m}$)
 - Integral focussing • Compact Ø 12 mm housing
- A = asphere**
The glass bi-Aspheric lens type A shows a fine structure (concentric rings) in the projected Gaussian beam profile, but not in the focus. This lens type is suitable for UH vacuum applications.
- M = laser monochromat or achromat**
These lenses are corrected for spherical aberration (monochromat) or additionally chromatic aberration- (achromat). Both exhibit an undisturbed Gaussian beam profile.
- RGBV = RGBV coupling lens (apochromat)**
Lenses of type RGBV are achromatically corrected RGBV coupling lenses designed for the simultaneous coupling of multiple wavelengths in the range 400 to 660 nm, see page 39.

| Table 1 Fiber Collimator 60FC.... with focal lengths 2.7-20 mm (housing Ø 12 mm) | | | | | | | | | | | | | | | | | | | | | |
|---|-------------------------------|---|------|------|------|------|-------|------|-------|------|------|------|------|------|--------|------|--------|------|------|------|------|
| row | curr. no | 1 | 2 | 3 | 4 | 5 | 6 | 7 | 8 | 9 | 10 | 11 | 12 | 13 | 14 ** | 15 | 16 | 17 | 18 | 19 | 20 |
| 1 | Lens type | A2.7 | A3.1 | M3.1 | M4 | A4 | A4.55 | M5 | A6.25 | A7.5 | A8 | M8 | A11 | M11 | RGBV11 | M12 | M12NIR | A15 | M15 | A18 | M20 |
| 2 | Focal length f' | 2.75 | 3.1 | 3.1 | 4 | 4 | 4.5 | 5.1 | 6.16 | 7.5 | 8 | 8.1 | 11 | 11 | 11 | 12 | 12 | 15.4 | 18.4 | 20.1 | |
| 3 | Numerical aperture NA | 0.55 | 0.68 | 0.25 | 0.25 | 0.56 | 0.42 | 0.25 | 0.24 | 0.3 | 0.3 | 0.16 | 0.25 | 0.23 | 0.2 | 0.23 | 0.22 | 0.16 | 0.18 | 0.15 | 0.16 |
| 4 | Clear apert. max. [mm] | 3.6 | 5 | 6.4 | 2 | 5 | 3.7 | 2.5 | 3.7 | 4.5 | 4.9 | 2.5 | 5.5 | 5.5 | 6.5 | 7.5 | 5.5 | 5.5 | 5.5 | 6.5 | |
| 5 | Coll. beam [mm ²] | 0.49 | 0.56 | 0.56 | 0.72 | 0.72 | 0.81 | 0.92 | 1.11 | 1.35 | 1.44 | 1.45 | 1.97 | 1.97 | 1.97 | 2.15 | 2.15 | 2.76 | 2.69 | 3.30 | 3.61 |
| 6 | Beam diverg. [mrad] | 0.86 | 0.77 | 0.77 | 0.59 | 0.59 | 0.53 | 0.47 | 0.39 | 0.32 | 0.3 | 0.29 | 0.22 | 0.22 | 0.22 | 0.2 | 0.2 | 0.15 | 0.16 | 0.13 | 0.12 |
| 7 | Correction - achrom. | | x | x | | x | | x | | x | | x | | x | RGBV | x | x | x | x | | |
| Spectral range Code no. of AR coating * Calculated for $\lambda = 670 \text{ nm}$ and NA=0.11 ** For the RGBV lens see page 29 *** IR chalcogenide lens | | | | | | | | | | | | | | | | | | | | | |
| 8 | 350 - 460 nm | 52 | | 52 | | 52 | | 52 | | 52 | | 52 | | 52 | | 52 | | 52 | | | |
| 9 | 400 - 600 nm | 01 | 01 | 01 | | 01 | 01 | 01 | 01 | 01 | 01 | 01 | 01 | 01 | 01 | 01 | 01 | 01 | 01 | | |
| 10 | 600 - 1050 nm | 02 | 02 | 02 | | 02 | 02 | 02 | 02 | 02 | 02 | 02 | 02 | 02 | 02 | 02 | 02 | 02 | 02 | | |
| 11 | 1050 - 1550 nm | 03 | 03 | 03 | | 03 | 03 | 03 | 03 | 03 | 03 | 03 | 03 | 03 | 03 | 03 | 03 | 03 | 03 | | |
| 12 | 1300 - 1750 nm | 45 | 45 | 45 | | | 45 | | 45 | | 45 | | 45 | | 45 | | 45 | | 45 | | |
| 13 | 1750 - 2300 nm | 09 | 09 | | | 09 | | 09 | | 09 | | 09 | | 09 | | 09 | | 09 | | | |
| 14 | 390 - 670 nm | 33 | | | | | 33 | | 33 | | 33 | | 33 | | 33 | | 33 | | | | |
| 15 | 630 - 980 nm | 10 | | | | | 10 | | 10 | | 10 | | 10 | | 10 | | 10 | | 10 | | |
| 16 | 980 - 1550 nm | 08 | | | | | 08 | | 08 | | 08 | | 08 | | 08 | | 08 | | 08 | | |
| 17 | 420 - 700 nm | 26 | | | | | | | | | | | | | | 26 | | | | | |
| 18 | 750 - 1550 nm | 37 | | | | | | | | | | | | | | 37 | | | | | |
| 19 | 400 - 670 nm | 51 | | 51 | | | | | | | | | | | 47 | | | | | | |
| 20 | 520 - 830 nm | | | | | | | | | | | | | | 18 | | | | | | |
| 21 | 650 - 1150 nm | 07 | | | | | | | | | | | | | 07 | | | | | | |
| 22 | 450 - 700 nm | 04 | | | | 04 | | | | | | | | | | | | | | | |
| 23 | 1750 - 3000 nm | 64 | | | | | 64** | | | | | | | | | | | | | | |
| 24 | for UH vacuum | | x | x | x | x | x | x | x | x | x | x | x | x | x | x | x | x | | | |
| 25 | Dimensions | [1] | | | | | | | | | | | | | | | | | | | |

Table 1.1 Beam divergence: beam expansion due to diffraction. Beam diameter as a function of the working distance A.

| Collimated | Lens type | A2.7 | A3 | M3.1 | M4 | A4 | A4.55 | M5 | A6.25 | A7.5 | A8 | M8 | A11 | M11 | RGBV11 | M12 | M12NIR | A15 | M15 | A18 | M20 |
|------------|-----------------|-------|------|------|------|------|-------|------|-------|------|------|------|------|-----|--------|-----|--------|------|------|------|-----|
| | Focal length f' | 2.75 | 3.1 | 3.1 | 4 | 4 | 4.5 | 5.1 | 6.16 | 7.5 | 8 | 8.1 | 11 | 11 | 11 | 12 | 12 | 15.4 | 18.4 | 20.1 | |
| 29 | Distance | 0.5 m | 1.00 | 0.95 | 0.95 | 0.93 | - | 0.97 | 1.03 | 1.17 | 1.38 | 1.47 | 1.48 | 2.0 | 2.0 | 2.2 | 2.7 | 2.8 | 2.7 | 3.3 | 3.6 |
| 30 | A | 1.0 m | 1.80 | 1.63 | 1.63 | 1.39 | - | 1.33 | 1.31 | 1.35 | 1.49 | 1.55 | 1.6 | 2.0 | 2.0 | 2.2 | 2.7 | 2.7 | 3.3 | 3.6 | |
| 31 | | 5.0 m | 8.6 | 7.7 | 7.7 | 6.0 | - | 5.3 | 4.7 | 4.0 | 3.4 | 3.3 | 2.9 | 2.9 | 2.9 | 3.1 | 3.2 | 3.1 | 3.5 | 3.8 | |

Table 1.2 Diameter of focussed beam as a function of distance A. For spot $\Omega < 100 \mu\text{m}$, micro-focus optics are used.

| Focused | Lens type | A2.7 | A3 | M3.1 | M4 | A4 | A4.55 | M5 | A6.25 | A7.5 | A8 | M8 | A11 | M11 | RGBV11 | M12 | M12NIR | A15 | M15 | A18 | M20 | |
|---------|-----------------|-------|------|------|------|------|-------|------|-------|------|------|------|------|------|--------|------|--------|------|------|------|------|------|
| | Focal length f' | 2.75 | 3.1 | 3.1 | 4 | 4 | 4.5 | 5.1 | 6.16 | 7.5 | 8 | 8.1 | 11 | 11 | 11 | 12 | 12 | 15.4 | 18.4 | 20.1 | | |
| 34 | Distance | 0.5 m | 0.86 | 0.77 | 0.77 | 0.59 | - | 0.53 | 0.47 | 0.39 | 0.32 | 0.30 | 0.29 | 0.22 | 0.22 | 0.22 | 0.20 | 0.20 | 0.15 | 0.16 | 0.13 | 0.12 |
| 35 | A | 1.0 m | 1.73 | 1.53 | 1.53 | 1.19 | - | 1.06 | 0.93 | 0.77 | 0.63 | 0.59 | 0.43 | 0.43 | 0.40 | 0.40 | 0.40 | 0.31 | 0.32 | 0.26 | 0.24 | |
| 36 | | 5.0 m | - | - | - | - | - | 4.66 | 3.86 | 3.17 | 2.97 | 2.93 | 2.16 | 2.16 | 1.98 | 1.98 | 1.54 | 1.58 | 1.29 | 1.18 | | |

Table 1.3 Pilot beam: approx. constant beam Ω across entire working range A, obtainable by fine adjustment. Position of beam waist at A2.

| Working range A | BW | Tab. 1 No. 15: M12 / f' = 12 | | | Beam diameter [mm] | | | Tab. 1 No. 20: M20 / f' = 20 | | |
|-----------------|----|------------------------------|----------|----------|--------------------|------|----------|------------------------------|--------|------|
| | | at A | at coll. | at waist | A2 [m] | at A | at coll. | at waist | A2 [m] | |
| 37 | | 0.5 m | 2.18 | 2.17 | 0.25 | 3.61 | 3.61 | 3.61 | 0.25 | |
| 38 | | 1.0 m | 2.18 | 2.17 | 0.50 | 3.61 | 3.61 | 3.60 | 0.50 | |
| 39 | | 2.0 m | 2.18 | 2.14 | 1.00 | 3.61 | 3.61 | 3.60 | 1.00 | |
| 40 | | 5.0 m | 2.24 | 2.18 | 1.90 | 3.27 | 3.61 | 3.56 | 2.50 | |
| 41 | | 10.0 m | 4.07 | 2.18 | 2.09 | 1.50 | 3.61 | 3.61 | 3.38 | 5.00 |
| 42 | | 20.0 m | 7.93 | 2.18 | 2.09 | 0.80 | 5.06 | 3.61 | 3.37 | 5.10 |
| 43 | | 50.0 m | 19.7 | 2.18 | 2.09 | 0.30 | 11.96 | 3.61 | 3.37 | 2.30 |

Fiber collimators 60FC-4-M5-33 Order Code

AR coating (see Table 1, row 8-23)

Lens type

A = asphere
(see Table 1, row 1)

M = monochromat or achromat

Fiber connection: 4 = FC-APC connection (8°-polish)

0 = FC-PC connection (0°-polish)

Option:

Add **T1** for titanium construction (amagnetic):

Exemplary Order Code : 60FC-4-M5-33-T1

Add **SS** for steel construction:

Exemplary Order Code : 60FC-4-M5-33-SS



Fiber Collimators 60FC-...

Material Options:

Nickel Silver, Titanium and Steel

Standard fiber collimators are made from nickel-silver with a coefficient of thermal expansion of about $19.5 \times 10^{-6} \text{ K}$ and have been proven to be very stable. Schäffer+Kirchhoff now offers to additional material options for the fiber collimator 60FC:

Nickel Silver Fiber Collimators (Standard)

- Exemplary Order Code: 60FC-4-M5-33

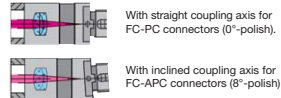
Titanium Fiber Collimators 60FC-...Ti

- with following additional features:
- low coefficient of expansion (similar to optical glass)
 - magnetic (relative material permeability near 1, for more details see page 15)
 - small weight
 - high pointing stability
 - Exemplary Order Code: 60FC-4-M5-33-Ti

Steel Laser Fiber Collimators 60FC-...SS

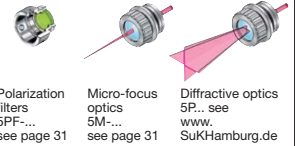
- with following additional features:
- low coefficient of expansion (similar to optical glass)
 - high pointing stability
 - Exemplary Order Code: 60FC-4-M5-33-SS

Fiber collimator 60FC-...



The fiber connection has an axial limit stop to ensure a constant focus position, particularly for fiber collimators with an inclined coupling axis.
Optional connector types: ST, DIN AVIO and F-SMA

Accessories

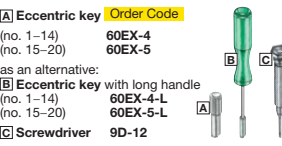


Dimensions



Adapters for mirror mounts Ø 25 mm, Ø 25.4 mm, and with system mount Ø 19.5 mm, see page 31.
Fiber collimators 60FC-A19.5..., with system mount Ø 19.5 mm (to fit directly into the "multicube" system), see page 46.

Adjustment Tools



Micro-Focus Optics 5M-...

| | Micro-Focus Optics 5M-... for fiber collimators in Table 1 with outer Ø 12 mm | | | | | | | | | | | | | | | | | | | | | |
|-----------|---|---|------|------|------|------|------|-----|------|------|------|-----|------|------|------|------|------|------|------|-------|-------|------|
| curr. no. | 1 | 2 | 3 | 4 | 5 | 6 | 7 | 8 | 9 | 10 | 11 | 12 | 13 | 14 | 15 | 16 | 17 | 18 | 19 | 20 | 21 | |
| 1 | Lens type | A2.7 | A3.1 | A4 | A4 | A4.5 | A6.2 | A8 | A11 | A15 | A18 | M12 | M20 | M25 | M30 | M40 | M50 | M60 | S50 | S88 | S150 | S325 |
| 2 | Focal length f' | 2.7 | 3.1 | 4 | 4 | 4.5 | 6.2 | 8 | 11 | 15 | 18 | 12 | 20 | 25 | 30 | 40 | 50 | 60 | 50 | 88 | 150 | 325 |
| 3 | Numerical aperture NA | 0.55 | 0.68 | 0.58 | 0.56 | 0.41 | 0.24 | 0.5 | 0.25 | 0.16 | 0.15 | 0.2 | 0.13 | 0.11 | 0.09 | 0.06 | 0.05 | 0.05 | 0.03 | 0.018 | 0.009 | |
| 4 | Clear aperture max. [mm] | 3.6 | 5 | 4.6 | 5 | 5 | 5 | 5 | 5 | 5 | 5 | 5 | 5 | 5 | 5 | 5 | 5 | 5 | 5 | 5 | 5 | 5 |
| | Spectral range | Code no. of AR coating ... IR chalcogenide lens | | | | | | | | | | | | | | | | | | | | |
| 5 | 350 - 460 nm | 52 | 52 | 52 | | | | | 52 | | | | | | | | | | | | | |
| 6 | 400 - 600 nm | 01 | 01 | 01 | 01 | 01 | 01 | 01 | 01 | 01 | 01 | 01 | 01 | 01 | 01 | 01 | 01 | 01 | 01 | 01 | 01 | 01 |
| 7 | 600 - 1050 nm | 02 | 02 | 02 | 02 | 02 | 02 | 02 | 02 | 02 | 02 | 02 | 02 | 02 | 02 | 02 | 02 | 02 | 02 | 02 | 02 | 02 |
| 8 | 1050 - 1550 nm | 03 | 03 | 03 | 03 | 03 | 03 | 03 | 03 | 03 | 03 | 03 | 03 | 03 | 03 | 03 | 03 | 03 | 03 | 03 | 03 | 03 |
| 9 | 1300 - 1750 nm | 45 | 45 | | | | | 45 | | 45 | | 45 | | | | | | | | | | |
| 10 | 1750 - 2300 nm | 09 | | | | | | 09 | 09 | 09 | 09 | 09 | 09 | 09 | 09 | 09 | 09 | 09 | 09 | 09 | 09 | 09 |
| 11 | 390 - 670 nm | 33 | | | | | | | | | | | | | | | | | 33 | 33 | 33 | 33 |
| 12 | 630 - 980 nm | 10/05 | | | | | | | | | | | | | | | | | 10 | 10 | 05 | 05 |
| 13 | 980 - 1550 nm | 08 | | | | | | | | | | | | | | | | | 08 | 08 | 08 | 08 |
| 14 | 420 - 700 nm | 26 | | | | | | | | | | | | | | | | | 26 | 26 | 26 | 26 |
| 15 | 750 - 1550 nm | 37 | | | | | | | | | | | | | | | | | 37 | 37 | 37 | 37 |
| 16 | 1750 - 3000 nm | 64 | | | | | | | | | | | | | | | | | | | | |
| 17 | Design | S | S | S | S | S | S | S | S | S | S | S | S | S | S | S | S | S | S | S | S | |
| 18 | Infrared lens | | x | | | | | | | | | | | | | | | | | | | |
| 19 | Dimensional drawing | □ | □ | □ | □ | □ | □ | □ | □ | □ | □ | □ | □ | □ | □ | □ | □ | □ | □ | □ | □ | □ |
| 20 | Length B [mm] | 4.75 | 4.4 | 4.6 | 4.6 | 4.5 | 4.5 | 4.5 | 4.5 | 4.5 | 4.5 | 4.5 | 4.5 | 4.8 | 4.4 | 4.5 | 4.5 | 4.4 | 4.5 | 4.9 | 4.9 | 4.9 |
| 21 | Work distance A [mm] | 1.26 | 1.6 | 2.2 | 2.2 | 2.37 | 3 | 5.4 | 7.4 | 13.4 | 16.5 | 9.9 | 17.9 | 22.8 | 26.7 | 36.7 | 48.2 | 58 | 48.7 | 82.4 | 149 | 320 |
| 22 | Suitable for UH vacuum | x | x | x | x | x | x | x | x | x | x | x | x | x | x | x | x | x | x | x | x | |

To a good approximation, the micro spot size is given by:

$$\Omega_{\text{spot}} \approx \frac{f' \text{micro-focus}}{f' \text{fiber collimator}} MFD$$
 with MFD varying with wavelength according to the adjacent table.

| | | |
|---------------|----------------------|-----|
| Fiber NA 0.11 | Wavelength λ | MFD |
| 480 nm | 3.4 μm | |
| 630 nm | 4.3 μm | |
| 780 nm | 5.7 μm | |
| 980 nm | 6.2 μm | |

The Rayleigh range is the depth of sharpness of laser focus that retains a Gaussian intensity distribution.

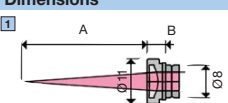
The beam waist increases by a factor of 1.41 for the range $2\zeta_0$.

$$2\zeta_0 = \frac{2\pi\Omega_{\text{spot}}^2}{\lambda \cdot 4}$$

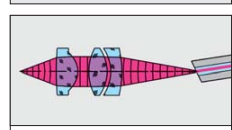
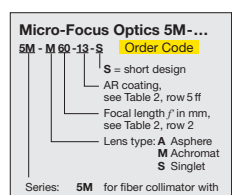
λ = wavelength in μm

Ω_{spot} = beam waist in μm

Dimensions

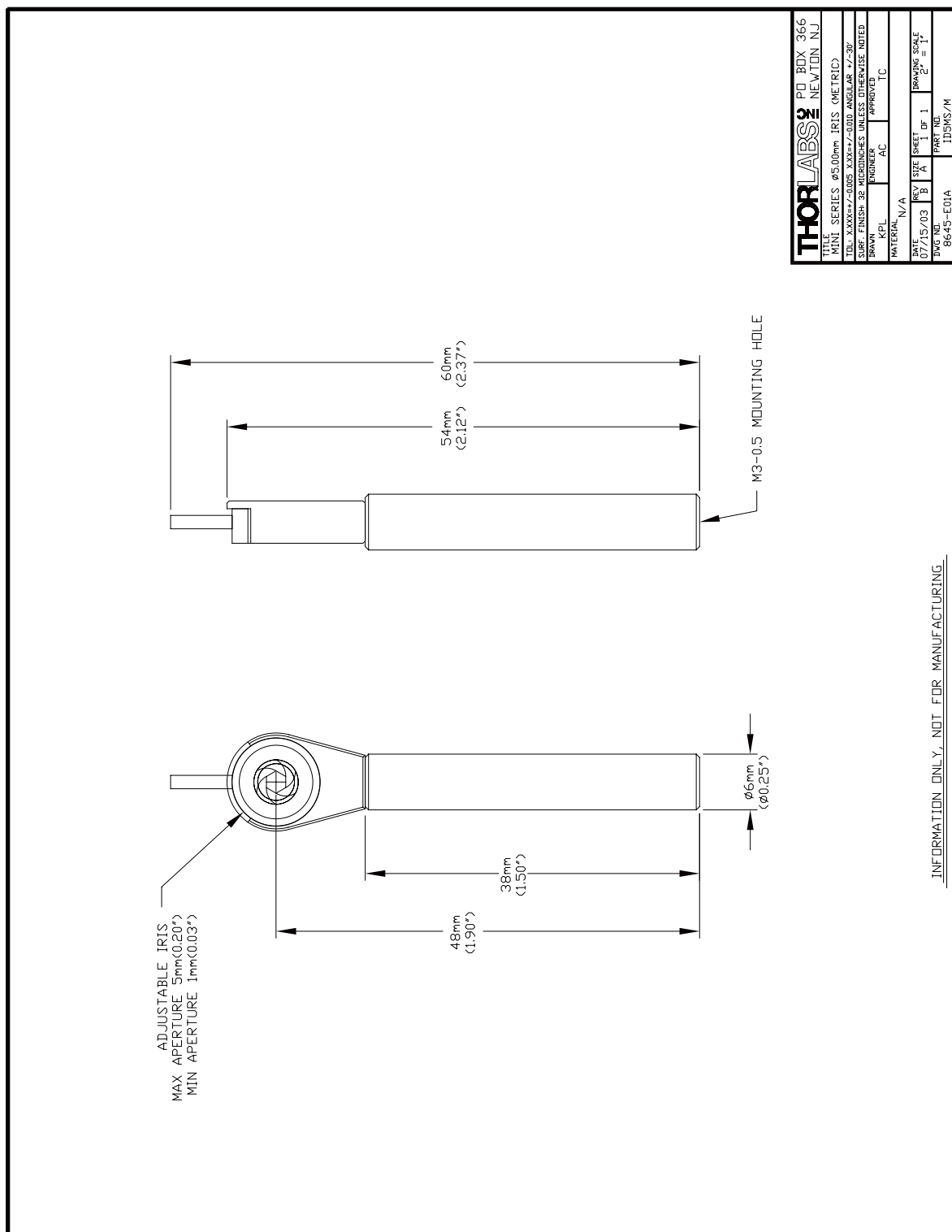


More information about micro-focus optics 13M-... and 25M-... is on page 33 or available upon request

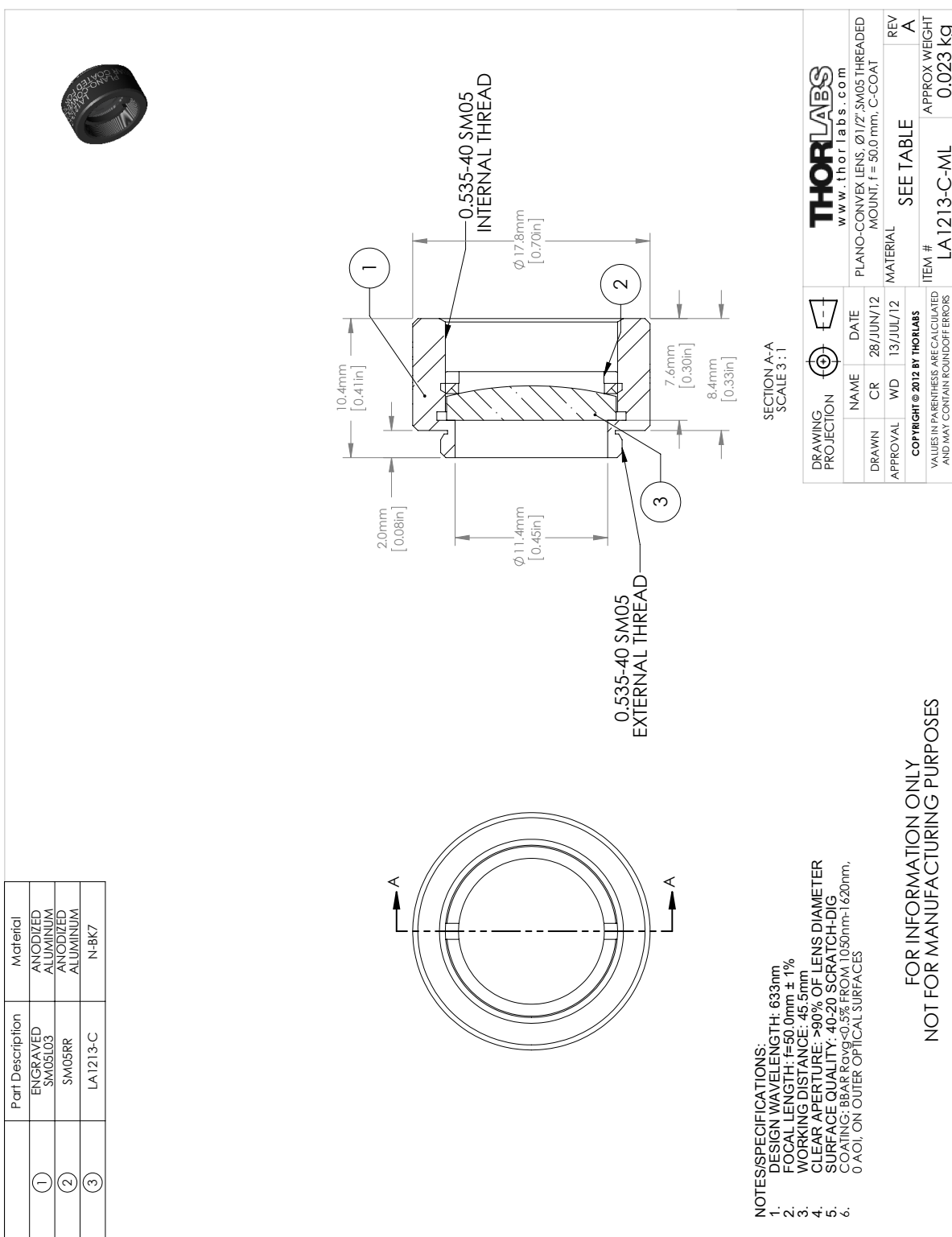


Optical path of a fiber collimator with attached micro-focus optics. Intensity distribution and beam shape are maintained.

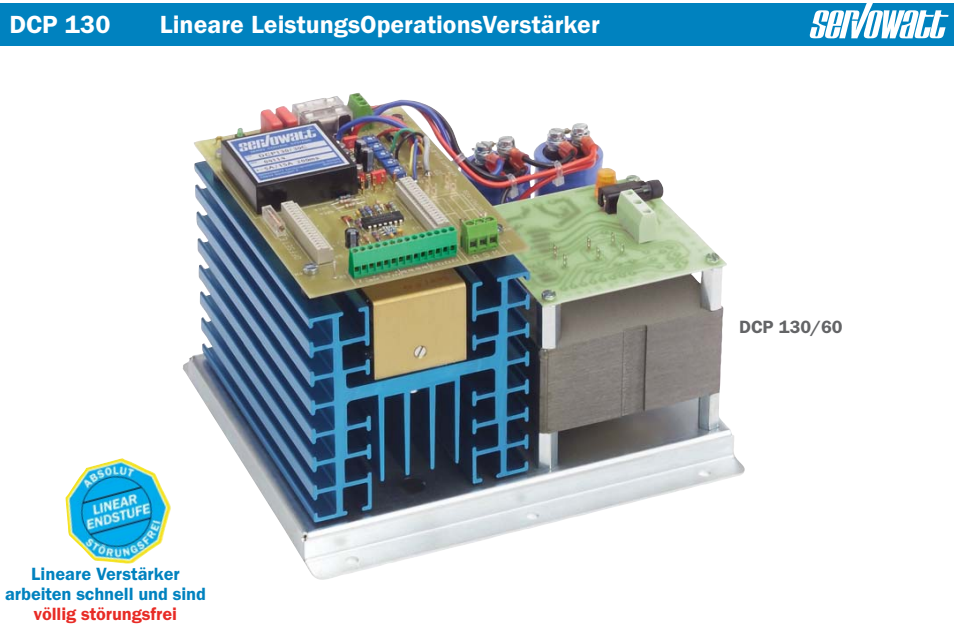
A.8 Thorlabs Iris ID5MS/M



A.9 Thorlabs Plano-convex Lens LA1213-C-ML



A.10 Servowatt Linear Power Operational Amplifier DCP130/60



DCP-Serie - Allgemeine Beschreibung

SERVOWATT

LeistungsOperationsVerstärker sind spezielle Baugruppen, die in einem Gerät die Eigenschaften von hochwertigen Operationsverstärkern mit einer Linearendstufe vereinen, die schnell, störungsfrei, extrem robust und dynamisch stabil arbeiten. Lineare Verstärker arbeiten auch bei hohen Leistungen **völlig störungsfrei**. Die Ausgangsspannung enthält daher keine störenden Signalkomponenten, Impulsnadeln, Harmonische oder Rauschen.

Alle Schaltungen, die bisher aus mehreren Stufen zusammengesetzt waren, können mit einer solchen Einheit phasenrein realisiert werden, wobei durch die hohe Stabilität auch komplexe Lasten zugelassen sind, ohne die üblichen Schwingneigungseffekte befürchten zu müssen. LOVs können nicht nur hochinduktive, sondern auch kapazitive Verbraucher ansteuern.

Die hohe interne Verstärkung bewirkt erstens eine sehr präzise Arbeitsweise, zweitens ergibt sich dadurch auch ein sehr niedrigermiger Ausgang bei Spannungsverstärkung und eine sehr hohe Quellenimpedanz bei Stromquellen. Fast die gesamte hohe interne Verstärkung in der Größenordnung von über 150 dB (ca. 50 Millionenfach) kann zurückgekoppelt werden.

Diese **präzise Ansteuerung für alle Arten von Lasten und Beschaltungen**, eignet sich bestens für Präzisionsanwendungen, wie z.B. für Meßaufbauten, Servozustellungen in Maschinen, die im µm-Bereich arbeiten, sowie extrem dynamische und genaue Motor- und Aktuator-Ansteuerungen.

Der Preis für diese Qualitäten ist der geringere Wirkungsgrad gegenüber getakteten (PWM= pulsweiten modulierten) 4Q-Reglern, d.h. die Endstufen erzeugen mehr Wärme als getaktete Regler. Um diesem Umstand entgegenzuwirken, sind die **Endstufen großzügig dimensioniert**, so daß diese auch im Dauerkurzschlußfall keinen Schaden nehmen.

Unser **bewährtes Design** zusammen mit besonders strengen Qualitätsnormen sowie eine 100-prozentige Eingangskontrolle der Leistungshalbleiter garantieren, daß diese Verstärker auch unter erschwerten Bedingungen zuverlässig arbeiten.

Leistungsspektrum der DCP-Serie



Übersicht DCP130-Reihe



Lineare Präzisions Leistungs-Operations-Verstärker. Standardversionen mit 130 Watt Ausgangsleistung

Die Leistungs-Operations-Verstärker der DCP 130-Reihe beinhaltet auf einer Chassisgrundfläche von 220mm x 200 mm eine Endstufe und das dazugehörige Hauptnetzteil mit einem Einphasen-Netztransistor für 230 Volt.

Ausgangsdaten (* bevorzugte Standardversionen)

| Ausgangsspannung (Voreingestellte Standardwerte) | | | | **Spitzenstromeinstellungen | |
|--|------------------------------|--------------------------------|-------------------|----------------------------------|-----------------------------------|
| Typ | Ausgangsspannung im Leerlauf | Ausgangsspannung bei Nennstrom | Ausgangsnennstrom | B 4-fach $\tau = 40\text{ms}$ | C 3-fach $\tau = 160\text{ms}$ |
| DCP 130/30 * | + - 30 V | + - 25 V | + - 5,0 A | 20 A | 15 A |
| DCP 130/42 | + - 42 V | + - 35 V | + - 3,0 A | 14,4 A | 10,8 A |
| DCP 130/60 * | + - 60 V | + - 50 V | + - 2,5 A | 10 A | 7,5 A |
| DCP 130/84 | + - 84 V | + - 71 V | + - 1,8 A | 7,2 A | 5,4 A |

****Der Dauernennstrom und der Spitzenstrom werden mit den Trimmern P1, P2, P3 und P4 werkseitig eingestellt. Die Spitzenstromdauer wird durch Auswahl der Kondensatoren C5 und C6 werkseitig eingestellt. Abweichende Einstellungen sind nach Absprache möglich, siehe auch Leistungsdiagramme.**

Eingangsdaten - Differenzverstärker E+ / E-

| Eingangsstufe von OpAmp | Standard | FET |
|---|----------------|---------------|
| Differenz-Eingangswiderstand | 100 M Ω | 10^{12} Ohm |
| Eingangsruhestrom (input bias current) | <2 nA | 5 pA |
| Eingangsruhestrom-Differenz | <1 nA | 1 pA |
| Offsetspannungs-Temperaturdrift | 0,3 μ V/K | 5 μ V/K |
| Gleichakteingangsspannungs-Unterdrückung / 10Hz | 135 dB | 95 dB |
| Eingangsoffsetstellbereich | +/-1 mV | +/- 10 mV |
| Eingangsräuschen Breitband, V = - 1000 | 7 μ Veff | 15 μ Veff |
| Maximale zulässige Eingangsspannung (E+ & E-) | +/-11 V | +/-11 V |
| Versorgungsspannungs-Durchgriff | -170 dB | -150 dB |

Die Eingangsoffsetspannung von ca. 1mV ist durch 25kOhm-Trimmer auf Null abgleichbar.

Transferdaten

| | | |
|---|----------------|----------------|
| Offene Verstärkung im Leerlauf (10 Hz) | 50.000.000 V/V | 10.000.000 V/V |
| Offene Verstärkung bei Last (80% Last, 10 Hz) | 30.000.000 V/V | 5.000.000 V/V |
| Regelgüte bei $V=-10$ somit besser als | 3.000.000 : 1 | 500.000 : 1 |
| Ausgangsspannung Slew-Rate (dUa/dt) | 12 V/ μ s | 12 V/ μ s |

Die 130 W Endstufe enthält Hochleistungstransistoren im Verlustleistungsgesamtwert von **1040 W**.

| | |
|--|-------------------|
| Arbeitstemperaturbereich bei Nennlast | -30 °C bis +45 °C |
| Maximale Kühlkörpertemperatur bei Nennlast | +90 °C |
| Gewicht netto 6,3kg, verpackt 8kg | |

Obige Daten gelten, wenn nicht anders angegeben, bei 25 Grad C und Nennanschlußspannungen. Änderungen vorbehalten.

Technische Vorteile von linearen Leistungsverstärkern:



servowatt

1. Verzerrungsfreie bipolare Regelung durch Null

Somit höchste dynamische Genauigkeit



Die präzise Führung von Strom und Spannung verlangt eine Regelung durch Null ohne Totzone und ohne Totzeit. Im abgebildeten Diagramm gehen Strom und Spannung stetig durch Null. Im Nullbereich bleibt der Verbraucher somit aktiv geführt.

2. Extrem schnelle Regelung

Nahezu verzögerungsfreies Reagieren in Regelkreisen



Hochdynamische Regelungen verlangen unverzögertes Reagieren von Spannungs- und Stromreglern. In diesem hochdynamischen Servosystem mit einem Moving-Coil DC-Motor beschleunigt dieser präzise von Null auf 2000 U/min in nur 2,7 ms!

3. Lineare Regelung

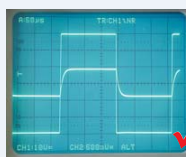
Unendliche Auflösung ohne Restwelligkeit



Bild A: gefiltertes PWM-Signal. Dynamische Regelvorgänge verlangen Verstärker ohne verzögernde Filter am Ausgang.
Bild B: Unendliche Auflösung und Präzision kann nur ein Linearverstärker erfüllen.

4. Absolute EMV-Störungsfreiheit

Keine Impulsstörungen, Oberwellen oder Rauschen im System



Diese linearen Leistungsendstufen arbeiten gleitend und sind daher völlig störungsfrei. Benachbarte Systeme werden nicht mit fremden Signalkomponenten, Impulsnadeln, harmonische Oberwellen oder Rauschen gestört.

5. Kurzschlußfeste Endstufen

Vorbildliche Zuverlässigkeit für anspruchsvolle Applikationen



Transistoren mit bis zu dem 8-fachen (!) Verlustleistungsgesamtwert garantieren hohe Zuverlässigkeit der Endstufen. Unser 4-Quadranten-Betrieb verlangt den Kurzschlußfall als Dauerbetrieb.

6. Hohe Leistungsbandbreite

Standardgeräte typisch mit 25kHz Sondergeräte bis 500kHz



Realtime-Regelungen verlangen eine hohe Leistungsbandbreite, gleichbedeutend mit einer hohen Spannungsänderungsgeschwindigkeit der Endstufe (Slew-Rate). Foto Frequenz 55kHz, Slew-Rate +/- 20V/µs Ausgang +/-30V / 4A

DCP130/30 Beschreibung (Beispiel gilt analog für alle Modelle) 

Als Beispiel: DCP130/30 ist ein universeller LeistungsOperations-Verstärker mit einer Ausgangsspannung von +-25 Volt gegen Masse, einem Dauer-Ausgangsstrom von +-5 A und Spitzen-Ausgangsstrom von +-10 bis max. +-20 A.

Folgende Eigenschaften sind kennzeichnend:

Hochwertige Eingangsstufe

ermöglicht das Verarbeiten von kleinen Spannungen und Strömen direkt an der Differenzeingangsstufe. Diese kann wie alle Operationsverstärker invertierend oder nichtinvertierend, integrirend, summierend usw. beschaltet werden. D.h. es ist kein zusätzlicher Steuer-Vorverstärker erforderlich.

Kurzschlußfeste Ausgangsstufe

ermöglicht die Endstufentypen A die Entnahme des max. Ausgangsstromes ohne zeitliche Begrenzung, jedoch ohne Spitzenstrom. Darüber hinaus liefert sie, je nach Endstufentypen, Type B mit 4-fachem Spitzenstrom über 40ms oder Type C mit 3-fachem Spitzenstrom über eine Zeitkonstante von 160ms. Auch andere Werte sind nach Absprache möglich.

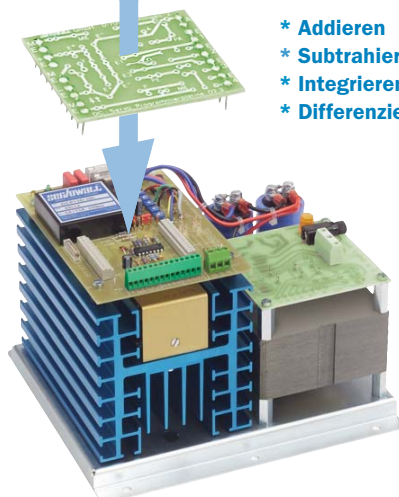
Stromversorgung:

Netzanschluss 230V wird angezeigt durch die orange Kontrollleuchte. Die Versorgung am Verstärker mit +-35V wird durch 2 grüne LED-Anzeigen sichtbar gemacht.

Fällt eine der UB- / UB+Sicherungen aus, so erlischt die entsprechende Anzeige. An der Netzplatine ist durch verschiedene Beschaltungs möglichkeiten die Entnahme von einer oder mehreren stabilisierten, potenti alfreien Spannungen möglich. Sie dienen zur Versorgung von verschiedenen Verbrauchern kleinerer Leistungen wie z.B. Sollwertgeber, Umsetzer, Überwachungen, Inkrementalgeber usw.

Mit der  **Beschaltung** analog rechnen:

- * Addieren
- * Subtrahieren
- * Integrieren
- * Differenzieren



Programmierplatine

erlaubt durch einfaches Umstecken eine schnelle Umprogrammierung der Verstärkerfunktion. Auf dieser Platine sind alle Eingänge E1, E2, E3, E4, E+, E-, A = Ausgang, ME = Masse Eingang eindeutig gekennzeichnet. Auf diesen Platinen werden alle passiven Beschaltungs-Bauelemente eingelötet.

In bestimmten Anwendungen sind Trimmer erforderlich, um z.B. die Verstärkung etc. anzupassen. Auch hierfür sind entsprechende Lötzellen vorgesehen. Platine 02.5 dient für allgemeine Zwecke, für Servo-anwendungen, Stromquellen usw. Der Verstärker wird normalerweise unbeschaltet geliefert.

Sonderausgang S

dient zur möglichen Stromrückführung. In diesem Fall werden an den Lötstützpunkten S und M niederohmige Widerstände eingelötet (Shunts) und die Last nicht gegen Masse, sondern gegen S geschaltet. Für die genaueste Stromrückführung in 4-Drahttechnik (mit 4-Pol-Meßshunts) werden S+ an E3 und S- an E4 verbunden.

Über denselben Sonderausgang S kann auch der Ausgang A über eine Sicherung FA zusätzlich abgesichert werden (Sicherungshalter ist vorgesehen). Dies ist dann von Bedeutung, wenn eine empfindliche Last unter keinen Umständen durch eine Störung oder bei einer Inbetriebnahme beschädigt werden darf.

Weitere Vorverstärkermodule



Sonderausführungen sind lieferbar für eine Vielfalt von Anwendungen: Spezielle Differenzeingangsstufen z.B. mit garantierter Drift kleiner 50 nV/ °C, mit FET's und Eingangsströmen kleiner 50 pA oder mit größerer Gleichtakt-Eingangsspannung sind möglich. Es sind auch besondere Versionen mit höherer Slew-Rate bis 50 V/µs verfügbar.

DCP 130 - Reihe **Beschreibung** (Beispiel gilt analog für alle Modelle)



Ausgangsstrom-Begrenzungen

Diese funktionieren statisch und dynamisch. Für kurze Beschleunigungs- und Bremsphasen bei Strombegrenzungsart C kann ein Impulstrom in dreifacher Höhe für die vorgegebene maximale Zeit von 160 ms fließen. Strombegrenzungsart B lässt einen 4-fachen Spitzenstrom für die Zeit von 12 ms fließen.

Danach klingt der Strom wieder auf seinen Nennwert ab. Die Strombegrenzungen werden mit zwei roten Leuchtdioden LED's angezeigt. Dauer- und Spitzentströme können für beide Polaritäten verschieden eingestellt sein. Andere Werte für Spitzentströme und Zeitdauer sind möglich.



Programmierplatine

Auf der Programmierplatine sind für E- und E+ Plätze für zwei antiparallel geschaltete Schutzdioden nach Masse ME vorgesehen. Bei invertierenden Schaltungen liegt die steuernde Eingangsspannung an E- fast auf Nullpotential. Beide Dioden begrenzen die Eingangsspannung auf ca. + - 600 mV. Wichtig bei auftretenden Störspannungen im Sollwerteingang! Für kleinere Eingangskapazität kann man auch schnellere Dioden antiserial verwenden und 4 von diesen in Serie/Parallel schalten. Auf der Programmierplatine sind zusätzlich für den Schutz von E+ zwei antiserial geschaltete Zener dioden nach Masse ME vorgesehen und vor dem Zenerdiopdenpärchen einen geeigneten Schutzwiderstand vorzuschalten.

Die Gleichtakt-Eingangsspannung (UE+ und UE-) sollte niemals den Bereich von + - 11 V überschreiten, da sonst mit unerwünschten Effekten zu rechnen ist.

Alle Geräte sind, ausreichende Kühlung vorausgesetzt, dauerkurzschlußfest ausgelegt.
Die eingestellten Werte für die Strombegrenzung werden bei Auslieferung versiegelt.(Garantie!)

Sicherungsfeld für Versorgung

Zu den 2 Sicherungen leuchten die entsprechenden grünen LEDs.

**Meßshunts, = Meßwiderstände
für die Stromerfassung**

für maximal $4 \times 2W = 8$ Watt
2 mal seriell, 2 mal parallel



für maximal $2 \times 5\text{W} = \mathbf{10\text{ Watt}}$,
2 mal parallel



für maximal $4 \times 5\text{W} = \mathbf{20\text{ Watt}}$
2 mal seriell, 2 mal parallel



Ausgangssicherung über Ausgang S

Es besteht die Möglichkeit, den Verstärker über den Ausgang S zusätzlich zur elektronischen Strombegrenzung mit einer Ausgangssicherung (Feinsicherung der Größe 5mm x 20mm oder 6,3mm x 32mm) auszurüsten. Diese Sicherung kann eine beliebige Charakteristik haben und somit nach Kundenvorstellungen eine empfindliche Last vor Überlastung und Schaden bewahren. Bei ersten Inbetriebnahmen kann eine solche Sicherung auch vorübergehend extern in Serie geschaltet werden.

Boucherot - Glied

In manch hartrückigen Fällen hochfrequenter Schwingungen der Ausgangsspannung kann es erforderlich sein, zwischen Ausgang A und Masse-Ausgang MA ein bedämpfendes RC-Glied (Boucherot-Glied) zu schalten. Unterhalb der Platine ist dafür Platz vorhanden.

Lineare Verstärker arbeiten schnell und sind völlig **störungsfrei**. Die Ausgangsspannung enthält keine fremden Signalkomponenten, Impulsnadeln, Harmonische oder Rauschen.

DCP130/30 Inbetriebnahme (Beispiel gilt analog für alle Modelle)

servowatt

Anschluß, Inbetriebnahme und Überprüfung der Funktion am Beispiel von DCP130/30

Anschluß:

Gerät mit aufgesteckter, beschalteter Programmierplatine an das 230V Netz anschließen. Es leuchten eine gelbe Netzkontrolllampe auf der Netzplatine und zwei grüne +35VDC LEDs auf der Verstärkerplatine auf. Ist dies nicht der Fall, so sind die Sicherungen zu kontrollieren. Bei ersten Versuchen und Experimenten ist es ratsam, einen 230V-Regeltrafo zum langsamen Hochregeln der Netzspannung zu verwenden. Der Verstärker arbeitet bereits ab 1/2 der Netzspannung in allen Funktionen.

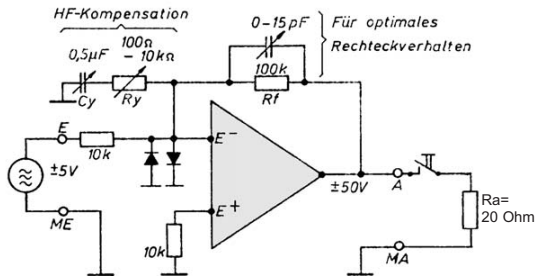
Spannungssteuerung:

Wird die Beschaltung zunächst für Prüfzwecke proportional gewählt (inverterend oder nichtinvertierend), so kann je nach gewählter Verstärkung mit einer entsprechenden bipolaren Steuerspannung der Verstärker angesteuert werden und die Ausgangsspannung mit einem Oszilloskop überprüft werden. Die Beträge von Eingangs- und Ausgangsspannung müssen von Null bis zur + -Vollaussteuerung streng proportional sein. Unbelastet beträgt die max. Ausgangsspannung ca. + -30V, bei Belastung mit + -5 A ca. + -25V. Wird dem Ausgang dauerhaft mehr als + -5 A entnommen, so wird die Strombegrenzung und die Ausgangsspannung je nach Last bis auf Null reduziert.

Strombegrenzung:

Sichert die Last und den Verstärker vor unzulässiger Überbelastung. Die entsprechenden Trimmer sind ab Werk eingestellt, versiegelt und dürfen nicht verändert werden (Garantie!). Eingebaute Leistungsreserven sind für Sicherheit und lange Lebensdauer notwendig und dürfen nicht vom Anwender nach Belieben ausgenutzt werden. Bei Type A begrenzt die Endstufe sofort auf den maximalen Dauerwert + -5A, bei Type B wird der Strom beim 4-fachen Wert begrenzt und klingt nach 40ms Zeitkonstante auf den Nennwert ab, bei Type C kann die Ausgangsstufe über 160 ms den 3-fachen Wert liefern.

Testschaltung



Offseteinstellung:

Nachdem die endgültige Beschaltung optimiert wurde, sollte als letztes eine Offseteinstellung vorgenommen werden. Dies sollte nach ca. 15 Minuten Einschaltzeit geschehen. Nach Definition ergibt ein Operationsverstärker die Ausgangsspannung Null bei Eingangsspannung Null.

Die durch die Eingangsruhestrome an Beschaltungswiderständen erzeugten Spannungen, sowie die verstärkereigene Offsetspannung, können mit dem Offsettrimmer intern kompensiert werden, so daß die Ausgangsspannung zu Null wird, wenn die beschalteten Eingänge an Eingangsmasse gelegt werden. Bei P-I-Beschaltung muß der Rückführkondensator mit einem hochohmigen Widerstand überbrückt werden, damit die Offseteinstellung erleichtert oder überhaupt ermöglicht wird. In der Standardausführung liegt der Offseteinstellbereich bezogen auf den Eingang E+/E- bei maximal + -1mV.

Verstärkungseinstellung:

Zur Einstellung der P- oder P-I-Verstärkung kann auf der Programmierplatine ein Trimmer (PA) eingelötet werden. Dies ist sehr hilfreich bei der Optimierung der Verstärkung im Servoregler zwischen hoher Verstärkung (Schwingneigung, steife Welle) und zu kleiner Verstärkung (große Laufruhe, aber nachgiebige Welle). Der Einstellbereich kann mit dem "Fußwiderstand" Rpa am Poti eingegrenzt werden. Verlustleistung am Trimmer beachten!

HF-Kompensation:

Ist der Verstärker überhaupt nicht oder nicht richtig kompensiert, so kann die Ausgangsspannung mit einer hochfrequenten Schwingung überlagert sein. Dies geschieht speziell bei kleinen Verstärkungen und muß vermieden werden, wenn der Verstärker programmgerecht arbeiten soll. Die entsprechenden Kompensationshinweise sind zu beachten.

Literatur:

Halbleiter-Schaltungstechnik, U. Tietze, Ch. Schenk
Springer Verlag, ISBN 3-540-15134-6

Professionelle Schaltungstechnik mit Operationsverstärkern
Horst Wupper, 1994 Franzis Verlag GmbH, ISBN 3-7723-6732-1

Schaltungs- & Formelsammlung für die Operationsverstärker-Anwendung, Prof.

Dipl.-Ing. Martin Zirpel, Franzis Verlag, ISBN 3-7723-6136-6 und 3-7723-6134-X

IC Op-Amp Cookbook, Walter G. Jung

Howard W.Sams & Co., Indianapolis 46268 USA, ISBN 0-672-22453-4

Umgang mit Operationsverstärkern, Fritz Bergtold,

Oldenbourg Verlag, ISBN 3-486-34001-8

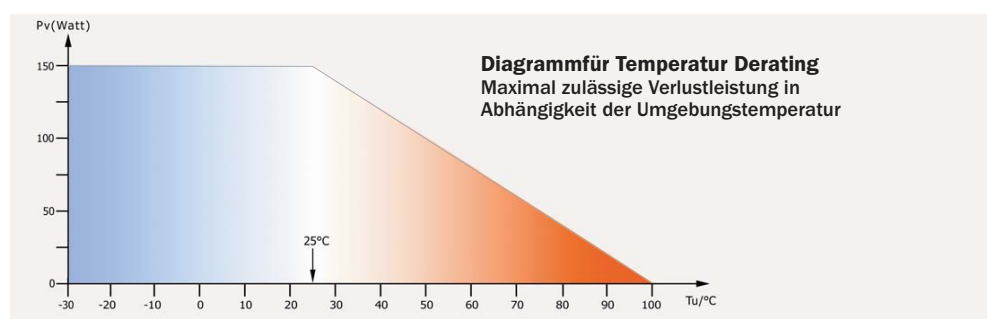
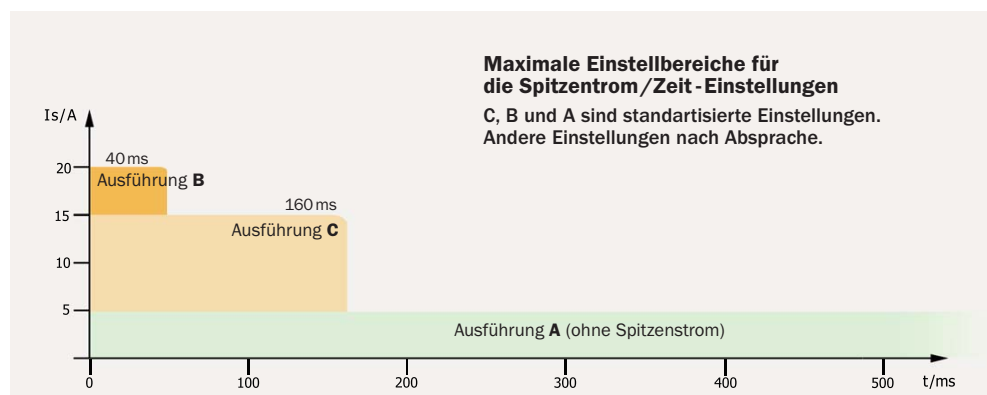
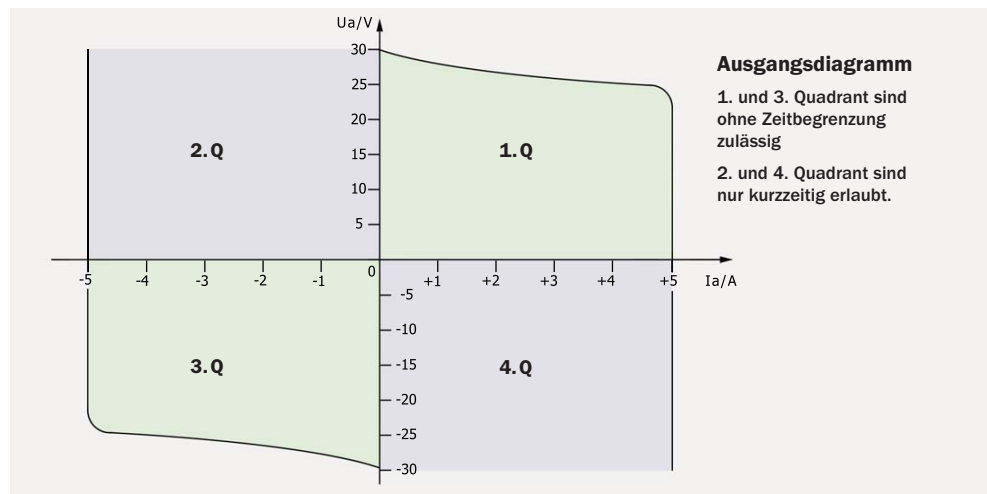
Operationsverstärker, Eigenschaften & Anwendungen, Hans-Jürgen Vahldiek

Teleskopos Verlag, ISBN 3-440-03745-2

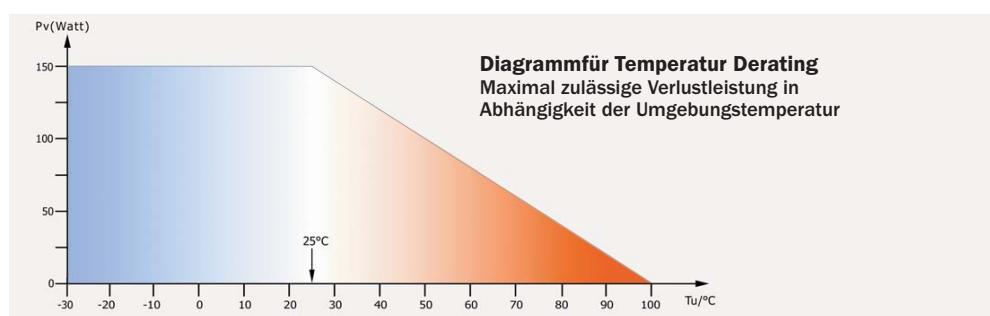
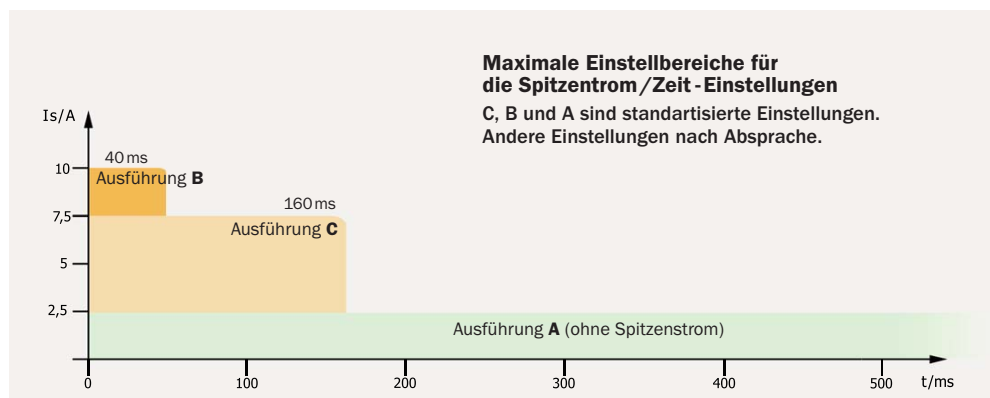
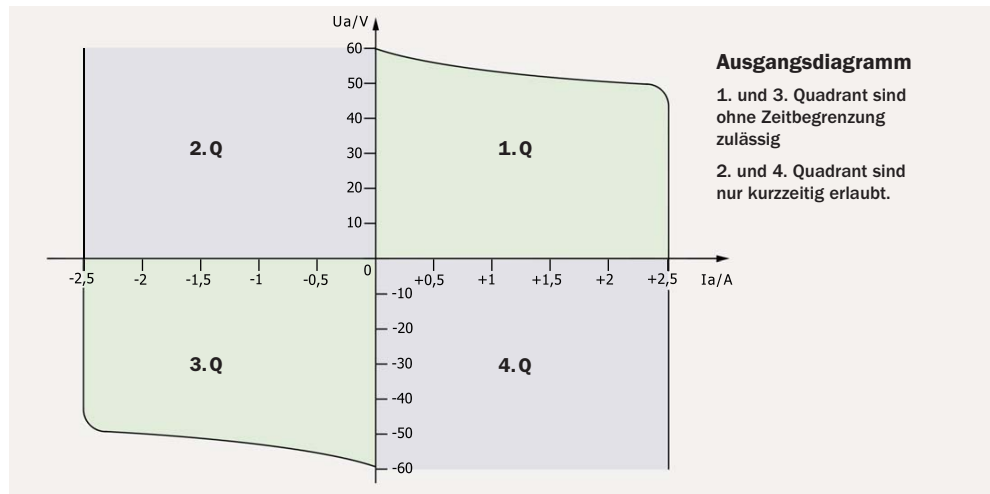
DCP 130/30

Leistungsdiagramme

servowatt

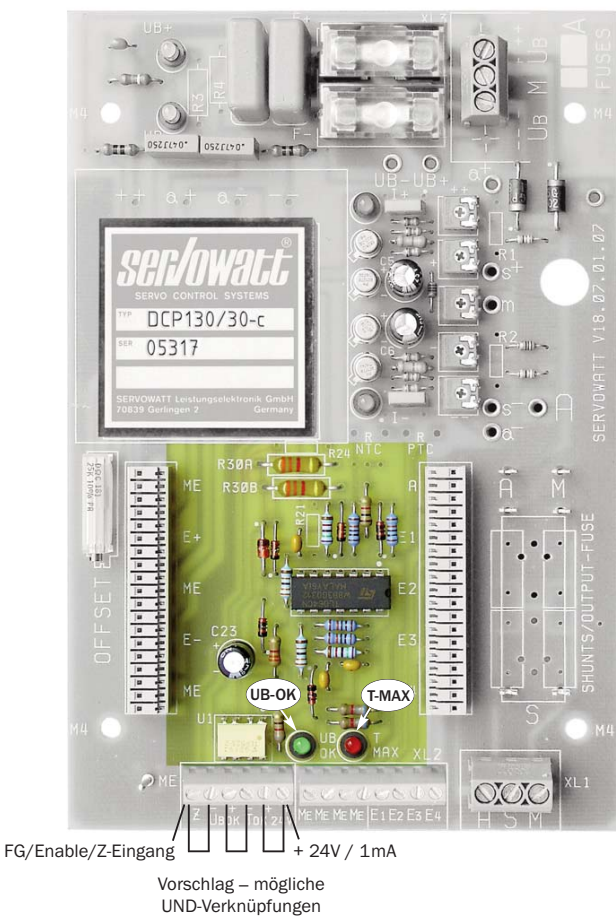


DCP 130/60 Leistungsdiagramme 



DCP 130-Reihe Überwachungsfunktionen (optional)

servowatt



**Daten der Optokopplerausgänge
U-OK und T-OK**

| | |
|--------------------------|--------|
| Maximaler Durchlaßstrom | 20 mA |
| Maximale Sperrspannung | 55 V |
| Maximale Verlustleistung | 100 mW |

Bitte Optokoppler-Maximalwerte beachten!

ENA= FG/Freigabe/Enable/Z-Eingang
Die Endstufe wird aktiviert durch Anlegen einer +24V-Steuerspannung an Z (Pin XL2.1) gegen Masse ME (Pin XL2.7 bis XL2.10). Die Schalt-schwelle liegt bei ca. +9 V. Die Endstufe wird mit Z-Spannung gleich Null stromlos geschaltet (Tristate-Zustand am Ausgang = hochohmig). Bei einem Servo kann man auf diese Weise die Welle frei durchdrehbar machen, z.B. zum Einrichten.

T-OK: Temperaturüberwachung

Steigt die Temperatur am Kühlkörper auf über ca. 90 Grad C, unterbricht der Optokoppler zwischen T-OK+(Pin XL2.5) und T-OK-(Pin XL2.4) und die rote LED T-MAX leuchtet auf. Diese Überwachungsfunktion ist gelatzt d.h. auch nach anschließendem Absinken der Kühlkörpertemperatur unter 90 Grad C bleibt der Optokoppler offen/hochohmig.

Erst nach Abschalten, Entladen der Hauptelkos (ca. 2 min.) und Wiedereinschalten der Hauptversorgungsspannung (Power-On-Reset) werden die Optokopplerkontakte T-OK wieder leitend.

Optional sind auf der Platine eine Unterspannungsüberwachung (UB-OK), und eine Temperaturüberwachung (T-OK) am Kühlkörper integriert. Jede dieser zwei Überwachungsfunktionen besitzt eine Leuchtdiode zur Anzeige und potentialfreie Optokoppler-ausgänge: UB-OK und T-OK.

**Ausgangsstrom-Begrenzungen
(serienmäßig)**

Diese funktionieren statisch und dynamisch. Für kurze Beschleunigungs- und Bremsphasen kann je nach Strombegrenzungsart C oder B ein Impulstrom in zwei- oder dreifacher Höhe für die vorgegebene maximale Zeit von 500 ms oder 200 ms fließen. Danach klingt der Strom wieder auf seinen Nennwert ab. Die Strombegrenzungen werden mit zwei roten Leuchtdioden LED I+ und LED I- angezeigt. Dauer- und Spitzenströme können für beide Polaritäten verschieden eingestellt sein. Andere Werte für Spitzenströme und Zeitdauer sind möglich. Alle Geräte sind, ausreichende Kühlung vorausgesetzt, dauerkurzschlußfest ausgelegt.

UB-OK: Unterspannungsüberwachung

Sinkt eine der beiden Hauptversorgungs- Spannungen UB+ oder UB- unter ca. 50%, unterbricht der Optokoppler zwischen UB-OK+(Pin XL2.3) und UB-OK-(Pin XL2.2). Die ansonsten grün leuchtende LED UB-OK erlischt. Beim Start/Anfahren muß die Hauptversorgungsspannung zumindest kurzzeitig ca. 75% der Leerlaufnennspannung erreichen (ca. 25 % Hysteresee, nicht gelatzt).

Beide potentialfreien Optokoppler-kontakte (NPN-Ausgänge) UB-OK und T-OK können miteinander und mit dem Z-Eingang in Reihe geschaltet werden (VerUNDen). Dafür steht an Pin XL2.6 die +24V-Hilfsversorgung (max. 1 mA) zur Verfügung. Diese Kontakte/Ausgänge sind im Rahmen der obigen technischen Daten frei beschaltbar. Für spannungssteuernde Verarbeitung müssen externe Pull-Up oder Pull-Down Widerstände vorhanden sein, wie z.B. in SPS-Steuerungen. Bitte Optokoppler-Maximaldaten beachten.

DCP 130-Reihe

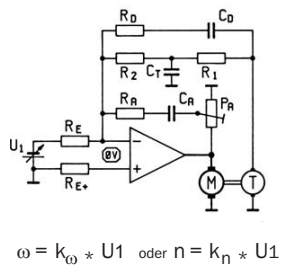
Beschaltungsmöglichkeiten

servowatt

Servo-Drehzahlregelungen

mit DC-Tachometer mit typischen Regelverhältnis 10.000: 1. In dieser Schaltung zeigen diese Verstärker ihre besonderen Qualitäten deutlich. Aufgrund der sehr hohen internen Verstärkung ist die Regelgüte ebenfalls sehr hoch und die Wellensteifigkeit gegen Störmomente, für viele überraschend, außergewöhnlich gut. Aus diesem Grunde können bestehende Aufgaben auch mit kleineren Motoren optimal gelöst werden.

Drehzahl-Servo mit Tachometer



Hochdynamisches Positionieren

mit hochwertigen Potentiometern und hochdynamischen Motoren. Mit einfachsten Mitteln lassen sich auf diese Weise hochgenaue und superschnelle Positionierungen realisieren. In einem Kreis wäre es z.B. möglich, 100 Positionen in der Zeit von 1 Sekunde nicht nur anzusteuern, sondern auch mit der erforderlichen Genauigkeit, d.h. inklusive Ausschwingen des Bewegungssystems zu positionieren. Bitte Info anfordern. Weniger spektakuläre Lösungen mit hervorragender Funktion lassen sich auch mit preiswerten Komponenten erreichen. Eine ganze Reihe von Potentiometern arbeiten heute sogar kontaktlos mit brauchbarer Genauigkeit.

Drehzahlregelung von hochdynamischen DC-Servomotoren mit DC-Tachometer

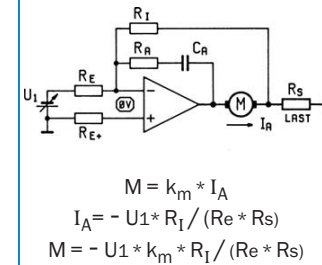
Winkelbeschleunigungen bis zu 200.000 rad/sec², entsprechend 2.000 U/min in 1 Millisekunde. Bis 10 Nm Impulsmoment. **Start-Stop Betrieb mit einem leisen Klick.** Solche extremen Geschwindigkeitsänderungen erfolgen sogar aperiodisch, d.h. ohne Überschwingen.



Kombinierte Servosysteme

durch gleichzeitige oder umgeschaltete Funktionen von Drehzahlregler und Drehmomentregler. Damit lassen sich z.B. für das Anfahren mit definierter Anpreßkraft gegen einen Anschlag (Schleifwerkzeuge) oder einen Abrichtdiamanten mit definiertem Moment positionieren. In anderen Applikationen werden kombinierte Spannungs-/Stromsteuerungen durchgeführt, um bestimmte Effekte zu erzielen.

Drehmoment-Servo



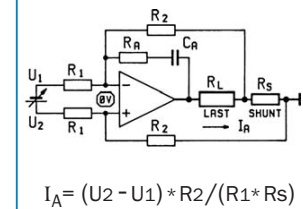
Geradeausverstärkung als bipolarer Spannungsregler / Verstärker

Geradeausverstärkung als bipolarer Spannungsregler/Verstärker, mit linearer oder besonders gewähltem Frequenzgang. Der interne Ausgangswiderstand / Quellwiderstand ist praktisch Null bzw praktisch nicht mehr messbar. Dies ist dann wichtig, wenn bei genauen Leistungsmessungen (z. B. Leistungs-Löschglieder in Lokomotiven) eine Quelle mit praktisch Null Ohm vorausgesetzt wird. Mit steigender Frequenz wird der Quellwiderstand am Ausgang zunehmend größer. In der Praxis darf man schon mit Null-Ohm Ausgangsimpedanz rechnen.

Bipolare Stromquelle

zum Einprägen eines Stromes auf alle Lasten, auch komplexe. Der Quellenwiderstand des Ausgangs ist praktisch unendlich, d.h. die Spannungen an einer komplexen Last z.B. einer EMK, L x di/dt und i x R werden allesamt unabhängig von ihrem Augenblickswert mit dem eingeprägten Strom durchflossen. Insbesondere Resonanzmessungen durch Frequenz-Wobbeln lassen sich mit solchen Stromquellen höchster Güte nicht nur qualitativ, sondern auch quantitativ genau durchführen.

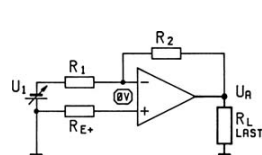
Stromregler mit Differenzeingang



Servoregelungen ohne Tacho

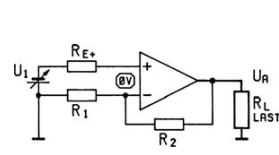
nur mit I x R-Kompensation. Regelverhältnisse von ca. 100:1 lassen sich praktisch nur mit DC-Motoren verwirklichen, die über eine sehr gute Bürstenkommutierung verfügen. Nur für unkritische Fälle geeignet. Wir empfehlen solche Schaltungen nicht.

Invertierender Verstärker



$$U_A = -U1 \cdot (R2 / R1)$$

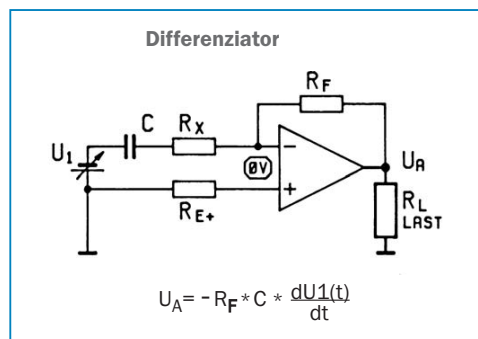
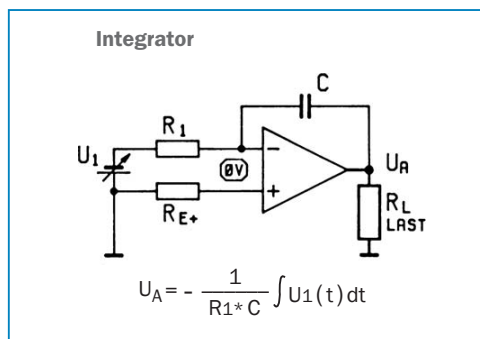
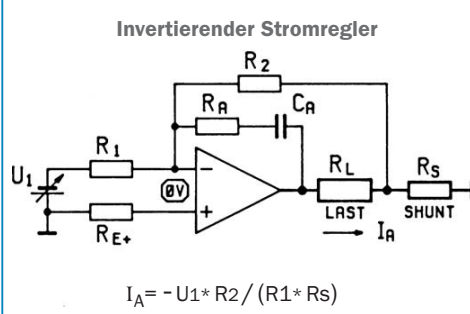
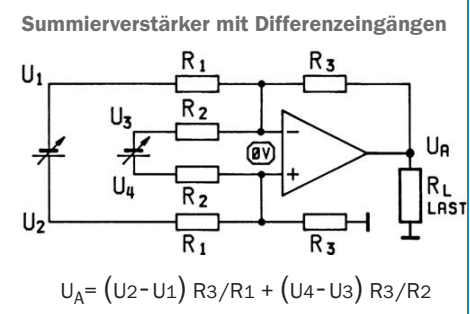
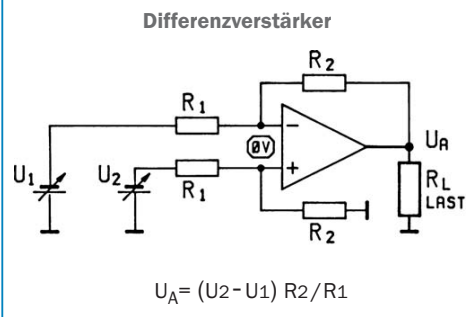
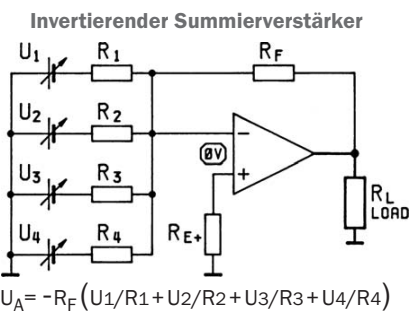
Nicht-invertierender Verstärker



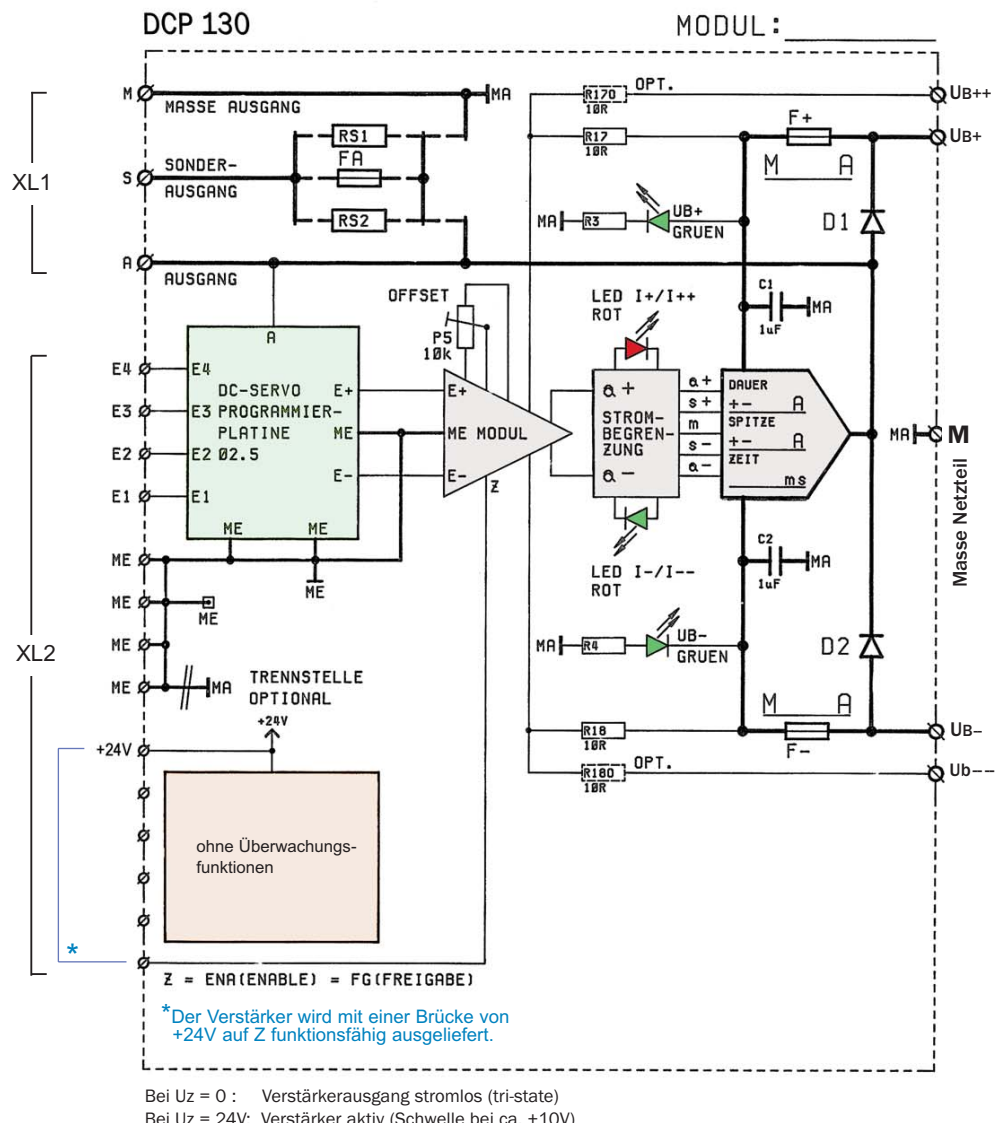
$$U_A = +U1 \cdot (1 + R2 / R1)$$

DCP 130-Reihe weitere Beschaltungsmöglichkeiten

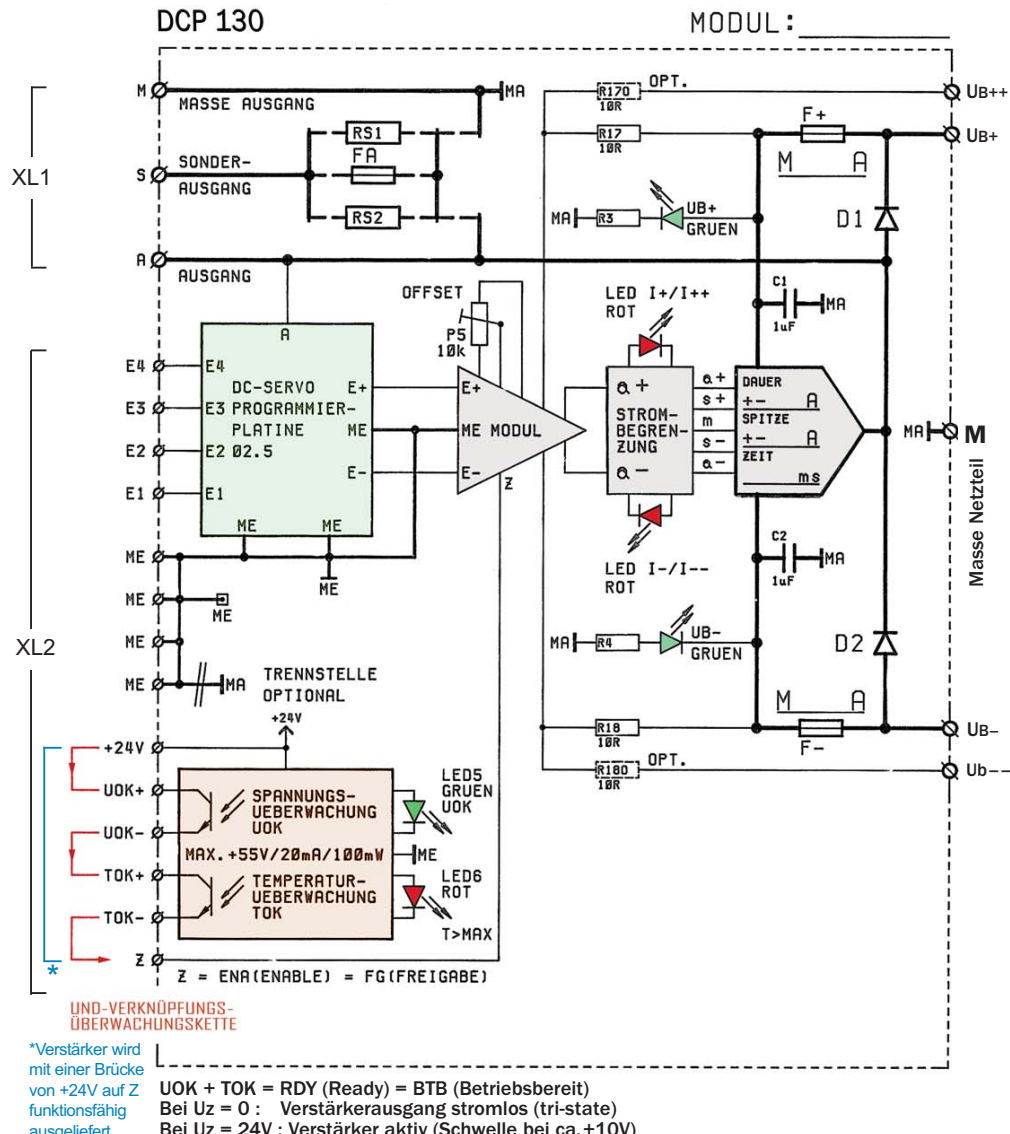
SERVOWATT



DCP 130-Reihe **Blockschatzbild ohne Überwachungsfunktionen** **servowatt**



DCP 130-Reihe **Blockschatzbild mit Überwachungsfunktionen** **servowatt**



DCP130 - Reihe Stabilisierte Zusatzversorgungen

servowatt

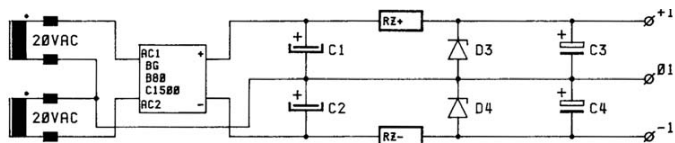
Für verschiedene Verbraucher kleinerer Leistungen wie z.B. Sollwertgeber, Potentionmeter, Referenzspannungsquellen, Umsetzer, Überwachungen, Inkrementalgeber usw. besteht die Möglichkeit, aus zwei 20VAC Hilfswicklungen verschiedene Zusatzversorgungen zu realisieren.

Folgende Möglichkeiten stehen Ihnen zur Verfügung:

- Vollweg-Gleichrichtung für kleine Restwelligkeit mit Plus- und Minusausgängen, vorzugsweise für höhere Leistungen
- Einweg-Gleichrichtung mit höherer Restwelligkeit, geeignet für kleinere Leistungen
- Einfache Stabilisierung mit Zenerdioden oder Referenz-Spannungsquellen
- Der Netztrafo in Standardausführung hat zwei 20VAC Zusatzwicklungen, die je bis 200mA belastet werden können. Für Kundenanwendungen können bis zu vier Wicklungen mit anderen Spannungswerten geliefert werden.

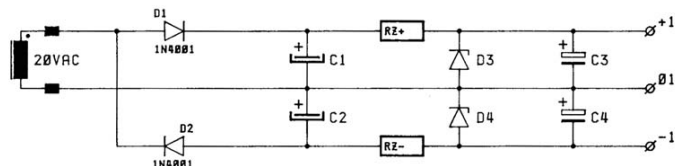
Schaltpläne für verschiedene Beschaltungsmöglichkeiten:

Mit Vollweggleichrichtung



Bipolare Spannungen zum Beispiel bis +- 24V DC
Für kleinere Leistungen, z.B. als Referenzspannungen

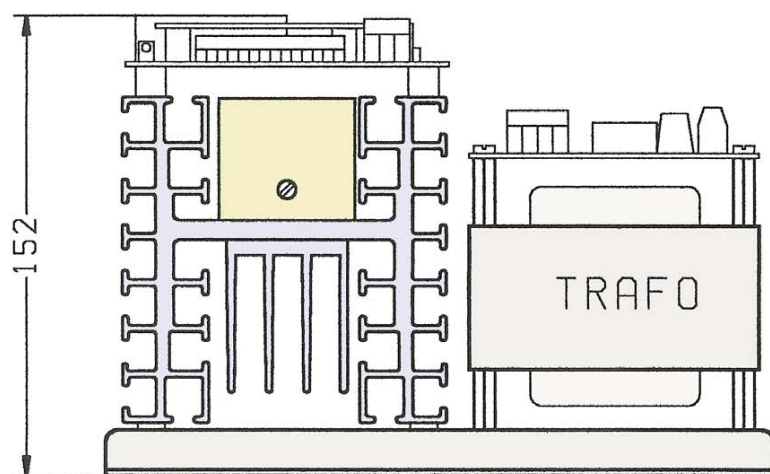
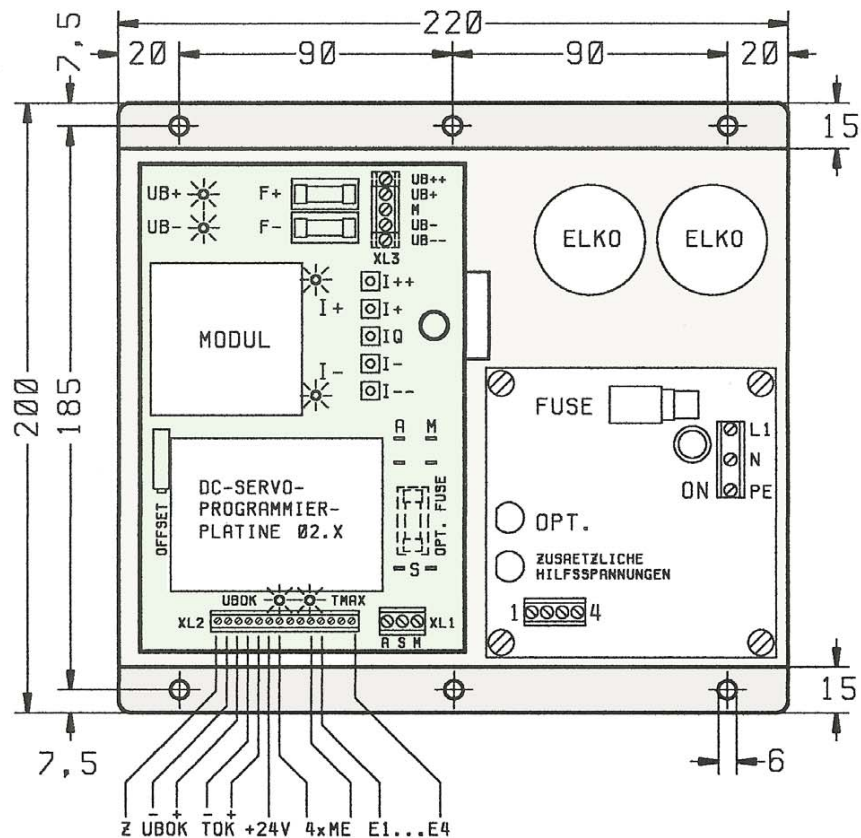
Mit Einweggleichrichtung



Bipolare Spannungen zum Beispiel bis +- 24V DC
Für kleinere Leistungen, z.B. als Referenzspannungen

DCP130 - Reihe Chassisabmessungen

servowatt



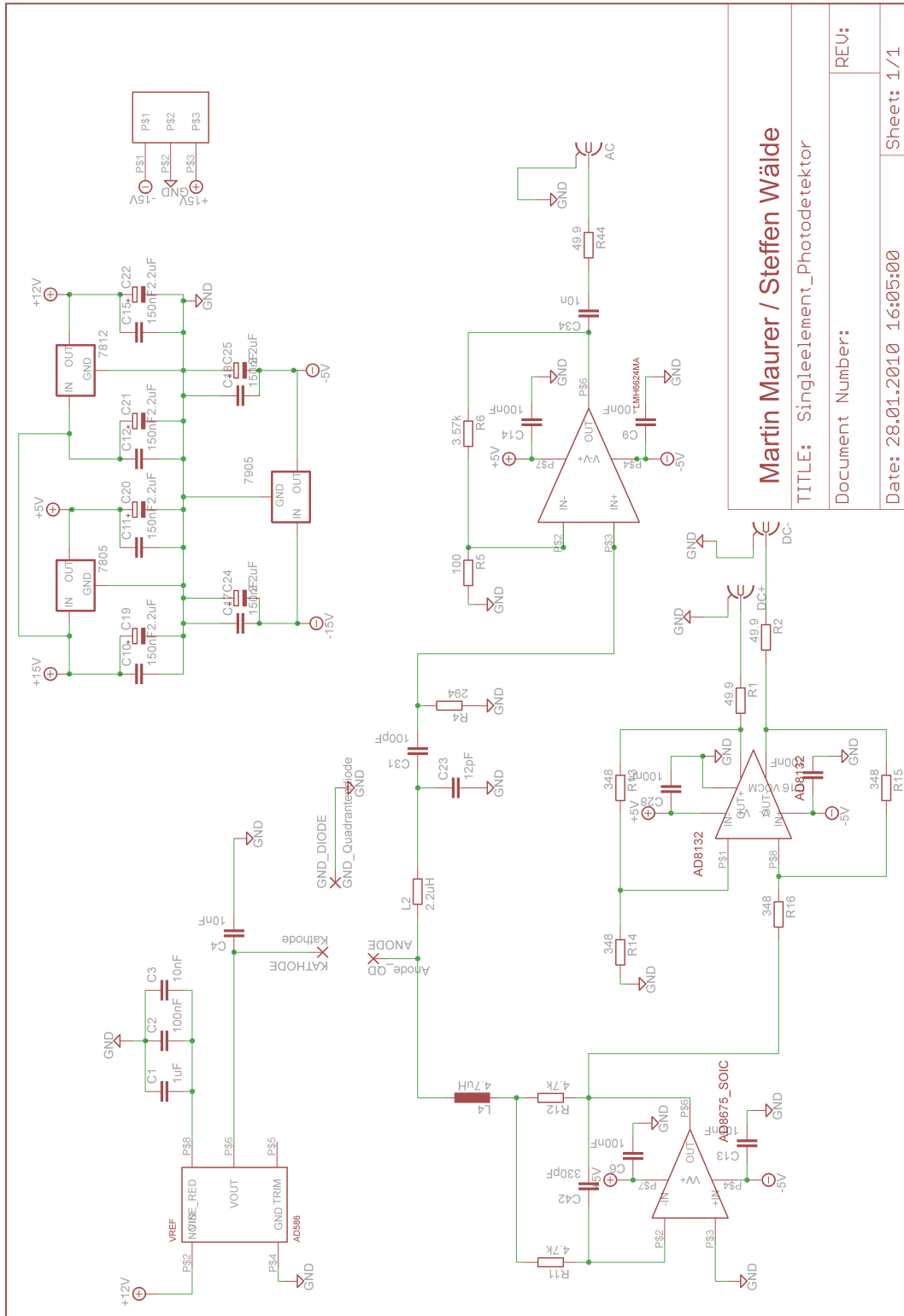
15

SERVOWATT GmbH, Graevenitz-Str. 1-5, 70839 Gerlingen, Tel: 0049-(0)7156-24041, Fax: -29944, Mail: info@servowatt.de

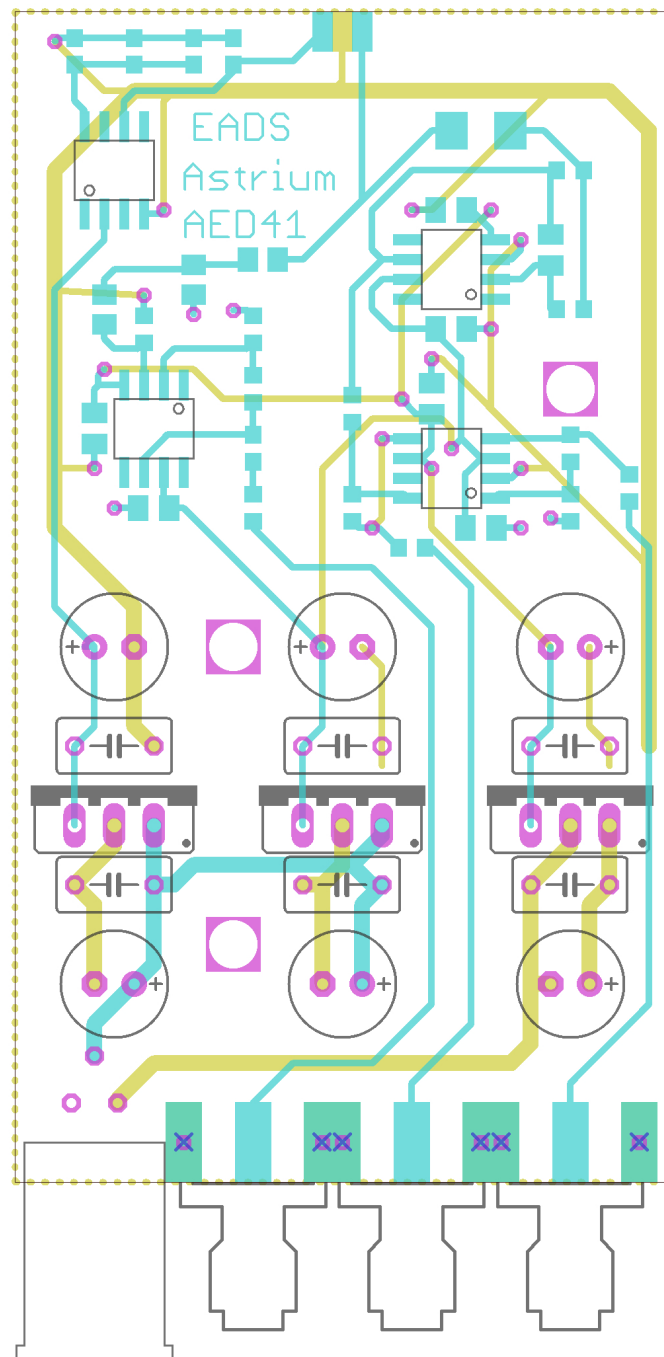
Appendix B

Circuit Diagrams

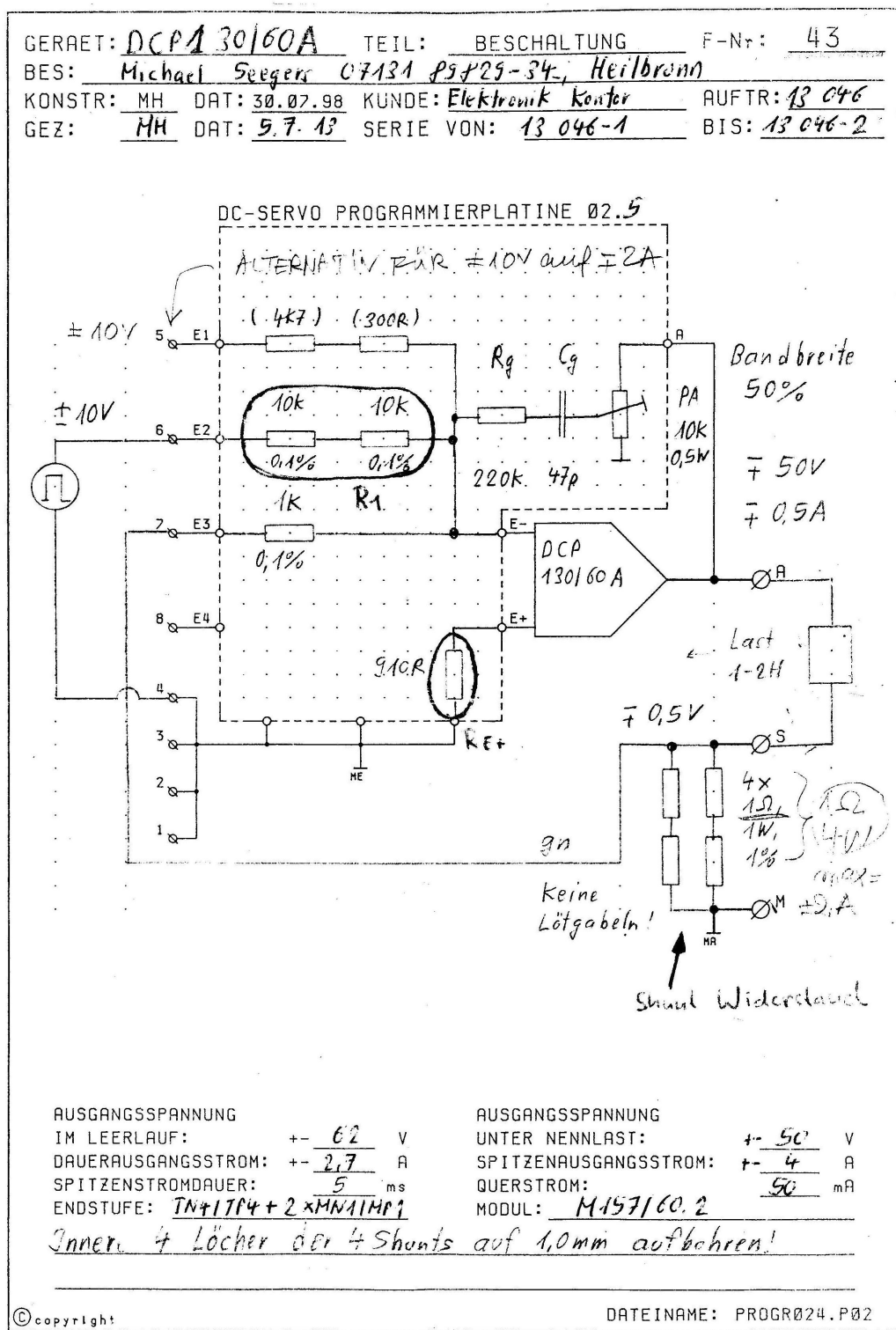
B.1 Circuit layout Singleelement Photodetektor



B.2 PCB layout Singleelement Photodetektor



B.3 DCP 130/60 adaption circuit layout



Bibliography

- [1] C. Moore, R. Cole and C. Berry. “Gravitational Wave Detectors and Sources”, <http://rhcole.com/apps/GWplotter/>.
- [2] P. Amaro-Seoane et al. “eLISA: Astrophysics and cosmology in the millihertz regime”. *GW Notes*, Vol. 6, p. 4-110, May 2013.
- [3] C. Brugger, B. Broll, E. Fitzsimons, U. Johann, W. Jonke, S. Lucarelli, S. Nikolov, M. Voert, D. Weise and G. Witvoet. “An experiment to test In-Field Pointing for eLISA”. *International Conference on Space Optics*, 2014.
- [4] D. Weise, P. Marenaci, P. Weimer, H. Reiner Schulte, P. Gath and U. Johann. “Alternative Opto-Mechanical Architectures for the LISA Instrument”. *Journal of Physics: Conference Series*, Vol. 154, Issue. 1, 2009.
- [5] B. Lange. “Managing Spherical Proof Masses in Drag-Free Satellites with Application to the LISA Experiment”. *Classical and Quantum Gravity*, Vol. 18, 2001.
- [6] T. Schuldt, M. Gohlke, D. Weise, U. Johann, A. Peters and C. Braxmaier. “Picometer and nanoradian optical heterodyne interferometry for translation and tilt metrology of the LISA gravitational reference sensor”. *Classical and Quantum Gravity*, Vol. 26, 2009.
- [7] T. Schuldt, M. Gohlke, H. Kögel, R. Spannagel, A. Peters, U. Johann, D. Weise and C. Braxmaier. “Picometre and nanoradian heterodyne interferometry and its application in dilatometry and surface metrology”. *Measurement Science and Technology*, Vol. 23, 2012.
- [8] T. Schuldt, M. Gohlke and A. Peters. “Optical subsystems for LISA”, <https://www.physik.hu-berlin.de/qom/research/sensor>.
- [9] E. Morrison, B. J. Meers, D. I. Robertson and H. Ward. “Automatic alignment of optical interferometers”. *Classical and Quantum Gravity*, Vol. 33, 1994.
- [10] E. Morrison, B. J. Meers, D. I. Robertson and H. Ward. “Experimental demonstration of an automatic alignment system for optical interferometers”. *Classical and Quantum Gravity*, Vol. 33, 1994.
- [11] H. Kögel, E. Fitzsimons, D. Gerardi, U. Johann, C. Braxmaier, and D. Weise. “Experimental investigations of an inertial reference sensor with spherical test mass and optical read out”. *Poster presented at the 10th International LISA Symposium Gainesville, USA (18-23 May) 2014*.

Bibliography

- [12] C. Birkenmaier. "Dimensioning, Setup and Test of a Heterodyne Frequency Generation for High Precision Laser Interferometry". Project Thesis, HTWG Konstanz, 2013.
- [13] C. Birkenmaier. "Development and Validation of an Electro Magnetic Levitation System for a Spherical Inertial Reference Sensor with Optical Readout". Bachelor's Thesis, HTWG Konstanz, 2013.
- [14] Xilinx Inc. *Virtex-5 Family Overview - DS100*, 2009.
- [15] National Instruments Corporation. *NI R Series Multifunction RIO User Manual - NI 781xR, NI 783xR, NI 784xR, NI 785xR Devices*, 2009.
- [16] National Instruments Corporation. *LabVIEW FPGA Module User Manual*, 2003-2004.
- [17] R. Paschotta. *Encyclopedia of Laser Physics and Technology*. Wiley-VCH, 2008.
- [18] S. Wälde and M. Maurer. "Dokumentation Quadrantdetektor und Singelelementdetektor". Technical report, 2010.
- [19] Hameg Instruments GmbH. *Programmable Power supply HM7044 - Manual*, 2004.
- [20] Ophir Photonics Solutions Ltd. *Ophir Photonic Nova II - Datasheet*.
- [21] Agilent Technologies. *E5061B Network Analyzer - User Manual*.
- [22] National Instruments Corporation. *M Series User Manual - NI 622x, NI 625x, and NI 628x Devices*, 2008.
- [23] LeCroy Corporation. *LeCroy WaveRunner Xi Series Oscilloscopes - Operator's Manual*, 2008.
- [24] J. Bechhoefer. "Feedback for physicists: A tutorial essay on control". *Reviews of Modern Physics*, Vol. 77, July 2005.
- [25] N. Ida, J. P. A. Bastos. *Electromagnetics and Calculation od Fields*. Springer, Second edition, 1997.
- [26] P. Mazzoldi, M. Nigro, C. Voci. *Fisica*. EdiSES, II edition, 2007.
- [27] R. C. Dorf. *The electrical engineering handbook*. CRC Press, Second edition, 1997.
- [28] Hirst Magnetic Instruments Ltd. *GM08 Gaussmeter Manual*.
- [29] Hirst Magnetic Instruments Ltd. *Axial Fluxgate Probe AFG100 - Operating Manual*.
- [30] E. Shameli. *Design, Implementation and Control of a Magnetic Levitation Device*. PhD thesis, University of Waterloo, 2008.